The Thesis Committee for Abdulwahab Saeed Alqahtani
Certifies that this is the approved version of the following Thesis:

New Polymer Rheology Models Based on Machine Learning

APPROVED BY
SUPERVISING COMMITTEE:

Matthew T. Balhoff, Supervisor

Gary A. Pope

New Polymer Rheology Models Based on Machine Learning

by

Abdulwahab Saeed Alqahtani

Thesis

Presented to the Faculty of the Graduate School of

The University of Texas at Austin

in Partial Fulfillment

of the Requirements

for the Degree of

Master of Science in Engineering

The University of Texas at Austin

August 2019

Dedication

To my parents, my wife and my son Ghaith.

Acknowledgements

I am forever grateful to Allah (God) for his countless blessings. I cannot take all of the credit for the success of this work. As such, I would like to acknowledge a few people of whom this work was made successfully possible.

First and foremost, I would like to express my sincere appreciation and gratitude to my academic advisor, Dr. Matthew Balhoff, for his continuous guidance, support and encouragement throughout this academic journey. He has been patient and generous with his time, and always quick to offer advice. I have gained immensely from his insights and I am honored to work with him. I would also like to extend my gratitude to Dr. Gary Pope for providing valuable comments and feedback on my thesis.

Special thanks are extended to my colleague Jacob Jaffray for providing assistance in the lab work. I am also thankful to my friend Thamer Alsulaimani for his insightful advices and suggestions on my study. I would also like to thank my sponsor Saudi ARAMCO for granting me this scholarship, and for their continuous support and follow up throughout my study.

Finally, my deep appreciation goes to my family, especially my parents and my wife, for providing me with endless support, encouragement and prays for me throughout my study. Without them, I may never have gotten to where I am today.

Abstract

New Polymer Rheology Models Based on Machine Learning

Abdulwahab Saeed Alqahtani, M.S.E.

The University of Texas at Austin, 2019

Supervisor: Matthew T. Balhoff

A successful polymer-type EOR project relies upon many factors, including an adequate characterization, description, and prediction of the polymer's rheology. A high polymer viscosity can improve the mobility and sweep efficiency, but can also lead to poor injectivity. Polymers are generally non-Newtonian and the rheology is a function of in-situ shear rate, polymer concentration, salinity, temperature, molecular weight, and molecular structure. A priori estimation of polymer rheology using models is important for design of polymer floods and prediction using numerical reservoir simulators. Existing models require many fitting parameters, are purely empirical, and can rarely be used for a priori estimation. The objective of this work was to develop new models to predict the viscosity of HPAM polymers used in enhanced oil recovery (EOR) and implement them into a chemical flooding numerical reservoir simulator. The study uses a combination of fundamental, physical models and machine learning methods to develop new predictive models. The data used in the study includes the measured polymer rheology at various polymer concentrations, molecular weights and types, temperatures, and brine salinity and hardness. Data are first fit to the 4-parameter Carreau's model and then advanced machine

learning techniques are used to develop the models of the Carreau parameters with the aforementioned solution properties. The models are then used to predict the rheology of new samples which are validated against data measured on an ARES G2 rheometer. All data fit the 4-parameter Carreau model well. The new models for the zero-shear viscosity, shear thinning index, and time constant are a function of temperature, polymer concentration, salinity, hardness, and molecular weight using less than ten parameters.

Table of Contents

List of Tables

List of Figures

CHAPTER 1. INTRODUCTION

1.1 OVERVIEW AND MOTIVATION

A typical conventional oilfield undergoes at least two stages of recovery throughout its life cycle: primary recovery and secondary recovery. Primary recovery is the phase during which the hydrocarbon is produced by the natural energy that exists in the reservoir such as the original reservoir pressure, rock and fluid expansion, gas cap, water influx from an underneath aquifer and gas in solution. Secondary recovery is the producing phase where the hydrocarbon recovery is mainly driven by an external source of energy such as gas injection or water flooding. The injected fluid helps maintain the reservoir pressure sufficient enough to produce at an economic level; this phase is often referred to as "pressure maintenance". Depending on the reservoir's productivity and recovery, an oilfield may undergo a third stage of recovery known as tertiary recovery. Tertiary recovery, or Enhanced Oil Recovery (EOR), is the stage in which specifically designed fluids, that interact with the rock and fluid system, are injected for the purpose of increasing oil recovery.

The average recovery percentage of a conventional oil field during the primary and secondary phases ranges between 35% to 50% of the original oil in place (OOIP) depending on the characteristics of the rock and fluid of the reservoir (Green & Willhite, 1998). EOR has been proven successful in producing much of the remaining oil and improving the ultimate recovery factor. For instance, Alkaline-Surfactant-Polymer (ASP) flooding produces about 25% incremental recovery of OOIP and polymer flooding (PF) about 14% of additional recovery of OOIP (Chang, et al., 2006).

The increasing interest of EOR combined with the complex nature of the rock-fluid system have led to the development of various EOR processes. Lake (1987) classified all

EOR methods into three different categories: chemical, thermal and solvents methods. EOR processes include but are not limited to polymer flooding, surfactant flooding, steam injection, and CO_2 injection.

Polymer flooding has been a source of interest in the EOR field due to its high success rate in recovering unswept oil reserves. Its viscosifying influence creates a favorable balance of mobilities between the injected fluid and the remaining oil; thus, maximizing the displacement and volumetric sweep efficiencies of the reservoir. For instance, it has been reported that polymer flooding has contributed to more 10% of recovery at Daqing field in northern China (Wang, et al., 2009). Therefore, polymer flooding applications have seen a progressive surge in science and engineering in recent years. A polyacrylamide-based polymer (e.g. HPAM) is one of the most extensively used polymers in chemical EOR processes due to their good solubility in water and cost-effective affordability (Manrique, et al., 2007).

Adequate characterization of polymer solution's viscosity plays a vital role in the success of a polymer flooding application. Polymers are generally non-Newtonian and the viscosity is a function of in-situ shear rate, polymer concentration, salinity, hardness, temperature, and molecular weight. Many researchers have studied the impact of those parameters on the viscosity of polymer's aqueous solution (Ward & Martin, 1981; Tam & Tiu, 1990; Nasr-EI-Din, et al., 1991; Sorbie, 1991; Levitt & Pope, 2008; Lee, et al., 2009; Hashmet, et al., 2014). This impact is complex in nature especially when considering the effect of more than one parameter at a time.

Laboratory experiments of polymer rheology is the most reliable approach for polymer viscosity characterization. However, experimental measurements are time-consuming and may be costly especially with the increased activity of polymer-related applications. This approach is even more exhaustive when covering a wide range of

parameters, which may be impractical to conduct. Thus, several empirical models have been developed for the purpose of predicting polymer solution's viscosity based on various conditions (Cannella, et al., 1988; Delshad, et al., 2008; Lee, et al., 2009; Kim, et al., 2010; Kang, et al., 2013; Hashmet, et al., 2014; Gao, 2014; Jouenne, et al., 2019). However, some of those correlations were established on limited range of data and are valid on specific assumptions. Other existing models require dozens of fitting parameters, are purely empirical, and can rarely be used for a priori estimation. As a result, these shortcomings may compromise the reliability and accuracy of polymer viscosity prediction. Additionally, this impact may affect the accuracy of results from a numerical reservoir simulator.

1.2 RESEARCH OBJECTIVE

A priori estimation of polymer rheology using robust modeling techniques is important for design of polymer floods and prediction using numerical reservoir simulators. Therefore, the objective of this study is to develop new predictive models to predict the viscosity of selective polymers used extensively in enhanced oil recovery for eventual implementation into a chemical flooding numerical reservoir simulator (e.g. UTCHEM). The study uses a database of existing experimental data and data from the literature for the rheology of polymers and use a combination of fundamental, physical models and machine learning methods to develop new predictive models. The data includes the measured polymer rheology at various shear rates, polymer molecular weights and types, temperatures, and brine salinity and hardness. Moreover, additional experimental measurements were conducted to gather more rheology data for the modeling. Data are first fit to the 4-parameter Carreau's model and then linear regression techniques are deployed to develop the models of the Carreau parameters with the aforementioned

solution properties. In addition, the study explores advanced machine learning algorithms, such as Random Forests and Artificial Neural Networks, to develop a more robust and reliable models to predict Carreau parameters at a given set of variables (concentration, salinity, etc.). The models are then used to predict the rheology of new samples accurately without the need to perform a whole set of rheology experimental measurements, which is time-consuming and expensive. Furthermore, the models can be used as an input parameter in a chemical flooding reservoir simulator, i.e. UTCEHM, to enhance the quality of rheology prediction and reduce uncertainty.

1.3 DESCRIPTION OF CHAPTERS:

In Chapter 2, a comprehensive literature review about the polymer rheology is discussed. It mainly covers fundamental concepts such as mobility control, polymer chemistry, viscoelasticity and modeling of polymer rheology. In addition, some existing model for predicting Carreau's parameters have been discussed. In Chapter 3, the rheology experimental procedure and measurements have been explained. Additionally, the modeling approaches used in this study, i.e. regression and advanced machine learning, have been thoroughly discussed. Following is Chapter 4, where the main results of our models are presented along with a discussion of the results and how it can be used. Then, conclusions and recommended future works are presented in Chapter 5. Following Chapter 5 are the references list and the appendixes.

CHAPTER 2. LITERATURE REVIEW

2.1 MOBILITY CONTROL

Polymers are mobility control agents and the understanding of fluid mobilities and the impact of polymers on them are of a great importance in the chemical EOR process. The highly-viscous injected polymer solution reduces the water mobility and thus can achieve a more efficient displacement (Green & Willhite, 1998). Manipulating the mobility of the fluids in the reservoir allows to control the flow of different fluids in a multiphase-fluid system. Therefore, oil recovery can be maximized, and water production can be minimized when a proper chemical EOR strategy is designed and implemented. Mobility is defined as follows (Dake, 1978):

$$\lambda_j = \frac{k k_{rj}}{\mu_j} \tag{2.1}$$

where λ_j is the mobility of phase j, k is the single-phase permeability, k_{rj} is the phase relative permeability, and μ_j is the phase viscosity. The mobility ratio (M) is the ratio of the displacing fluid mobility to the displaced phase mobility (Craig, 1971):

$$M = \frac{\lambda_{dsplacing}}{\lambda_{displaced}} = \frac{k_{rd}}{\mu_d}\frac{\mu_o}{k_{ro}} \tag{2.2}$$

A favorable mobility ratio is less than or equal to one ($M <= 1$), and when the ratio is greater than one ($M > 1$) it is considered unfavorable (Craig, 1971). Polymer is an example of a displacing fluid in chemical EOR whereas oil and connate reservoir water are the displaced fluid.

2.2 POLYMER CHEMISTRY

Most of the polymers used in EOR applications fall into two categories: polyacrylamide (PAM) and biopolymers. For instance, partially hydrolyzed

polyacrylamide (HPAM) and xanthan gum are common examples of synthetic polymers and biopolymer, respectively. In order to understand the reasons that led to the prominence of the aforementioned examples in EOR applications, it is necessary to consider the general characteristics of the polymer structures. Table 2.1 shows different molecular structures, their corresponding characteristics, and polymer examples. These characteristics define the criteria needed to select the optimum polymer and, based on them, HPAM is an excellent polymer for chemical EOR applications.

Table 2.1: Polymer structures and their characteristics (Zhao, 1991)

Structure	Characteristics	Sample polymers
-O- in the backbone	Low thermal stability, thermal degradation at high temperature, only suitable at temperature less than 80 ^{o}C	Polyoxyethylene, sodium alginate, sodium carboxymethyl cellulose, HEC, xanthan gum
Carbon chain in the backbone	Good thermal stability, degradation not severe at temperatures less than 110 ^{o}C	Polyvinyl, sodium polyacrylate, polyacrylamide, HPAM
--COO- in hydrophilic group	Good viscosifier, less adsorption on sandstones due to the repulsion between chain links, but precipitation with Ca^{2+} and Mg^{2+}, less chemical stability	Sodium alginate, sodium carboxymethyl cellulose, xanthan gum, HPAM
–OH or –CONH2 in hydrophilic group	No precipitation with Ca^{2+} and Mg^{2+}, good chemical stability, but no repulsion between chain links, thus less viscosifying powder, high adsorption due to hydrogen bond formed on sandstone rocks	Polyvinyl, HEC, Polyacrylamide, HPAM

2.2.2 The chemistry of PAM & HPAM

PAM is a class of polymers whose monomeric unit is the acrylamide molecule. When PAM undergoes a chemical reaction caused by water, the product is called hydrolyzed polyacrylamide. HPAM is a partially hydrolyzed synthetic straight-chain polymer of acrylamide monomers (Sorbie, 1991). The term "partially" implies that not all the acrylamide monomers have been hydrolyzed. HPAM molecular structure is a flexible chain known as random coil. It is obtained by copolymerization or hydrolysis of acrylamide and acrylate sodium (Olajire, 2014). Hydrolysis of PAM is done either under base or acidic conditions. It reacts with a base or acid and causes the negatively-charged anionic carboxyl groups (COO^-) to be distributed along the backbone chain. In other words, the hydrolysis converts of the amide groups ($CONH_2$) to carboxyl groups (COO^-) and the mole fraction of the converted amide groups is known as the degree of hydrolysis. HPAM may typically have a degree of hydrolysis in the range of 30%-35% (Lake, 1989). The degree of hydrolysis has a large impact on certain properties such as polymer adsorption, water solubility, and the rheological properties of HPAM solution. Shupe (1980) states that polymer will not be water soluble if the degree of hydrolysis is too low, and if it is too high, its properties will be sensitive to salinity and hardness.

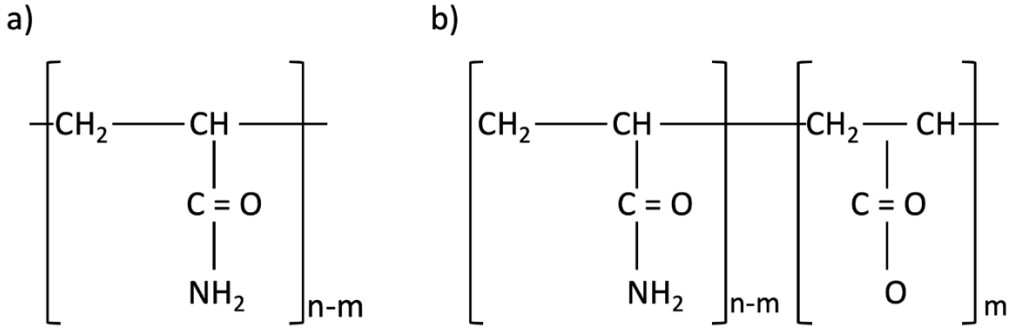

Figure 2.1: Structure of (a) polyacrylamide (PAM) and (b) partially hydrolyzed polyacrylamide (HPAM)

The large molecular weight of HPAM is the primary source for its viscosity-increasing feature (Lake, 1989). At low salinity, this feature is greatly emphasized when the negative charges on the backbone chain of the polymer repel each other, causing the flexible chain structure to elongate and, as a result, the viscosity increases. On the other hand, when the brine salinity is increased, by adding an electrolyte such as NaCl, this repulsion is shielded by an ionic layer of electrolytes and, thus, the flexible chain is compressed causing a lower viscosity.

2.3 RHEOLOGY

2.3.1 Experimental measurements of viscosity

There are different types of viscometers that are designed to determine the rheological properties of fluids, including polymer solutions used in EOR processes. One example is the capillary viscometer system shown in Figure 2.2, which is a basic viscometer used in the EOR field.

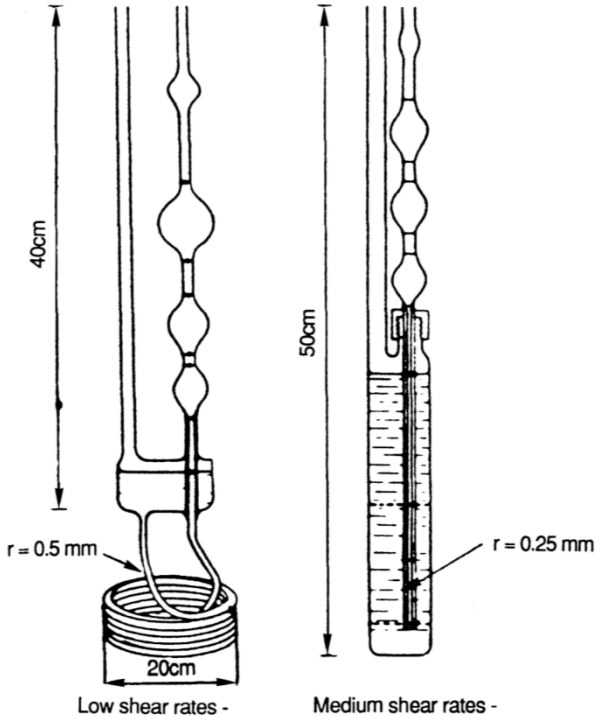

Figure 2.2: Capillary rheometer systems for viscosity measurements (Chauvetean, 1982)

Another common type is the Couette rheometer. Shown in Figure 2.3 is the geometry of the Couette rheometer. It has an outer cylinder that rotates at a defined angular velocity producing flow and creating torque on the inner cylinder. The sensor unit that records the torque is placed on the inner cylinder. The outside cylinder is jacketed for temperature control. The major advantage here is the absence of turbulent flow on low-viscosity fluids at high and low shear rates (Carreau, et al., 1997).

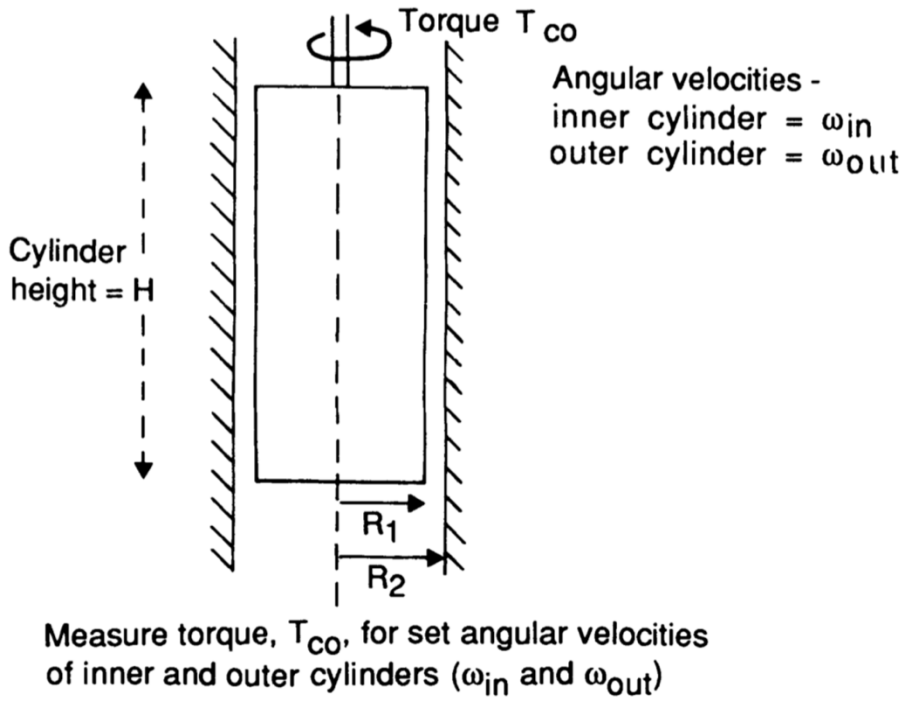

Figure 2.3: Geometry of the Couette rheometer (Sorbie, 1991)

2.3.2 Shear-thinning Behavior

A Newtonian fluid is characterized by the linear relationship between its shear stress and shear rate. However, polymer solutions generally exhibit non-Newtonian behavior, specifically shear-thinning, where the viscosity decreases with shear rate. This effect is often termed pseudoplastic fluid. The decrease in viscosity with shear rate is attributed to the fact that polymer chains disentangle and become oriented as the shear rate increases, resulting in uncoiled chains at intermediate and high shear rates (Han, 2007). Figure 2.4 shows typical viscosity versus shear rate behavior of a polymer solution, which demonstrates the shear-thinning effect.

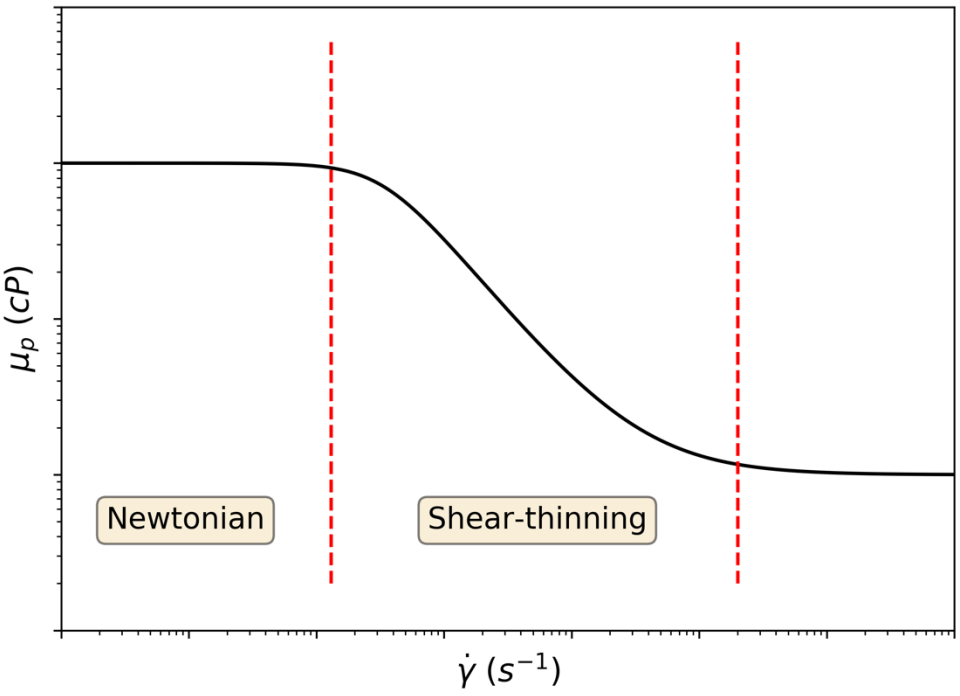

Figure 2.4: Typical viscosity versus shear rate curve of a shear-thinning fluid log-log scale

The behavior of shear-thinning is described by many constitutive models, the simplest being the power-law model (Bird, et al., 1960), which is given by:

$$\mu = K\dot{\gamma}^{n-1} \tag{2.3}$$

where n is the shear-thinning index and K is the flow consistency factor. For a Newtonian fluid, $n = 1$ and K is the constant viscosity. Although the power-law equation satisfies the shear-thinning behavior within the pseudoplastic regime, it fails to describe the viscosity at high and low shear rates, which often are Newtonian plateaus (Sorbie, 1991). A more

comprehensive model for pseudoplastic regimes is the Meter's equation (Meter & Bird, 1964), which is given by:

$$\mu_p - \mu_\infty = \frac{\mu_p^0 - \mu_\infty}{1 + \left(\frac{\dot{\gamma}}{\dot{\gamma}_{1/2}}\right)^{P_\alpha - 1}} \tag{2.4}$$

where μ_p, μ_p^0 and μ_∞ are apparent viscosity, zero-shear plateau viscosity, and the high-shear plateau viscosity (typically the solvent viscosity), respectively. $\dot{\gamma}$ and $\dot{\gamma}_{1/2}$ are the shear rate and the shear rate at which the viscosity is 50% of μ_p^0. P_α is a fitting constant. The 4-parameter Carreau's model (Carreau, 1972), also captures the Newtonian plateaus at low and high shear rate and shear-thinning behavior at intermediate shear rates,

$$\mu_p - \mu_\infty = \left(\mu_p^0 - \mu_\infty\right)\left(1 + (\lambda\dot{\gamma})^2\right)^{\frac{n-1}{2}} \tag{2.5}$$

where λ and n are time constant and shear-thinning index, respectively, and both of them are fitting parameters. For intermediate shear rates, the Carreau model mimics the behavior of the power-law model (Sorbie, 1991). The Carreau model provides the best fit to the experimental data and, therefore, it is the model that is most applied in this study (Bird, et al., 1974; Abdel-khalik, et al., 1974; Chauveteau & Zaitoun, 1981).

2.4 POLYMER PROPERTIES AND THEIR EFFECT ON RHEOLOGY

2.4.1 Polymer Concentration

The viscosity of polymer solution is very sensitive to polymer concentration. Figure 2.5 shows an example of the viscosity behavior of Xanthan for several different polymer concentrations. Several equations have been proposed to describe the effect of concentration on viscosity. Among the equations, the Flory-Huggins equation (Flory,

1953) describes the relationship between the zero-shear viscosity, the polymer concentration, and the intrinsic viscosity:

$$\frac{\eta_{sp}}{C_p} = \left(A_{p1} + A_{p2}C_p + A_{p3}C_p^2 + A_{p4}C_p^3 + \ldots\right) \tag{2.6}$$

where C_p is the polymer concentration, A_{p1}, $A_{p2}\ldots A_{pi}$ are fitting constants, and η_{sp} is the specific viscosity and is defined by:

$$\eta_{sp} = \frac{\mu_p^0 - \mu_s}{\mu_s} \tag{2.7}$$

where μ_s is the solvent viscosity. Although the equation is infinite series, a finite number of terms is used for dilute solution (Sorbie, 1991; Sheng, 2010). The Martin equation (Martin, 1951) is another equation that is used for describing the zero-shear viscosity of dilute polymer solutions. The Martin equation in the logarithmic form is given by:

$$\ln\left(\frac{\eta_{sp}}{C_p}\right) = \ln(k_1) + k_2 C_p \tag{2.8}$$

where k_1 is the intrinsic viscosity ($[\eta]$), and k_2 is a constant. Note that a Taylor-Series expansion of equation 2.8 yields an infinite series identical in form to the Taylor-Series expansion, where the coefficients are given by:

$$A_{pi} = k_1 k_2^{i-1} \tag{2.9}$$

In practice, the coefficients are often treated as individual fitting constants. Fittings parameters of equations 2.6 or 2.8 can be obtained directly from curve fitting to experimental data and can be used in prediction models. Figure 2.6 shows a plot of the left-hand side of Eq. 2.8 versus the polymer concentration. The extrapolation to zero polymer concentration yields the intrinsic viscosity and the slope yields k_2. Lovell (1996) stated some experimental data may show a sign of curvature especially at high polymer concentration and such phenomenon should be carefully identified. He concluded that if the experimental data is linearly smooth, Martin's equation is capable of providing a good estimation of the intrinsic viscosity. Carreau et al. (1997) defined the intrinsic viscosity as

a measure of the hydrodynamic volume of polymer molecule in a given solvent. In mathematical terms, the intrinsic viscosity is given by:

$$[\eta] = \lim_{C_p \to 0} \left(\frac{\mu_p^0 - \mu_s}{\mu_s C_p} \right) = \lim_{C_p \to 0} \left(\frac{\eta_{sp}}{C_p} \right) \qquad (2.10)$$

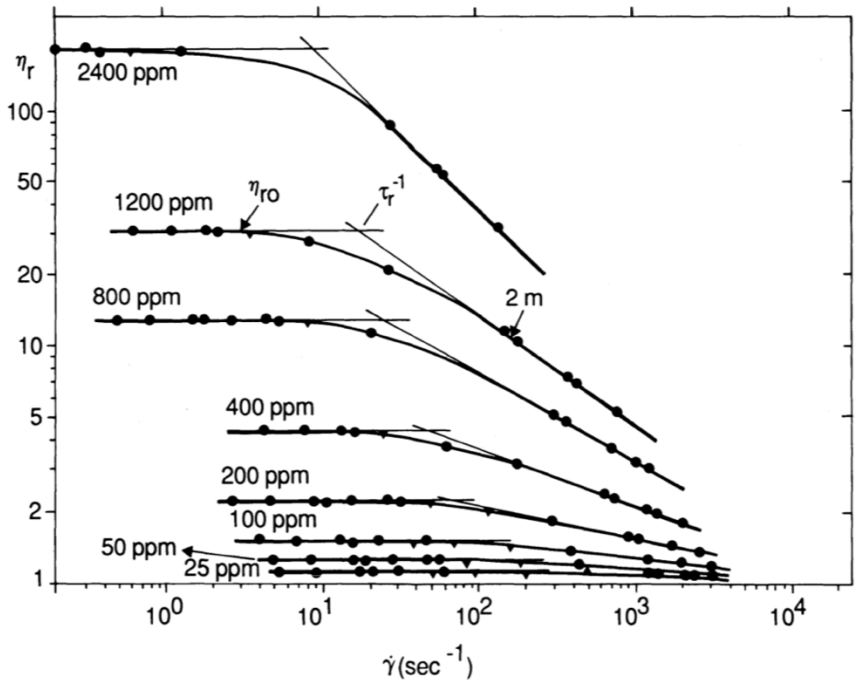

Figure 2.5: Viscosity behavior of Xanthan solution at 5g/l and 30°C (Chauvetean, 1982)

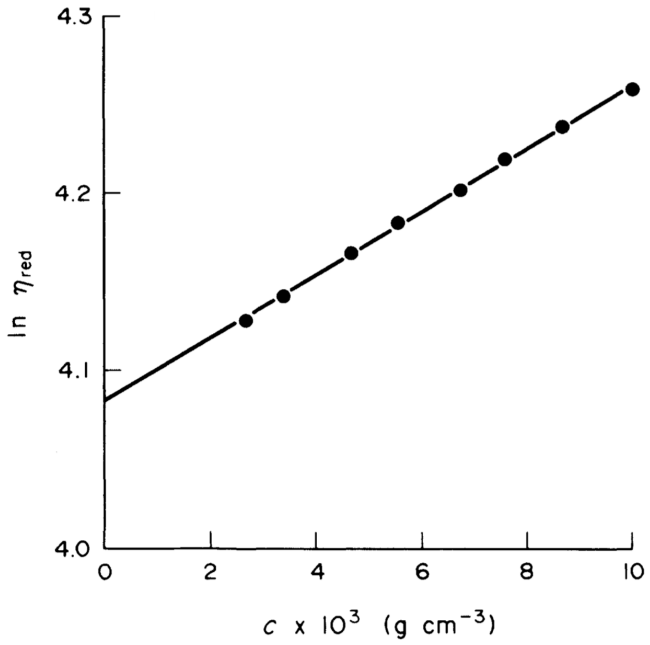

Figure 2.6: Fit of poly(f-butyl acrylate) polymer data to Martin's equation at 25°C (Lovell, 1996)

2.4.2 Salinity

The viscosity of most polymer solutions tends to decrease with increasing salinity (Lake, 1989). When an electrolyte, e.g. NaCl salt, is added to polymer solution, the negatively-charged field produced by the molecular chain (COO^-) is screened out by the counter ions such as Na^+. As a result, the repulsive force along the chain is reduced and the chain is compressed, which leads to a reduction in the viscosity. Figure 2.7 shows the effect of salinity, specifically NaCl concentration, on HPAM polymer solution viscosity. However, the magnitude of the reduction in viscosity is associated with the valency of salts (Tam & Tiu, 1990). For instance, divalent salt, such as $MgCl_2$ and $CaCl_2$, may cause a larger reduction in viscosity than monovalent salts, such as NaCl, for the same given conditions, as shown in Figure 2.8.

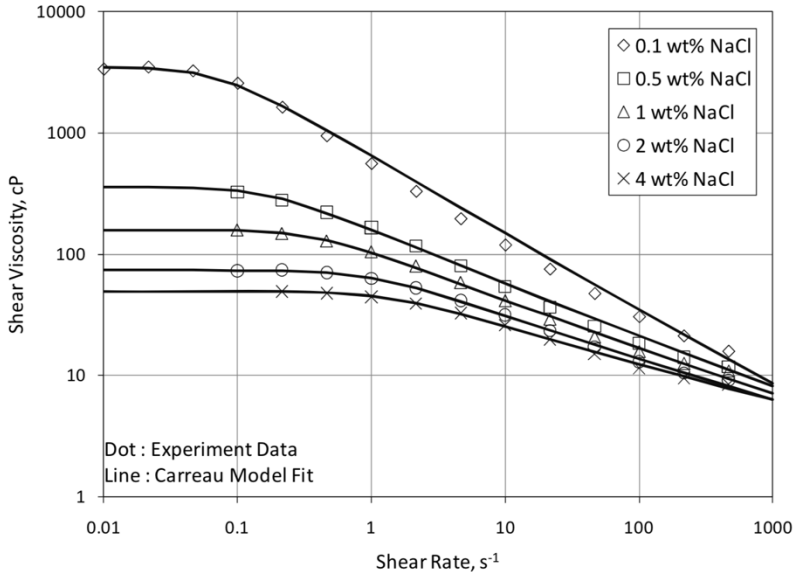

Figure 2.7: Effect of NaCl concentration on shear viscosity (2000 ppm FP3630S at 25℃) (Lee, et al., 2009)

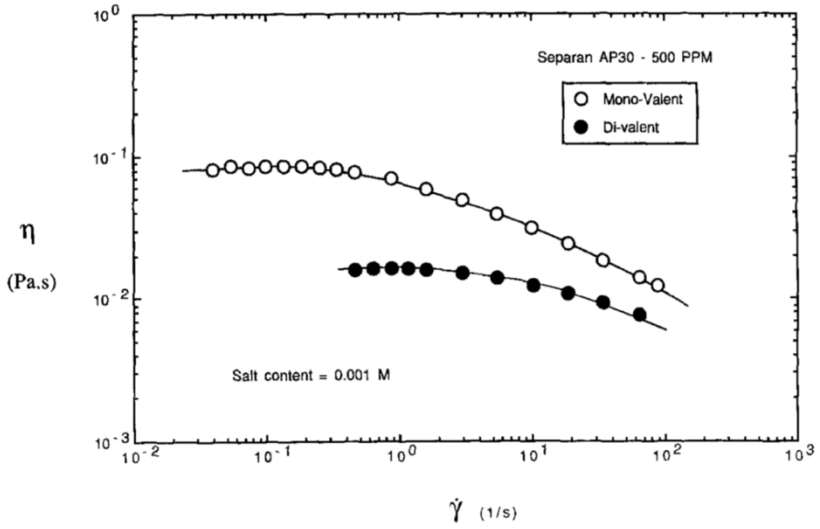

Figure 2.8: Comparison of the effects of monovalent and divalent (hardness) salts on the viscosity (500 pprn Separan AP30 polymer solution) (Tam & Tiu, 1990)

It has been shown, empirically, that intrinsic viscosity of HPAM decreases with salinity in a power law relationship of the form:

$$[\eta] = k_1 = kC_{sep}^{S_p} \tag{2.11}$$

Where k_1 is the intrinsic viscosity, C_{sep} is the effective salinity in meq/mL, k and S_p are fitting parameters and S_p is less than 1.0. C_{sep} is defined in UTCHEM, the University of Texas chemical flood simulator, (UTCHEM, 2018) as follows:

$$C_{sep} = \frac{C_{51} + (\beta_p - 1)C_{61}}{C_{11}} \tag{2.12}$$

Where C_{51} and C_{61} are the monovalent and divalent (hardness) concentrations in meq/mL, C_{11} is water concentration in the polymer solution in fraction, and β_p is a fitting parameter whose typical value is 10 (Sheng, 2010). Substitution of Eq. 2.11 into the Martin equation or Flory-Huggins equation gives an equation for viscosity as function of both concentration and salinity. Substituting Eq. 2.11 into Eq. 2.8 yields:

$$\ln\left(\frac{\eta_{sp}}{C_p}\right) = \ln\left(kC_{sep}^{S_p}\right) + k_2 C_p \tag{2.13}$$

Eq. 13 may be fitted to experimental rheology data to obtain the fitting parameters for a certain polymer type, which can be used later for prediction of zero-shear viscosity at any given polymer, monovalent, and hardness concentrations.

2.4.3 Temperature

Polymer viscosity increases as the temperature of the polymer solution decreases, as shown in Figure 2.9. This is attributed to the fact that the activities between the polymer molecules chains are excited when the temperature is increased, leading to less friction between them. As a result, the polymer solution viscosity is reduced. The Arrhenius

equation represents the relationship between the apparent viscosity of polymer solution and its temperature as follows:

$$\mu_p = A_p \exp\left[\frac{E_a}{RT}\right] \tag{2.14}$$

where A_p is the frequency factor of polymer solution, E_a is the activity energy, R is the universal gas constant, and T is the absolute temperature. Both A_p and E_a are function of the polymer concentration, solvent, and the distribution of the molecular weight (Shah & Parsania, 1984). Polymers typically have much larger E_a values than low molecular weight liquids and it increases with chain rigidity (Carreau, et al., 1997). The variation of polymer viscosity due to a change in the temperature can be quantified by the following equation:

$$\frac{\Delta\mu_p}{\mu_p} = -\frac{E_a}{RT^2}\Delta T \tag{2.15}$$

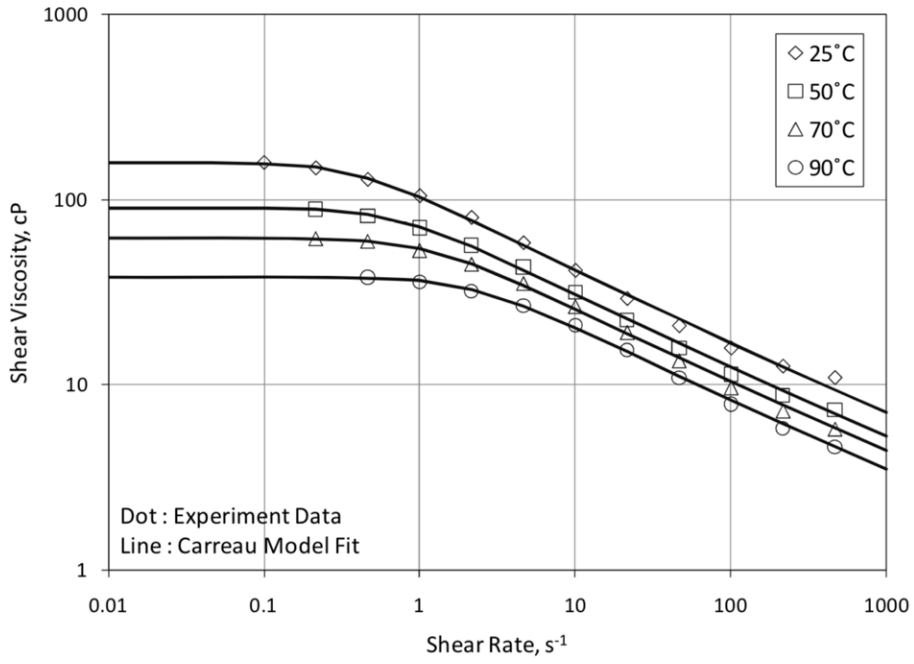

Figure 2.9: Effect of temperature on the apparent viscosity (2000 ppm FP3630S, 1% NaCl) (Lee, et al., 2009)

2.4.4 Molecular Weight

Generally, larger molecular size leads to a higher viscosity of polymer solution (Sorbie, 1991). The Mark-Houwink relation suggests that the intrinsic viscosity of a polymer solution depends on the molecular weight of the polymer as follows:

$$[\eta] = K'M^a \tag{2.16}$$

where $[\eta]$ is the intrinsic viscosity in cm^3/g, *K'* and *a* are polymer-specific constants in a particular solvent at a given temperature. The value of *a* typically ranges between 0.5 to 1.5 and *K*' between $3\text{-}700\times10^{-5}$ cm^3/g (Sorbie, 1991). Therefore, for any given polymer solution, the intrinsic viscosity increases as the polymer's molecular weight increases.

2.5 VISCOELASTICITY:

A viscoelastic fluid exhibits both elastic and viscous characteristics when a stress is applied. The two components comprising the viscoelasticity, viscosity and elasticity, individually exhibit completely different behavior. For a simple viscous Newtonian fluid, the viscosity behavior of the fluid is described by the following Newtonian stress-strain rate relationship:

$$\tau = \mu\dot{\gamma} \tag{2.17}$$

where τ is the shear stress. On the other hand, when a material has the ability to return to its original shape after undergoing deformation, this material is elastic. The elastic component can be described by Hooke's law as follows:

$$\tau = G'\gamma \tag{2.18}$$

where *G*' is the elastic modules of the material and γ is the strain caused by a given stress. For a viscoelastic fluid, Maxwell (Young & Lovell, 1991) proposed a possible constitutive relationship between the fluid stress and the strain:

$$\frac{\tau}{\mu} + \frac{1}{G'}\frac{\partial\tau}{\partial t} = \dot{\gamma} \tag{2.19}$$

The Maxwell model assumes a pure viscous damper and a pure spring, which are described by Newton's law and Hooke's law, respectively, which are connected in series.

Rheological characterization of purely viscous fluids is traditionally achieved through steady shear flow measurements. That is, a simple experimental setup where the tested fluid is contained between two parallel plates, one of which is stationary. However, this type of measurements is incapable of providing sufficient information about the structure of the fluid. As a result, this type of measurement is deemed unsatisfactory for viscoelastic fluid characterization. Alternatively, dynamic oscillatory rheological measurements are used to characterize both the viscous and the elastic properties of a material. Unlike the steady shear measurement where a unidirectional and continuous movement is imposed, the basic principle behind the oscillatory measurement is to induce a sinusoidal movement in the sample and measure the resultant stress response. Viscoelastic fluids show a response that contains in-phase and out-of-phase components. These components reveal the extents of solid-like and liquid-like behavior. The viscoelastic behavior is characterized by the storage or elastic modulus, G', and the loss or viscous modulus, G'', which are defined by the in-phase component and out-of-phase component, respectively. The elastic modulus provides information about the elastic behavior of the material and the viscous modulus characterizes the viscous behavior. Therefore, the dynamic oscillatory measurement is an effective tool for understanding the structure of a viscoelastic system and adequately charactering its dynamic properties.

An important characteristic element observed in materials as a result of viscoelastic deformation is the relaxation time (τ_r). The relaxation time is the time required for the viscoelastic polymer solution to respond to the changes of flow behavior in the porous medium (Sheng, 2010). In other words, it is the time required for the polymer molecule to relax after undergoing elongation due to varying flow geometry. The elongation

phenomenon of a polymer molecule is described in the following section. One way of characterizing the viscoelasticity of a polymer is by computing the ratio of the relaxation time to the characteristic experimental time (t_c). This ratio is known as the Deborah number (N_{Deb}), and it is given by:

$$\mathrm{N_{Deb}} = \frac{\tau_r}{t_c} \tag{2.20}$$

A large N_{Deb} corresponds to a solid-like behavior and a small N_{Deb} results in a viscous-like behavior. The estimation of the relaxation time can be determined by several methods (Bird, et al., 1987; Xia, et al., 2004). However, one common estimation of the relaxation time is found from the *G*' and *G*" cross plots, where the inverse of frequency at which both plots intersect is the relaxation time (Sorbie, 1991; Castelletto, et al., 2004; Erincik, et al., 2017). Figure 2.10 shows a typical *G*' and *G*" cross plots obtained from a dynamic frequency test.

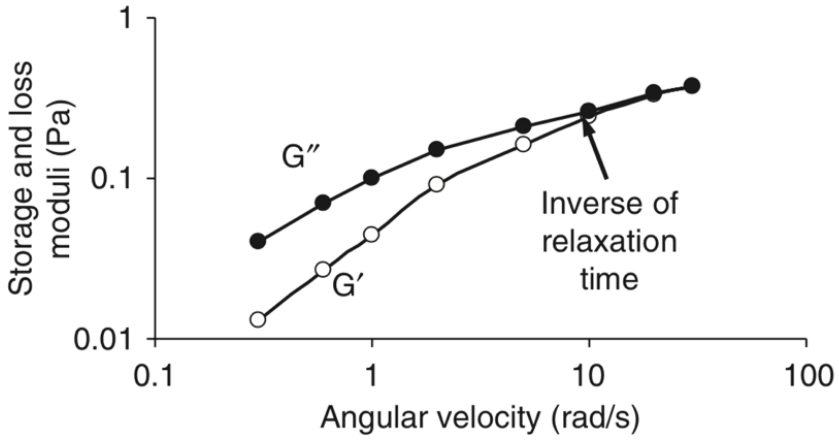

Figure 2.10: Typical *G*' and *G*" cross plots (Sorbie, 1991)

2.6 POROUS MEDIUM IN-SITU RHEOLOGY OF HPAM

The rheology of polymers is generally affected by many factors including the molecular weight, the degree of hydrolysis and other solvent-related properties. However, one important factor that has a great influence on the polymer rheology, especially HPAM, is the flow medium. Thus, the rheology of polymer solutions as they flow through a porous medium is discussed in this section.

The microscopic structure and geometry of the pores and pore throats play an important role in defining the flow behavior and the rheology of the flexible-coil polymers, e.g. HPAM. In addition, the tortuous flow path exists in porous media introduces additional complexity to the in-situ rheology of polymer solutions. An accurate representation of the porous medium structure by a robust mathematical model is a significant aspect of modeling the in-situ rheology and flow behavior. Many studies have adopted the continuum approach for describing the fluid flow in porous media, e.g. Darcy's law, without considering the pore structure, especially at the microscopic level. Although, such an approach has been successfully applied, it has failed to explain many flow observations at the microscopic scale (Sorbie, 1991). Thus, many direct microscopic examinations of pore structure have been implemented for modeling the porous medium at the pore scale. However, the concept of capillary bundles (tubes) have been prominently used in representing porous medium. Despite the shortcomings of the capillary bundles model, such as the inability to incorporate the anisotropy of permeability and pore size distribution, it has surprisingly shown good results when correlating the in-situ rheological properties.

Many theoretical approaches have been developed to analyze the in-situ rheology of polymer solutions. Sorbie (1991) presented four general possible approaches as follows:

i. A numerical solution to solve the fluid mechanical calculation

ii. Developing empirical correlations for such quantities as in-situ effective shear rate, Deborah number, etc.

iii. Deriving certain flow properties using the Effective Medium Theory.

iv. Network calculations involving non-Newtonian effects.

Among them all, the second approach has dominated the modeling of in-situ rheology. As stated, this approach involves the developing empirical correlations for different rheological quantities. For example, for a purely shear-thinning fluid, the capillary bundles model for a porous medium is coupled with the power law model for fluid to describe of the in-situ rheology. Hirasaki and Pope (1974), Teeuw and Hesselink (1980), and Cannella et al. (1988) among others have introduced similar models based on the very same approach. One advantage of this empirical approach is that the elastic and inelastic fluids are both considered. In addition, the obtained simple expressions from such an approach may provide an indication about the physics of the flow (Sorbie, 1991). Based on this approach, the effective shear rate, that is the shear rate in porous medium, or the equivalent shear rate, should be considered for the flow calculation in porous media. Thus, the effective shear rate is derived using the formula at the capillary wall and is given by:

$$\dot{\gamma}_{eff} = \left(\frac{3n+1}{4n}\right)\alpha\frac{4u}{\sqrt{8k\phi}} \tag{2.21}$$

Where n is the flow exponent, sometimes referred to as shear-thinning index, (n=1 for Newtonian fluid), u is the Darcy velocity in porous media, ϕ is the porosity, and α is a fitting parameter. Cannella et al. (1988) proposed a slightly different expression by which the fluid saturation and the fluid relative permeability are incorporated as follows:

$$\dot{\gamma}_{eff} = C\left(\frac{3n+1}{4n}\right)^{\frac{n}{n-1}}\frac{u}{\sqrt{kk_{rw}S_w\phi}} \tag{2.22}$$

where k_{rw} is the water relative permeability, S_w is the water saturation, and C is the shear correction factor. When C = 6, the above equation fits a wide range of core flood data

(Cannella, et al., 1988). Furthermore, since this approach assumes a power-law fluid, the apparent viscosity corresponding to the effective shear rate is given by Eq. 2.3. Koh, et al. (2017) defined the effective shear rate based on the fractional flow theory as follows:

$$\dot{\gamma}_{eff} = C\left(\frac{3n+1}{4n}\right)^{\frac{n}{n-1}} \frac{4uf_w}{\sqrt{8kk_{rw}S_w\phi}} \tag{2.23}$$

where f_w is given by:

$$f_w = \frac{1}{1+\frac{k_{ro}\mu_w}{k_{rw}\mu_o}} \tag{2.24}$$

where k_{ro} and k_{rw} are oil and water relative permeabilities, respectively. $C = 4$ was reported to match the apparent viscosity of polymer in core floods regardless of the core properties (Koh, et al., 2017). Moreover, permeability reduction should be considered where polymer retention or adsorption may occur. If permeability reduction is ignored, assuming it exists, the effective shear rate may be underestimated and ultimately the apparent viscosity is overestimated.

2.7 SHEAR-THICKENING VISCOSITY

As stated previously, most polymer solutions exhibit shear-thinning behavior when undergoing simple shear flow. However, when a polymer solution flows through a capillary with varying cross-sections, e.g. porous media, the polymer fluid is stretched and therefore another flow behavior evolves, namely elongational or extensional flow. In elongational flow, also known as shear-free flow (Bird, et al., 1987) and dilatant flow behavior, the apparent viscosity increases with increasing shear rate, i.e. shear-thickening. This increase in viscosity is attributed to the elongation of macromolecules which results in a detectable increase in the viscous friction and marks the start of the dilatancy (Sheng,

2010). Mathematically, the normal stress differences-elongation rate relationship is described as follows:

$$(\tau_{zz} - \tau_{xx}) = \eta(\dot{\varepsilon})\dot{\varepsilon} \quad (2.25)$$

where η is the elongational or shear-thickening viscosity, and $\dot{\varepsilon}$ is the elongation rate. Importantly, the elongational rate, the stretch rate, and the deformation rate are all terms used interchangeably by different authors and they refer to the same thing (Chauveteau & Zaitoun, 1981; Sorbie, 1991; Sheng, 2010). Although the elongation rate is a better parameter for describing the elongational flow behavior, especially at the constriction points along the flow path, several studies indicate that it is difficult to establish the elongational flow and, as a result, the determination of elongational viscosity becomes a hurdle. However, for fluids that exhibit shear-thinning behavior, i.e. polymer solutions, it is suggested that the elongational viscosity at low elongational rate is approximately three times the low shear-rate viscosity (Stevenson, 1972).

Although most polymers are shear-thinning, those that are viscoelastic show shear-thickening behavior at moderate-to-high fluid velocities (shear rates) in porous media. This behavior has been captured by many researchers including Hirasaki and Pope (1974), Heemskerk et al. (1984), and Masuda et al. (1992). Their attempts were focused on modeling the shear-thickening behavior of polymer solution in terms of molecular parameters and fluid flow conditions. However, (Delshad, et al., 2008) proposed a more comprehensive model for the apparent viscosity (μ_{app}) that covers the full flow velocity spectrum and accounts for both shear-thinning and shear-thickening behavior. Their approach was based on oscillatory and steady shear viscosity measurements as well as polymer flow core-flood experiments. Their empirical model is given by:

$$\mu_{app} = \mu_\infty + \left(\mu_p^0 - \mu_\infty\right)\left[1 + \left(\lambda + \gamma_{eff}\right)^\alpha\right]^{\frac{n-1}{\alpha}} + \mu_{max}\left[1 - \exp\left(-\left(\lambda_2 \tau_r \gamma_{eff}\right)^{n_2 - 1}\right)\right] \quad (2.26)$$

where μ_{max}, λ_2, and n_2 are empirical constants. Their model consists of two parts; shear-thinning component demonstrated by Carreau's model and shear-thickening (μ_{el}) component. The subscript in μ_{el} indicates the elongational viscosity, which is the viscosity attributed to the elongation rate that occur during shear-thickening. Delshad et al. (2008) assumed that μ_{el} is an empirical function of Deborah Number. Therefore, by assuming that the average residence time (τ_E) is equal to the inverse of the effective shear rate (Masuda, et al., 1992), the Deborah number can be defined as follows:

$$N_{Deb} = \frac{\tau_r}{\tau_E} = \tau_r \dot{\gamma}_{eff} \qquad (2.27)$$

The model has been verified against a wide range of shear viscosity and core flood data of several polymer solutions and showed an excellent fit with the laboratory data. Furthermore, the model was implemented in UTCHEM, the University of Texas chemical-flooding reservoir simulator, and successfully history-matched published polymer-flood results (Delshad, et al., 2008).

2.8 EXISTING RHEOLOGY MODELS

Many researchers have developed models that describe the polymer rheology, specifically the viscosity, under different fluid-flow conditions. Some of them have already been covered in the previous sections, i.e. shear-thinning models such as Carreau's model. However, in this section, we will focus on a number of selective models that are either very widely used or related to the core of this study.

2.8.1 Lee et al. (2009):

The need for a comprehensive database for polymer rheological properties is important for the development of EOR applications. Lee et al. (2009) claimed that the existing rheological data of polymers available in the literature was not sufficient for establishing a comprehensive database and additional data was needed. Thus, extensive rheological measurements were conducted on selected polymer types, mainly HPAM, to investigate the dependence of the apparent viscosity of polymer solution on various process variables such as polymer concentration and salinity (monovalent and divalent). The experimental data, which was captured through shear-steady and dynamic oscillatory viscosity measurements, was designed to cover a wide range of polymer properties and reservoir conditions such that the proposed models can be sufficiently comprehensive and capable to perform under various flow circumstances. Table 2.2 shows the tested polymers and their properties.

Table 2.2: Polymers tested (Lee et al., 2009)

Polymer	M_w (Dalton)	Degree of hydrolysis	Description	Supplier
FP 3630S	20×10^6	25-30%	HPAM	SNF Floerger
FP 3330S	8×10^6	25-30%	HPAM	SNF Floerger
AN-125	8×10^6	20-30%	Poly(AM-co-AMPS)	SNF Floerger

Although the apparent viscosity characterization of HPAM polymer solutions includes elasticity, Lee et al.'s (2009) focus was aimed at the bulk rheology characterization and therefore only the shear-thinning part was investigated. However, the authors also developed models for viscoelasticity, which will be discussed in detail.

Previously, it was shown that the shear-thinning behavior of the viscosity-shear rate relationship is best described by the Carreau model (Carreau, 1972). In addition, the

general apparent viscosity model by Delshad et al. (2008) utilizes Carreau's model for the shear-thinning part. Thus, the authors considered this model in their study and their objective was to correlate Carreau's model parameters with different variables.

2.8.1.2 Zero-shear viscosity:

Several researchers have developed equations that describe the relationship between the zero-shear viscosity of polymer solution and the polymer concentration such as Flory-Huggins and Martin's equations. While both equations may provide accurate estimation (for dilute solutions), Lee et al. used Martin's equation to predict $\mu_p{}^0$. The Martin equation, Eq. 2.8 that was used in their study is a function of polymer concentration and solvent viscosity, which we assume is water. Although Eq. 2.8 does not incorporate the effect of salinity, it is embedded in the fitting constants of their equations. Based on the experimental data of the bulk viscosity measurements, two correlations have been developed for predicting k_1 and k_2. Those correlations are obtained by fitting the experimental viscosity data and are a function of salinity, specifically the monovalent and divalent concentrations. The correlations are given by:

$$k_1 = \exp\left[\left(\frac{b_1 C_1 + b_2}{C_1 + b_3}\right)\left(\frac{C_1 + (b_4 C_2)^{b_5}}{C_1}\right)^{b_6}\right] \tag{2.28}$$

$$k_2 = \exp\left[\left(a_1 \exp(a_2 C_1) + a_3 \exp(a_4 C_1)\right)\left(\frac{C_1 + (a_5 C_2)^{a_6}}{C_1}\right)^{a_7}\right] \tag{2.29}$$

where C_1 and C_2 are the sodium ion (Na^+) and calcium ion (Ca^{++}) concentrations in g/ml, respectively. Table 2.3 lists the values of fitting constants in Eq. 28 and Eq. 29 for each of the polymers tested.

Table 2.3: Correlation parameters for Eq. 28 & Eq. 29 (Lee, et al., 2009)

Polymer	a_1	a_2	a_3	a_4	a_5	a_6	a_7
FP 3630S	1.69	-70.33	5.66	7.232	276	2.915	-0.03668
FP 3330S	0.6554	-451.7	6.577	-2.545	91.17	1.627	-0.03947
AN-125	0.5638	-965.4	6.696	-6.018	6.099	0.9851	-0.03561
	b_1	b_2	b_3	b_4	b_5	b_6	
FP 3630S	8.009	0.01639	0.00146	0.3328	0.5708	-0.09762	
FP 3330S	7.895	0.009923	0.0008793	0.6247	0.7171	-0.1241	
AN-125	7.926	0.004737	0.0004234	0.1819	0.7579	-0.126	

2.8.1.3The shear-thinning index (n) and the time constant (λ):

Similarly, the experimental data was studied to investigate the changes of n and λ with respect to different conditions, i.e. concentrations and salinities. As a result, the following two empirical correlations that cover different conditions were obtained:

$$n = 1 - 0.075\ln\left(\frac{{\mu_p}^0}{\mu_\infty}\right) \quad (2.30)$$

$$\lambda = \left[d_1 \ln\left(\frac{{\mu_p}^0 - \mu_w}{\mu_w C_p}\right)\right]^{d_2} \quad (2.31)$$

Table 2.4 lists the Eq. 2.31 parameters for the studied polymers.

Table 2.4: Correlation parameters for Eq. 2.31 (Lee, et al., 2009)

Polymer	d_1	d_2
FP 3630S	0.1009	7.146
FP 3330S	0.09175	8.273
AN-125	0.09668	9.06

Lee et al. (2009) models may provide a reasonable estimation of Carreau's model parameters at given conditions. However, the study lacks a validation of the proposed models against a set of test data, a typical practice performed for new models. The validation reflects the accuracy extent of the model and in the absence of it, one might be

reluctant to use these models. Moreover, the proposed models seem to be complicated and involve many parameters which may potentially lead to inducing errors by missing or mistaking one of the parameters. Certainly, a simple, short and reliable models are then needed to address this issue.

2.8.2 Kim et al. (2010):

Kim et al. (2010) measured the viscoelastic properties of for the same polymers used in Lee et al. (2009) study as a function of polymer concentration, salinity, and harness concentration. In addition, it was stated previously that τ_r is a key parameter that defines the viscoelastic behavior of different polymers. Thus, the objective of this study was to develop a viscoelastic property database for different EOR-employed polymers and develop empirical models to predict τ_r as a function of the same process variables described by Lee et al. (2009).

Dynamic strain sweep test was implemented to determine the range of liner viscoelasticity levels at constant temperature and frequency. In addition, dynamic frequency sweep test was implemented to measure the elastic (G') and viscous (G") moduli within specified range of frequency. The aforementioned viscoelastic experiments were conducted for a wide range of polymer concentration, salinity and temperature. Figure 2.11 and Figure 2.12 show G' and G" responses for HPAM polymer at different polymer and NaCl concentrations, respectively.

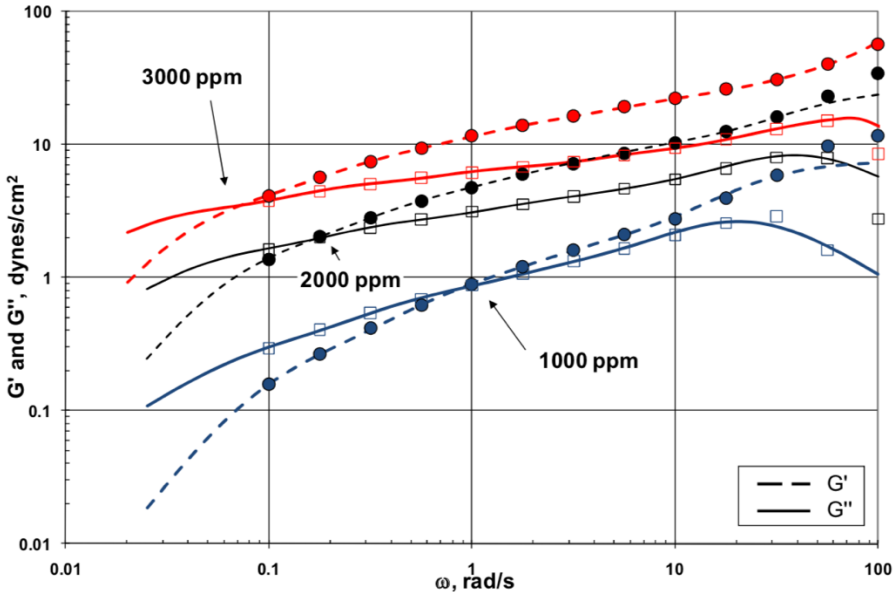

Figure 2.11: Dynamic frequency test (Symbol: experimental data; Line: GMM model fitted curve). Impact of polymer concentration on G' and G" moduli (FP3630 at 0.1 wt% NaCl) (Kim, et al., 2010)

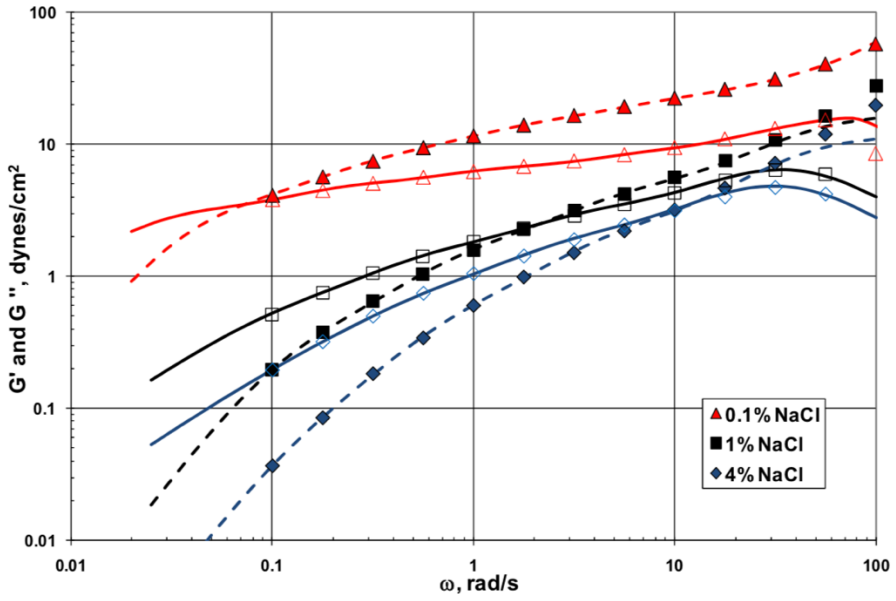

Figure 2.12: Dynamic frequency test (Symbol: experimental data; Line: GMM model fitted curve). Impact of NaCl concentration on G' and G" moduli (FP3630 at 3000 ppm polymer) (Kim, et al., 2010)

The relaxation time of HPAM polymers cannot be precisely estimated directly from the aforementioned viscoelastic measurements due to the complex nature of relaxation phenomenon. In fact, it can only be characterized by an almost continuous relaxation spectrum (Bird et al., 1987; Larson, 1999). Therefore, the Generalized Maxwell Model (GMM) is deployed to obtain the relaxation spectrum of a polymer, which is given by:

$$G'(\omega) = \sum_{i=1}^{N} G_i \frac{(\omega\tau_i)^2}{1 + (\omega\tau_i)^2} \tag{2.32}$$

$$G''(\omega) = \sum_{i=1}^{N} G_i \frac{(\omega\tau_i)^2}{1 + (\omega\tau_i)^2} \tag{2.33}$$

Where τ_i is the relaxation time of the ith element and G_i is the elastic modulus at τ_i. Then, the cross-over point method is used to determine the longest relaxation time, which is considered a good initial estimate. After that, a non-linear regression algorithm is used to fit the GMM models to the *G*' and *G*" experimental data. Finally, the estimated relaxation time data was fitted and consequently a number of empirical correlations for the characteristic relaxation time parameter were developed as a function of polymer concentration, NaCl concentration, divalent ion concentration. The proposed relaxation time correlations are as follows:

$$\tau_r = A_1 {C_p}^2 + A_2 C_p + \tau_0 \tag{2.34}$$

where A_1, A_2, and τ_0 are empirical constants. Since the value of τ_0 was not reported in the paper and given that τ_r should equal to zero when the concentration is zero, τ_0 is assumed zero. A_1 and A_2 are given by:

$$A_1 = a_0 + a_1 \left(\frac{a_2 C_1 + a_3}{C_1 + a_4}\right)\left(\frac{(\mathrm{C}_1 + \exp(\mathrm{a}_5 \mathrm{C}_2)^{\mathrm{a}_6})^{a_7}}{(C_1)^{a_8}}\right) \tag{2.35}$$

$$A_2 = b_0 + \left(\frac{b_1 C_1 + b_2}{C_1 + b_3}\right)\left(\frac{(\mathrm{C}_1 + \exp(b_4 \mathrm{C}_2)^{b_5})^{b_6}}{(C_1)^{b_7}}\right) \tag{2.36}$$

Table 2.5 lists the parameters a_i and b_i for the studied polymers. It should be noted that the correlation parameters listed in the following table are different than Lee, et al. (2009)'s paper.

Table 2.5: Correlation parameters for relaxation time (Kim, et al., 2010)

Polymer	a_0	a_1	a_2	a_3	a_4	a_5	a_6	a_7	a_8
FP3630S	5271.1	2.57	-116.06	2.79	0.00136	1000	-83.25	1	0.79
FP3330S	7215.3	1	-251.97	0.11	-0.00039	1000	-897.78	1	0.53
AN125	6173.8	1	-47.89	0.02	-0.00039	1000	-100.01	1	0.47
	b_0	b_1	b_2	b_3	b_4	b_5	b_6	b_7	
FP3630S	10	41.79	-0.847	0.001	1000	-6.46	1	0.026	
FP3330S	-3.03	0.00218	-2.02x10-6	0.011	1000	-11.05	1	1.821	
AN125	3	2662.8	-2.362	0.02	1000	1	-1494.88	0.016	

Moreover, the effect of temperature has been studied and several viscosity measurements have been conducted under various temperatures levels. It was noticed that high values of temperature resulted in lower values of *G*' and *G*", which led to a slightly lower value of relaxation time. The author suggested that the dependence of the relaxation time on the temperature is best described by William-Landel-Ferry (WLF) equation (Ferry, 1980) which is given by:

$$\ln\left(\frac{\tau_r}{\tau_{r,ref}}\right) = \frac{-\alpha(T - T_{ref})}{\beta + T - T_{ref}} \qquad (2.37)$$

where T is the temperature and T_{ref} is a reference temperature corresponding to $\tau_{r,ref}$. The best-fit constants, α and β, for the studied polymers are presented in Table 2.6.

Table 2.6: WLF Constant for EOR Polymers (Kim, et al., 2010)

Polymer	α	β
FP3630S	5.32	456.84
FP3330S	3.54	246.14
AN125	2.92	892.47

2.8.3 Jouenne et al. (2019)

Jouenne et al. (2019) introduced empirical models to predict Carreau's equation parameters (μ_p^0, n, and λ) as a function of two variables, the intrinsic viscosity and the time constant at the diluted regime of the polymer solution, according to their definitions. These models are based extensively on bulk rheology measurements of various acrylamide-based polymer solutions used in EOR applications. The solutions were prepared at a wide range of polymer concentration, brine salinities (6-250 g/L), and temperatures (25-90 ºC). After measuring the bulk viscosity at different shear rates, the measurement data for each sample solution was fitted with Carreau's equation by the least-squares regression and Carreau's model parameters were obtained. Figure 2.13 shows the viscosity versus shear rates of FP-3630S polymer.

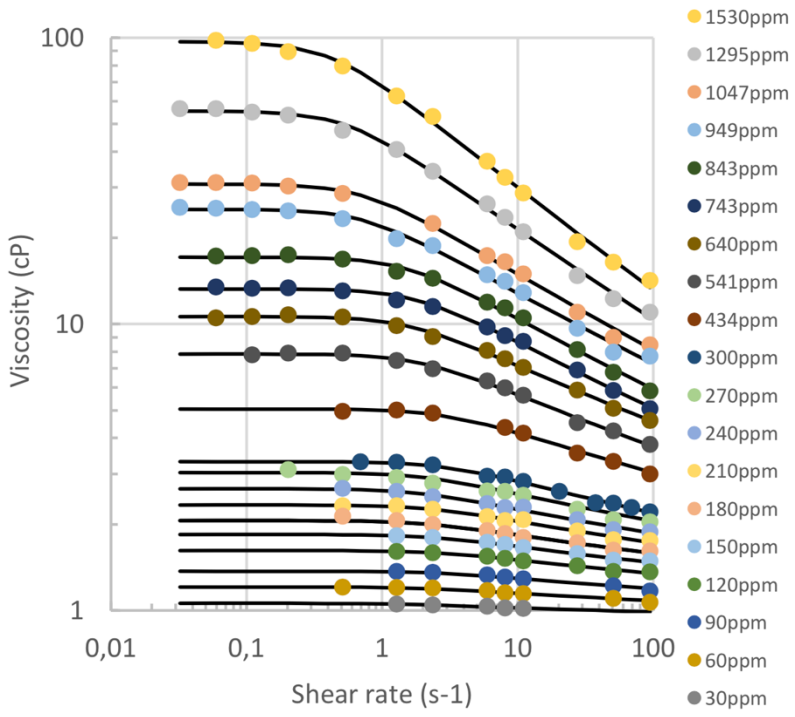

Figure 2.13: Viscosity profile at different polymer concentrations for FP3630S polymer in 6 g/L brine at 25 °C (Jouenne, et al., 2019)

In principle, the modeling approach in this study is based on the physical relationship between the apparent viscosity, the intrinsic viscosity and the polymer concentration, i.e. η-$[\eta]$-C relationship. Numerous researchers have studied the η-$[\eta]$-C relationship for various type of polymer systems and ultimately developed mathematical models that describe this relationship (Adam and Delsanti, 1983; Bouldin et al., 1988; Grigoresku and Kulicke, 2000). They, among many others, claimed that the specific viscosity obeys the following form of correlation:

$$\eta_{sp} = C_p[\eta] + a_1(C[\eta])^{b_1} + a_2(C[\eta])^{b_2} \qquad (2.38)$$

where a_1, a_2, b_1, and b_2 are fitting constants. A noticeable similarity between Eq. 2.38 and the Huggins-Flory equation can be easily observed especially for the first two terms. η_{sp} was plotted against the overlap parameter, i.e. the product of polymer concentration and the intrinsic viscosity ($C_p[\eta]$), for a wide range of polymer types and a unique curve was obtained as shown in Figure 2.14.

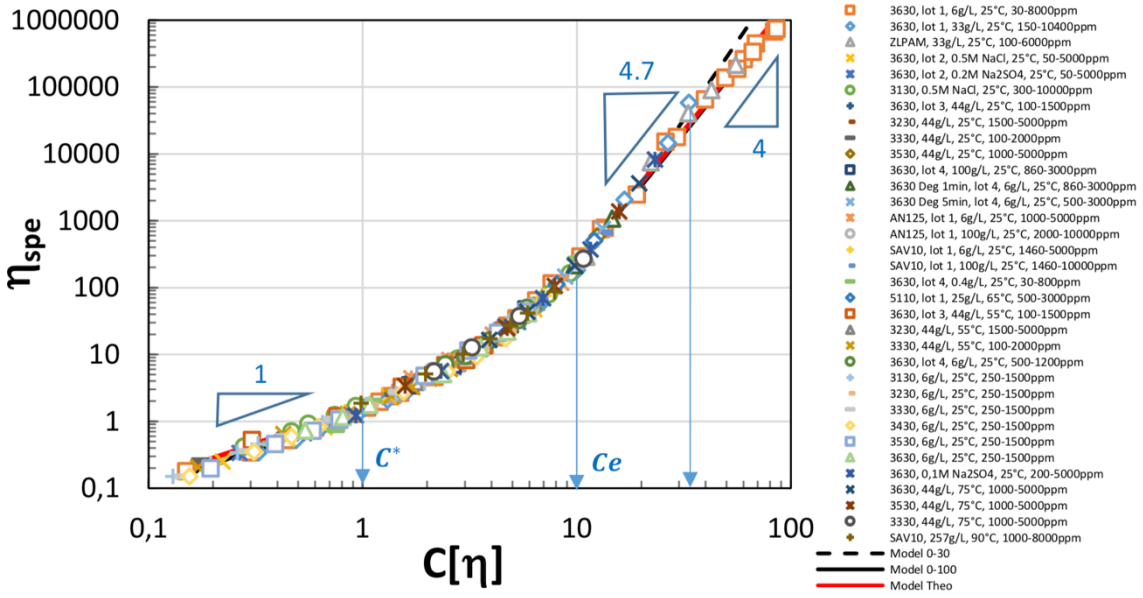

Figure 2.14: Specific viscosity versus overlap parameter for various polymers (Jouenne, et al., 2019)

This curve was fitted with Eq. 2.38 and the fitting constants are listed in Table 2.7.

Table 2.7: Correlation parameters for Eq. 2.38

a_1	a_2	b_1	b_2
0.56	0.0026	2.17	4.72

Jouenne et al. (2019) proposed the following model for the shear-thinning index (n) as a function of $C[\eta]$:

$$n = 1 - \left(0.796 - 0.687 \times \exp(-0.059 \times \mathrm{C[\eta]})\right) \qquad (2.39)$$

Figure 2.15 shows the relationship between n and $C[\eta]$ for the same polymer solutions.

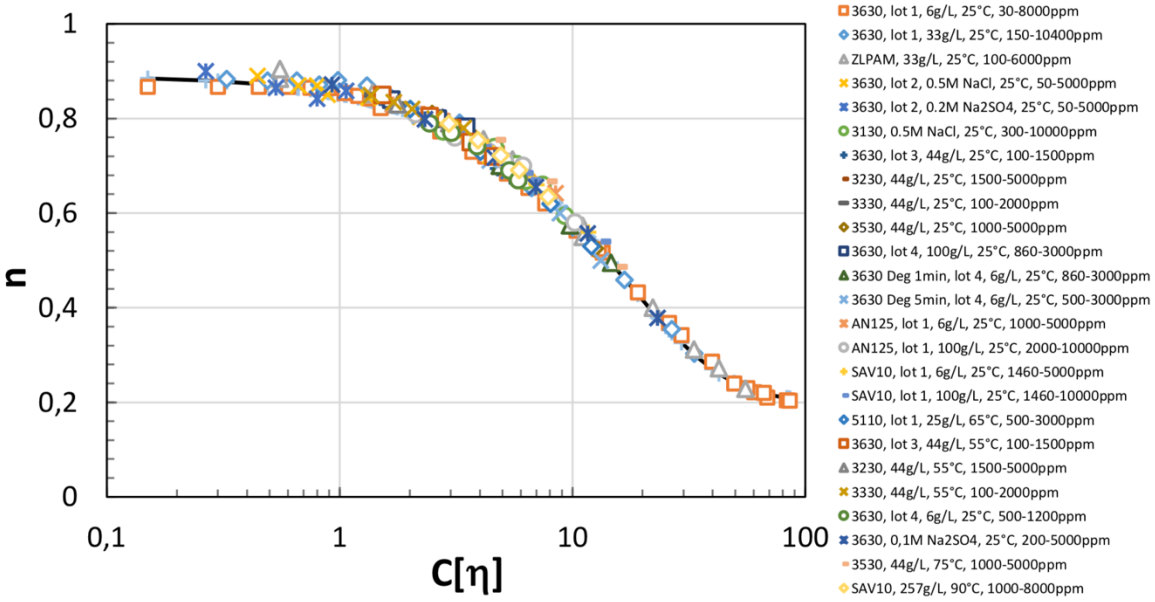

Figure 2.15: Shear-thinning index versus the overlap parameter for various polymers (Jouenne, et al., 2019)

Furthermore, when Carreau's model parameter, λ, was plotted against $C[\eta]$ for each sample solution, it showed an inconsistent trend as shown in Figure 2.16. As a result, Jouenne et al. (2019) introduced the relaxation time at the diluted regime ($C[\eta] < 1$),

denoted as λ_d. The relaxation time curve was normalized by λ_d for each sample and the resultant curve is shown in Figure 2.17.

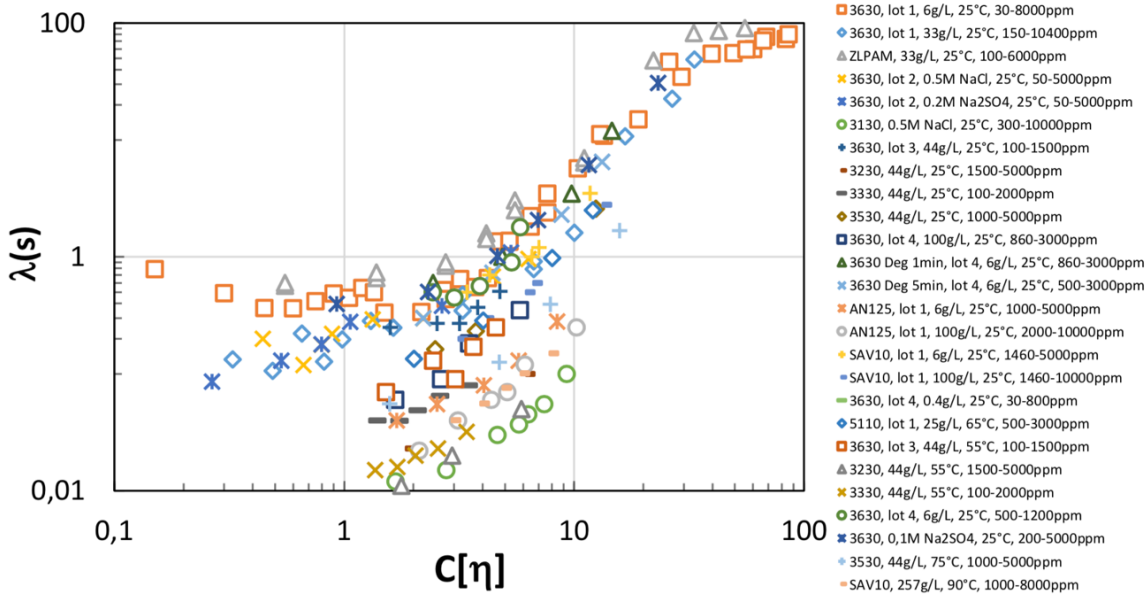

Figure 2.16: λ versus the overlap parameter for various polymers (Jouenne, et al., 2019)

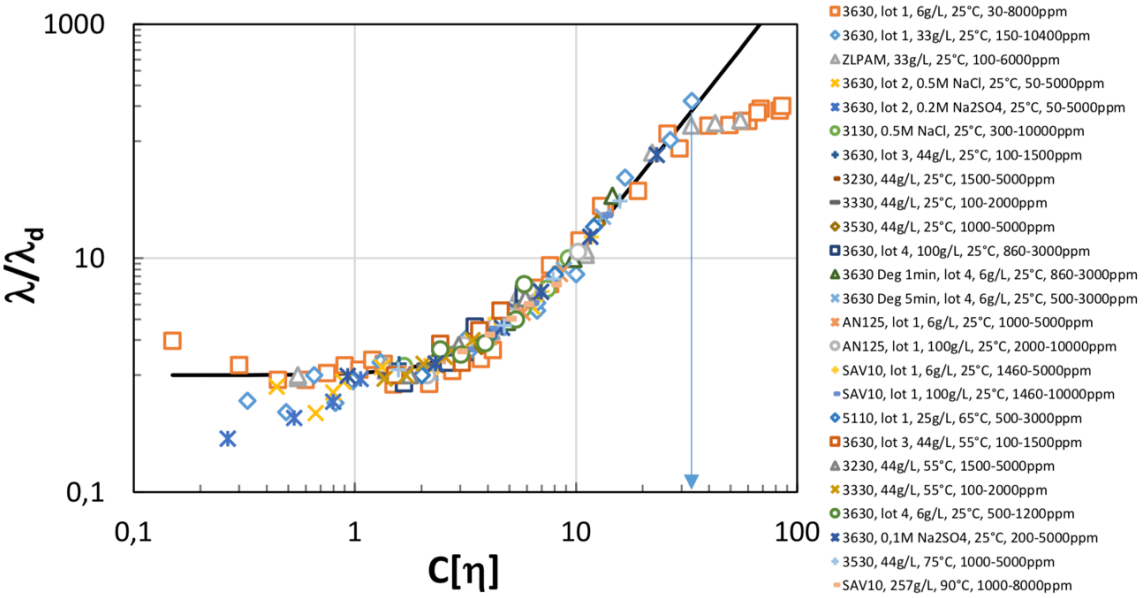

Figure 2.17: Normalized λ/λ_d versus the overlap parameter for various polymers (Jouenne, et al., 2019)

Jouenne et al. (2019) proposed the following correlation that was obtained by data-fitting the curve in Figure 2.17:

$$\frac{\lambda}{\lambda_d} = 1 + 0.04(C[\eta])^{2.4} \quad (2.40)$$

It is clear from Eq. 2.40 that a prior knowledge of λ_d is needed in order to estimate the relaxation time of a valid polymer type. Thus, Jouenne et al. (2019) introduced the Zimm model, which is considered a good estimation of the relaxation time at the diluted regime due to inactivity of the molecular chains at this regime. Zimm model is given by:

$$\lambda_z = \frac{\eta_s[\eta]M_w}{T} \quad (2.41)$$

where M_w is the molecular weight and T is the temperature. The units of the aforementioned parameters were not reported in the paper. Subsequently, the best-fit λ_d from the experimental data was plotted against the calculated λ_z from the previous equation and the following relationship was obtained:

$$\lambda_d = 1.474\lambda_z = 1.474\frac{\eta_s[\eta]M_w}{T} \quad (2.42)$$

where η_s is the solvent viscosity.

2.8.3.2 Limitation:

This work involved extensive efforts to implement a comprehensive model for polymer rheology prediction. One of the advantages is the variety of polymer types incorporated in the study. The data includes 9 polymer types with various polymer concentration and brine salinities. In addition, the fact that only one universal equation to predict zero-shear viscosity or shear-thinning index can be applied to many polymer types at any concentration is an outstanding approach which can save a lot of time and effort when implemented. However, their proposed models may hold some limitations and can potentially be improved. For instance, the equation pertaining the zero-shear viscosity, the

η_{sp} model, does not directly include the salinity as a variable in the model (it is incorporated into the intrinsic viscosity). This poses a significant issue when dealing with a chemical flood reservoir simulator since the salinity throughout the reservoir changes. In addition, the shear-thinning index of any polymer solution should equal to one when the polymer concentration is zero (the solvent is a Newtonian fluid). but the model (and data) in Jouenne et al. (2019) show that the shear thinning index approaches 0.89 as polymer concentration approaches zero. We also point out that Jouenne et al. (2019) refer to the Carreau's model parameter λ as "relaxation time" whereas here and elsewhere is referred to as a time constant (Sorbie, 1991); it is not directly related to the relaxation time of a viscoelastic fluid.

2.9 MACHINE LEARNING

Machine learning, sometimes referred to as statistical learning, is an automated data analysis process that attempts to understand the data and identify possible connections between the data features. Statistical learning can be interpreted as a set of tools used to understand the data (James, et al., 2013). In addition, the automation part of the machine learning's algorithm, which includes learning from data, building and updating the model and establishing prediction, is a satisfactory feature of a machine learning model. Machine learning problems fall in one of two types of learning techniques; supervised learning and unsupervised learning. Supervised learning is the learning process based on input-output pairs and correlate input to an output (Russell & Norvig, 2010). In unsupervised learning, there is only input data and the learning goal is identify the relationship between the variables and learn the structure of the data (James, et al., 2013). A common example of unsupervised learning is cluster analysis, or clustering. Russell & Norvig (2010) defines

clustering as the detection of clusters within input data that are potentially meaningful. For instance, grouping customers by purchasing behavior and spending levels.

There are many machine learning techniques and the decision to choose which one would provide the best prediction is not an easy task. Normally, some sophisticated machine learning techniques, such as Neural Networks, can provide very satisfactory results but require extensive effort to build the algorithm. Nevertheless, the same problem can be handled by a simpler machine learning technique and still provide a satisfactory result. Therefore, one needs to understand the complexity of the problem and acquire an adequate education about the different machine learning methods for an optimum method selection. In this study, the type of learning task is supervised learning as the input data is labeled and the output is supplied. The output is the polymer solution rheology, specifically the viscosity (and/or relaxation time), and it is a function of multiple variables including the salinity, type of electrolyte, polymer concentration, molecular weight, and temperature of the polymer solution.

Kang et al. (2013) developed a machine learning model to predict polymer rheology. They used Artificial Neural Networks (ANN) technique to predict the polymer viscosity as a function of shear rate, polymer concentration, salinity, hardness concentration, and temperature. They used data from Lee et al. (2009). The ANN model result was verified against the experimental data and Lee et al. (2009) model's estimation and it showed an excellent match, as shown in Figure 2.18.

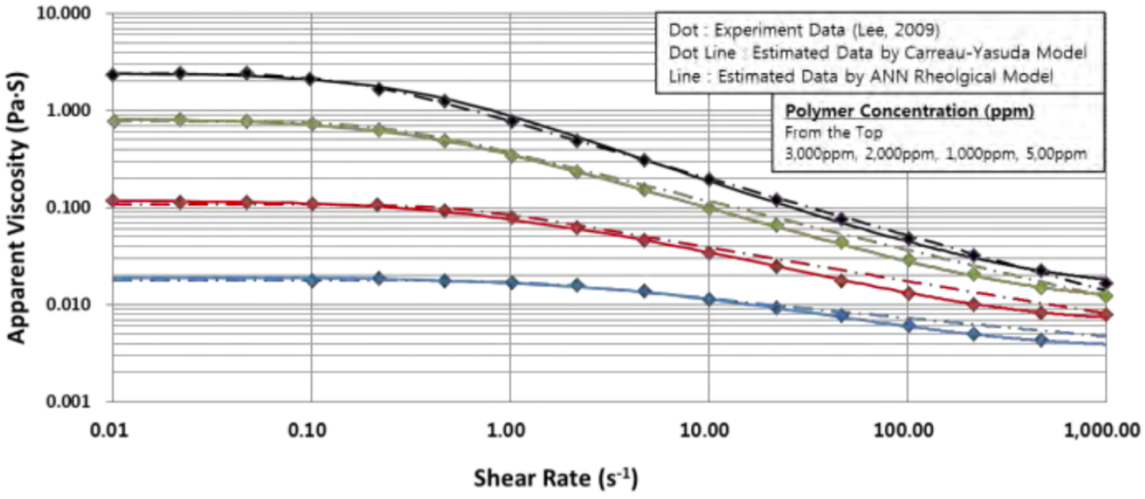

Figure 2.18: Comparison between measured data and model estimations depending on polymer concentration for FP3330S polymer (Kang, et al., 2013)

The rheological ANN model is designed to predict the viscosity at any given polymer concentration, salinity, temperature, and shear rate. For every polymer solution sample, there is one value for each of the aforementioned variables except the shear rate, where each sample may have 10-15 data points on average, leading to much bigger training dataset. This large number of training data may cause a considerable reduction in the algorithm performance, compared to our methodology where the predicted parameters are Carreau's model parameters based on polymer solution properties. This issue will be more significantwhen additional training data is added in the future. Moreover, it appears that the final results, i.e. the viscosity profiles generated by the model, contains about 85% data from the training set. Therefore, this may be seen as a biased way of testing for the model and it may not reflect the true performance and accuracy of the model. Rather, perhaps a full-range of viscosity profiles should be generated from and compared against a pure test data that was not trained by the model.

2.10 UTCHEM OVERVIEW

UTCHEM is a multicomponent, multiphase, three-dimensional, and multi-compositional chemical flooding reservoir simulator developed by the University of Texas at Austin (Delshad et al., 1996; Delshad et al., 2002). The simulator was originally developed in 1978 by Pope and Nelson for the purpose of simulating chemical EOR applications such as polymer and surfactant floods (UTCHEM, 2018). UTCHEM has many capabilities that account for various complex multiphase flow behaviors, heterogeneity of porous media (e.g. dual porosity model), modeling of up to four fluid phases (single-component gas, aqueous, oleic, and microemulsion), properties associated with these phases (e.g. relative permeability, interfacial tension, capillary pressure, viscosity, etc.), and various chemical and physical transformations (e.g. geochemical reactions), among others (Delshad, et al., 1996; Delshad, et al., 2002; UTCHEM, 2018). Some of the applications of UTCHEM include surfactant flooding, high pH alkaline/surfactant/polymer (ASP) flooding, polymer flooding, conformance control using polymer gels, microbial enhanced oil recovery, tracer tests, and formation damage (Delshad, et al., 2002; Delshad, et al., 2008; Li & Delshad, 2014; Al-Shalabi, et al., 2015; Lotfollahi, et al., 2016; UTCHEM, 2018; Lashgari, et al., 2019). The simulator uses block-centered finite-difference scheme to discretize the differential equations and solve them using implicit in pressure and explicit in concentration (IMPEC) method (UTCHEM, 2018).

2.10.1 Modeling of Bulk viscosity

UTCHEM uses the Flory-Huggins equation (Eq. 2.6) (Flory, 1953) with the C_{sep} term (Eq 2.10) to calculate the zero-shear viscosity at any polymer concentration and salinity. In addition, the simulator employs either Meter's equation (Eq. 2.4) (Meter &

Bird, 1964) or Carreau's equation to describe the shear-thinning behavior of polymer solution as a function of the effective shear rate (Eq. 2.22). The correlation constants associated with the aforementioned equations are all input parameters that need to be known prior running the simulator.

2.10.2 Unified Viscosity Model (UVM)

To account for the effect of polymer viscoelasticity on polymer viscosity and residual oil, UTCEHM utilizes the unified viscosity model (Eq. 2.20) (Delshad, et al., 2008) that covers the full spectrum of Newtonian, shear-thinning, and shear-thickening behavior of polymer solution flowing in porous media. As explained earlier in this chapter, the model comprised of two components, shear-thinning (μ_{sh}) and shear-thickening, or elongational, (μ_{el}) viscosities. Unlike in the bulk viscosity model described earlier, the shear-thinning viscosity part of UVM uses Carreau's model. The fitting parameters of the shear-thinning viscosity, Carreau's parameters, are input parameters of the in UTCHEM except λ, which is given by (UTCHEM, 2018):

$$\lambda = \beta_1 \exp\left(\beta_2 C_p\right) \tag{2.43}$$

where β_1 and β_2 are input parameters obtained from laboratory measurements. On the other hand, the correlation parameters of the shear-thickening viscosity (μ_{el}) are all inputs in the simulator and should be determined prior running the simulator.

CHAPTER 3. EXPERIMENTAL APPROACH AND METHODOLOGY

3.1 POLYMER PREPARATION AND RHEOLOGY EXPERIMENTS

The experimental procedure and the apparatus used for preparing and testing the polymers are explained here. In the experiments, an HPAM polymer, FP 3630S, with a molecular weight of 20 million Dalton was prepared and tested using state-of-the-art preparation equipment, methods, and a rheometer. The objective of the experiments was to collect rheology data in addition to that available in the literature.

3.1.1 Equipment

Equipment used in this study included a weight balance, an overhead mixer, and a rotational rheometer. All weight measurements of liquid water, polymer powder, and other additives were conducted using a Discovery weight balance manufactured by Ohaus®. The balance measures the mass of a component with a precise readability of 0.0001g. Figure 3.1 shows the weight balance used in this study. Correct mixing of polymer solution is important to ensure full hydration of polymer powder and electrolytes. For that reason, a Caframo® BDC2002 overhead mixer equipped with a propeller stirrer was used (Figure 3.2). The stirrer has a speed range of 40–2002 rpm with a precise speed adjustment. Because polymer powder or solvent may contain some debris and small particles, a filtration unit was used to ensure that any dust or particles are removed from the polymer solution stock. For the rheological properties' measurements, an Advanced Rheometric Expansion System (ARES-G2) rheometer by TA Instruments® was used, as shown in Figure 3.3. The ARES is a mechanical rheometer that can subject a sample to strain deformation. This strain deformation is applied by the air bearing motor, also referred to as the Actuator, and it can be operated in dynamic (sinusoidal) mode, steady mode, and

step strain and step stress mode. The resultant torque and normal stress responses generated by the sample are measured by the Force Rebalance Transducer (FRT).

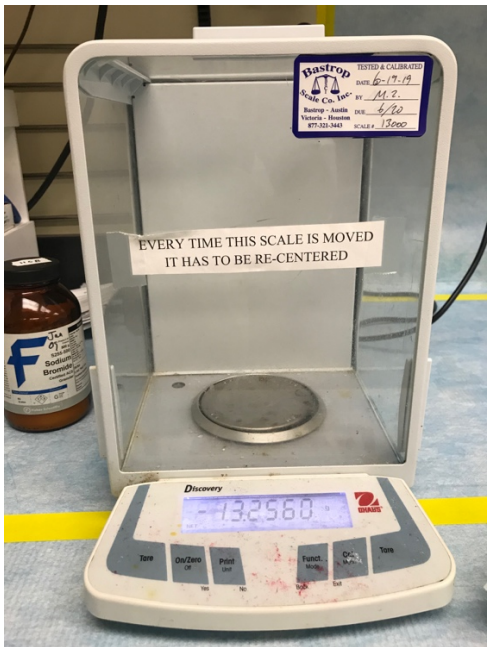

Figure 3.1: Discovery™ weight balance

Figure 3.2: Caframo® BDC2002 overhead stirrer

Figure 3.3: TA Instruments® advanced rotational rheometer (ARES-G2)

3.1.2 Polymer Solution Preparation

Preparing the polymer solution involves three stages: weight measurement, polymer hydration, and electrolyte addition. The first stage, weight measurement, is crucial to the reliability of the rheology measurement. First, 497.5 g of deionized water (DI) and 2.5 g of polymer powder were measured by the balance. However, the official procedure calls for using brine. As a result, a NaCl-concentrated brine was used for the final polymer stock. Then, the polymer hydration stage begins by filling the mixing container with the DI water/brine and placing it under the overhead mixer. The stirrer should be located at the center of the container, and the end distance to the container bottom is approximately 1 cm. Next, the overhead mixer is set at 500 rpm. Once the vortex is formed and stable, the polymer powder is slowly added onto the shoulder of the vortex. The polymer solution was

mixed for about 4 to 5 hours at room temperature. The polymer solution stock was prepared at a 5,000 ppm concentration. An argon gas blanket was used for 30 minutes to minimize oxygen contact.

3.1.3 Filtration and Dilution

Once the polymer solution was properly mixed and prepared, the filtration process begins. The brine was filtered with 0.45 micron and the aqueous polymer solution was filtered through a 1.2-micron Millipore cellulose filter under 15-psi argon pressure. Then, the time was recorded when the collected fluid volume was at 60, 80, 180, and 200 mL. The filtration ratio (FR) is calculated as follows:

$$FR = \frac{t_{200ml} - t_{180ml}}{t_{80ml} - t_{60ml}} \tag{3.1}$$

where t_i is the time at the i amount of filtered fluid. The FR of the polymer solution should be less than 1.2 to pass the filtration test.

After that, the filtered polymer solution was diluted with DI water, NaCl-concentrated solution, and $CaCl_2$-concentrated solution to obtain the final composition of the polymer sample for the measurement. In this study, since the objective is solely bulk rheology measurements and not intended for coreflood experiments, the polymer stock solution was not filtered. However, later it was decided to do the filtration test on the final samples.

3.1.4 Rheological Measurements

Once the samples were fully prepared, they were brought to the rheometer lab for rheological measurements. Tests were implemented on each sample using an ARES-G2

rheometer (Figure 3.3). In this experiment, two types of tests were conducted: a steady shear sweep test and an oscillation frequency sweep test.

3.1.4.1 Steady Shear Sweep Test

Steady flow sweep test provides the shear viscosity of the solution as a function of the shear rate at a given temperature. The range of the shear rate for this test is from 0.01 to 500 s^{-1} with four measurement points in each log decade. The resultant viscosity profile exhibits a shear-thinning behavior, as expected. Figure 3.4 shows a typical result of the steady shear sweep test of the FP3630S polymer.

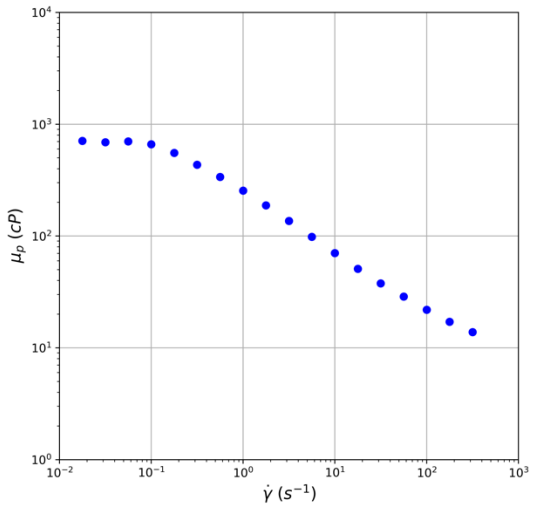

Figure 3.4: Plot of steady shear sweep test results of 2500 ppm FP3630S polymer at 0.1% NaCl, 750 ppm $CaCl_2$, and 25°C

3.1.4.2 Oscillation Frequency Sweep Test

The oscillation frequency test provides the viscoelastic properties of the polymer solution, such as the storage modulus (G′), loss modulus (G″), and complex viscosity. The temperature and strain are held constant in a frequency sweep, and the viscoelastic properties are monitored as the frequency is varied. The frequency sweep tests were run over a limited range of 0.1 to 100 rad/s. Figure 3.5 shows a typical result of the frequency sweep test of the FP3630 polymer.

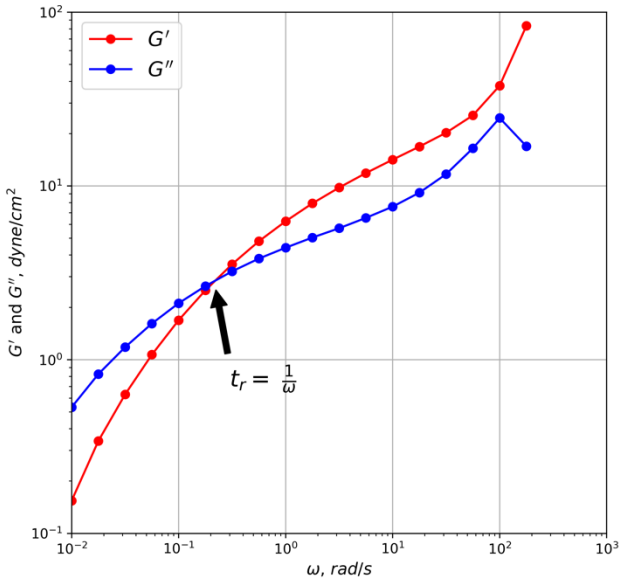

Figure 3.5: Plot of oscillation frequency sweep test results of 4000 ppm FP3630S polymer at 0.1% NaCl, 750 ppm $CaCl_2$, and 25°C

3.2 RHEOLOGY DATA COMPILATION

A large dataset of viscosity versus shear rate for various polymer solutions (with variation in polymer type, molecular weight, concentration, salinity, hardness, and temperature) is essential to this study. Rheological data for three different polymer types were compiled and studied: two HPAM polymers with different molecular weights, 8 and 20 million Dalton, and one 2-acrylamido 2-methyl propane sulfonate (AMPS) polymer with a molecular weight of 8 million Dalton, as described in chapter 2 (Table 2.2). In addition, Table 3.1 shows the range of properties (e.g., polymer concentration) for each polymer type. As shown in the table below, samples vary in polymer concentration, salinity, and hardness.

Data compiled in this study are bulk rheology measurements, i.e. bulk viscosity versus shear rate, for different polymer samples. The data were initially obtained from three sources: from UT's Center for Petroleum and Geosystems Engineering's Chemical EOR database, from the laboratory experiment described in this chapter, and from the literature (Lee et al., 2009). CPGE's database comprises rheology data obtained and archived at UT-Austin by researchers for reference and further use. However, after a rigorous review of the collected data, it was found that most of the data are inconsistent and have large discrepancies due to their different objectives and uses (e.g. ASP flooding). For instance, the majority of the data were designed for coreflood of which some of them use a natural brine with complex mineral compositions. In addition, a large number of samples use alkaline agents, and many contain a wide range of different chemical additives that are suited for core flood experiments. Eventually, 40 samples from CPGE's database along with about 200 samples from Lee (2009) study were consistent and aligned with our objective and therefore were used.

Table 3.1: Properties of the three polymers analyzed in the study.

Polymer	Polymer concentration (ppm)	NaCl concentration (ppm)	Hardness, (ppm)	Temperature (°C)
FP 3630S	500 ~ 3000	0 ~ 40,000	0 ~ 1500	25 ~ 90
FP 3330S				
AN-125				

3.3 CURVE FITTING OF DATA TO CARREAU'S MODEL

Long periods of time, frustration, and exhaustion are commonly encountered when manually using large datasets. Even conventional spreadsheet software (e.g., Microsoft Excel) cannot handle enormous amounts of data, and failures can happen. Therefore, an automated process using a programing code—algorithms— is an efficient solution to problems associated with large amounts of data. This section discusses the algorithm developed and used for fitting the rheological data to Carreau's model (Eq. 2.5). The algorithm was designed to read and analyze the data, identify abnormalities and outliers, verify fulfillment of pre-defined criteria, and finally fit data to Carreau's model. The entire process takes only 5 to 10 seconds to analyze 400 samples, each having about 14 pairs of data points (viscosity and shear rate). The algorithm was originally built in MATLAB and later the code was rewritten in Python.

The bulk rheological data are generally available in a text file. If many samples are tested, each sample will have its own text file. Data are compiled from these individual files and stored in a master Excel spreadsheet, with each sample having a unique number. The layout of the spreadsheet consists of three columns: the unique number, shear rate, and viscosity. The data must be coded in this particular format for the code to be machine readable.

The algorithm begins by reading the data and determining the number of the samples in the spreadsheet. If no data are available, if the data layout is incorrect, or if the algorithm does not recognize the data, the code will display an error message and the program will abort. After that, the code will loop throughout the dataset. Through each iteration, the sample will undergo several checkpoints, which are a set of pre-defined criteria designed to ensure the quality of the fits and to remove possible outliers. Those criteria are listed in Table 3.2.

Table 3.2: Criteria for determining accurate data at each sample

#	Criterion	Yes?	No?	Remarks
1	Negative values	Terminate	Proceed	
2	Sample's number of viscosity data points greater than 8?	Proceed	Terminate.	Samples that have a smaller number of data points than the criterion will be recorded in a separate list.
3	Low shear-rate abnormal plateau?	Identify and remove abnormal points	Proceed	This step is achieved by computing the slope at the low shear rates.
4	High shear-rate abnormal trend?	Identify and remove abnormal points	Proceed	Similar to the previous criterion

To illustrate criteria 3 and 4, the code calculates the slope of the log of the data at the lowest and highest shear rates. In the low-shear-rate region, when the data diverge from the plateau level, the slope at the point will start to increase. The code will recognize the points that are off trend and subsequently will eliminate them. For the high-

shear-rate region, a plateau should occur, typically in the 10^3 to 10^4 1/s range. However, more often the plateau may not be seen, due to the limited range of shear rate; i.e. the maximum shear rate is around 500 s^{-1}. In addition, sometimes the data will kick off and may tend to level off too early. At that point, an increase in the slope should be expected; as a result, the code will be able to detect it and ignore the off points. When all the criteria are successfully passed, the data are fitted to Carreau's model, and best-fit parameters μ_p^0, n, and λ are calculated for each sample. μ_∞ is taken as the water viscosity at the sample's temperature. Eventually, the code will generate a spreadsheet that includes the sample's number, polymer name, its properties, and its best-fit Carreau's parameters. Figure 3.6 shows an example of viscosity profile and its derivative.

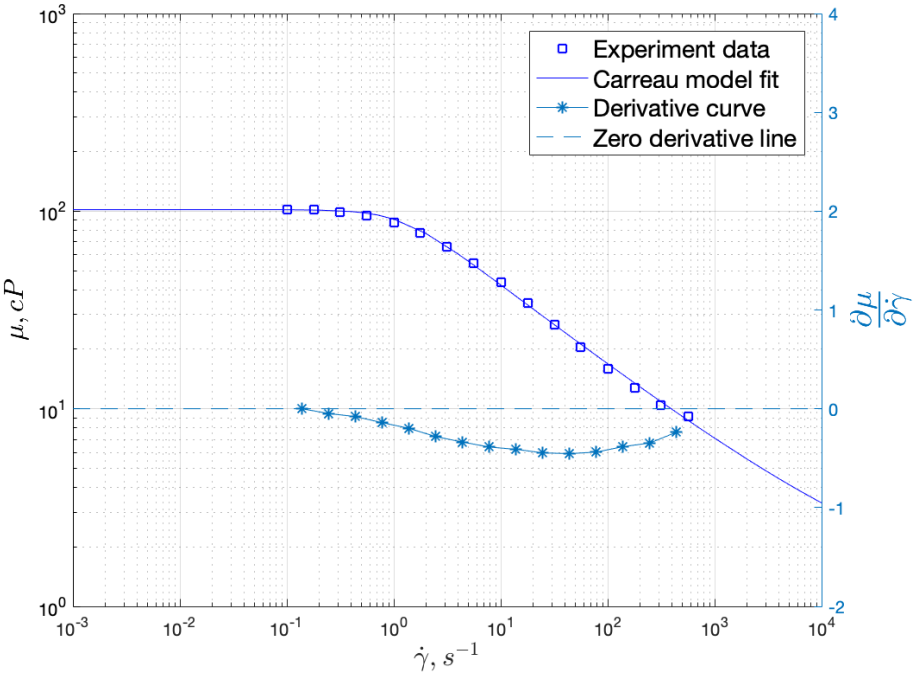

Figure 3.6: Plot showing an example of viscosity profile of 3200 ppm FP-3630S polymer and 6.5 wt% total salinity at 62°C

3.4 CURVE FITTING OF CARREAU'S MODEL PARAMETERS TO POLYMER CHARACTERISTICS

As discussed in chapter 1, the ultimate goal is to develop a mathematical tool to predict Carreau's parameters at any given polymer concentration, salinity, hardness, etc. In this section, the approaches adopted to fit Carreau's parameters to polymer properties are discussed in three subsections, each corresponding to one of Carreau's parameters. The units used for C_p and C_{sep} in all the models in this study are mass fraction and meq/mL, respectively.

3.4.1 Zero Shear Viscosity (μ_p^0)

The Flory-Huggins equation (Eq. 2.6) (Flory, 1953) and Martin's equation (Eq. 2.9) (Martin, 1951) were initially proposed to describe the relationship between the viscosity and polymer concentration (at constant salinity) for dilute solutions. Later, the effective salinity term (Eq. 2.11) was added to the same equations in order to account for the effect of salinity and hardness. In this study, the modified Martin's equation (Eq. 2.12) was considered for predicting the zero-shear viscosity as a function of polymer concentration, salinity, and hardness. Temperature dependence is not directly included in the equation, but it does include the solvent viscosity, typically water, which is itself a function of temperature. Figure 3.7 illustrates the effect of temperature on the polymer solution's viscosity. The y-axis shows the left-hand side of Martin's equation, which includes the ratio of polymer viscosity to the water viscosity. It is clear that the ratio remains nearly constant with increasing temperature, therefore eliminating the impact of the temperature. For FP3630S, the point at 90°C is lower but it is not clear if this is significant or just experimental variation.Overall, all the effect of temperature on polymer viscosity is contained in the solvent viscosity, especially for lower molecular weight polymers.

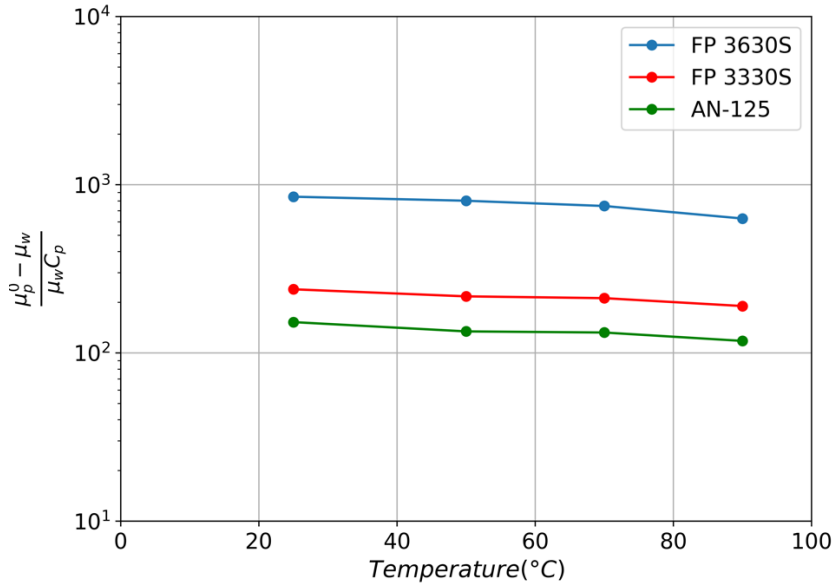

Figure 3.7: Effect of temperature on the LHS of Martin's equation of the three polymers at C_p = 2000 ppm and 1% NaCl

In the fitting process, the dataset is first divided according to the number of polymer types. Each subdivision is curve-fitted individually to Martin's equation, but all share the same fitting approach, i.e. the least-squares minimization method. Although there are plenty of resources where least-squares regression algorithms can be obtained, this study adopted the Lmfit package, a non-linear least-squares minimization and curve-fitting library for Python. Among the package's many classes and functions, the Model class was picked for this task. The Model class is used for curve-fitting where one has a parametrized model function meant to explain some phenomena and the goal is to adjust the numerical values for the model so that it most closely matches the data. Therefore, Martin's equation was supplied to the Model class along with the measured data, and the class returned the best-fit parameters of the equation. Variables and fitting constants of the parameterized model, i.e. Martin's equation, should be, and were, clearly designated, and the fitting

constants should be given initial hint values. Upper and lower limits of the fitting constants can also be provided if the user knows the numerical extent of the constant. Finally, when the code is executed and the curve-fitting is completed, each polymer type should have its own fitting constants of Martin's equation. The fitting results and the best-fit Martin's parameters for each polymer type used in this study are presented in chapter 4.

3.4.2 Shear-thinning index (*n*)

The shear-thinning index in Carreau's model is the parameter that describes the steepness of the curve in the shear-thinning region when viscosity versus shear rate is plotted on a log-log plot. Figure 3.8 demonstrates the effect of *n* on a typical viscosity profile of a shear-thinning polymer. Note that the shape of the curve is significantly altered by the value of *n*. Thus, establishing an accurate mathematical tool to predict a value of *n* that is a function of polymer properties (concentration, salinity, etc.) may be challenging, although such a tool would be effective and user-friendly.

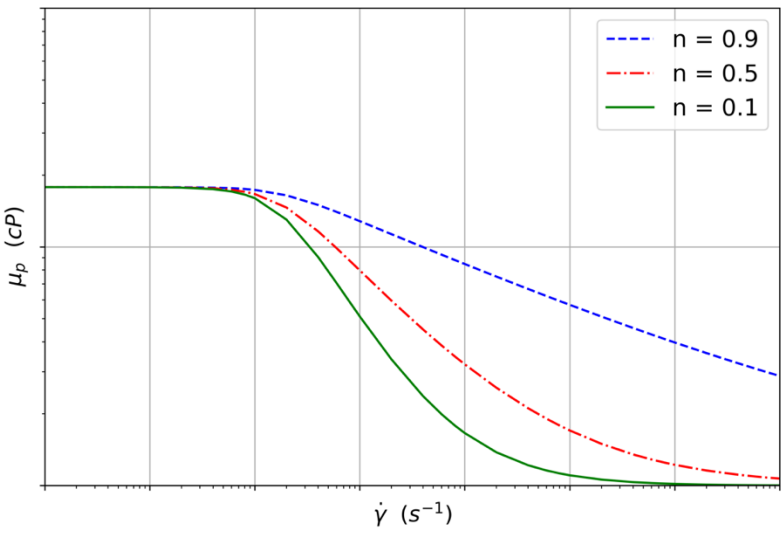

Figure 3.8: Plots of viscosity profiles with different shear-thinning indexes

Here, a new equation is proposed that relates n to polymer concentration, and effective salinity has been developed, as follows:

$$n = n_\infty + \left[\exp\left(-D_{p1}C_p\right) - n_\infty\right] \exp\left(-D_{p2}\frac{C_p}{C_{sep}}\right) \tag{3.2}$$

where n_∞, D_{p1}, and D_{p2} are fitting constants. The equation has the important property that as n approaches unity (Newtonian fluid) in the limit that polymer's concentration is zero. It asymptotically approaches a constant value n_∞ (between 0 and 1) at high polymer concentrations.

Similar to the fitting procedure of $\mu_p{}^0$, the dataset is divided according to the polymer type. Using the least-squares method, the best-fit n values, C_p, and C_{sep} *were* fitted to Eq. 3.2. The fitting results and constants per polymer are presented in chapter 4.

3.4.3 Time constant (λ)

The time constant tends to be the most challenging of Carreau's parameters to correlate with polymer concentration and salinity. To date, no mathematical model exists that correlates the time constant directly with the polymer concentration, salinity, and hardness.

Several ideas and mathematical models have been explored for estimating lambda (λ), including but not limited to theoretical derivation of existing equation and direct correlation with $\mu_p{}^0$ (Lee et al., 2009; Jouenne et al. 2019). Previous results were generally unsatisfactory. However, in this study, a multivariable linear regression (MLR) has been implemented with some success. Simply stated, MLR is a statistical linear regression in which the output is a function of more than one feature, i.e., a variable. In mathematical notation:

$$y(w, x) = w_0 + w_1x_1 + w_2x_2 + \cdots + w_ix_i \tag{3.3}$$

where y is the predicted value, x_i is the variable(s), w_0 is the intercept, and $w = (w_1, w_2, \ldots, w_i)$ are the coefficients. In this study, the input values of the predicted target (λ) and its features were the natural logarithm of themselves. That is, Eq. 3.3 becomes:

$$\ln(\lambda) = w_0 + w_1 \ln(C_p) + w_2 \ln(C_{sep}) \tag{3.4}$$

Prior to applying the curve-fitting, the features' datasets were normalized. The idea behind this standardization is that it will transform the data such that its distribution will have a mean value of 0 and a standard deviation of 1. Features standardization is a common requirement for many regression and machine-learning applications: they may behave poorly if the individual features do not more or less look like standard, normally distributed data. The standardization centers the data by subtracting the mean value of each feature and scales it by dividing it by the feature's standard deviation. In terms of an equation, standardization is given by:

$$z = \frac{x - u}{s} \tag{3.5}$$

where z is the normalized value of x, x is the target feature, u is the mean of the dataset of feature x, and s is the standard deviation of the dataset of feature x. A linear regression algorithm from Scikit-Learn was used to fit the data linearly (i.e., Eq. 3.4), with coefficients to minimize the residual sum of squares between the observed targets in the dataset, and the targets predicted by the linear approximation. The final equation after combining the constants and solving for λ is given as follows:

$$\lambda = a_0 \, C_p^{a_1} C_{sep}^{a_2} \tag{3.6}$$

where a_1, a_2 and a_3 are polymer-related constants. The fitting results are presented in chapter 4.

3.5 MACHINE-LEARNING

The machine learning approach differs from the regression approach in three ways: the construction of the model, the execution environment, and the advanced programming required. For instance, in the previous case of Carreau's parameters regression, the proposed models are simply mathematical formulas, which do not require a special environment for execution. In contrast, the construction of a machine-learning model, such as Random Forests, is more complicated and requires a strong background in programming. These models, or algorithms, are built using a programming language, such as Python or MATLAB, and an integrated development environment is needed to create and execute such models; the machine learning models used in this study were all written in Python. The models used in this study are Random Forests and Artificial Neural Networks, and their algorithms were outsourced from Scikit-Learn, an open-source machine-learning package written in Python. Each method will be discussed in detail, and their results will be presented in chapter 4.

3.5.1 Random Forests (RF)

Random Forests (Breiman, 1996) is a tree-based machine learning method that can be applied to regression and classification problems. It is a collection of multiple decision trees "forest" that are trained simultaneously, and the output is the mean prediction of each individual tree. It has gained much popularity in the last few years due to its robust predictive capability.

3.5.1.1Definition of Decision Tree

Consider the following illustrative example. Table 3.3 shows hypothetical polymer rheological data. This table was used in building the decision tree and predicting the polymer viscosity, the output based on polymer concentration, and the salinity.

Table 3.3: Data used in constructing a regression tree.

Viscosity (cp)	Polymer Concentration (ppm)	Salinity (ppm)
10	500	1500
90	1000	500
50	1000	1000
20	1000	2000
550	2000	0
220	2000	800
120	2000	1500
90	2000	2000
800	3000	0
300	3000	1200
180	3000	2000
1400	4000	0
900	4000	500
490	4000	1500
290	4000	2000

Figure 3.9 shows an example of a regression tree fit to the data in Table 3.3. It consists of a series of split points that are assigned based on either pre-defined criteria or randomness. At each split, two branches form. The top first node shows that the split is assigned at a 1500 ppm polymer concentration. The right-hand branch corresponds to conditions in which the polymer concentration is greater than or equal to 1500 ppm, and the left-hand branch corresponds to less than 1500 ppm. The right-hand branch is further subdivided according to the salinity. For instance, the leaf, which is the output value, for the left-hand side is 43 cp. This value is computed as the mean average of the responses that fall in that leaf. Figure 3.10 illustrates the regions corresponding to the tree in Figure 3.9 as a function of polymer concentration and salinity. Regions R_1, R_2, and R_3 are the results of the splitting

rules assigned to the tree and are known as the “leaves” of the tree. As stated earlier, values of the regions, or leaves, are given by the mean of the datapoints that fall in each region.

A decision tree can grow very deep, in the sense that the leaves are at the bottom of the tree, as the typical decision tree is drawn upside down. The extent of how deep a decision tree can go is primarily governed by the amount of data and the number of features. Nevertheless, a decision tree algorithm should have a stopping criterion at which no further splitting is made. For instance, if the number of datapoints in a single region is 3, no further splitting should be made. Moreover, the choice of which feature to use for splitting and at what value the splitting should occur is largely dependent on the problem itself. Normally, the optimal split is the one that yields the minimum sum-of-squared errors. However, there is no general rule for choosing the optimal split feature or value.

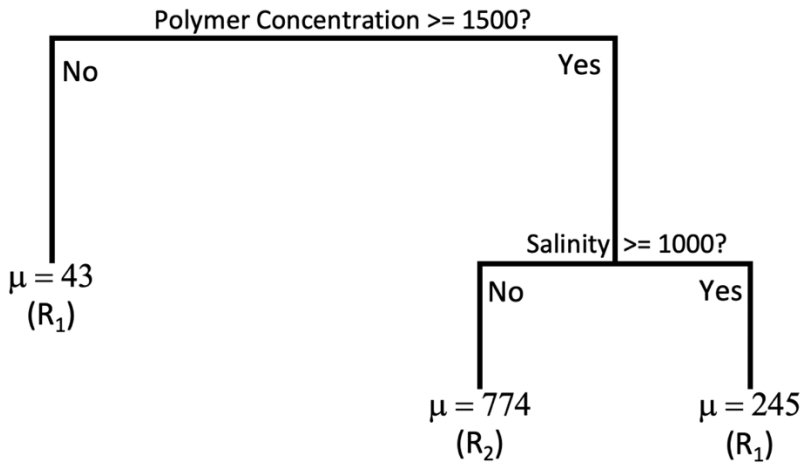

Figure 3.9: A decision tree example. This example was construction using data from Table 3.3.

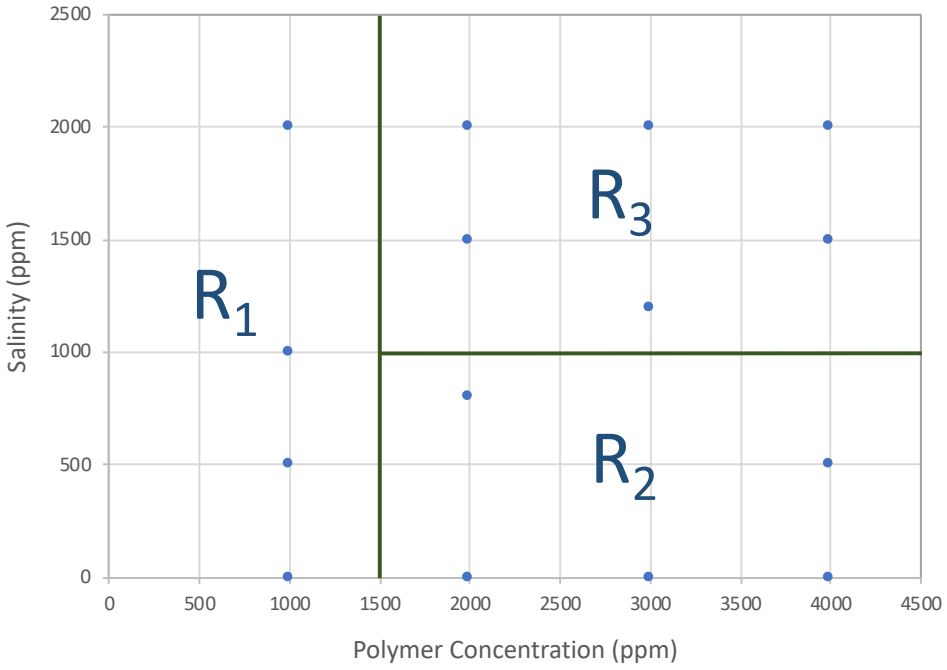

Figure 3.10: The three-region partition for the rheological dataset from the regression tree illustrated in Figure 3.9.

3.5.1.2Random Forests Algorithm

Using the concept of decision trees, it is easier to comprehend the idea of Random Forests. As previously stated, Random Forests algorithm is a set of decision trees that are trained in a completely independent manner. This means that the splitting rules are completely independent between the trees, and those rules are drawn randomly. Also, each tree is trained by a different dataset, called "bootstrap samples," taken from the same training dataset, which adds additional randomness. The major advantage of the randomness in RF is the significant reduction in variance without effecting the bias (Marsland, 2015). Furthermore, another important parameter of RF is the optimal number of trees, which is technically case-dependent. Normally, trees are continually added until no further improvement is seen in terms of error reduction. Once the RF is constructed and

the trees are trained, the output value is the mean of multiple values produced from each tree.

In this study, RF was used for the same objective as the regression approach: to predict Carreau's parameters based on polymer solution properties. Similar to the regression part, the data were subdivided according to the polymer type. Each subdivision was treated independently. The RF algorithm from the Scikit-Learn package, Random Forests Regressor, was used to build the RF model.

The number of trees is a crucial contributor to the accuracy of the model. Since there is no exact rule about how to determine the number of trees, a sensitivity analysis was conducted to gauge the optimal number of trees that corresponds to the highest coefficient of determination (R^2). For example, Figure 3.11 shows the R^2 across a range of trees up to 1000 of μ_p^0 dataset of the FP-3330S polymer. As can be seen, at a small number of trees (<150), R^2 is unstably fluctuating and can fall as low as 0.75. However, as the number of trees increases, R^2 becomes more stabilized and asymptotically converges to 0.93. While a higher number of trees provides more accuracy, the question arises as to maximum height. To answer this question, other contributing factors should be considered, such as the size of the training data, the hardware capabilities (e.g., processor, memory, etc.) and the required programming skills. In this study, the dataset is not overly large, and a regular computer can efficiently fulfill this study's objective. Therefore, considering the computational time and the accuracy (R^2), the optimal number of trees used in this study was between 50 and 600 trees, depending on the targeted Carreau's parameter.

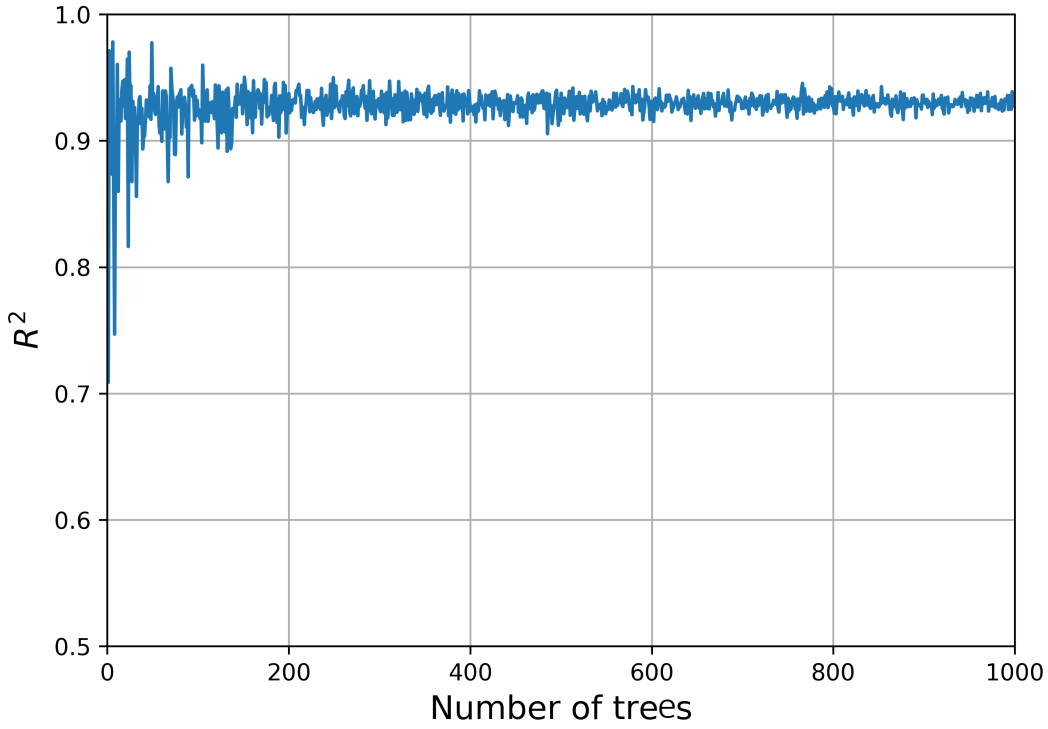

Figure 3.11: Plot shows the accuracy of the model with varying numbers of trees for the RF algorithm

Figure 3.12 shows an example of one tree (of 500) from an RF model built for predicting $\mu_p{}^0$ of the FP-3630S polymer. At each node, i.e. rectangle, the splitting feature and its condition are shown at the top. Then, following next is the mean squares error (MSE), which is the mean of the error squared between the actual viscosity data of the samples that fall in that node and the node's average viscosity value. Clearly, the nodes at the early stages of the tree tend to have higher MSE. Therefore, further splitting was applied until the minimum number of samples per node was reached, which is set at two samples.

Recall that the tree, the splitting feature, and the value of the splitting feature were all randomly selected.

Furthermore, the training-to-test ratio is another critical factor for virtually any machine-learning model. Generally, the larger the ratio the more accurate the RF model can be. However, the size of the whole dataset should be taken into consideration while determining the ratio. In this study, the ratio is selected at 0.9, meaning that 90% of the data for each polymer type is used for training and validating, and the remaining 10% is reserved for testing the model once trained. This ratio was also used in the other machine-learning model in this study.

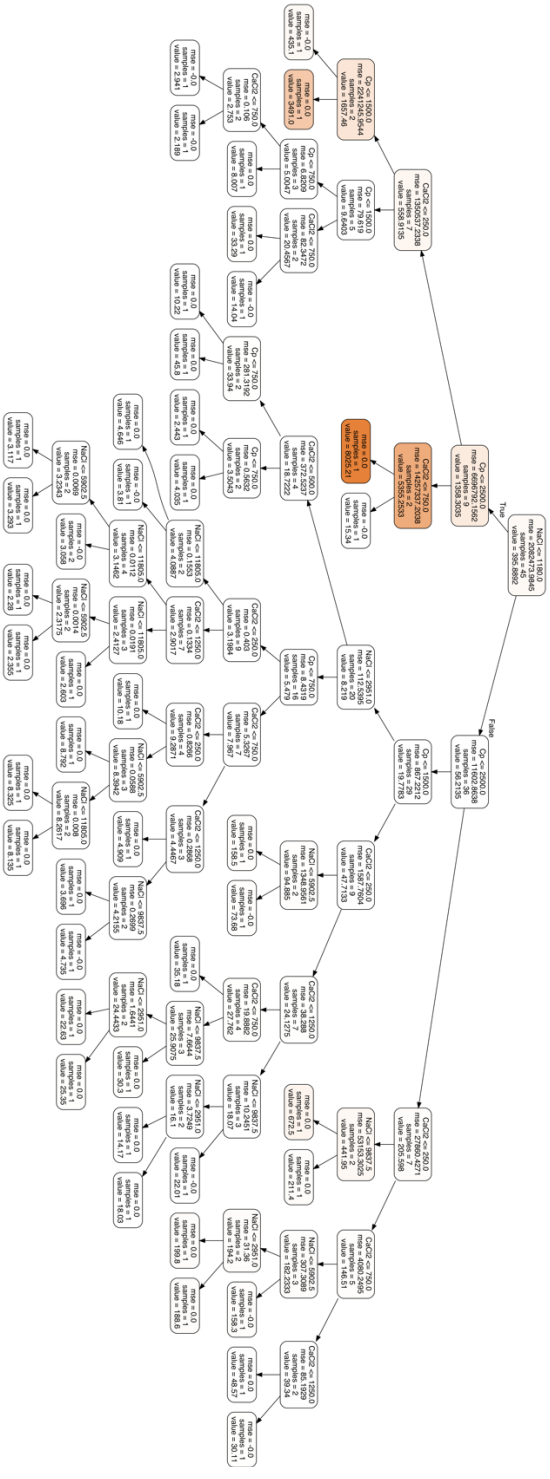

Figure 3.12: A decision tree example drawn from an RF model for μ_p^0 of the FP3630S polymer

3.5.2 Artificial Neural Networks

Artificial Neural Networks (ANN), also called multilayer perception (MLP), are a sophisticated and powerful deep-learning model that consists of interconnected nodes (neurons) and layers that form a set of networks. It is called "neural" because it was inspired by neuroscience and the biological neurons that constitute animal brains (Goodfellow, 2016). Figure 3.13 shows a typical configuration of an artificial neural network. It comprises three main elements: input layer, hidden layer(s), and output layer. The input layer holds a number of neurons corresponding to the number of features of the problem. The output layer contains neurons equal to the number of expected outputs. For example, if the viscosity and relaxation time are to be predicted based on polymer concentration, salinity, and hardness, then the input and output layers should have 3 and 2 neurons, respectively.

The hidden layers are the most critical element of ANN because that is where the calculation occurs. The hidden layers may have as many layers as the problem dictates, but they must have at least one layer. There is no exact rule about how many neurons should be in each hidden layer because that quantity depends on problem-related factors such as numbers of features and outputs. However, there are some practice-based suggestions to start with and perhaps modify as necessary. Each neuron in the hidden layers is connected to the neurons in the prior and post layers. Each connection, represented by an arrow in Figure 3.13, is quantified by a parameter, the weight (w). In addition, each neuron should have a bias value (b). The training data are fed into the input layer, and the information flows through the hidden layers, where computations are executed, finally reaching the output layer. The process is called the "feed-forward neural networks algorithm," given that the information flows forward from the input layer to the output layer. The value of

the neuron is communicated from the neurons in the preceding layer through the following equation:

$$z = \sum_{i=1}^{m} w_i x_i + b \tag{3.7}$$

where z is the current neuron value, w_i is the connection weight between the current and previous neurons, x_i is the value of the preceding neuron, b is the bias of the current neuron, and m is the number of neurons in the previous layer.

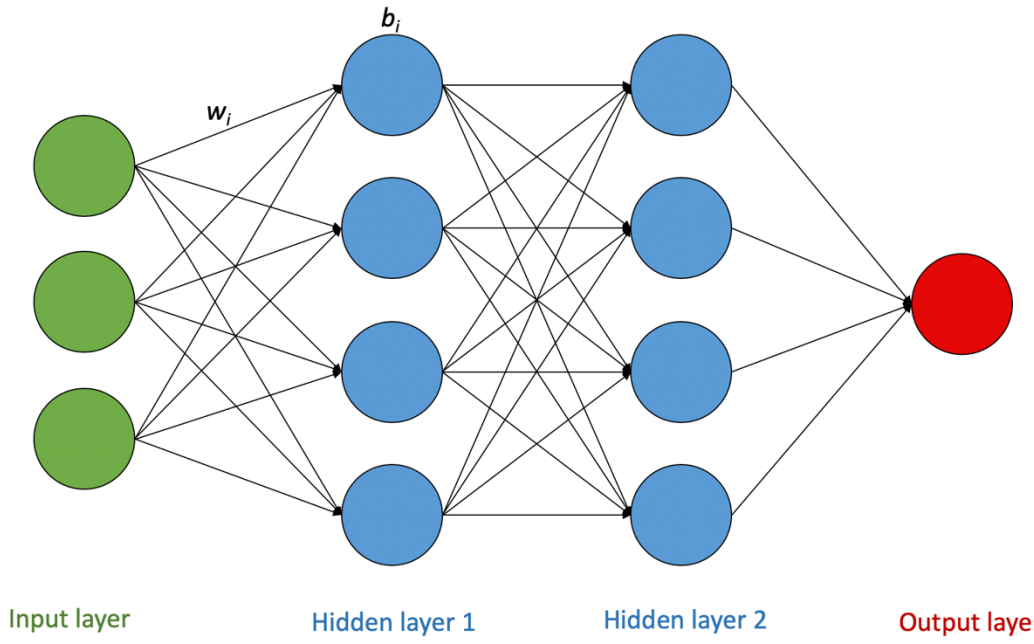

Figure 3.13: Schematic showing typical neural network with two hidden layers.

Furthermore, activation functions are used at the end of a hidden neuron to introduce nonlinear complexities to the model. Their main purpose is to convert an input signal of a neuron to an output signal. That output signal now is used as an input in the next layer. Thus, when the value of z is calculated, it is further used in the activation function. The most common types of activation functions are:

- Logistic function:

$$f(x) = \frac{1}{1 + e^{-x}} \quad (3.8)$$

- Hyperbolic tan function (tanh):

$$f(x) = \tanh(x) \quad (3.9)$$

- Rectified linear unit function (ReLU):

$$f(x) = \max(0, x) \quad (3.10)$$

Figure 3.14 shows the graphical representation of the aforementioned activation functions. An activation function can be very useful in mapping the neural networks, although some models do not include an activation function; those models use a linear activation function, $f(x) = x$. However, a neural network without activation function would simply be a linear regression model, which is limited in its complexity and has less power to learn complex functional mappings from data.

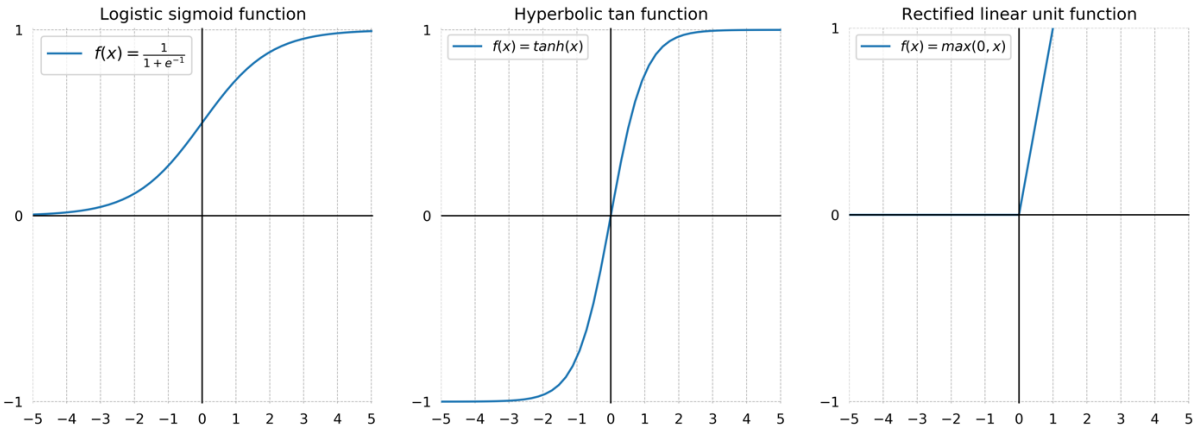

Figure 3.14: Types of activation functions

Initially, when the model undergoes the training process, initial values for w and b are assigned based on either user input, randomness, or algorithm input. After that, the input values (e.g., polymer concentration, salinity, etc.) from the training set are fed, and

the model performs computations throughout all the neurons until the output. Then, the model compares the results with the actual output and calculates the error. After that, assuming the error is greater than the threshold, the algorithm will adjust the weights and biases based on the actual output by performing a backward calculation. This technique is called "back propagation." The process is repeated until the minimum error condition is achieved.

In this study, the ANN model was trained with the same data used in the previous models. The data were subdivided into three groups according to the polymer type, as was done in the preceding models. A feed-forward artificial neural network with a back-propagation algorithm, "MLPRegressor" from the Scikit-Learn library, was used in this study. The objective is similar to the previous methods: to predict Carreau's model parameters based on polymer solution properties. Construction of the ANN model entailed a series of trial-and-error attempts in order to produce the best accuracy. During the construction process, three main features of ANN were studied: the activation function, the solver, and the number of neurons in each hidden layer. The three activation functions mentioned earlier were examined. Each function was applied and its performance compared with the others. Eventually, ReLU was found to yield the most accurate predictions.

The second important feature is the solver function, which is for the weight optimization. The MLPRegressor offers three types of solver algorithms:

- LBFGS: is an optimizer in the family of quasi-Newtonian methods
- SGD: refers to stochastic gradient descent
- Adam: refers to a stochastic gradient-based optimizer proposed by Kingma and Ba (2014)

Similar to the activation function, all three solvers were studied. As a result, LBFGS was found to be the best for having the highest accuracy. Finally, the number of hidden layers was examined. Sometimes, an exceedingly large number of hidden layers may result in an overfitting scenario, and vice versa. Thus, the models were initially built with one hidden layer, and the results were investigated. After several trials, the optimal number of hidden layers used in the ANN model was found to be two. In addition, both layers have a varying number of neurons, depending on the target parameter. However, the number of neurons per layer is in the range between 7 and 5 neurons, except for the zero-shear viscosity models, which needed up to 15 neurons per hidden layer. In the following chapter, the results of the ANN models, along with a comparison between all the models, will be presented.

CHAPTER 4. RESULTS AND DISCUSSION

4.1 CURVE FITS OF RHEOLOGY DATA TO CARREAU'S MODEL

As discussed in chapter 3, an algorithm was developed to fit the rheological data of multiple polymer samples to Carreau's model. The error minimization method used in this curve-fitting algorithm is the least absolute error, i.e. L1-norm. Many researchers use the least-squares error (L2-norm) to curve-fit rheological data to a shear-thinning model, i.e. Carreau's model. However, least-squares method tends to be more biased toward the low shear-rate viscosity since they are much higher in magnitude than the high-shear rate viscosity. As a result, least-squares method may not fit very well at higher shear rates. Figure 4.1 shows the least error fit matches the data better than the least-squares error fit, especially at higher shear rates.

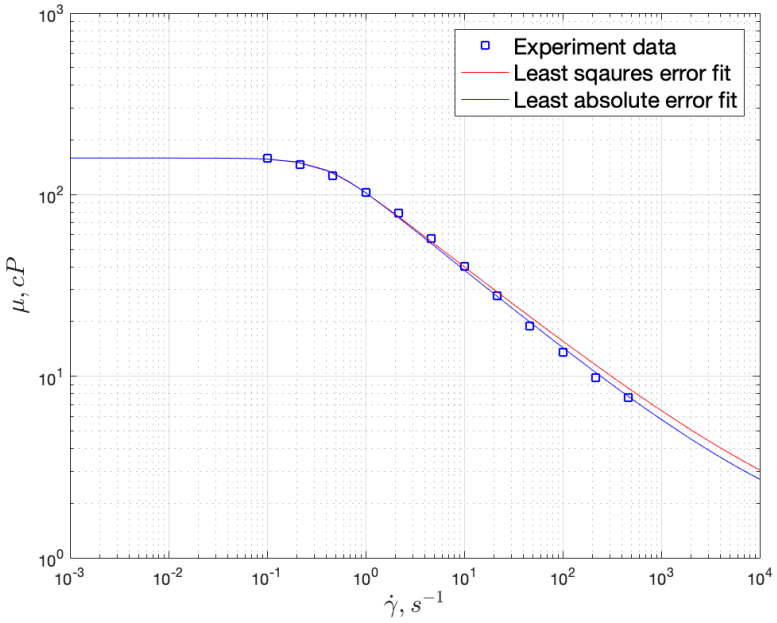

Figure 4.1: Curve-fit error minimization difference for 2500 ppm FP-3630S polymer at 0.5 wt% salinity

The algorithm can detect common abnormalities and outliers associated with rheology measurements. One the most common anomalies encountered is the decrease of viscosity at low shear rates, as shear-thinning fluids generally exhibit a viscosity plateau at low shear rates. Another common abnormal behavior is often observed at the higher end of the shear rate, where the viscosity should approach another Newtonian plateau (greater than or equal to the solvent viscosity) but the data often erroneously trend upward at very high viscosities.

The algorithm uses the derivative of the viscosity curve for detecting such anomalies. For instance, the derivative of the curve at the low-shear- rate plateau should be zero (or at close to zero). Therefore, an offset from the zero derivative into the positive derivative region indicates a problematic situation. This suggests that the viscosity trend starts to decrease with decreasing shear rate.

Figure 4.2 shows a viscosity curve of an HPAM polymer that demonstrates abnormal behavior at the low-shear-rate plateau. A second curve on the plot shows the derivative of the viscosity curve. As can be seen in the low-shear-rate region, moving from right to left, the derivative curve was near the zero-derivative line from 2.5 until 0.5 s^{-1} where a sharp increase diverted the curve into the positive region. Thus, a positive derivative indicates a decrease in viscosity, and the significance of the drop is realized through the sharp increase in the derivative. Unlike the typical case of a viscosity profile (shown in Figure 4.3) where a low-shear-rate viscosity plateau is observed, the corresponding derivative is nearly zero. Subsequently, the algorithm successfully managed to identify the off-trend anomaly. As a result, the points that lie off the trend of the plateau are omitted before the fitting process begins.

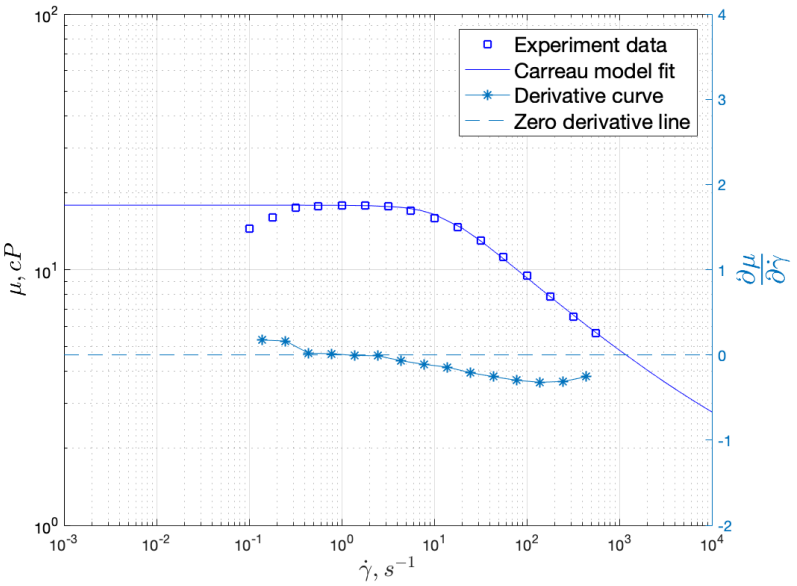

Figure 4.2: Plot showing a profile of 3000 ppm FP-3330S polymer and 2.5 wt% NaCl at 68°C with an anomaly at a low shear rate

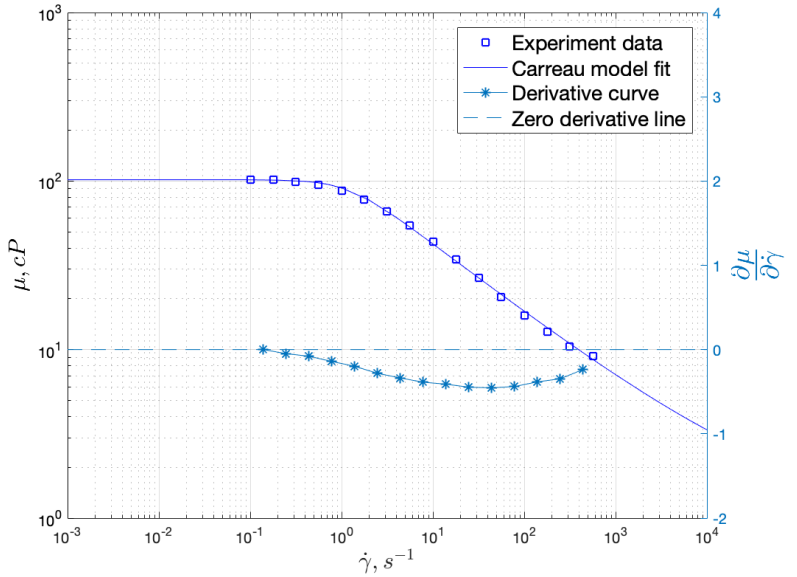

Figure 4.3: Plot showing an intact viscosity profile of 3200 ppm FP-3630S polymer and 6.5 wt% total salinity at 62°C

Figure 4.4 shows another common spurious trend in the high-shear region. As shown in the figure, a sharp viscosity increase occurs at the highest shear rate. The corresponding derivative curve shows a similar sharp increase, resulting in a positive derivative value. Subsequently, the algorithm detected this error and excluded it from the fitting process. In summary, this algorithm was designed to tackle the discussed errors, which were very frequently seen during rheology measurements. However, there is a possibility that other unmentioned errors associated with rheology measurements might be encountered. Thus, human quality-check becomes a necessary step to ensure the fitting is accurate.

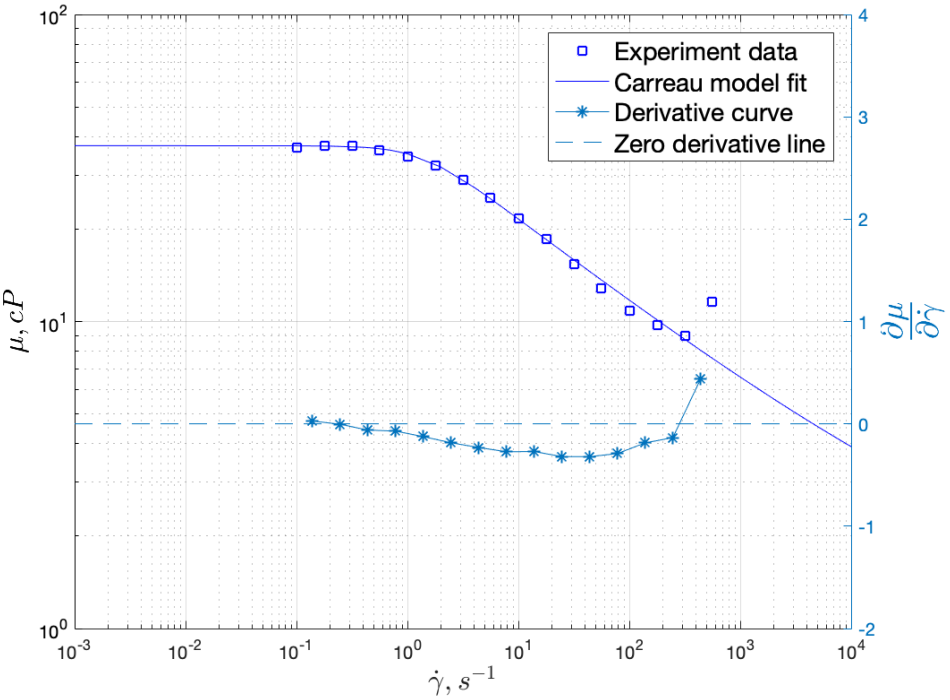

Figure 4.4: Plot showing a profile of 2000 ppm FP-3630S polymer with 3 wt% total salinity at 25°C with an anomaly at a high-shear rate

4.2 FITTINGS OF CARREAU'S MODEL PARAMETERS TO POLYMER CHARACTERISTICS BY REGRESSION

This section presents the final results of fitting Carreau's model parameters using conventional regression techniques. Three equations, Eq. 2.13, Eq. 3.2, and Eq. 3.6, were fitted with the experimental data, and the resultant fitting constants are presented in this section. The three equations correspond to Carreau's model parameters: the zero-shear viscosity, the shear-thinning index, and the time constant. A Python code was developed to accomplish this task; Python packages, Lmfit and Sickit-Learn were utilized. The fitting method used in all the fittings is the least-squares, that is, a minimization of the sum of squared errors. The results are presented in 45° plots in which the x-axis represents the actual data from the experiments and the y-axis represents the data obtained from the regression model.

4.2.1 Zero Shear Viscosity (μ_p^0)

Recall that the equation used for the zero-shear viscosity prediction is the modified Martin equation (Eq. 2.13), which is given by:

$$\ln\left(\frac{\eta_{sp}}{C_p}\right) = \ln\left(kC_{sep}^{S_p}\right) + k_2 C_p$$

Figure 4.5 through Figure 4.7 show example applications of Martin's equation on the three tested polymers. Each plot has multiple dots, which represent the experimental data, and lines, which corresponds to the fit of Martin's equation. The color-labeled dots and line corresponds to a certain salinity, as indicated by the legend. It is clearly shown that the data successfully obeys Martin's equation. This implies that the Martin equation is valid to use within the range of polymer concentrations employed in this study.

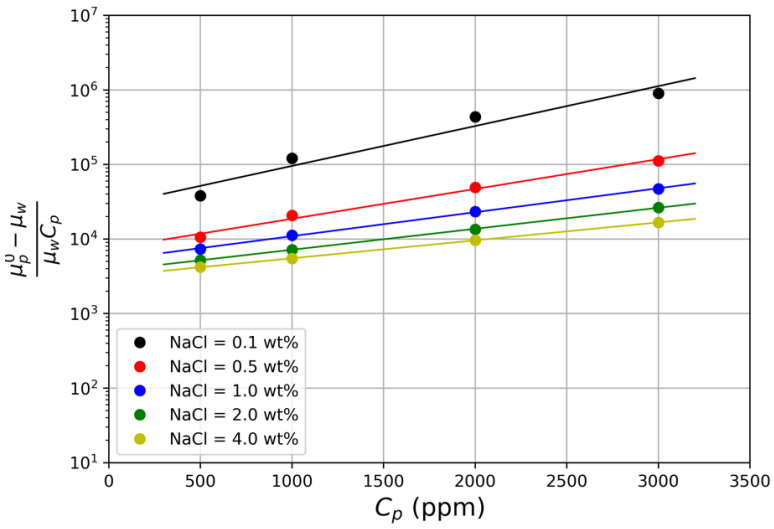

Figure 4.5: Fit of Martin equation to FP-3330S polymer data at 25°C

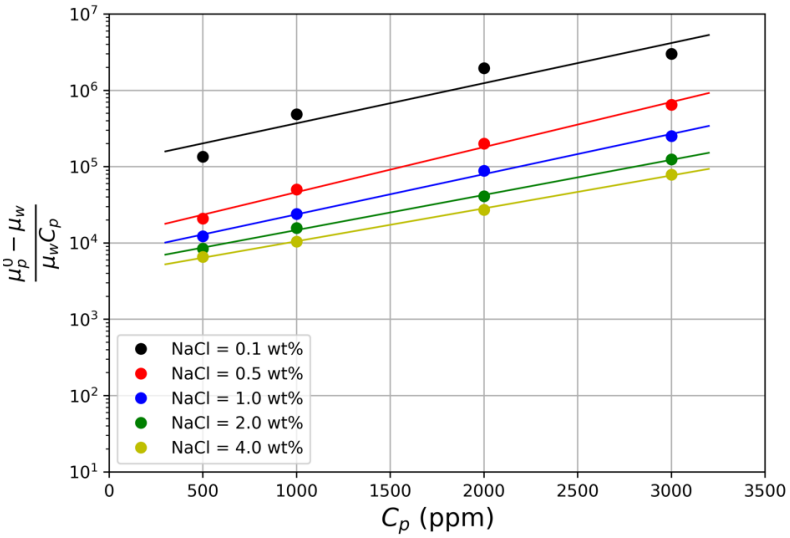

Figure 4.6: Fit of Martin equation to FP-3630S polymer data at 25°C

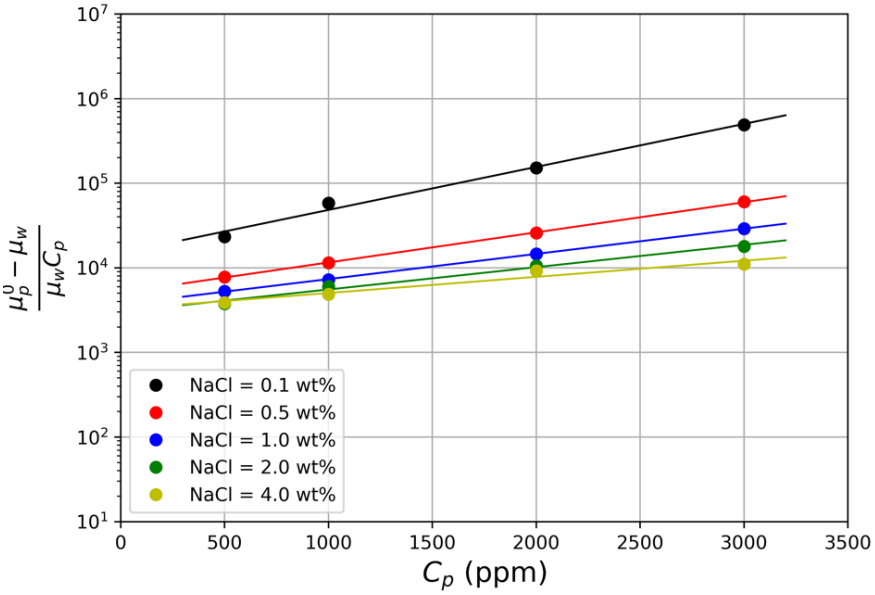

Figure 4.7: Fit of Martin equation to AN125 polymer data at 25°C

Furthermore, Figure 4.8 shows an example of a comparison between Martin equation and 3rd order Flory-Huggins equations. As can be seen, both models were found to match the experimental data well. Thus, given that Martin equation requires a smaller number of fitting parameters, it further supports the use of Martin equation in this study. The coefficients of Flory-Huggins equation is posted on the same figure. Additionally, Figure 4.9 through Figure 4.11 demonstrate a comparison between Martin, Flory-Huggins and Jouenne et al. (2019) equations. Recall that Jouenne et al. (2019) equation (Eq. 2.38) is given by:

$$\eta_{sp} = C_p[\eta] + 0.56(C[\eta])^{2.17} + 0.0026(C[\eta])^{4.72}$$

As can be seen, Jouenne et al. (2019) model tends to overestimate the specific viscosity especially at lower salinity. This mismatch may be attributed to many factors including

different polymer stocks and batches that were used to develop the model compared to the polymer used in this study and different polymer preparation procedures.

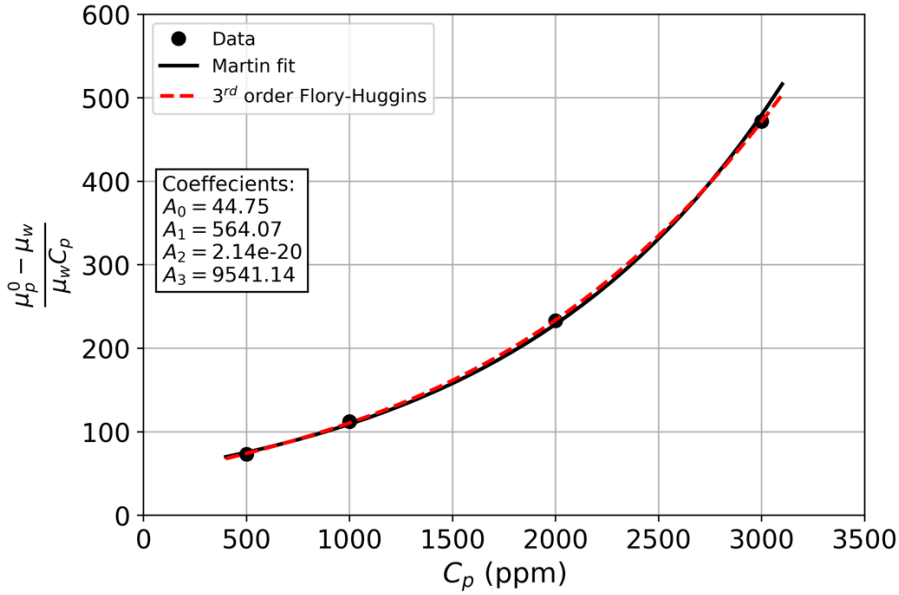

Figure 4.8: Comparison between Martin equation and 3rd order Flory-Huggins Equation for FP-3330S at 1% NaCl and 25°C

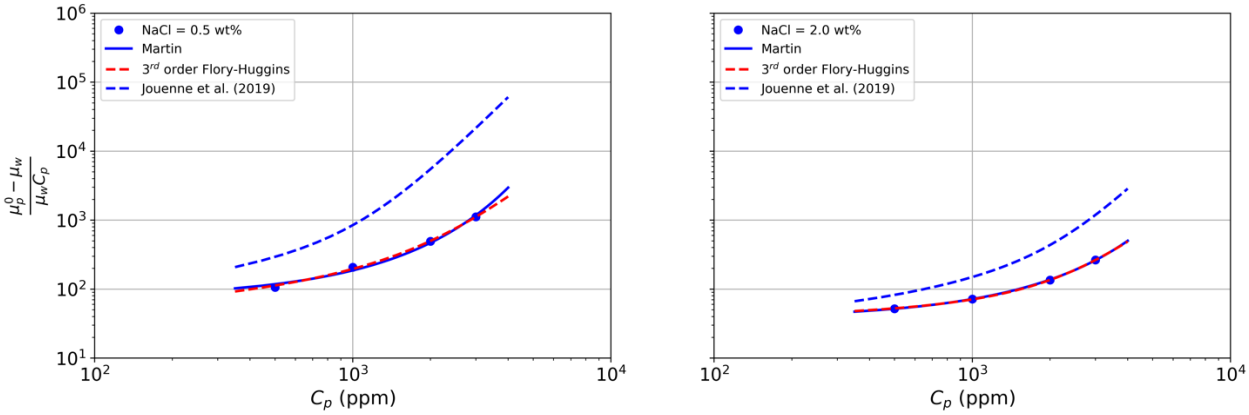

Figure 4.9: Comparison between Martin, 3rd order Flory-Huggins and Jouenne et al. (2019) models for FP-3330S at 0.5 & 2 wt% NaCl and 25°C

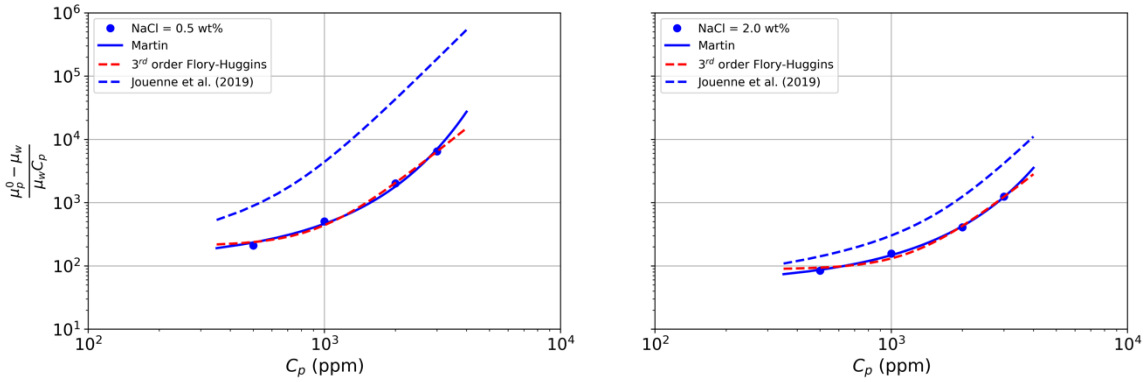

Figure 4.10: Comparison between Martin, 3rd order Flory-Huggins and Jouenne et al. (2019) models for FP-3630S at 0.5 & 2 wt% NaCl and 25°C

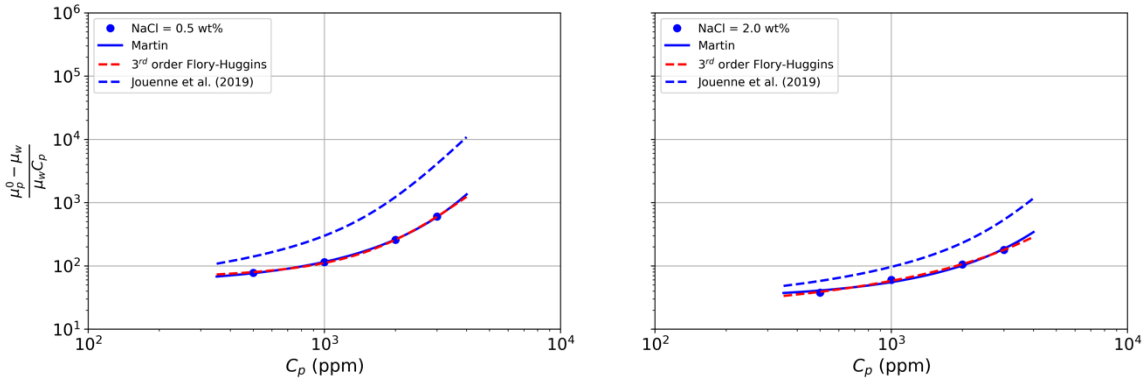

Figure 4.11: Comparison between Martin, 3rd order Flory-Huggins and Jouenne et al. (2019) models for An-125 at 0.5 & 2 wt% NaCl and 25°C

Figure 4.12 through Figure 4.14 show the fitting results of three different polymers to the Martin equation. In Figure 4.12, the FP-3330S polymer data show a good match between the actual data and the model's prediction. The low viscosity values match better than the high values. This is because most of the data are concentrated in the low-value viscosity region, due to the presence of salt and the hardness content in most of the samples. This phenomenon is also seen in other polymer types. The FP-3630S polymer data are shown in Figure 4.13. As can be seen, the model reasonably matches the data. The fitting result of the third polymer, AN-125, is shown in Figure 4.14. The model prediction exhibits

an excellent match with the actual data, as most of the data cluster around the 45° line. In summary, Eq. 2.13 successfullycorrelates the zero-shear viscosity with various polymer characteristics within a satisfactory range of accuracy. The fitting constants of Eq. 2.13 and the β_p parameter of C_{sep} (Eq. 2.12) for each polymer type are listed in Table 4.1.

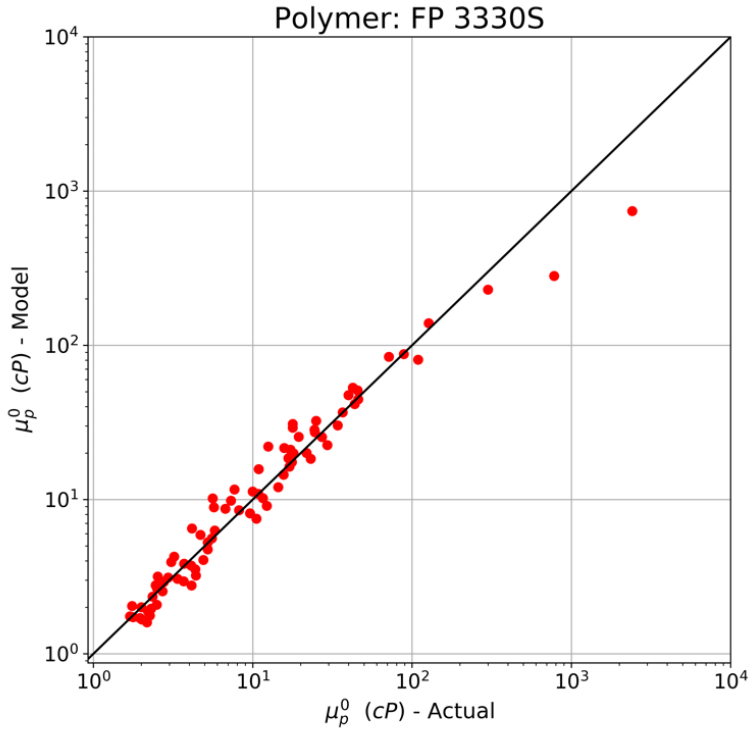

Figure 4.12: Comparison between predicted and measured data of $\mu_p{}^0$ for the FP3330S polymer

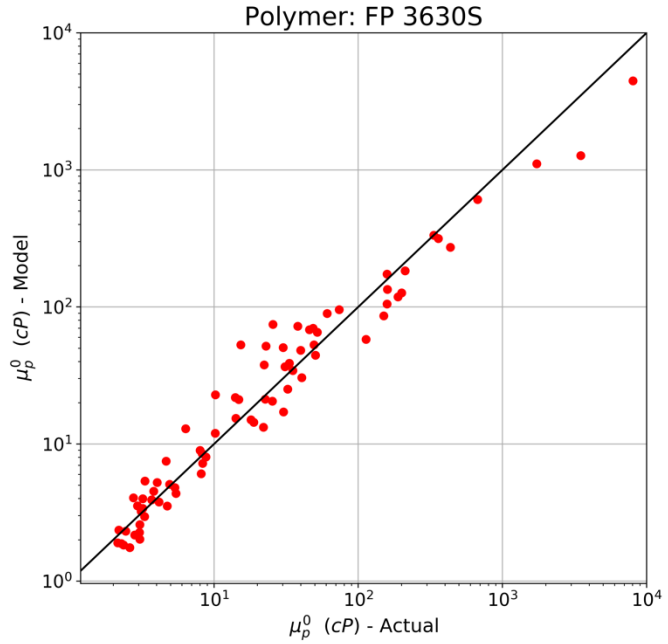

Figure 4.13: Comparison between predicted and measured data of $\mu_p{}^0$ for the FP3630S polymer

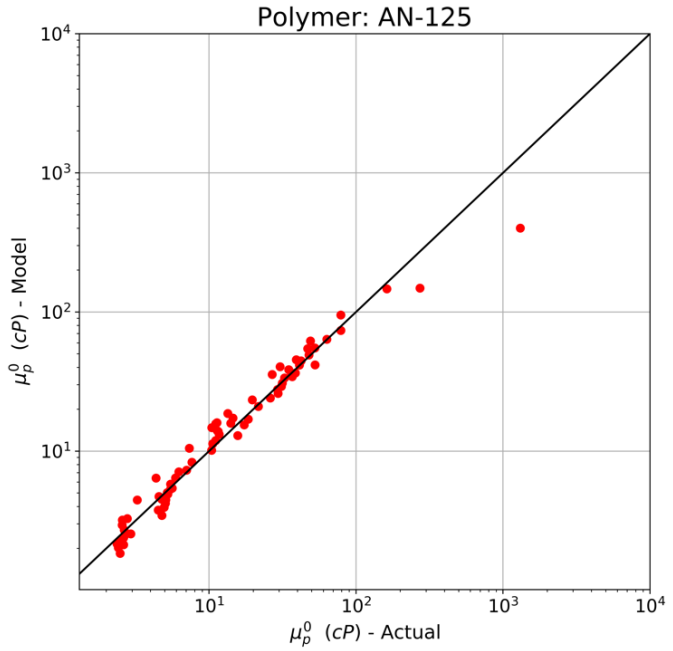

Figure 4.14: Comparison between predicted and measured data of $\mu_p{}^0$ for the AN-125 polymer

Table 4.1: Correlation parameters of Eq. 2.13 for the tested polymers

Parameter	FP 3330S	FP 3630S	AN-125
k_1	2600	3830	1970
k_2	565	850	590
S_p	-0.73	-0.87	-0.63
β_p	30	39	10

4.2.2 Shear-thinning index (n)

An equation was proposed for the shear thinning index, n, (Eq. 3.2), which is given by:

$$n = n_\infty + \left[\exp\left(-D_{p1}C_p\right) - n_\infty\right]\exp\left(-D_{p2}\frac{C_p}{C_{sep}}\right)$$

Figure 4.15 through Figure 4.17 show an example of n versus polymer concertation at different salinities with each distinctly-colored line has a constant salinity. The dots represent the data whereas the curve is the fit of the previous equation, Eq. 3.2. the figure clearly shows the alignment between the data and the equation which further supports the capability of the equation to predict n.

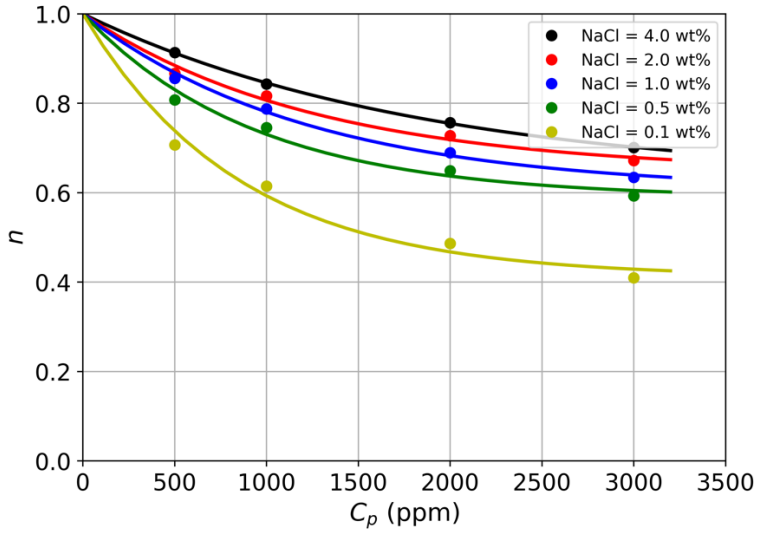

Figure 4.15: Fit of Eq. 3.2 to FP-3330S polymer data at 25°C

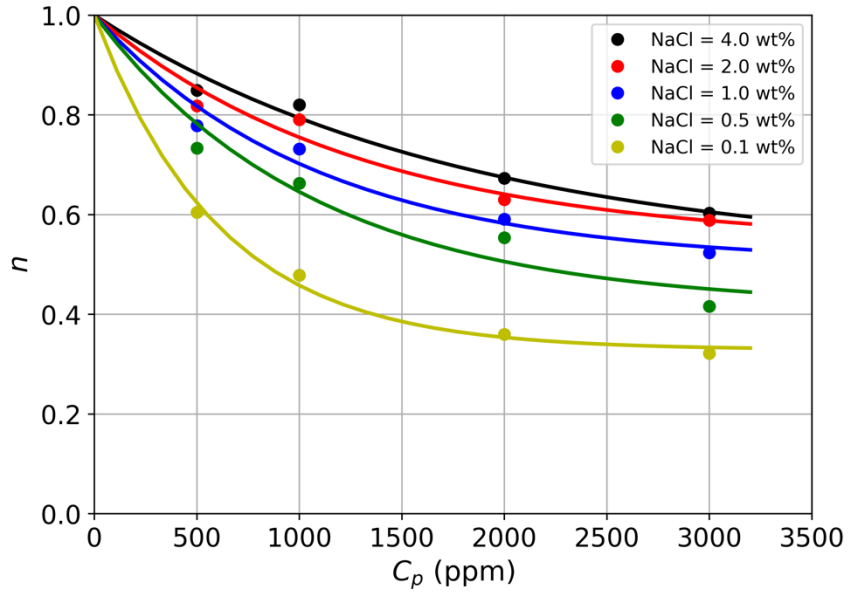

Figure 4.16: Fit of Eq. 3.2 to FP-3630S polymer data at 25°C

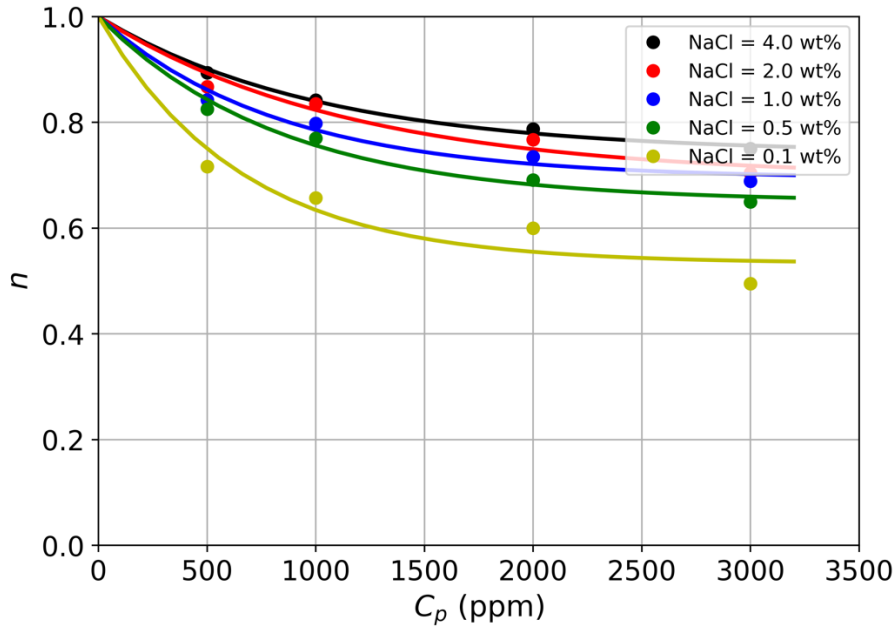

Figure 4.17: Fit of Eq. 3.2 to AN-125 polymer data at 25°C

Subsequently, the data were fit to this equation, and the results are presented in Figure 4.18. This figure includes all the three polymer types, each designated by a different color. As can be seen, the model provides a good match with the data for all polymer solutions. Figure 4.19 shows the normalized error of n predictions for the three polymers. It is clear that FP-3630S has the highest mean normalized error (5%) amongst the polymer types, although still low. The results support the conclusion that the proposed equation is capable of providing accurate and reliable predictions of *n* for the tested polymers. The best-fit parameters for Eq. 3.2 are listed in Table 4.2 for each polymer type.

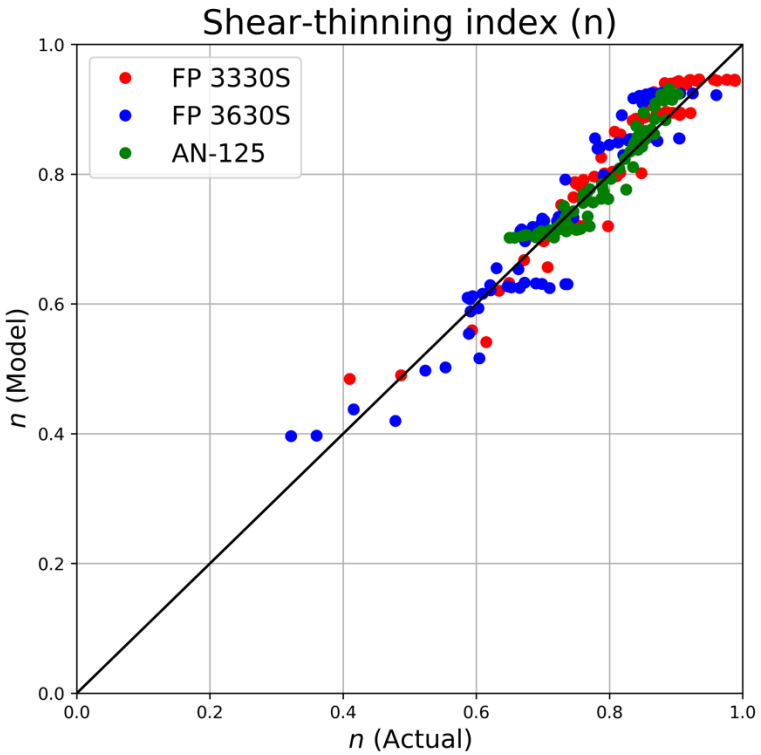

Figure 4.18: Comparison between the predicted and actual results of *n* for all the tested polymers

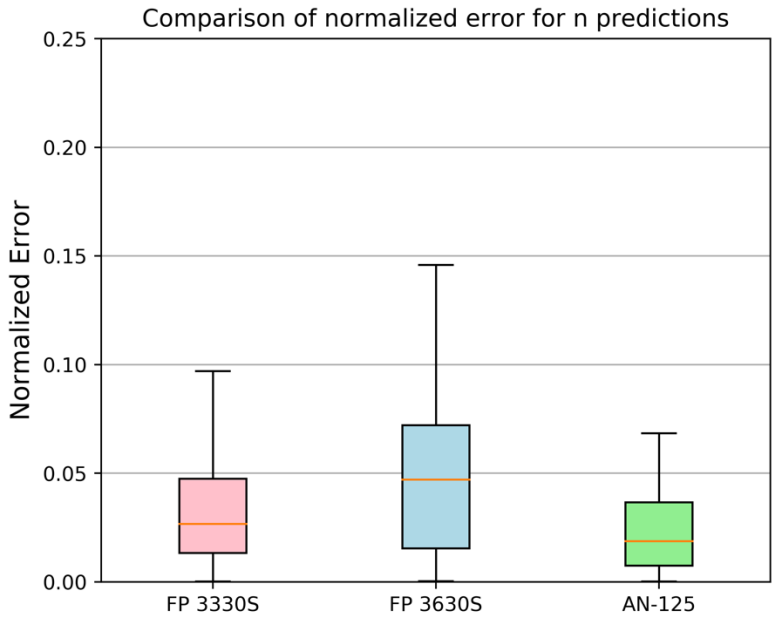

Figure 4.19: Boxplot of normalized errors for n prediction of the three tested polymers

Table 4.2: Correlation parameters of Eq. 3.2 for the tested polymers

Parameter	***FP 3330S***	***FP 3630S***	***AN-125***
$\mathbf{D_{p1}}$	104	147	100
$\mathbf{D_{p2}}$ ***(meq/mL)***	34	51	138
$\mathbf{n_{\infty}}$	0.5	0.4	0.66

4.2.3 Time constant (λ)

As stated in chapter 3, a multivariable linear regression (MLR) was implemented to fit λ with the polymer concentration and effective salinity. Recall that the resulting equation (Eq. 3.6) is given as:

$$\lambda = a_0 \, C_p^{a_1} C_{sep}^{a_2}$$

Figure 4.20 though Figure 4.22 show an example of λ versus polymer concertation at different salinities with each distinctly-colored line has a constant salinity. The dots represent the actual values whereas the curve is the fit of the previous equation, Eq. 3.6.

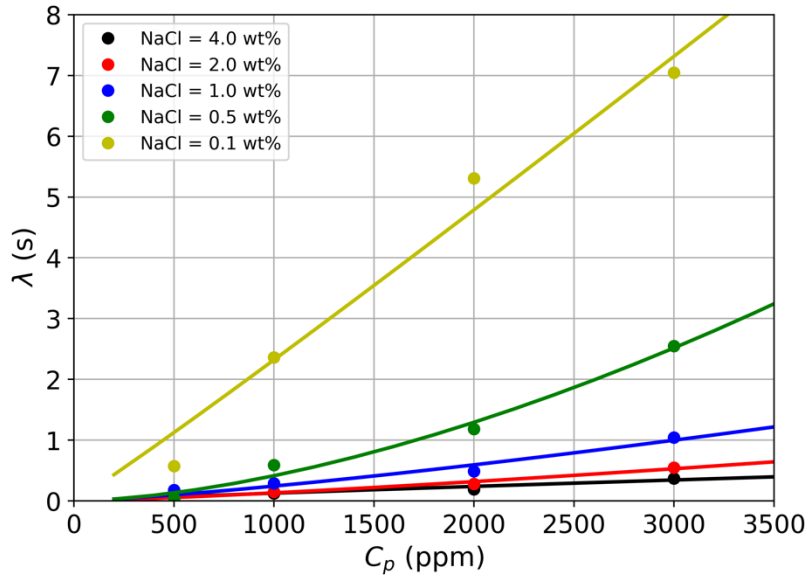

Figure 4.20: Fit of Eq. 3.6 for FP-3330S polymer data at 25°C

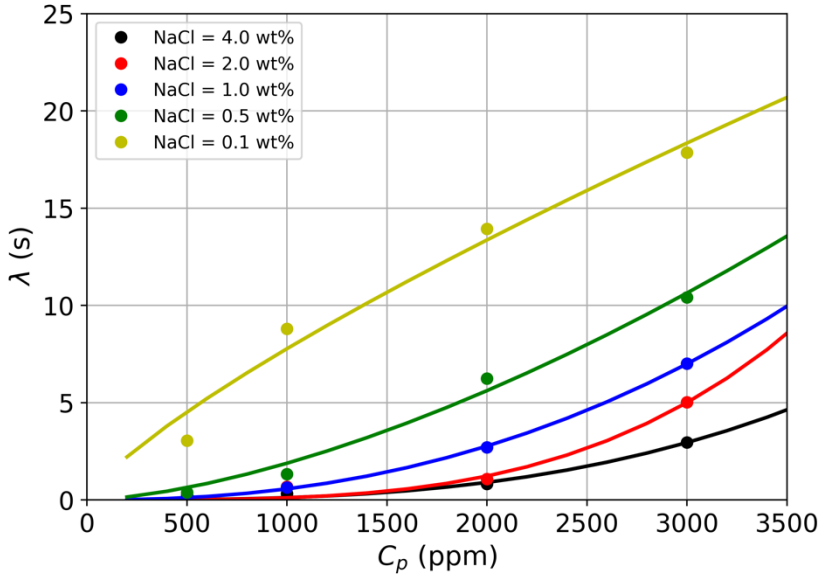

Figure 4.21: Fit of Eq. 3.6 for FP-3630S polymer data at 25°C

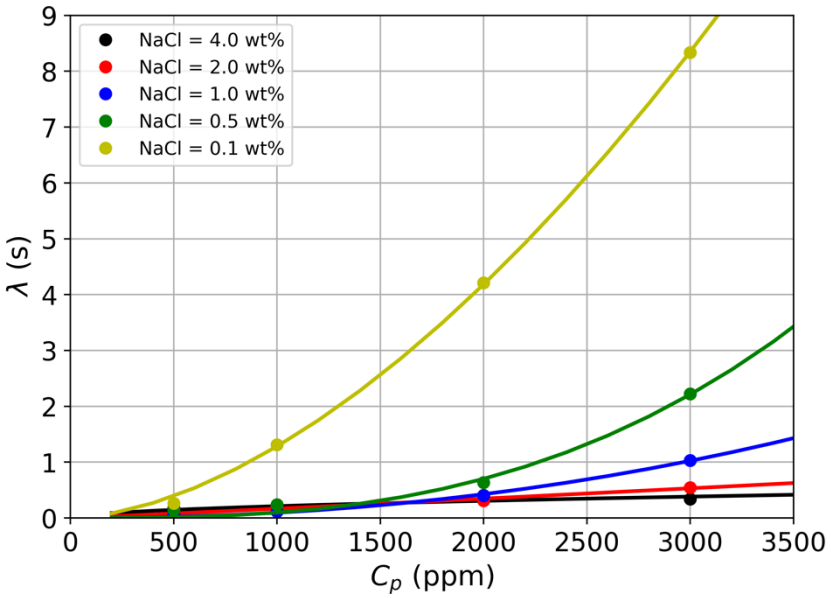

Figure 4.22: Fit of Eq. 3.6 for AN-125 polymer data at 25°C

Figure 4.23 shows the model predictions versus the actual data of all the polymers. Similar to previous Carreau's parameters, FP-3630S predictions seem to be worse than the predictions of the other two polymers. Figure 4.24 shows R^2 regression scores (R^2) of λ for each polymer type. FP3630S marked the lowest R^2 and FP3330S demonstrated the best consistent match of the data of the three tested polymers. Overall, the model for every polymer type provides a reasonably good estimation. The best-fit parameters of the λ equation is listed in Table 4.3.

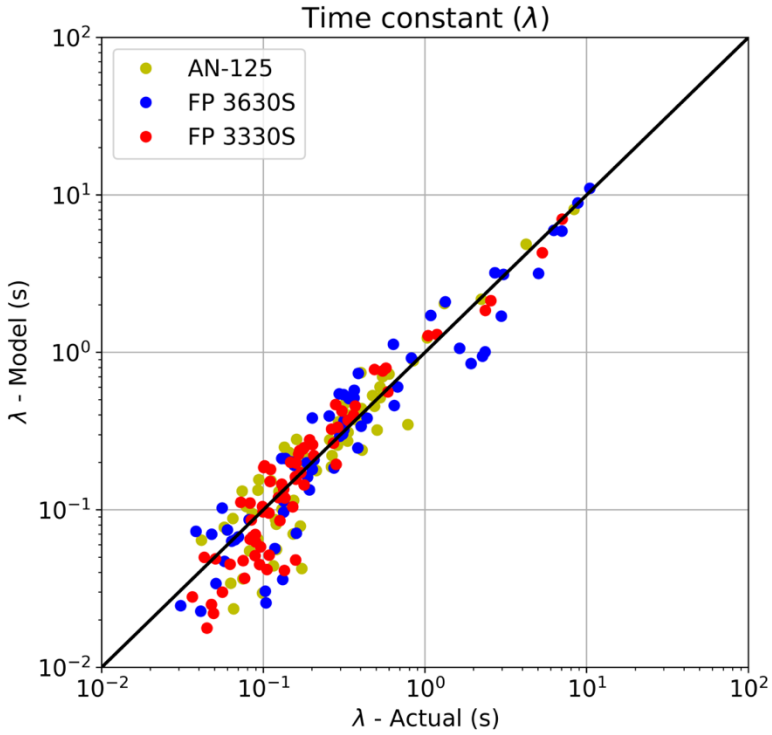

Figure 4.23: Comparison between predicted and actual values of λ for the tested polymers

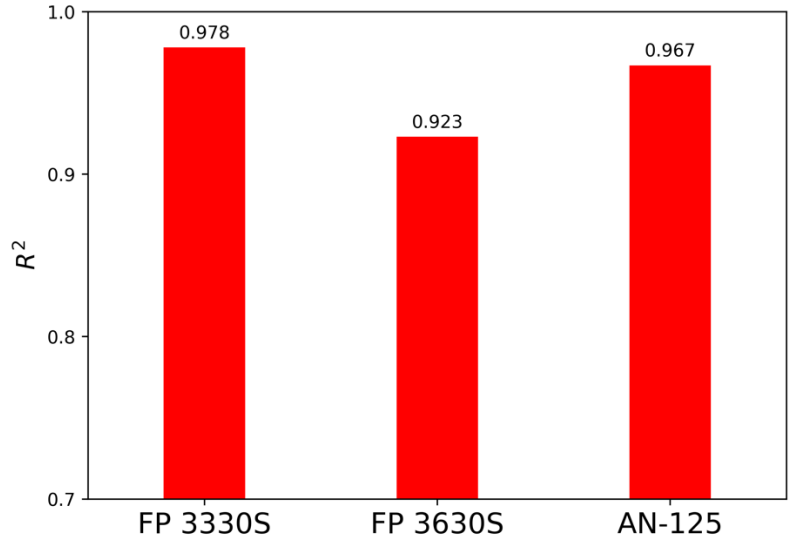

Figure 4.24: Bar plot of R^2 scores of λ correlation for the tested polymers

Table 4.3: Correlation parameters of Eq. 3.6 for the tested polymers

Parameter	FP 3330S	FP 3630S	AN-125
a_0 (s)	77	3470	420
a_1	0.96	1.39	1.25
a_2	-0.78	-0.92	-0.82

4.3 MACHINE LEARNING APPROACH

In this section, the predictions from two machine-learning methods, Random Forests and Artificial Neural Networks, are presented. Similarly, the results are displayed in 45° plots, which show the actual data in the x-axis and the model prediction in the y-axis. In addition, unlike the regression results, there are two adjacent plots per parameter: the training data and the test data. Typically, in machine-learning applications, the dataset is divided into two sets: training and testing. The training data are used to train the model; it represents 75-90% of the original dataset. The test dataset used for testing the ML model. Test data are completely excluded from the model and are called out only after the model has been already built for validation and comparison with the actual results. Results of each machine-learning model will be presented individually in the following subsections.

4.3.1 Random Forests (RF)

Predictions obtained by the Random Forests model are excellent, and they outperformed the predictions made by the regression methods. Three RF models were developed for each polymer type, each equipped with 500 tree estimators. Figure 4.25 shows the results for the zero-shear viscosity of the three tested polymers. The left-hand side plots (blue dots) are the training set, whereas the right-hand side plots represent the test dataset. This plotting scheme is repeated in all the plots throughout the machine-

learning section. As can be seen in the figure, RF models show a very good match with the actual data, having an average R^2 of 0.95. Unlike the regression case, the RF model performance is nearly similar for all three polymers. Figure 4.26 shows the predictions of the shear-thinning index by RF. Comparing the training and the testing plots of all the polymers, the RF results have an excellent match with the actual data. Figure 4.27 shows the results of the time constant (λ). The RF predictions have a satisfactory match with the actual data for all the polymers. Overall, the RF method has proved to be a robust predictive tool with exceptional accuracy. Despite its simple underlying concept, it minimizes uncertainty and provides more accurate estimations than do traditional regression methods.

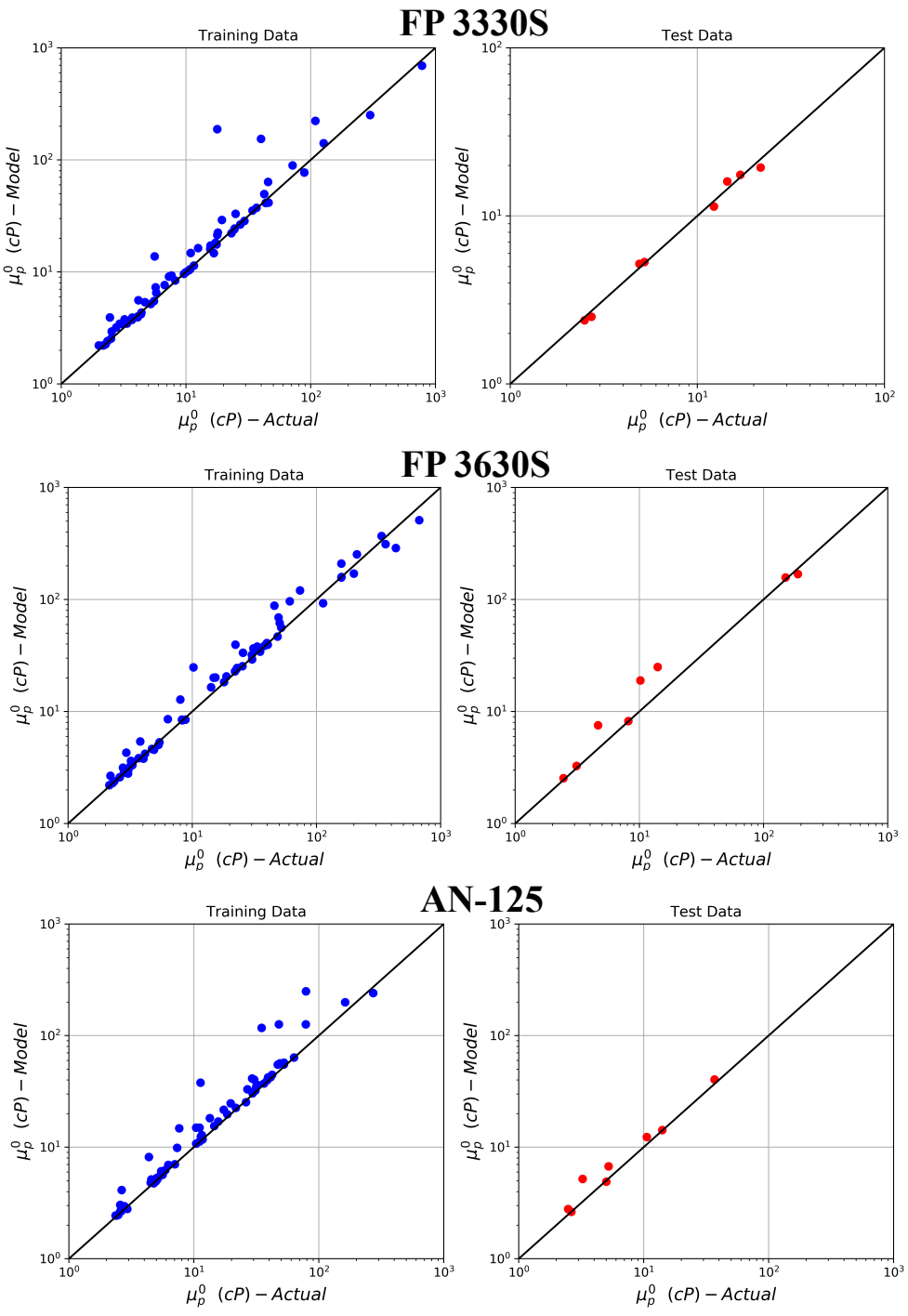

Figure 4.25: Comparison of measured and predicted values of zero-shear viscosity by the RF model

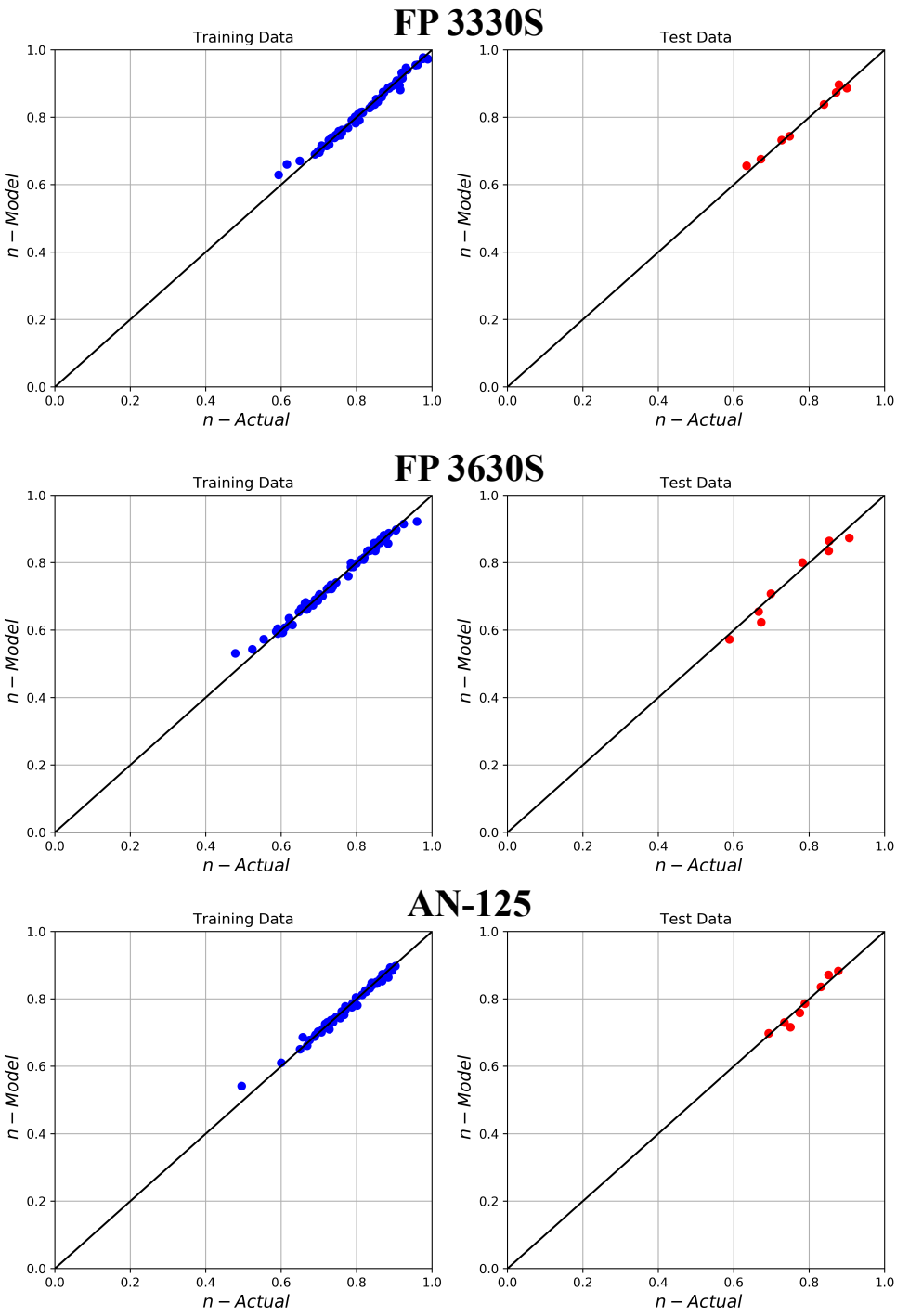

Figure 4.26: Comparison of measured and predicted values of the shear-thinning index by the RF model

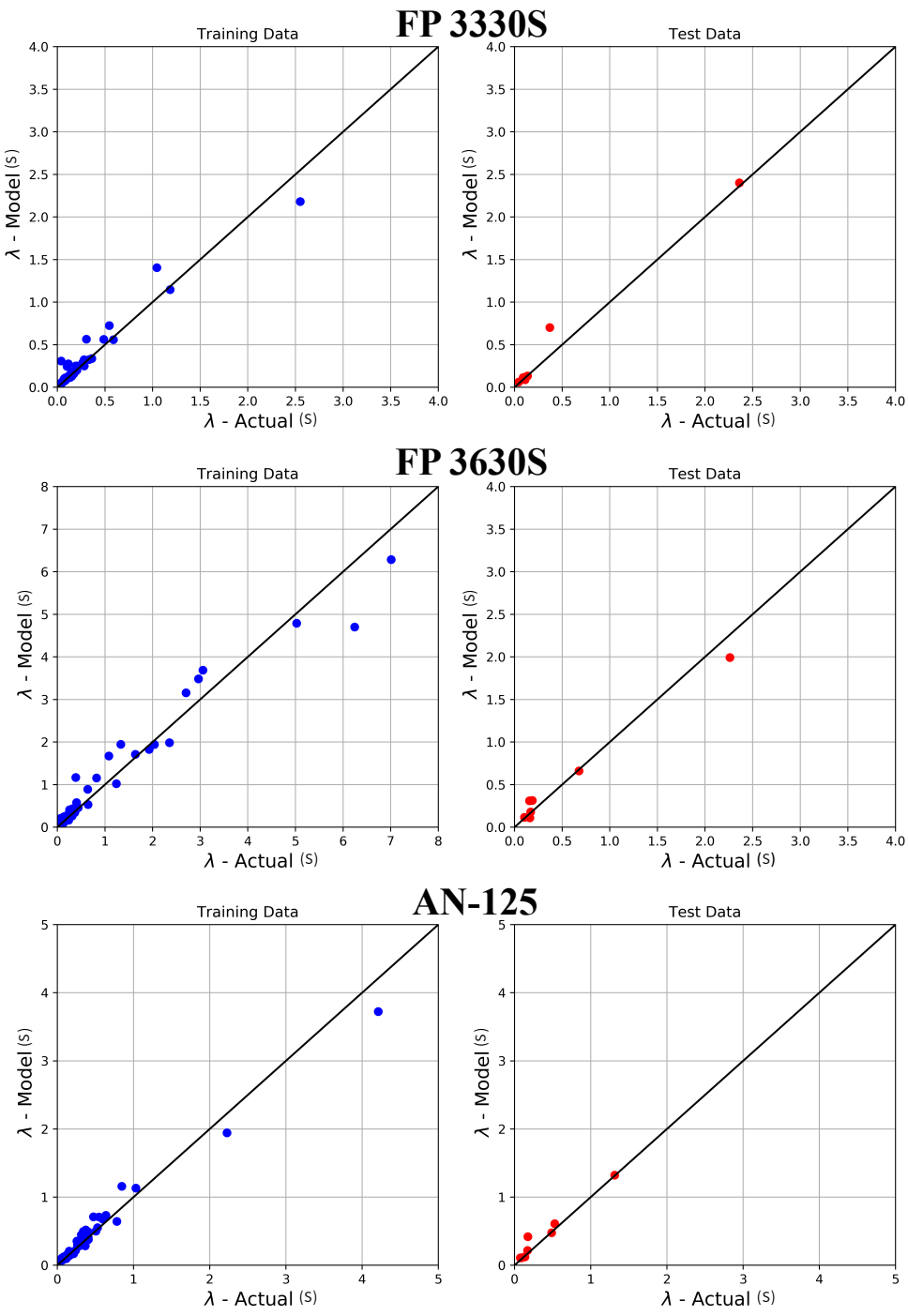

Figure 4.27: Comparison of measured and predicted values of the time constant by the RF model

4.3.2 Artificial Neural Networks (ANN)

As stated in chapter 3, ANN is one of the most powerful and complex deep- learning methods. In this study, feed-forward artificial neural networks with back- propagation adjustments were applied. The algorithm was outsourced from the Scikit-Learn package.

Figure 4.28 shows the ANN predictions for the zero-shear viscosity for tested polymers. According to this figure, ANN models seem to outperform RF and regression models. Both the training and the testing sets show an excellent match with the actual data. Moreover, similar performance is seen on the predictions of the shear-thinning index and the time constant by ANN models, as shown in Figure 4.29 and Figure 4.30. Table 4.4 summarized the ANN models' properties.

Table 4.4: Properties of ANN models

Parameter	**Activation Function**	**Solver**	**Number of hidden layers**	**Number of neurons per hidden layer**
$\mu_p{}^0$	ReLU	LBFGS	2	15
n				7
λ	ReLU & Logistics			7

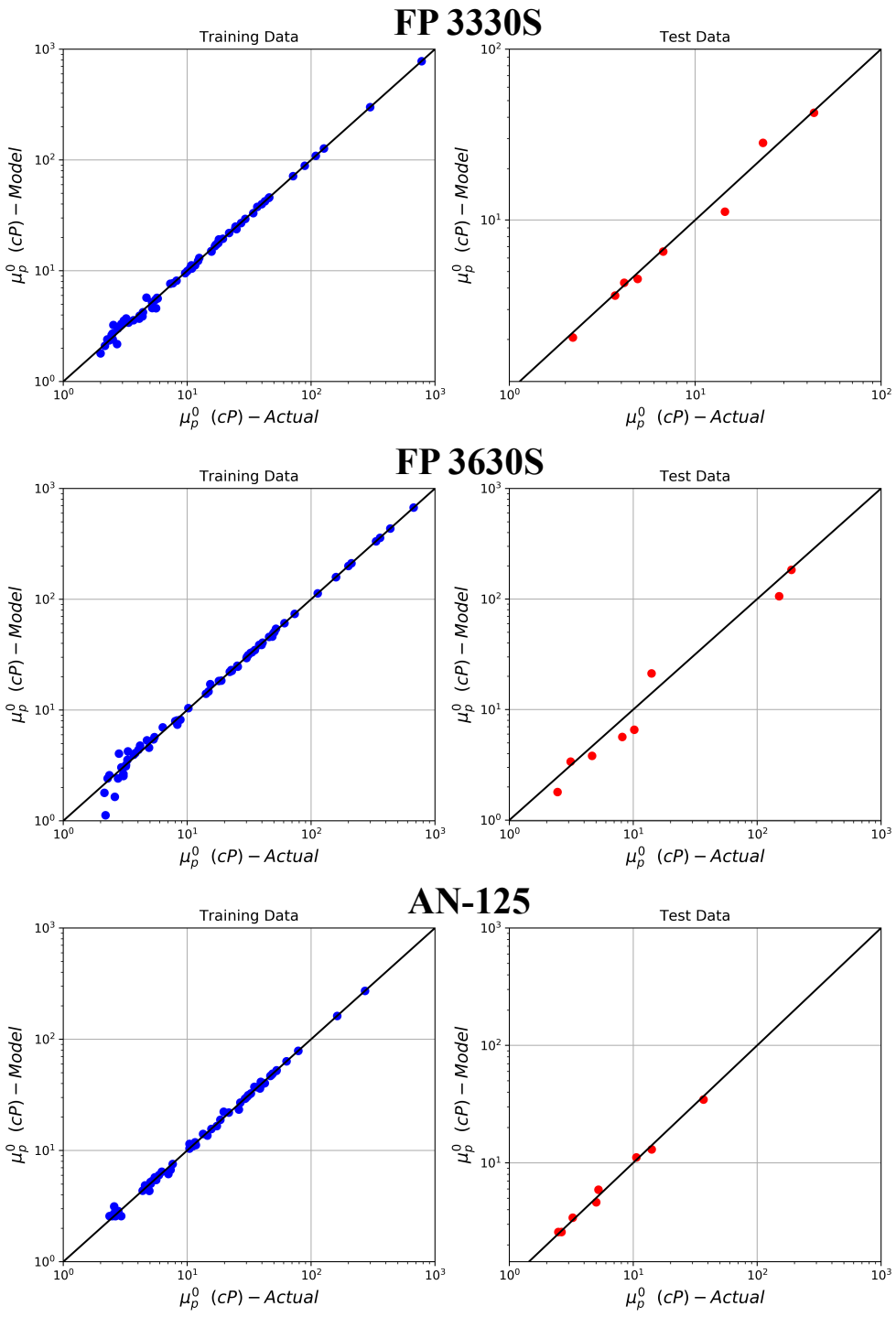

Figure 4.28: Comparison of measured and predicted values of zero-shear viscosity by the ANN model

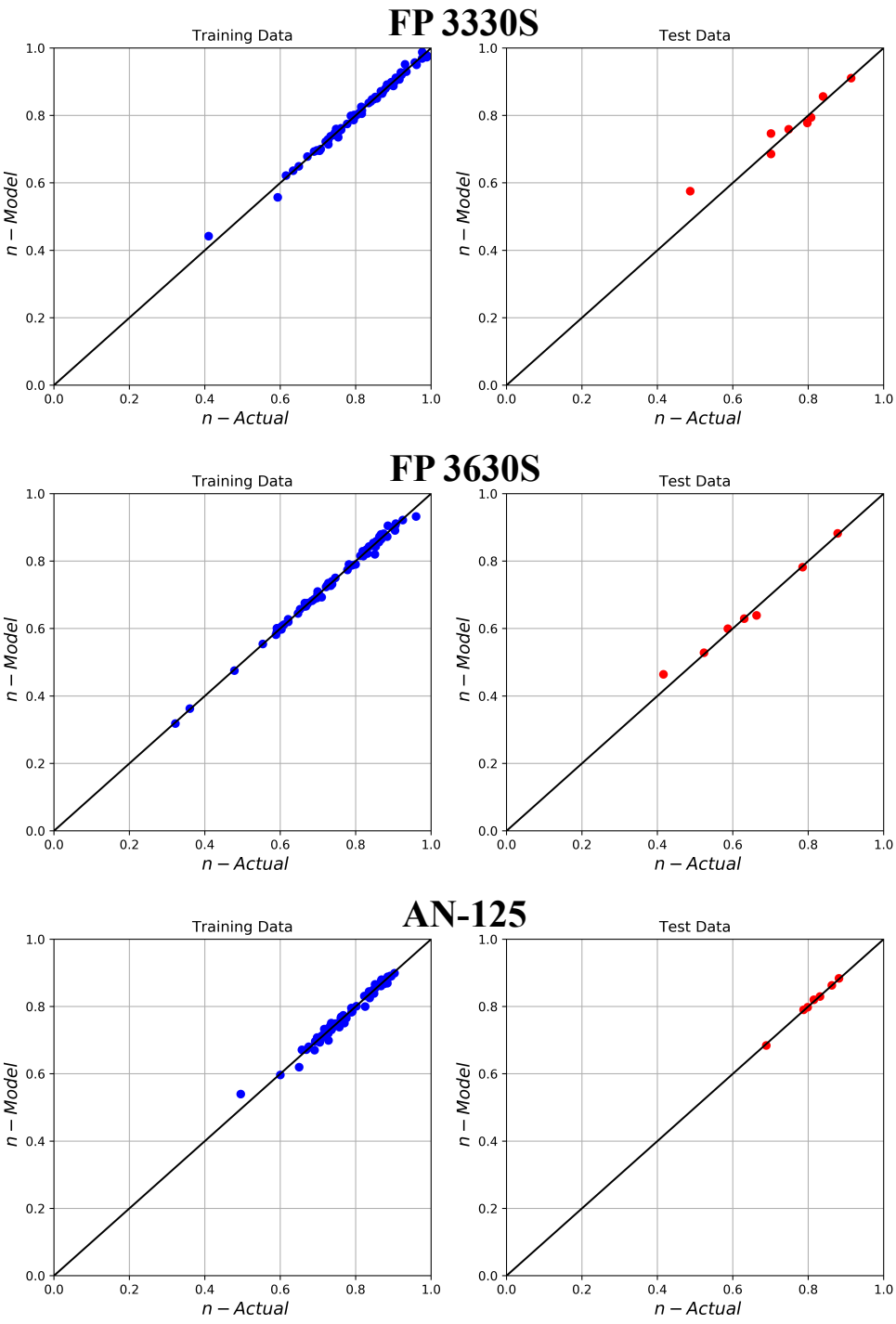

Figure 4.29: Comparison of measured and predicted values of shear-thinning index by the ANN model

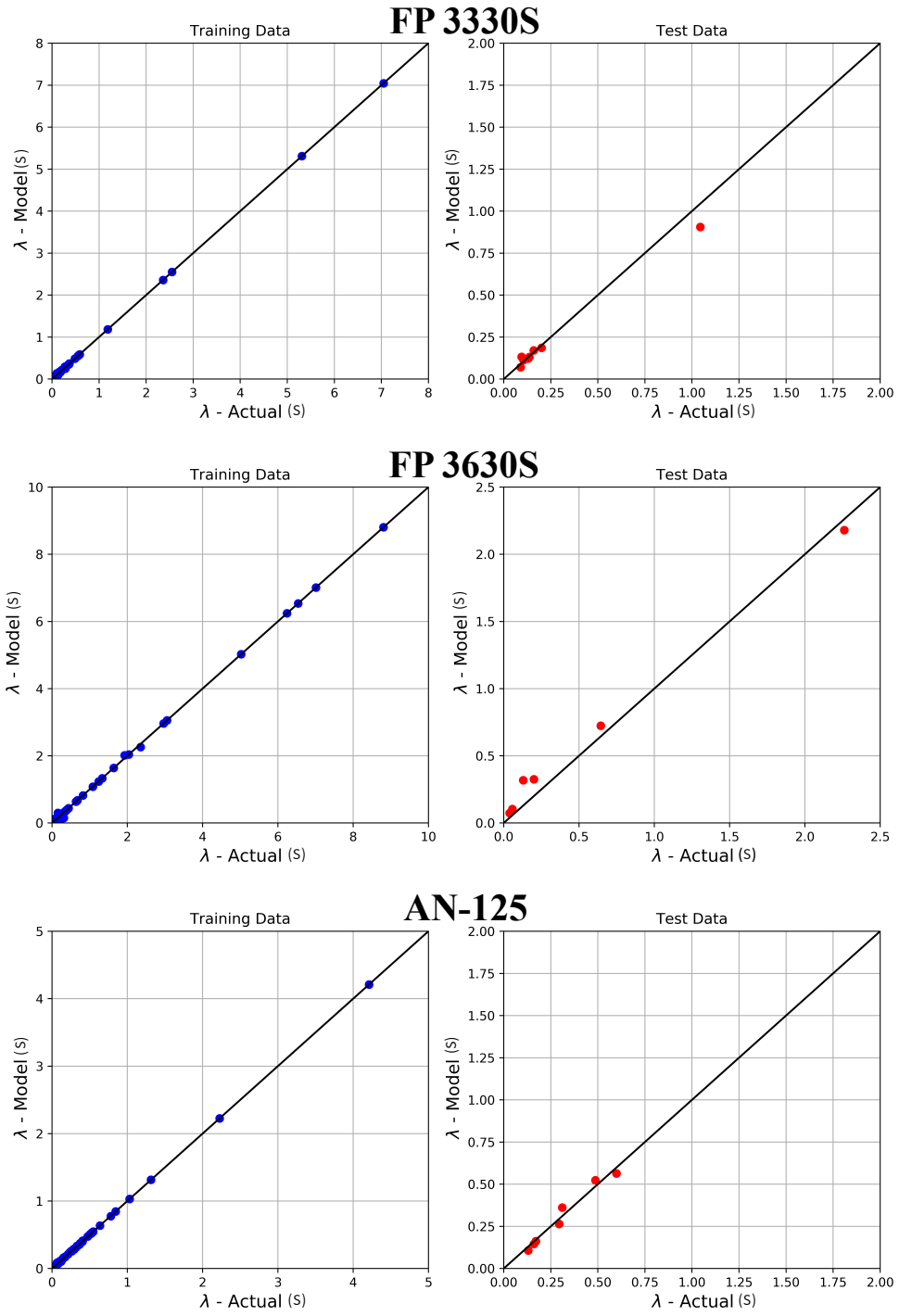

Figure 4.30: Comparison of measured and predicted values of the time constant (λ) by the ANN model

4.4 COMPARISON AND DISCUSSION

The results of Carreau's model parameters from each proposed model were presented in the previous sections. Each model has shown a satisfactory result with an acceptable error tolerance, as illustrated by the 45° plots. However, those plots do not show how the model actually performs across the entire spectrum of the shear rate. This step is very important because it gives an insightful idea about the models' performance, especially when they are implemented in a reservoir simulator. Therefore, in this section, out-of-the-box test samples from each polymer type were randomly selected. The three models were applied to those selected samples, and the results were tested against the actual experimental data.

Figure 4.32 and Figure 4.33 show the viscosity profiles of the FP-3330S polymer at different polymer concentrations and salinities. The black dots represent the data obtained by the actual best-fit of Carreau's parameters, which match the experimental data nearly perfectly. The blue, green, and red curves represent the regression model, the RF model, and the ANN model, respectively. All the models provide a very good fit of the data. The regression model (blue curve), seems to hold the least matching accuracy of all the models. In addition, the RF and ANN models seem to be equally effective for scoring the least error. Both models perform similarly and exceptionally well, with an average R^2 of 0.98.

Moreover, viscosity profiles of the higher molecular weight polymer, FP-3630S, are shown in Figure 4.34 and Figure 4.35. The regression model provides a good estimation overall for this polymer type. Its good performance is greatly pronounced during the shear-thinning phase. The regression model tends to offset the farthest during the low-shear rate region ($\dot{\gamma} < 1$) at the highest polymer concentration samples. This indicates that the estimation of the zero-shear viscosity by the regression model at a high polymer

concentration may not be the best approach, despite the accurate estimations of the other two Carreau's parameters by the same approach. Moreover, the RF model, surprisingly, appears to outperform the ANN model in this polymer type. Although both models, RF and ANN, have a similar performance and accuracy, the RF model estimation is better at the lowest polymer concentrations (500 ppm).

Figure 4.36 and Figure 4.37 show the viscosity profiles of the AN-125 polymer. Nearly all models appear to exhibit an excellent match with the actual data. Extra credit may go to the ANN model for its exceptional performance with this specific polymer type. The remaining results for all the samples of the tested polymers used in this study are presented in Appendices B, C and D.

What Do These Results Mean?

The results described earlier indicate that the modeling approaches used in this study have proved to be reliable and consistent. These results have demonstrated the models' capability of simulating the rheological properties while minimizing the uncertainty. For instance, by looking at ANN model predictions, one can realize its useful impact on rheological studies, especially ones that involve chemical EOR applications.

Furthermore, this study revealed the powerfulness of some advanced machine learning models, i.e., RF and ANN. The result of combining EOR and ML sciences led to the development of more reliable and accurate predictive tools that can add tremendous value to relevant research studies and applications. Products of this combination can be further applied to similar problems or perhaps can replace existing models or correlations. For instance, one potential application that can benefit from ML is the modeling of the relaxation time of a viscoelastic polymer, e.g., HPAM, based on its polymer solution characteristics.

Results presented in this study have exceeded the projected expectations, especially the results pertaining to RF and ANN models. This success is attributed to the logic and sophistication of the ML algorithms of such methods. ML can review large volumes of data and identify specific trends and patterns efficiently. In addition, ML algorithms are exceptionally good at handling data that are multi-dimensional and multi-variety. Thus, such advantages make ML a desirable approach for modeling and prediction.

The models presented in this study can be very useful in many EOR-related applications. For instance, a quick and easy way to calculate a polymer solution's viscosity is by knowing its concentration and salinity. However, an important application is implementation into a reservoir simulator (e.g. UTCHEM). The proposed models can enhance the accuracy of the polymer solution viscosity calculated in the simulator. Also, it may significantly reduce the uncertainty and improve the simulator's reliability.

The implementation of machine learning methods into the reservoir simulator depends primary on the programming language of the simulator's source code. However, regardless of the type of language used, the implementation is fairly easy. Once the machine learning model is constructed, it can be exported on a separate executable file. In addition, this file contains the necessary arguments, parameters, and numerical constants that are used for the prediction. For instance, ANN model should have a vector, or matrix, that contains the weights of connectors and biases of the neurons. But, this exported file does not necessarily have the source code of the ANN algorithm, which is in fact a preferable advantage since its size it much smaller than the original file. Furthermore, in terms of computation time, the prediction performed through the exported "executable" file depends mainly on the size of the model. For example, an ANN model with 50 hidden layers is expected to take much more time than with 2 hidden layers. Additional several

factors may also impact the speed of the execution such as the compiler, processor, RAM size, etc.

In this study, the model and the training dataset used are not super enormous and computer is MacBook Pro™ with 2.3 GHz Intel Core i5 and 8 GB RAM. Figure 4.31 shows the computation time for RF and ANN. The reported time is in milliseconds and it covers the prediction of the three Carreau's parameters for up to 1000 samples (or grids) simultaneously. As can be observed, the ANN extraordinarily outperforms the RF model by approximately 40 fold. This can be explained by comparing the input variables of both algorithms (e.g. number of trees in RF or number of hidden layers and neurons in ANN). However, given that the properties of the current models have been fully optimized, it is safe to say that ANN model is giving much better results in terms of both prediction accuracy and computation time. To further illustrate the computation performance, if both ML models are implemented into a reservoir simulator, RF would take a total of 3.8 minutes and ANN would take a total of 5.7 seconds to calculate the viscosity at 10,000 grid blocks model for 1000 time steps. Indeed, the previous calculation are assumed to be executed on a regular computer machine similar to the one described earlier. Nevertheless, the computation performance can be greatly enhanced by utilizing a more advanced computer machines, using a different and more efficient programming language (e.g. C, C++, or Fortran), and introducing parallel computation techniques.

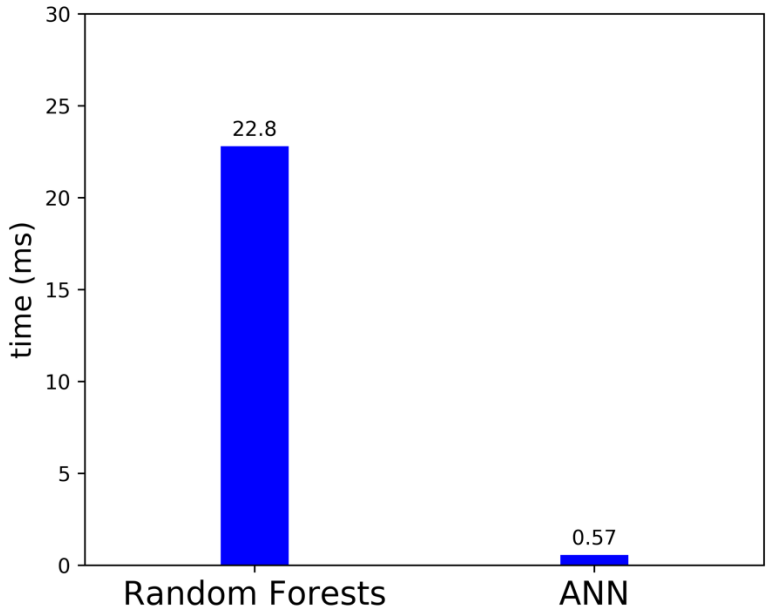

Figure 4.31: Computation time of RF and ANN models

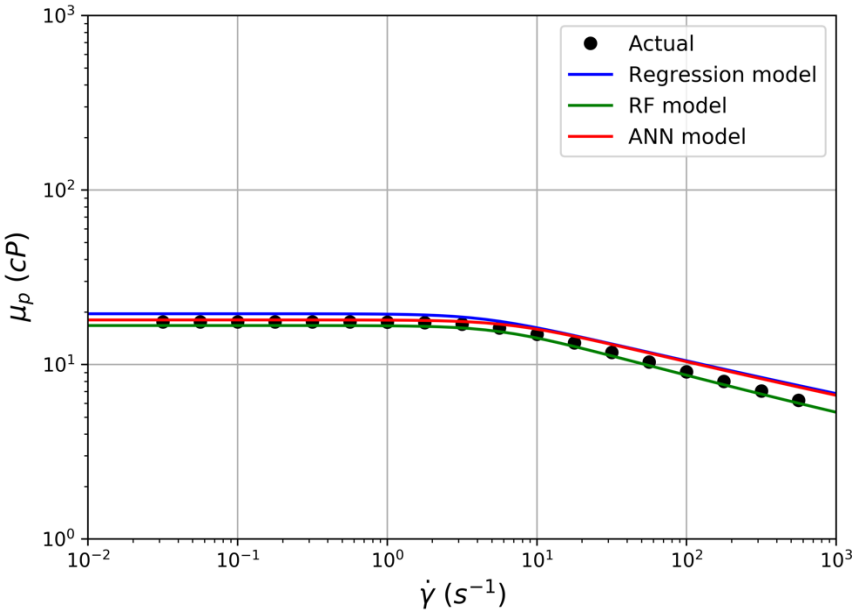

Figure 4.32: Comparison of viscosity profiles for 2000 ppm FP3330S polymer at 0.5 wt% NaCl, 0.05 wt% Ca^{++}, and 25°C

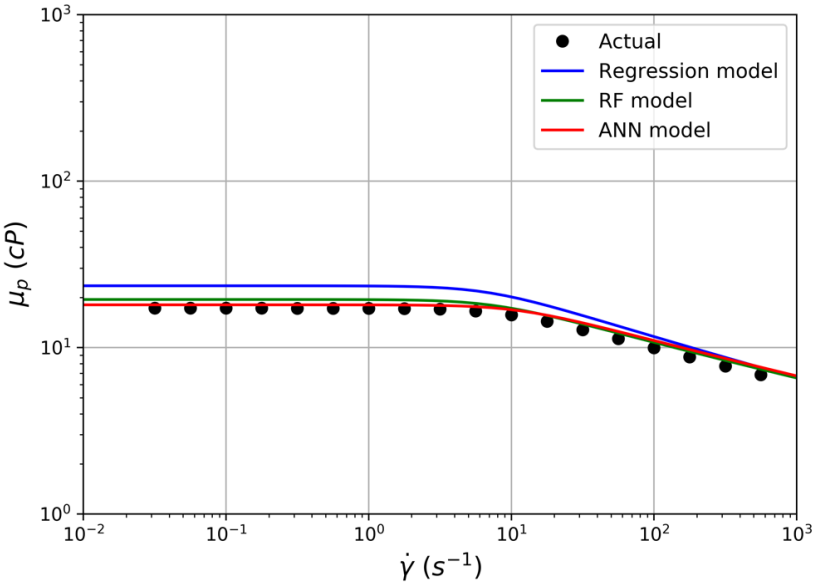

Figure 4.33: Comparison of viscosity profiles for 3000 ppm FP3330S polymer at 1 wt% NaCl, 0.15 wt% Ca^{++}, and 25°C

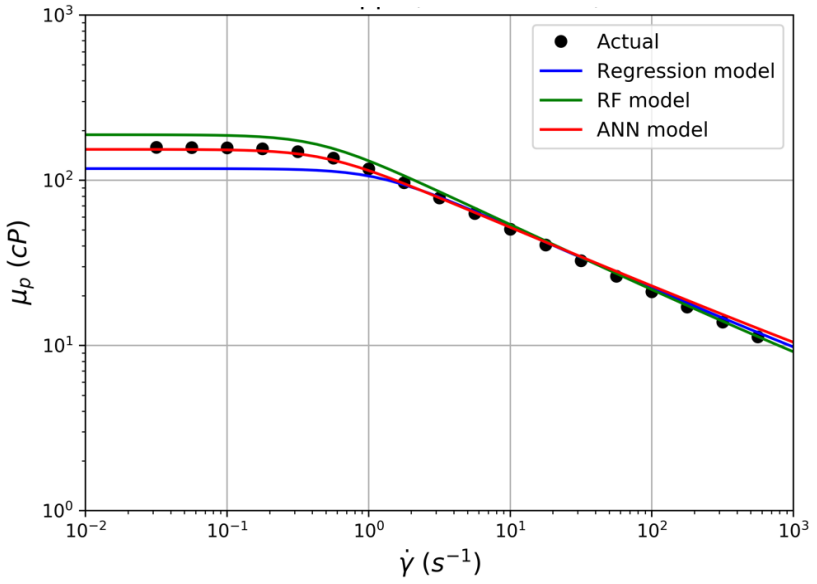

Figure 4.34: Comparison of viscosity profiles for 3000 ppm FP3630S polymer at 2 wt% NaCl, 0.05 wt% Ca^{++}, and 25°C

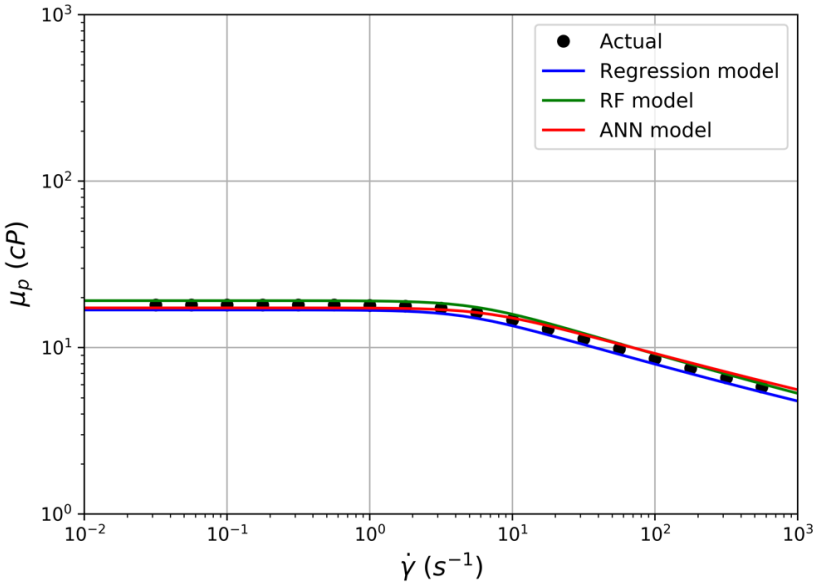

Figure 4.35: Comparison of viscosity profiles for 3000 ppm FP3630S polymer at 1 wt% NaCl, 0.15 wt% Ca^{++}, and 25°C

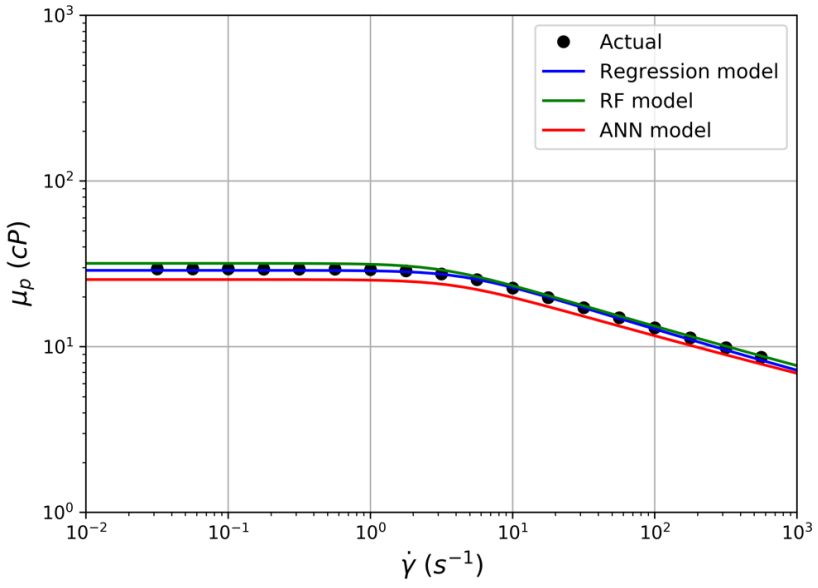

Figure 4.36: Comparison of viscosity profiles for 3000 ppm AN-125 polymer at 4 wt% NaCl, 0.15 wt% Ca^{++}, and 25°C

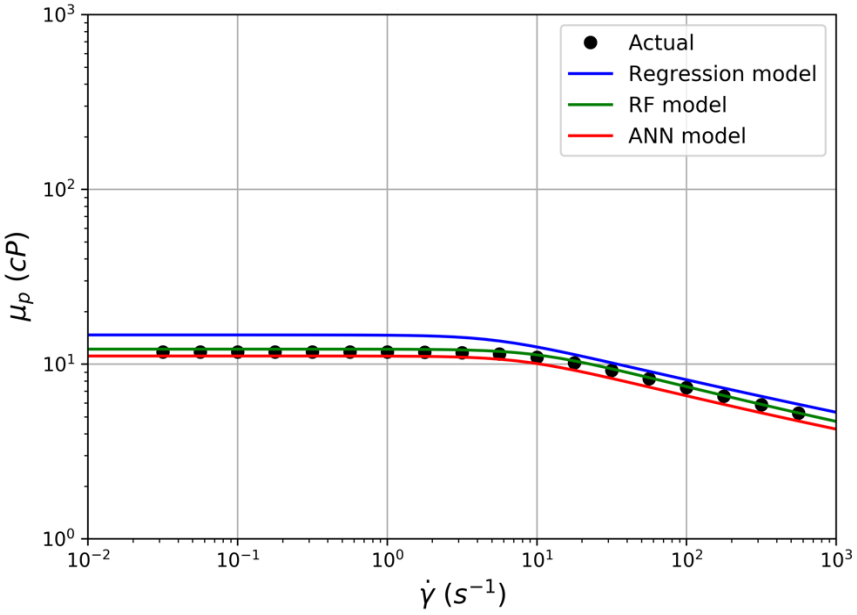

Figure 4.37: Comparison of viscosity profiles for 2000 ppm AN-125 polymer at 1 wt% NaCl, 0.15 wt% Ca^{++}, and 25°C

CHAPTER 5. CONCLUSIONS AND FUTURE WORK

5.1 CONCLUSIONS

The conclusions of this work are briefly summarized here.

- The algorithm developed for fitting raw rheological data (i.e., viscosity versus shear rate) to Carreau's model was shown to be successful at processing thousands of data points in a short time, while detecting and eliminating outliers, and providing an excellent fit. The algorithm uses the derivative of the viscosity versus shear rate curve to detect outliers and anomalies at low and high shear rate.
- It was shown that least absolute error minimization (L1-norm) fits much better than the least-squares error method (L2-norm), especially at higher shear rates.
- Martin equation and 3rd order Flory-Hugging equation were shown to give acceptable fits of the zero-shear viscosity versus C_p for polymer concentrations below 3000 ppm despite both theoretically valid for only dilute solutions. However, Martin's equation is much easier to use and requires only three fitting parameters compared to five for the Flory-Huggins equation. Therefore, Martin equation was used in this study.
- A new equation for shear-thinning index was developed and predicted its value with satisfactory accuracy; the new equation adheres to theoretical limits e.g. n approaches unity (Newtonian fluid) in the limit that polymer concentration is zero.
- Multivariable linear regression of the time constant (λ) to polymer solution characteristics has been shown to be a very good estimation, which can be coupled with the other proposed equations to estimate the polymer solution viscosity at any given shear rate.
- The regression equations and their best-fit parameters are given as follows:

Parameter	*Equation*
μ_p^0 *(Martin's equation)*	$\ln\left(\frac{\eta_{sp}}{C_p}\right) = \ln\left(k_1 C_{sep}^{S_p}\right) + k_2 C_p$
n	$n = n_\infty + \left[\exp(-D_{p1} C_p) - n_\infty\right] \exp\left(-D_{p2} \frac{C_p}{C_{sep}}\right)$
λ	$\lambda = a_0 \, C_p^{a_1} C_{sep}^{a_2}$
C_{sep}	$C_{sep} = \frac{C_{51} + (\beta_p - 1) C_{61}}{C_{11}}$

Parameter	FP 3330S	FP 3630S	AN-125
μ_p^0			
k_1	2600	3830	1970
k_2	565	850	590
S_p	-0.73	-0.87	-0.63
β_p	30	39	10
n			
D_{p1}	104	147	100
D_{p2} (meq/mL)	34	51	138
n_∞	0.5	0.4	0.66
λ			
a_0 (s)	77	3470	420
a_1	0.96	1.39	1.25
a_2	-0.78	-0.92	-0.82

- The rheological machine-learning methods, Random Forests and Artificial Neural Networks, provided more accurate estimations than the regression methods. Both were developed using Scikit-Learn Python package.
- ANN algorithm tends to outperform RF in both accuracy and computation time. This may be attributed to the fact that ANN uses a sophisticated network that thoroughly review the data and understand its trends whereas RF follows a less complex approach. In terms of computational time, the running speed of ANN is

approximately 40 times faster than the RF. This difference may be even higher when the computation is executed on an advanced machine.

- The usability of the developed model can range from a research use to implementation into a reservoir simulation. Given the acceptable accuracy and computation time of ML models, the accuracy of reservoir simulation applications that involve polymer flooding may be improved by incorporating these models into reservoir simulators.

5.2 FUTURE WORK:

Some recommended future work includes the following goals:

- Continuously improve the existing models by compiling additional rheology data, either by conducting rheology experiments or by collecting data from literature and feeding it into these models. For instance, prepare additional high polymer-concentrated samples (C_p > 3000 ppm) and higher salinity content (> 4 wt%). Although the range of hardness in this study is suitable (500-1500 ppm), it might be a good idea if lower hardness content is tested (between 0-500 ppm). This is because the solution viscosity is very sensitive to hardness. In essence, more data will result in a better model.
- Investigate new types of EOR-related polymers such as AM-ATBS co-polymers (SAV 10), Scleroglucan, and HPAM polymers with different M_w and degrees of hydrolysis.
- Explore and implement different ML models and techniques, such as Support Victor Machine (SVM) and Recurrent Neural Networks. While no machine learning algorithm necessary guarantees the best results unless it is implemented, it

might be a wise idea to implement new ML models and compare their results against other existing models.

- Develop new models to address the relaxation time of viscoelastic polymers based on the polymers' solution characteristics. Perhaps, the same model used in this study are a good suggestion to implement. Other modeling approaches may be explored as well. However, extensive data compilation of relaxation times is essentially needed to ensure the developed model gives its best.
- Include additional features into new and existing models, such as degree of hydrolysis and molecular weight. Other features that can be added are the lot number of the polymer batch and the rheometer type. This can help to assess the degree of discrepancy found in the results between different rheometers and batches of polymers.
- Implement the new models to a chemical flood reservoir simulator. The models can be either one of the regression or the ML models. However, from a computational performance prospective, ANN would the most efficient, beside its very good accuracy.

Appendix A

The samples used in this study, their properties, and their best-fit Carreau's parameters are listed below.

Sample #	Polymer type	C_p (ppm)	NaCl (ppm)	Ca^{++} (ppm)	Temperature (°C)	μ_p^0 (cp)	μ_w (cp)	n	λ (s)
1	AN-125	500	1000	0	25	11.3	0.8903	0.7165	0.2618
2	AN-125	500	1000	1000	25	2.642	0.8903	0.8675	0.0820
3	AN-125	500	5000	0	25	4.359	0.8903	0.8250	0.1444
4	AN-125	500	5000	500	25	2.777	0.8903	0.8837	0.0572
5	AN-125	500	10000	0	25	3.229	0.8795	0.8311	0.0718
6	AN-125	500	10000	500	25	2.561	0.8903	0.8510	0.0414
7	AN-125	500	10000	1000	25	2.637	0.8903	0.8815	0.1151
8	AN-125	500	10000	1500	25	2.363	0.8903	0.8772	0.0628
9	AN-125	500	20000	0	25	2.573	0.8903	0.8674	0.0594
10	AN-125	500	20000	500	25	2.934	0.8903	0.8686	0.3653
11	AN-125	500	20000	1000	25	2.483	0.8903	0.8846	0.0746
12	AN-125	500	20000	1500	25	2.411	0.8903	0.8912	0.0984
13	AN-125	500	40000	0	25	2.620	0.8903	0.8940	0.1724
14	AN-125	500	40000	500	25	2.621	0.8903	0.9026	0.2940
15	AN-125	500	40000	1500	25	2.482	0.8903	0.8891	0.0655
16	AN-125	1000	1000	0	25	52.67	0.8903	0.6571	1.3140
17	AN-125	1000	1000	500	25	7.635	0.8903	0.8019	0.1751
18	AN-125	1000	1000	1000	25	5.478	0.8903	0.8309	0.1248
19	AN-125	1000	1000	1500	25	4.560	0.8903	0.8532	0.0853
20	AN-125	1000	5000	0	25	11.1	0.8903	0.7700	0.2391
21	AN-125	1000	5000	500	25	7.033	0.8903	0.8145	0.1704
22	AN-125	1000	5000	1000	25	5.618	0.8903	0.8348	0.1300
23	AN-125	1000	5000	1500	25	4.765	0.8903	0.8414	0.0647
24	AN-125	1000	10000	0	25	7.431	0.8795	0.7861	0.1222
25	AN-125	1000	10000	500	25	5.916	0.8903	0.8227	0.1114
26	AN-125	1000	10000	1000	25	5.197	0.8903	0.8372	0.0783
27	AN-125	1000	10000	1500	25	5.023	0.8903	0.8499	0.1199
28	AN-125	1000	20000	0	25	6.238	0.8903	0.8353	0.2127

29	AN-125	1000	20000	500	25	5.468	0.8903	0.8488	0.1539
30	AN-125	1000	20000	1000	25	5.083	0.8903	0.8471	0.1187
31	AN-125	1000	20000	1500	25	4.945	0.8903	0.8529	0.1528
32	AN-125	1000	40000	0	25	5.238	0.8903	0.8420	0.1303
33	AN-125	1000	40000	500	25	5.045	0.8903	0.8670	0.1693
34	AN-125	1000	40000	1000	25	4.507	0.8903	0.8625	0.0920
35	AN-125	1000	40000	1500	25	4.775	0.8903	0.8399	0.1204
36	AN-125	2000	1000	0	25	272.3	0.8903	0.5999	4.2110
37	AN-125	2000	1000	500	25	29.2	0.8903	0.7279	0.4733
38	AN-125	2000	1000	1000	25	13.41	0.8903	0.7314	0.0845
39	AN-125	2000	1000	1500	25	10.44	0.8903	0.7609	0.0630
40	AN-125	2000	5000	0	25	47.748	0.8795	0.6947	0.7530
41	AN-125	2000	5000	500	25	26.09	0.8903	0.7340	0.4049
42	AN-125	2000	5000	1000	25	14.52	0.8903	0.7599	0.1601
43	AN-125	2000	5000	1500	25	11.37	0.8903	0.7614	0.0832
44	AN-125	2000	10000	0	25	27.701	0.8795	0.7367	0.4797
45	AN-125	2000	10000	0	50	15.789	0.5669	0.7197	0.2181
46	AN-125	2000	10000	0	70	11.394	0.4151	0.7387	0.1982
47	AN-125	2000	10000	0	90	7.417	0.3018	0.6876	0.0816
48	AN-125	2000	10000	500	25	21.676	0.8795	0.7419	0.2952
49	AN-125	2000	10000	1000	25	14.366	0.8795	0.7589	0.1517
50	AN-125	2000	10000	1500	25	11.775	0.8795	0.7568	0.0903
51	AN-125	2000	20000	0	25	20.787	0.8795	0.7738	0.5777
52	AN-125	2000	20000	500	25	18.470	0.8903	0.7752	0.3316
53	AN-125	2000	20000	1000	25	11.560	0.8903	0.7606	0.0806
54	AN-125	2000	20000	1500	25	11.080	0.8903	0.7702	0.0829
55	AN-125	2000	40000	0	25	17.867	0.8795	0.7910	0.5177
56	AN-125	2000	40000	500	25	15.660	0.8903	0.7909	0.2629
57	AN-125	2000	40000	1000	25	10.590	0.8903	0.7890	0.0938
58	AN-125	2000	40000	1500	25	10.410	0.8903	0.7885	0.0924
59	AN-125	3000	1000	0	25	1310	0.8903	0.4950	8.3370
60	AN-125	3000	1000	500	25	78.750	0.8903	0.6689	0.8461
61	AN-125	3000	1000	1000	25	47.830	0.8903	0.7065	0.5276
62	AN-125	3000	1000	1500	25	34.880	0.8903	0.7246	0.3717
63	AN-125	3000	5000	0	25	162.10	0.8903	0.6499	2.2250
64	AN-125	3000	5000	500	25	63.210	0.8903	0.6752	0.5985

65	AN-125	3000	5000	1000	25	39.200	0.8903	0.6977	0.3136
66	AN-125	3000	5000	1500	25	38.630	0.8903	0.7567	0.7812
67	AN-125	3000	10000	0	25	79.614	0.8795	0.6790	1.0482
68	AN-125	3000	10000	500	25	52.450	0.8903	0.6924	0.5261
69	AN-125	3000	10000	1000	25	41.150	0.8903	0.7101	0.4049
70	AN-125	3000	10000	1500	25	36.840	0.8903	0.7368	0.5049
71	AN-125	3000	20000	0	25	48.910	0.8903	0.7044	0.5455
72	AN-125	3000	20000	500	25	42.220	0.8903	0.7192	0.4869
73	AN-125	3000	20000	1000	25	36.400	0.8903	0.7275	0.4016
74	AN-125	3000	20000	1500	25	31.520	0.8903	0.7220	0.2568
75	AN-125	3000	40000	0	25	30.400	0.8903	0.7501	0.3392
76	AN-125	3000	40000	500	25	32.610	0.8903	0.7378	0.3335
77	AN-125	3000	40000	1000	25	31.00	0.8903	0.7354	0.2873
78	AN-125	3000	40000	1500	25	29.460	0.8903	0.7372	0.2661
79	FP 3330S	500	1000	0	25	17.800	0.8903	0.7069	0.5725
80	FP 3330S	500	1000	500	25	2.453	0.8903	0.9157	0.1582
81	FP 3330S	500	1000	1000	25	1.744	0.8903	0.9882	7.7500
82	FP 3330S	500	1000	1500	25	1.692	0.8903	0.9762	8.3670
83	FP 3330S	500	5000	0	25	5.606	0.8903	0.8075	0.0400
84	FP 3330S	500	5000	500	25	2.503	0.8903	0.8916	0.0948
85	FP 3330S	500	5000	1000	25	1.999	0.8903	0.9308	0.0364
86	FP 3330S	500	5000	1500	25	1.772	0.8903	0.9879	7.6260
87	FP 3330S	500	10000	0	25	4.053	0.8795	0.8403	0.1270
88	FP 3330S	500	10000	500	25	2.712	0.8903	0.8829	0.1052
89	FP 3330S	500	10000	1000	25	2.302	0.8903	0.9612	6.6660
90	FP 3330S	500	10000	1500	25	1.953	0.8903	0.9759	7.2650
91	FP 3330S	500	20000	0	25	3.210	0.8903	0.8667	0.0840
92	FP 3330S	500	20000	500	25	2.347	0.8903	0.8996	0.0764
93	FP 3330S	500	20000	1000	25	2.197	0.8903	0.9197	0.0477
94	FP 3330S	500	20000	1500	25	2.008	0.8903	0.9564	7.0950
95	FP 3330S	500	40000	0	25	2.757	0.8903	0.9136	0.1084
96	FP 3330S	500	40000	500	25	2.490	0.8903	0.9037	0.0558
97	FP 3330S	500	40000	1000	25	2.261	0.8903	0.9207	0.0492
98	FP 3330S	500	40000	1500	25	2.167	0.8903	0.9342	0.0447
99	FP 3330S	1000	1000	0	25	109.00	0.8903	0.6149	2.3610
100	FP 3330S	1000	1000	500	25	4.693	0.8903	0.8343	0.0723

101	FP 3330S	1000	1000	1000	25	3.077	0.8903	0.9054	0.0855
102	FP 3330S	1000	1000	1500	25	2.532	0.8903	0.9214	0.0431
103	FP 3330S	1000	5000	0	25	19.40	0.8903	0.7456	0.5891
104	FP 3330S	1000	5000	500	25	5.532	0.8903	0.8400	0.1518
105	FP 3330S	1000	5000	1000	25	3.704	0.8903	0.8787	0.0825
106	FP 3330S	1000	5000	1500	25	2.937	0.8903	0.9064	0.0505
107	FP 3330S	1000	10000	0	25	4.147	0.8795	0.8492	0.1872
108	FP 3330S	1000	10000	500	25	5.209	0.8903	0.8392	0.0993
109	FP 3330S	1000	10000	1000	25	4.105	0.8903	0.8701	0.0892
110	FP 3330S	1000	10000	1500	25	3.362	0.8903	0.8942	0.0748
111	FP 3330S	1000	20000	0	25	7.293	0.8903	0.8163	0.1472
112	FP 3330S	1000	20000	500	25	5.216	0.8903	0.8531	0.1265
113	FP 3330S	1000	20000	1000	25	4.352	0.8903	0.8714	0.0960
114	FP 3330S	1000	20000	1500	25	3.685	0.8903	0.8836	0.0622
115	FP 3330S	1000	40000	0	25	5.774	0.8903	0.8432	0.1239
116	FP 3330S	1000	40000	500	25	4.896	0.8903	0.8521	0.0890
117	FP 3330S	1000	40000	1000	25	4.390	0.8903	0.8729	0.0888
118	FP 3330S	1000	40000	1500	25	4.124	0.8903	0.8861	0.1347
119	FP 3330S	2000	1000	0	25	803.96	0.8795	0.4870	5.6776
120	FP 3330S	2000	1000	500	25	16.720	0.8903	0.7536	0.2008
121	FP 3330S	2000	1000	1000	25	7.660	0.8903	0.8108	0.0702
122	FP 3330S	2000	1000	1500	25	5.698	0.8903	0.8478	0.0530
123	FP 3330S	2000	5000	0	25	91.155	0.8795	0.6339	1.1929
124	FP 3330S	2000	5000	500	25	17.580	0.8903	0.7492	0.1752
125	FP 3330S	2000	5000	1000	25	9.993	0.8903	0.7958	0.1098
126	FP 3330S	2000	5000	1500	25	6.729	0.8903	0.8147	0.0560
127	FP 3330S	2000	10000	0	25	42.914	0.8795	0.6878	0.5069
128	FP 3330S	2000	10000	0	50	25.162	0.5669	0.6611	0.2487
129	FP 3330S	2000	10000	0	70	17.989	0.4151	0.6701	0.1910
130	FP 3330S	2000	10000	0	90	11.770	0.3018	0.6601	0.1387
131	FP 3330S	2000	10000	500	25	17.061	0.8795	0.7527	0.1820
132	FP 3330S	2000	10000	1000	25	10.658	0.8795	0.7864	0.1051
133	FP 3330S	2000	10000	1500	25	8.306	0.8795	0.8121	0.0878
134	FP 3330S	2000	20000	0	25	25.118	0.8795	0.7250	0.2744
135	FP 3330S	2000	20000	500	25	15.600	0.8903	0.7607	0.1591
136	FP 3330S	2000	20000	1000	25	11.570	0.8903	0.7946	0.1335

137	FP 3330S	2000	20000	1500	25	9.609	0.8903	0.8035	0.0985
138	FP 3330S	2000	40000	0	25	18.010	0.8903	0.7569	0.1934
139	FP 3330S	2000	40000	500	25	14.440	0.8903	0.7770	0.1576
140	FP 3330S	2000	40000	1000	25	12.240	0.8903	0.7920	0.1355
141	FP 3330S	2000	40000	1500	25	10.550	0.8903	0.8041	0.1079
142	FP 3330S	3000	1000	0	25	2410.0	0.8903	0.4098	7.0460
143	FP 3330S	3000	1000	500	25	39.880	0.8903	0.7010	0.3050
144	FP 3330S	3000	1000	1000	25	17.810	0.8903	0.7529	0.1161
145	FP 3330S	3000	1000	1500	25	12.480	0.8903	0.7975	0.1018
146	FP 3330S	3000	5000	0	25	299.70	0.8903	0.5932	2.5490
147	FP 3330S	3000	5000	500	25	45.910	0.8903	0.6973	0.3608
148	FP 3330S	3000	5000	1000	25	24.400	0.8903	0.7333	0.1788
149	FP 3330S	3000	5000	1500	25	15.720	0.8903	0.7614	0.1002
150	FP 3330S	3000	10000	0	25	128.10	0.8795	0.6238	1.0374
151	FP 3330S	3000	10000	500	25	43.560	0.8903	0.6969	0.3335
152	FP 3330S	3000	10000	1000	25	24.540	0.8903	0.7261	0.1672
153	FP 3330S	3000	10000	1500	25	17.240	0.8903	0.7533	0.1106
154	FP 3330S	3000	20000	0	25	71.550	0.8903	0.6717	0.5459
155	FP 3330S	3000	20000	500	25	36.690	0.8903	0.7042	0.2643
156	FP 3330S	3000	20000	1000	25	27.190	0.8903	0.7269	0.2045
157	FP 3330S	3000	20000	1500	25	21.770	0.8903	0.7480	0.1701
158	FP 3330S	3000	40000	0	25	45.500	0.8903	0.7010	0.3694
159	FP 3330S	3000	40000	500	25	34.140	0.8903	0.7206	0.2713
160	FP 3330S	3000	40000	1000	25	29.390	0.8903	0.7416	0.2818
161	FP 3330S	3000	40000	1500	25	23.130	0.8903	0.7447	0.1588
162	FP 3630S	500	1000	0	25	60.940	0.8903	0.6044	3.0550
163	FP 3630S	500	1000	500	25	2.941	0.8903	0.8834	0.1596
164	FP 3630S	500	1000	1000	25	2.189	0.8903	0.9601	6.5390
165	FP 3630S	500	5000	0	25	10.220	0.8903	0.7335	0.3862
166	FP 3630S	500	5000	500	25	3.205	0.8903	0.8616	0.0700
167	FP 3630S	500	5000	1000	25	2.443	0.8903	0.8850	0.0571
168	FP 3630S	500	5000	1500	25	2.149	0.8903	0.9249	0.2379
169	FP 3630S	500	10000	0	25	6.320	0.8795	0.7594	0.2299
170	FP 3630S	500	10000	500	25	3.117	0.8903	0.8354	0.0636
171	FP 3630S	500	10000	1000	25	3.035	0.8903	0.8672	0.1317
172	FP 3630S	500	10000	1500	25	2.280	0.8903	0.9061	0.1039

173	FP 3630S	500	20000	0	25	4.646	0.8903	0.8183	0.1367
174	FP 3630S	500	20000	500	25	3.293	0.8903	0.8516	0.1177
175	FP 3630S	500	20000	1000	25	2.816	0.8903	0.8547	0.0508
176	FP 3630S	500	20000	1500	25	2.355	0.8903	0.8627	0.0308
177	FP 3630S	500	40000	0	25	3.810	0.8903	0.8493	0.1333
178	FP 3630S	500	40000	500	25	3.058	0.8903	0.8448	0.0574
179	FP 3630S	500	40000	1000	25	3.058	0.8903	0.8740	0.1027
180	FP 3630S	500	40000	1500	25	2.603	0.8903	0.8777	0.0410
181	FP 3630S	1000	1000	0	25	435.10	0.8903	0.4784	8.8040
182	FP 3630S	1000	1000	500	25	8.007	0.8903	0.7819	0.1481
183	FP 3630S	1000	1000	1000	25	3.320	0.8903	0.8718	0.0300
184	FP 3630S	1000	1000	1500	25	2.761	0.8903	0.9048	0.0260
185	FP 3630S	1000	5000	0	25	45.800	0.8903	0.6630	1.3320
186	FP 3630S	1000	5000	500	25	8.252	0.8903	0.7850	0.1548
187	FP 3630S	1000	5000	1000	25	4.035	0.8903	0.8466	0.0363
188	FP 3630S	1000	5000	1500	25	3.198	0.8903	0.9042	0.0599
189	FP 3630S	1000	10000	0	25	22.654	0.8795	0.7010	0.5804
190	FP 3630S	1000	10000	500	25	8.792	0.8903	0.7848	0.2006
191	FP 3630S	1000	10000	1000	25	4.909	0.8903	0.8282	0.0556
192	FP 3630S	1000	10000	1500	25	3.696	0.8903	0.8677	0.0383
193	FP 3630S	1000	20000	0	25	14.830	0.8903	0.7908	0.6761
194	FP 3630S	1000	20000	500	25	8.325	0.8903	0.7996	0.1875
195	FP 3630S	1000	20000	1000	25	5.346	0.8903	0.8508	0.1335
196	FP 3630S	1000	20000	1500	25	4.157	0.8903	0.8529	0.0478
197	FP 3630S	1000	40000	0	25	10.180	0.8903	0.8203	0.3144
198	FP 3630S	1000	40000	500	25	8.135	0.8903	0.8126	0.1922
199	FP 3630S	1000	40000	1000	25	5.438	0.8903	0.8309	0.0816
200	FP 3630S	1000	40000	1500	25	4.735	0.8903	0.8527	0.0668
201	FP 3630S	2000	1000	0	25	3491.0	0.8903	0.3600	13.9400
202	FP 3630S	2000	1000	500	25	33.290	0.8903	0.6693	0.3642
203	FP 3630S	2000	1000	1000	25	14.040	0.8903	0.7373	0.1288
204	FP 3630S	2000	5000	0	25	360.85	0.8795	0.4999	2.5607
205	FP 3630S	2000	5000	500	25	30.990	0.8903	0.6659	0.2940
206	FP 3630S	2000	5000	1000	25	22.630	0.8903	0.7211	0.3083
207	FP 3630S	2000	5000	1500	25	14.170	0.8903	0.7458	0.1298
208	FP 3630S	2000	10000	0	25	150.17	0.8795	0.5723	2.1213

209	FP 3630S	2000	10000	0	50	91.610	0.5669	0.5744	1.3709
210	FP 3630S	2000	10000	0	70	62.468	0.4151	0.5795	0.9353
211	FP 3630S	2000	10000	0	90	38.304	0.3018	0.5700	0.4649
212	FP 3630S	2000	10000	500	25	35.214	0.8795	0.6647	0.3685
213	FP 3630S	2000	10000	1000	25	25.718	0.8795	0.7017	0.3286
214	FP 3630S	2000	10000	1500	25	18.177	0.8795	0.7310	0.2125
215	FP 3630S	2000	20000	0	25	74.377	0.8795	0.6253	1.0878
216	FP 3630S	2000	20000	500	25	40.530	0.8903	0.6845	0.6437
217	FP 3630S	2000	20000	1500	25	18.850	0.8903	0.7234	0.1854
218	FP 3630S	2000	40000	0	25	51.192	0.8795	0.6809	0.9813
219	FP 3630S	2000	40000	500	25	32.400	0.8903	0.6973	0.4370
220	FP 3630S	2000	40000	1000	25	30.300	0.8903	0.6989	0.3832
221	FP 3630S	2000	40000	1500	25	22.010	0.8903	0.7272	0.2726
222	FP 3630S	3000	1000	0	25	8025.2	0.8903	0.3216	17.8550
223	FP 3630S	3000	1000	500	25	159.10	0.8903	0.5905	1.6370
224	FP 3630S	3000	1000	1000	25	25.580	0.8903	0.7097	0.1562
225	FP 3630S	3000	1000	1500	25	15.340	0.8903	0.7369	0.0683
226	FP 3630S	3000	5000	0	25	1730	0.8903	0.4158	10.4200
227	FP 3630S	3000	5000	500	25	199.80	0.8903	0.5868	2.3530
228	FP 3630S	3000	5000	1000	25	38.060	0.8903	0.6649	0.2101
229	FP 3630S	3000	5000	1500	25	22.900	0.8903	0.7336	0.1691
230	FP 3630S	3000	10000	0	25	686.69	0.8795	0.5076	5.5535
231	FP 3630S	3000	10000	500	25	188.60	0.8903	0.5940	2.2610
232	FP 3630S	3000	10000	1000	25	48.570	0.8903	0.6523	0.3124
233	FP 3630S	3000	10000	1500	25	30.110	0.8903	0.6986	0.2002
234	FP 3630S	3000	20000	0	25	333.70	0.8903	0.5886	5.0250
235	FP 3630S	3000	20000	500	25	158.30	0.8903	0.6093	1.9260
236	FP 3630S	3000	20000	1000	25	51.980	0.8903	0.6470	0.3381
237	FP 3630S	3000	20000	1500	25	39.860	0.8903	0.6893	0.3154
238	FP 3630S	3000	40000	0	25	211.40	0.8903	0.6028	2.9630
239	FP 3630S	3000	40000	500	25	150.20	0.8903	0.6210	2.0380
240	FP 3630S	3000	40000	1000	25	113.10	0.8903	0.6206	1.2390
241	FP 3630S	3000	40000	1500	25	50.500	0.8903	0.6724	0.4021

Appendix B. FP-3330S plots

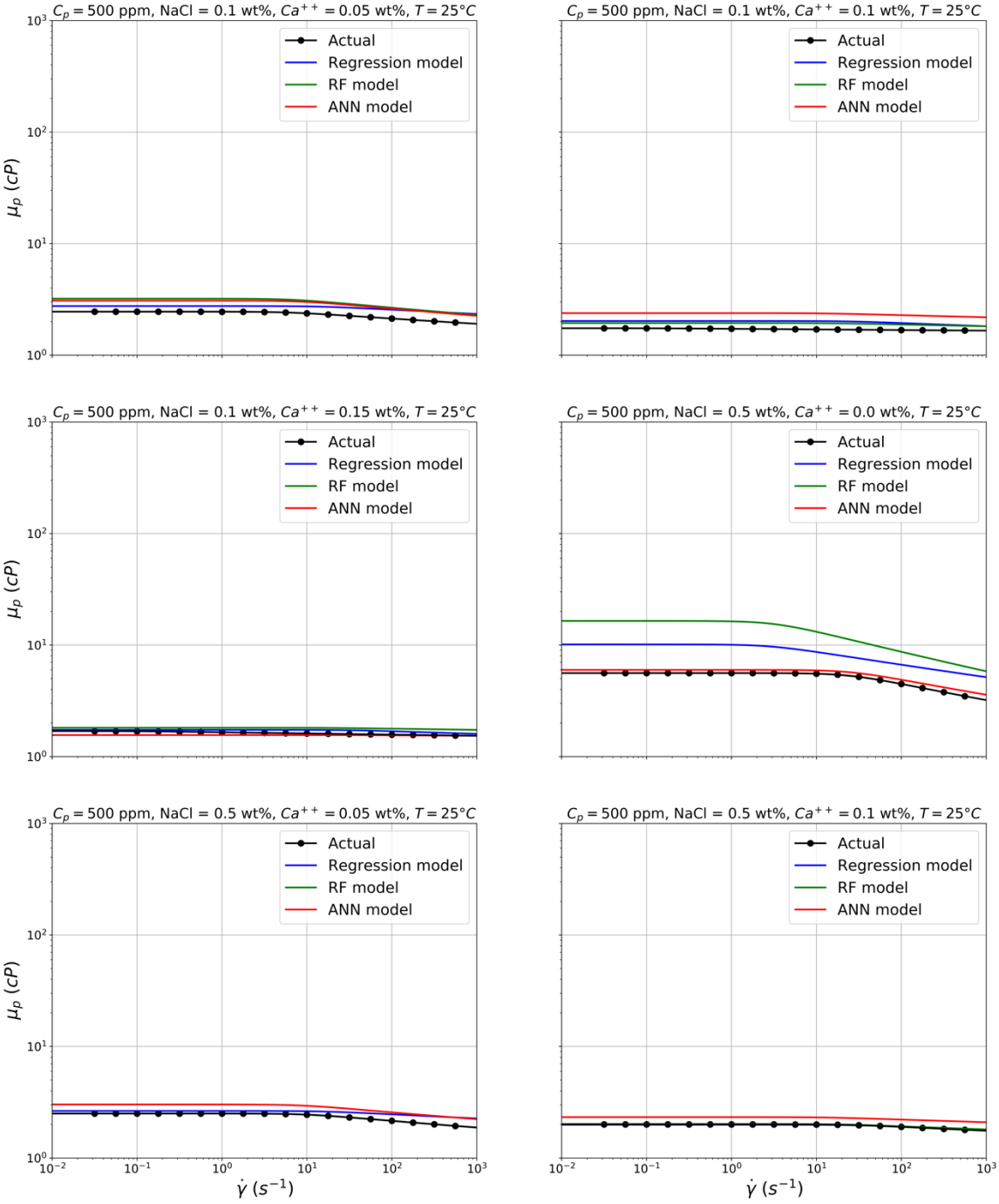

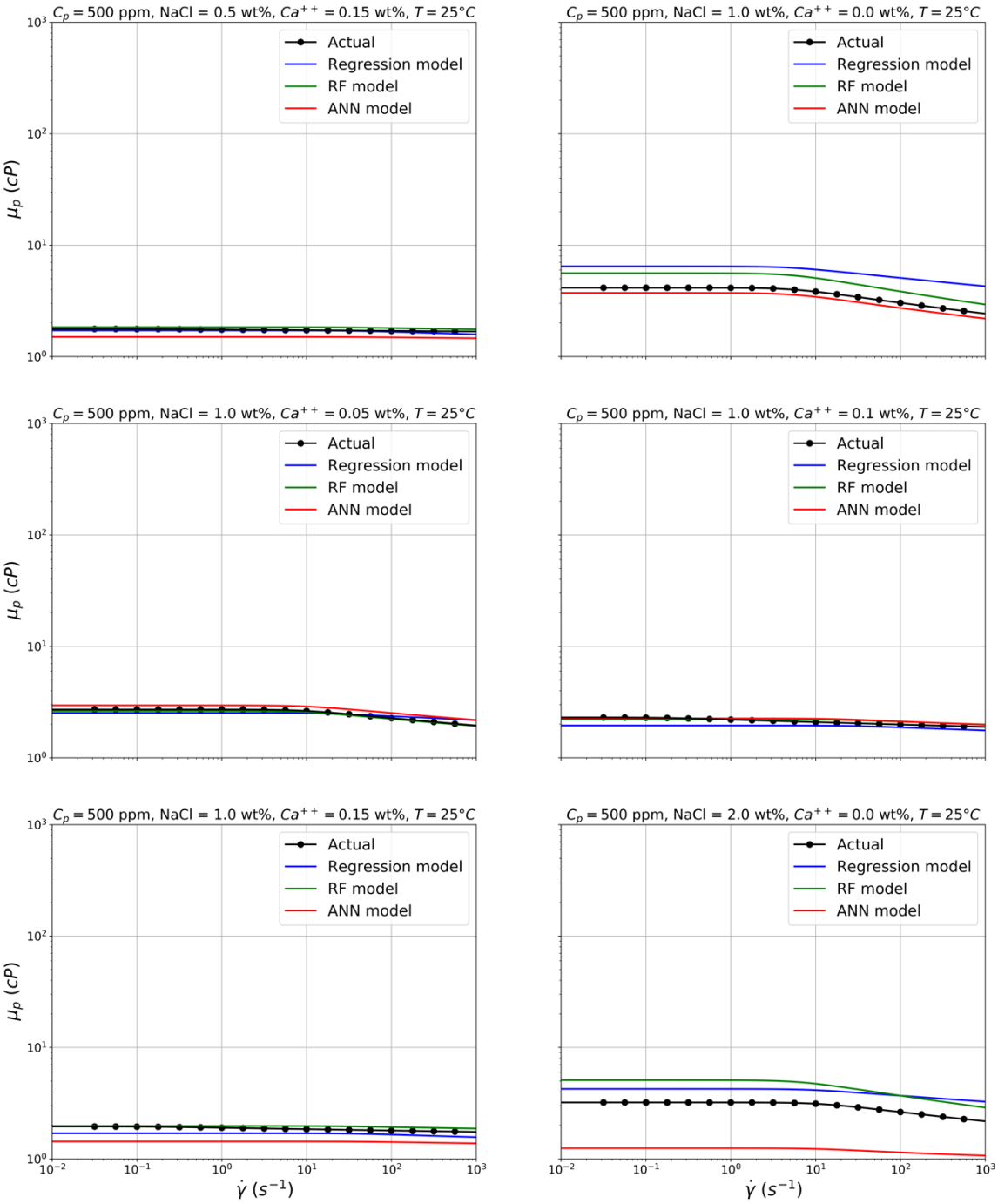
$C_p = 500$ ppm, NaCl = 0.5 wt%, $Ca^{++} = 0.15$ wt%, $T = 25°C$
$C_p = 500$ ppm, NaCl = 1.0 wt%, $Ca^{++} = 0.0$ wt%, $T = 25°C$
$C_p = 500$ ppm, NaCl = 1.0 wt%, $Ca^{++} = 0.05$ wt%, $T = 25°C$
$C_p = 500$ ppm, NaCl = 1.0 wt%, $Ca^{++} = 0.1$ wt%, $T = 25°C$
$C_p = 500$ ppm, NaCl = 1.0 wt%, $Ca^{++} = 0.15$ wt%, $T = 25°C$
$C_p = 500$ ppm, NaCl = 2.0 wt%, $Ca^{++} = 0.0$ wt%, $T = 25°C$
Actual
Regression model
RF model
ANN model
μ_p (cP)
$\dot{\gamma}$ (s^{-1})

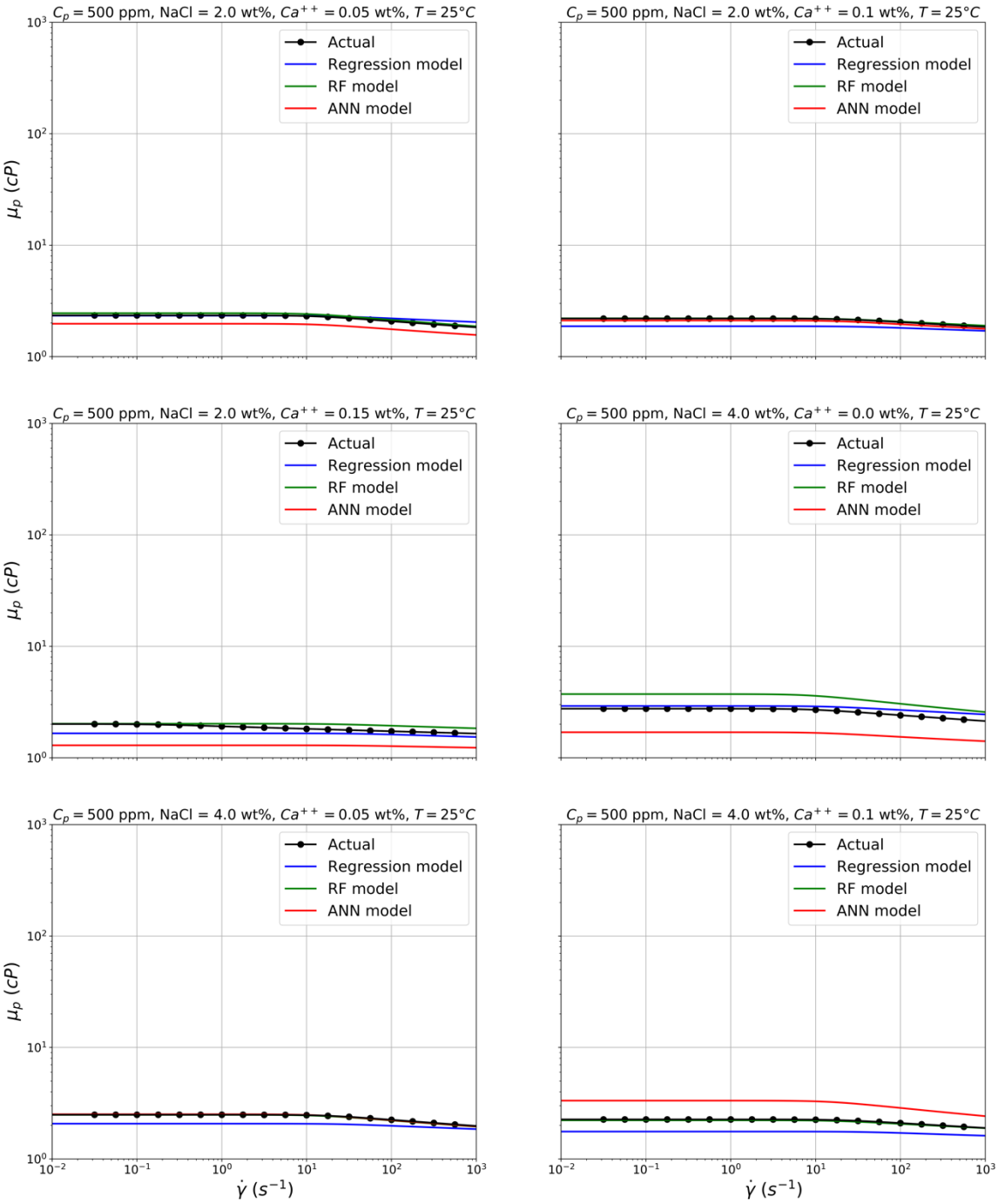
$C_p = 500$ ppm, NaCl = 2.0 wt%, $Ca^{++} = 0.05$ wt%, $T = 25°C$
$C_p = 500$ ppm, NaCl = 2.0 wt%, $Ca^{++} = 0.1$ wt%, $T = 25°C$
$C_p = 500$ ppm, NaCl = 2.0 wt%, $Ca^{++} = 0.15$ wt%, $T = 25°C$
$C_p = 500$ ppm, NaCl = 4.0 wt%, $Ca^{++} = 0.0$ wt%, $T = 25°C$
$C_p = 500$ ppm, NaCl = 4.0 wt%, $Ca^{++} = 0.05$ wt%, $T = 25°C$
$C_p = 500$ ppm, NaCl = 4.0 wt%, $Ca^{++} = 0.1$ wt%, $T = 25°C$
Actual
Regression model
RF model
ANN model
μ_p (cP)
$\dot{\gamma}$ (s^{-1})

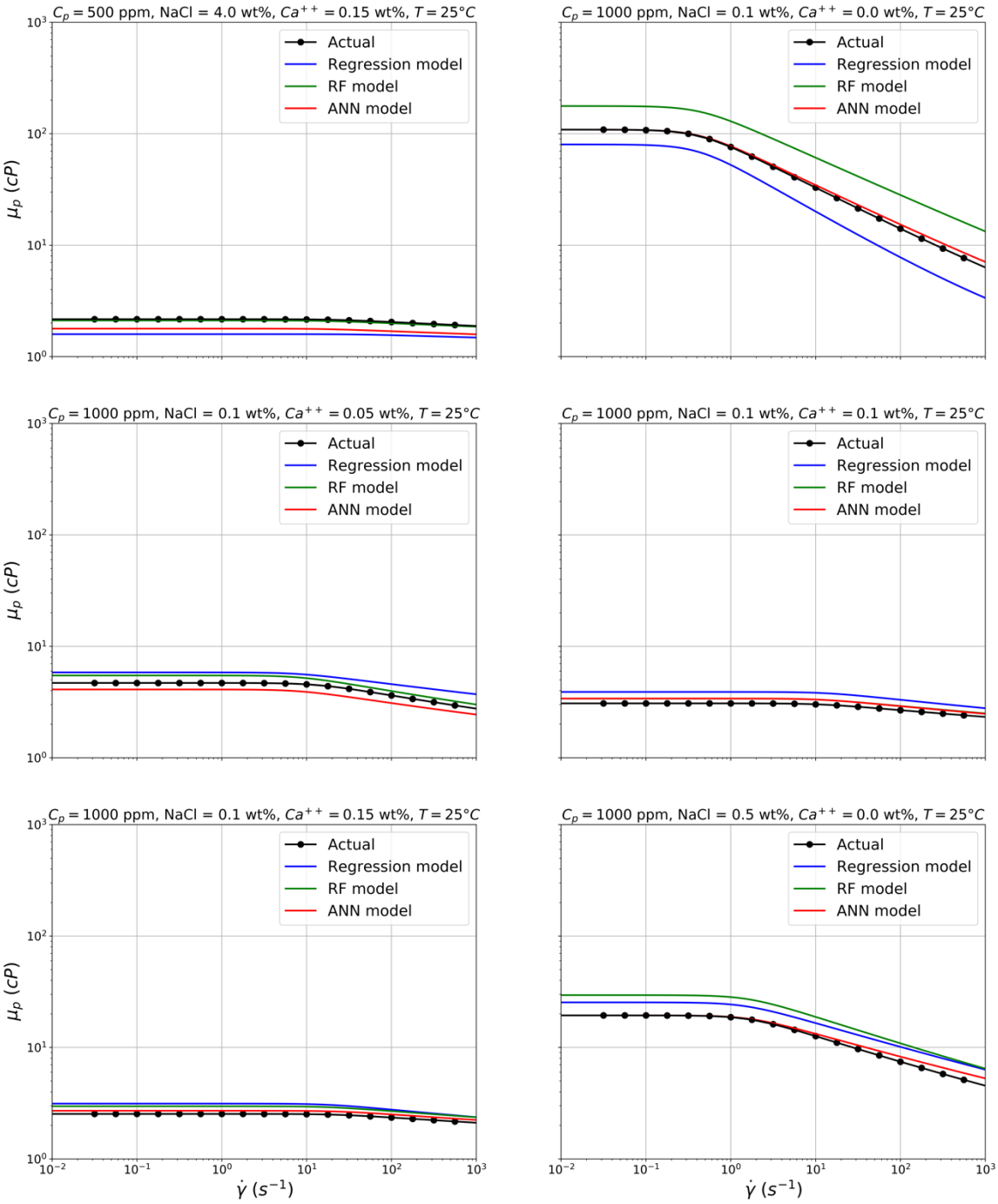
$C_p = 500$ ppm, NaCl = 4.0 wt%, $Ca^{++} = 0.15$ wt%, $T = 25°C$
$C_p = 1000$ ppm, NaCl = 0.1 wt%, $Ca^{++} = 0.0$ wt%, $T = 25°C$
$C_p = 1000$ ppm, NaCl = 0.1 wt%, $Ca^{++} = 0.05$ wt%, $T = 25°C$
$C_p = 1000$ ppm, NaCl = 0.1 wt%, $Ca^{++} = 0.1$ wt%, $T = 25°C$
$C_p = 1000$ ppm, NaCl = 0.1 wt%, $Ca^{++} = 0.15$ wt%, $T = 25°C$
$C_p = 1000$ ppm, NaCl = 0.5 wt%, $Ca^{++} = 0.0$ wt%, $T = 25°C$
Actual
Regression model
RF model
ANN model
μ_p (cP)
$\dot{\gamma}$ (s^{-1})

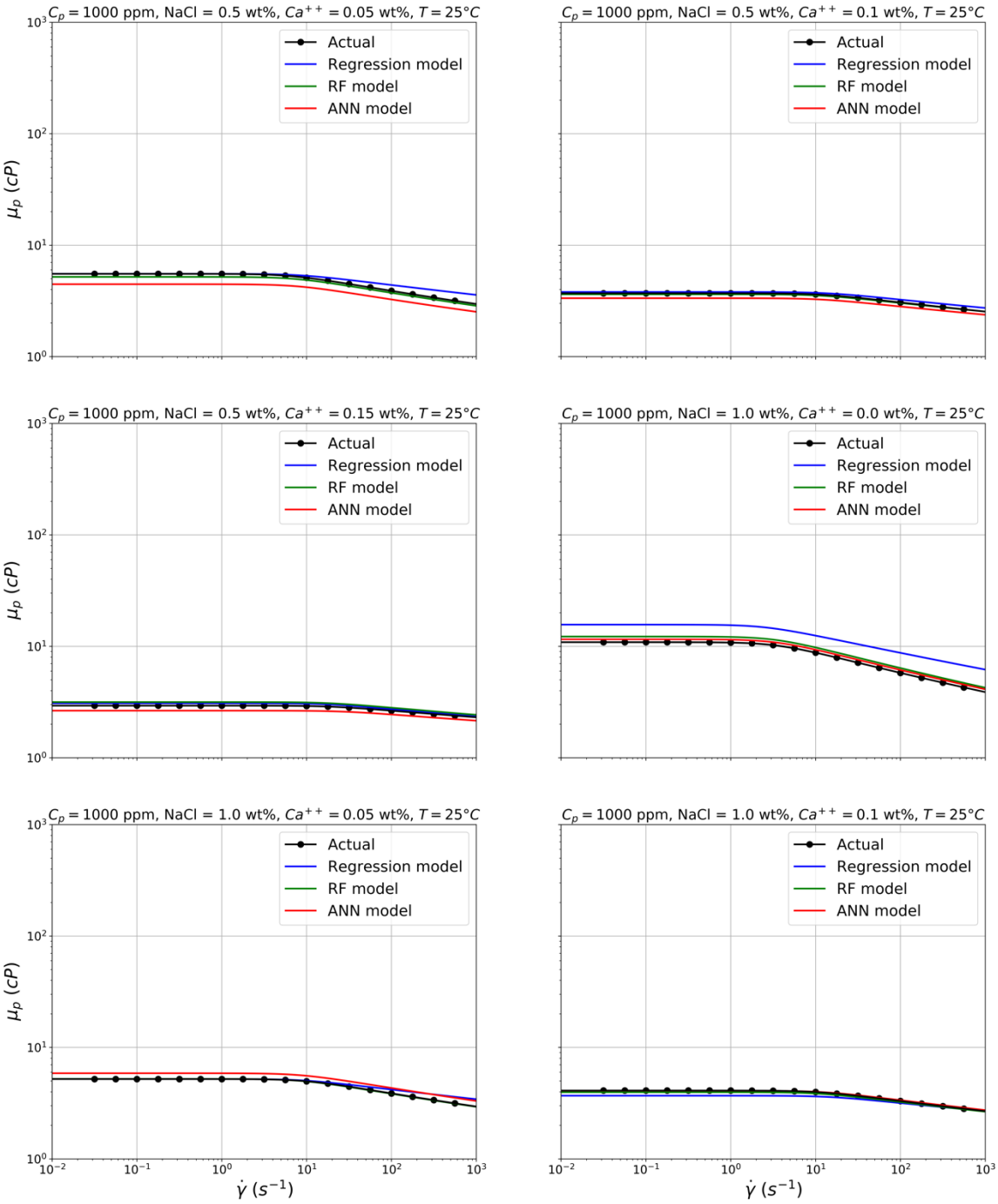
$C_p = 1000$ ppm, NaCl = 0.5 wt%, $Ca^{++} = 0.05$ wt%, $T = 25°C$
$C_p = 1000$ ppm, NaCl = 0.5 wt%, $Ca^{++} = 0.1$ wt%, $T = 25°C$
$C_p = 1000$ ppm, NaCl = 0.5 wt%, $Ca^{++} = 0.15$ wt%, $T = 25°C$
$C_p = 1000$ ppm, NaCl = 1.0 wt%, $Ca^{++} = 0.0$ wt%, $T = 25°C$
$C_p = 1000$ ppm, NaCl = 1.0 wt%, $Ca^{++} = 0.05$ wt%, $T = 25°C$
$C_p = 1000$ ppm, NaCl = 1.0 wt%, $Ca^{++} = 0.1$ wt%, $T = 25°C$
Actual
Regression model
RF model
ANN model
μ_p (cP)
$\dot{\gamma}$ (s^{-1})

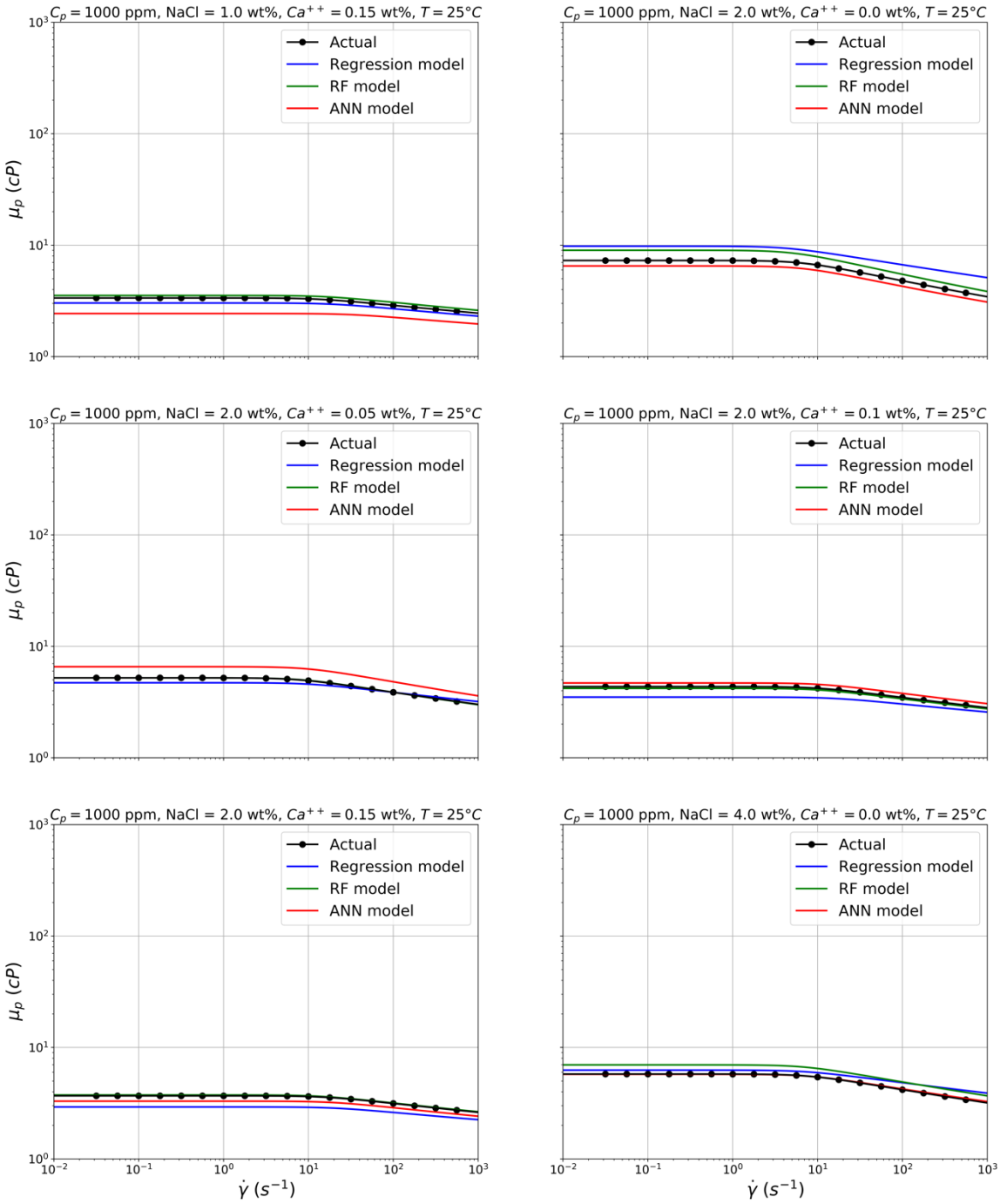
$C_p = 1000$ ppm, NaCl = 1.0 wt%, $Ca^{++} = 0.15$ wt%, $T = 25°C$
$C_p = 1000$ ppm, NaCl = 2.0 wt%, $Ca^{++} = 0.0$ wt%, $T = 25°C$
$C_p = 1000$ ppm, NaCl = 2.0 wt%, $Ca^{++} = 0.05$ wt%, $T = 25°C$
$C_p = 1000$ ppm, NaCl = 2.0 wt%, $Ca^{++} = 0.1$ wt%, $T = 25°C$
$C_p = 1000$ ppm, NaCl = 2.0 wt%, $Ca^{++} = 0.15$ wt%, $T = 25°C$
$C_p = 1000$ ppm, NaCl = 4.0 wt%, $Ca^{++} = 0.0$ wt%, $T = 25°C$
Actual
Regression model
RF model
ANN model
μ_p (cP)
$\dot{\gamma}$ (s^{-1})

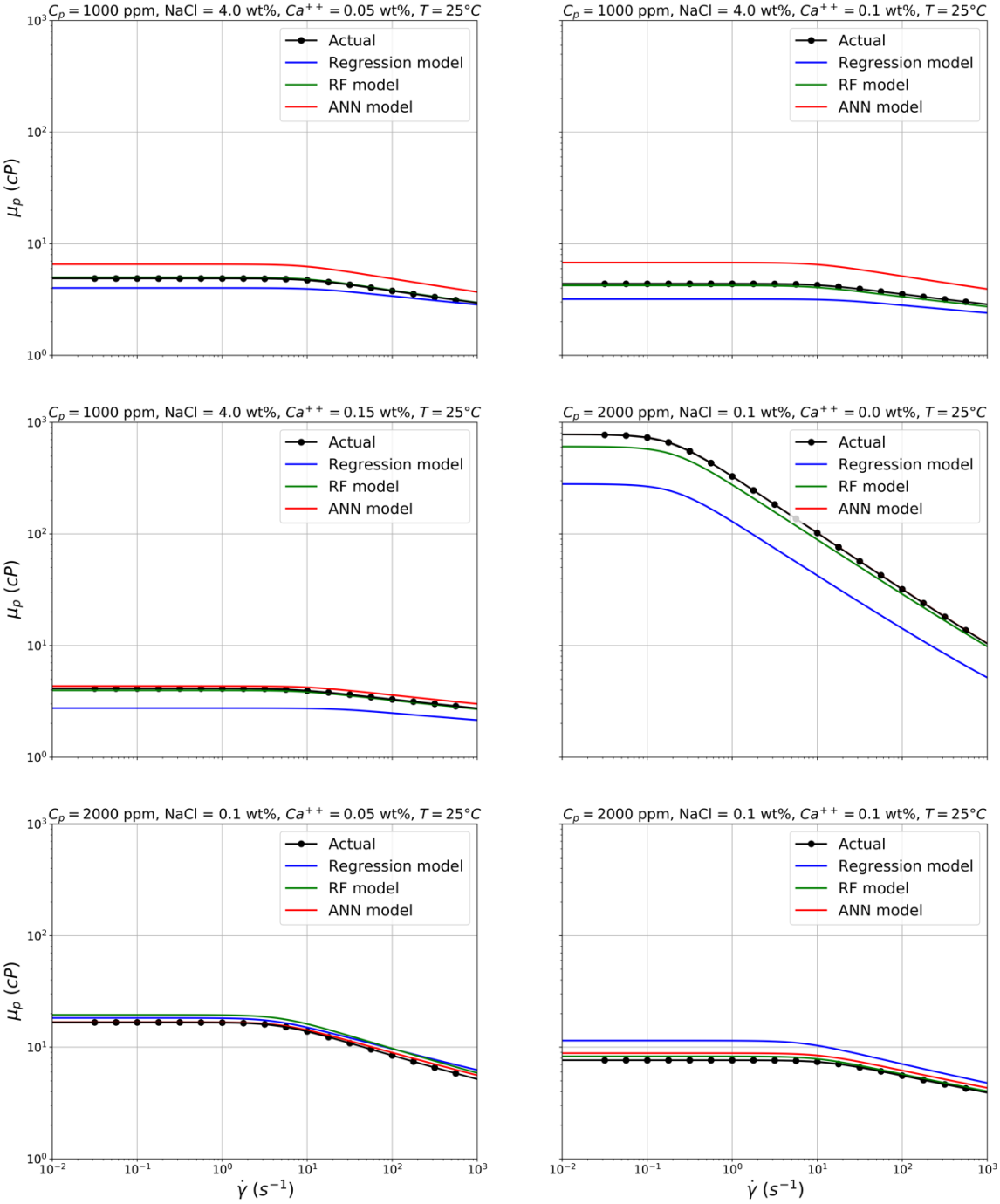
$C_p = 1000$ ppm, NaCl = 4.0 wt%, $Ca^{++} = 0.05$ wt%, $T = 25°C$
$C_p = 1000$ ppm, NaCl = 4.0 wt%, $Ca^{++} = 0.1$ wt%, $T = 25°C$
$C_p = 1000$ ppm, NaCl = 4.0 wt%, $Ca^{++} = 0.15$ wt%, $T = 25°C$
$C_p = 2000$ ppm, NaCl = 0.1 wt%, $Ca^{++} = 0.0$ wt%, $T = 25°C$
$C_p = 2000$ ppm, NaCl = 0.1 wt%, $Ca^{++} = 0.05$ wt%, $T = 25°C$
$C_p = 2000$ ppm, NaCl = 0.1 wt%, $Ca^{++} = 0.1$ wt%, $T = 25°C$
Actual
Regression model
RF model
ANN model
μ_p (cP)
$\dot{\gamma}$ (s^{-1})

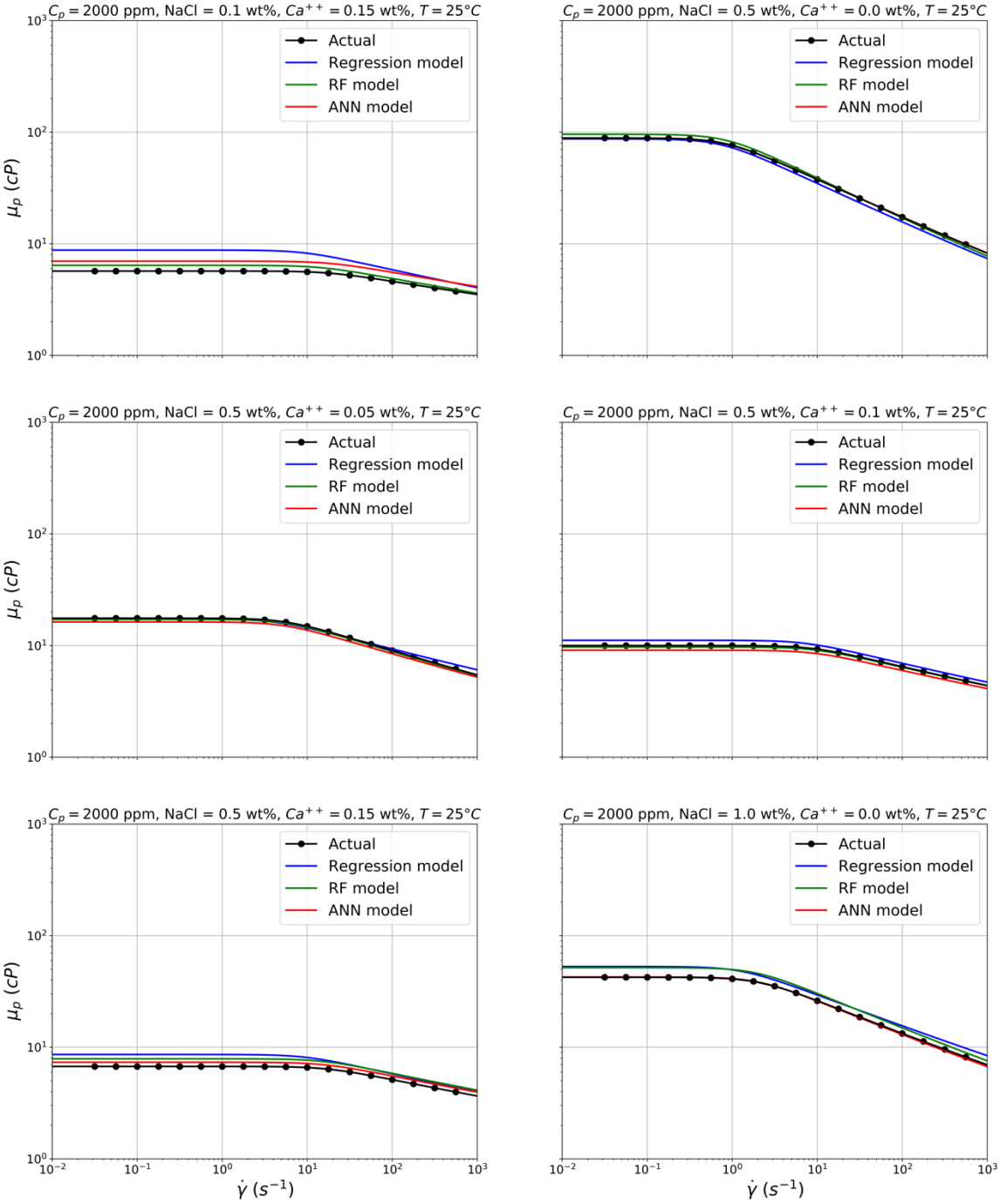
$C_p = 2000$ ppm, NaCl = 0.1 wt%, $Ca^{++} = 0.15$ wt%, $T = 25°C$
$C_p = 2000$ ppm, NaCl = 0.5 wt%, $Ca^{++} = 0.0$ wt%, $T = 25°C$
$C_p = 2000$ ppm, NaCl = 0.5 wt%, $Ca^{++} = 0.05$ wt%, $T = 25°C$
$C_p = 2000$ ppm, NaCl = 0.5 wt%, $Ca^{++} = 0.1$ wt%, $T = 25°C$
$C_p = 2000$ ppm, NaCl = 0.5 wt%, $Ca^{++} = 0.15$ wt%, $T = 25°C$
$C_p = 2000$ ppm, NaCl = 1.0 wt%, $Ca^{++} = 0.0$ wt%, $T = 25°C$
Actual
Regression model
RF model
ANN model
μ_p (cP)
$\dot{\gamma}$ (s^{-1})

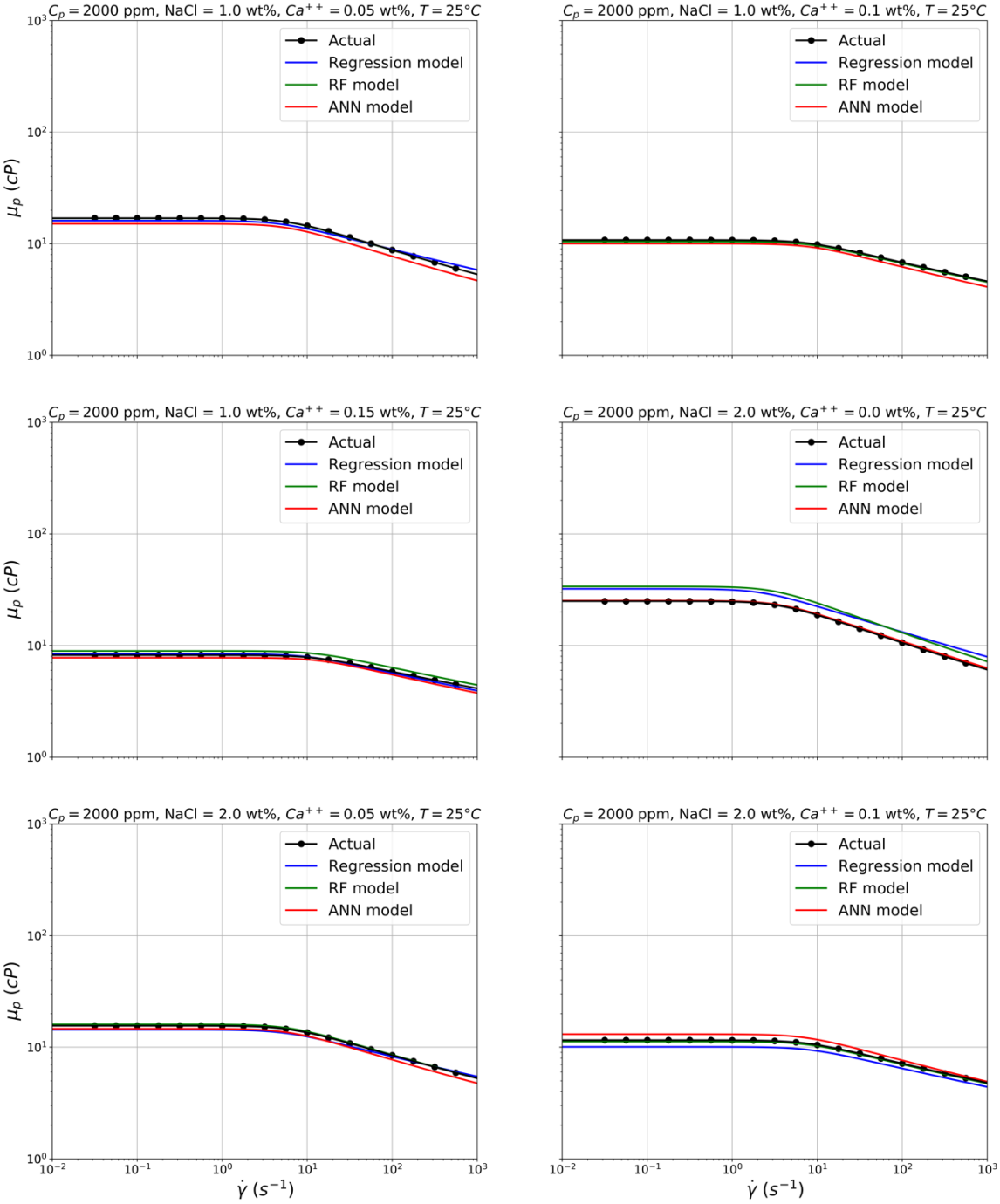
$C_p = 2000$ ppm, NaCl = 1.0 wt%, $Ca^{++} = 0.05$ wt%, $T = 25°C$
$C_p = 2000$ ppm, NaCl = 1.0 wt%, $Ca^{++} = 0.1$ wt%, $T = 25°C$
$C_p = 2000$ ppm, NaCl = 1.0 wt%, $Ca^{++} = 0.15$ wt%, $T = 25°C$
$C_p = 2000$ ppm, NaCl = 2.0 wt%, $Ca^{++} = 0.0$ wt%, $T = 25°C$
$C_p = 2000$ ppm, NaCl = 2.0 wt%, $Ca^{++} = 0.05$ wt%, $T = 25°C$
$C_p = 2000$ ppm, NaCl = 2.0 wt%, $Ca^{++} = 0.1$ wt%, $T = 25°C$
Actual
Regression model
RF model
ANN model
μ_p (cP)
$\dot{\gamma}$ (s^{-1})

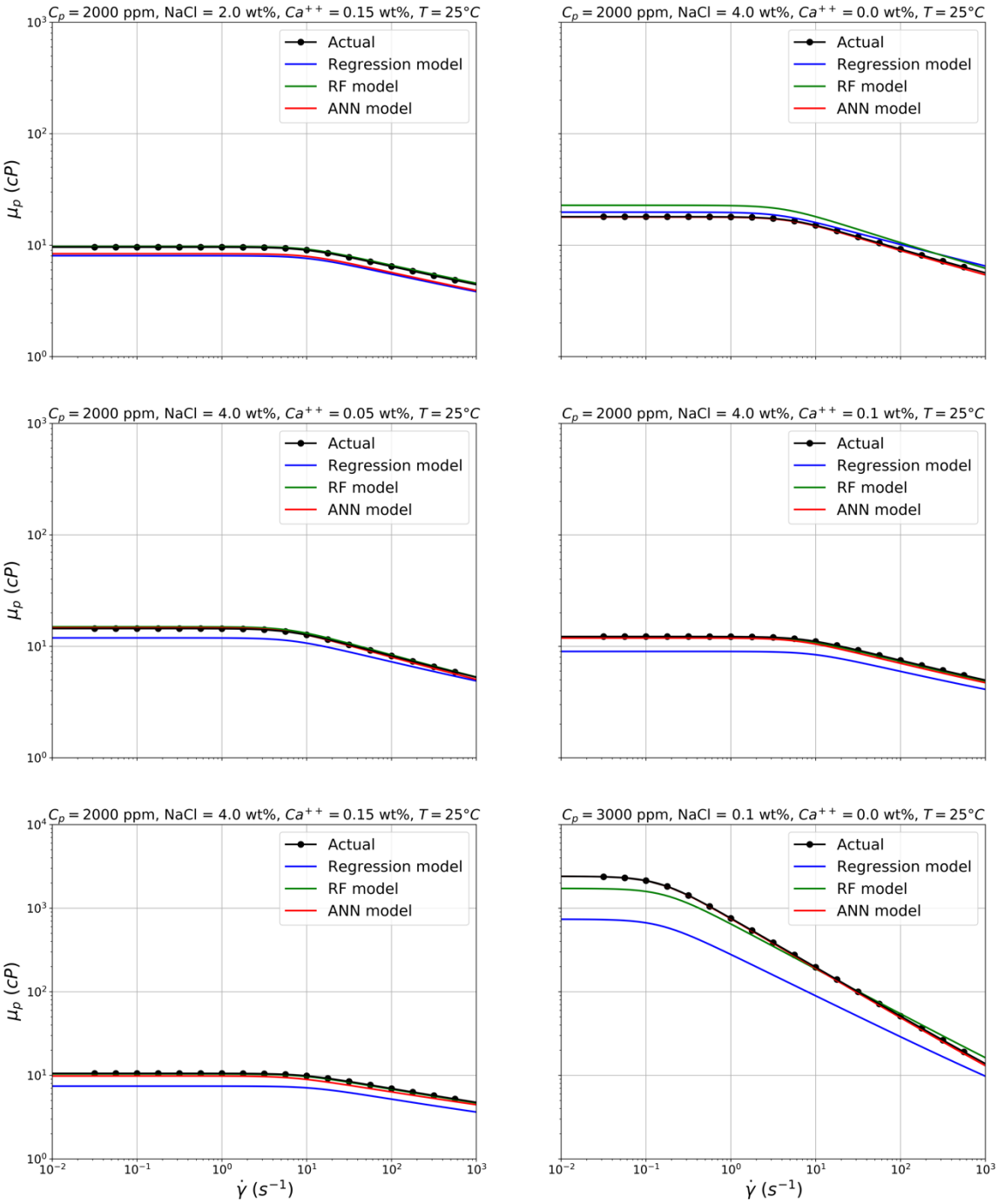
$C_p = 2000$ ppm, NaCl = 2.0 wt%, $Ca^{++} = 0.15$ wt%, $T = 25°C$
$C_p = 2000$ ppm, NaCl = 4.0 wt%, $Ca^{++} = 0.0$ wt%, $T = 25°C$
$C_p = 2000$ ppm, NaCl = 4.0 wt%, $Ca^{++} = 0.05$ wt%, $T = 25°C$
$C_p = 2000$ ppm, NaCl = 4.0 wt%, $Ca^{++} = 0.1$ wt%, $T = 25°C$
$C_p = 2000$ ppm, NaCl = 4.0 wt%, $Ca^{++} = 0.15$ wt%, $T = 25°C$
$C_p = 3000$ ppm, NaCl = 0.1 wt%, $Ca^{++} = 0.0$ wt%, $T = 25°C$
Actual
Regression model
RF model
ANN model
μ_p (cP)
$\dot{\gamma}$ (s^{-1})

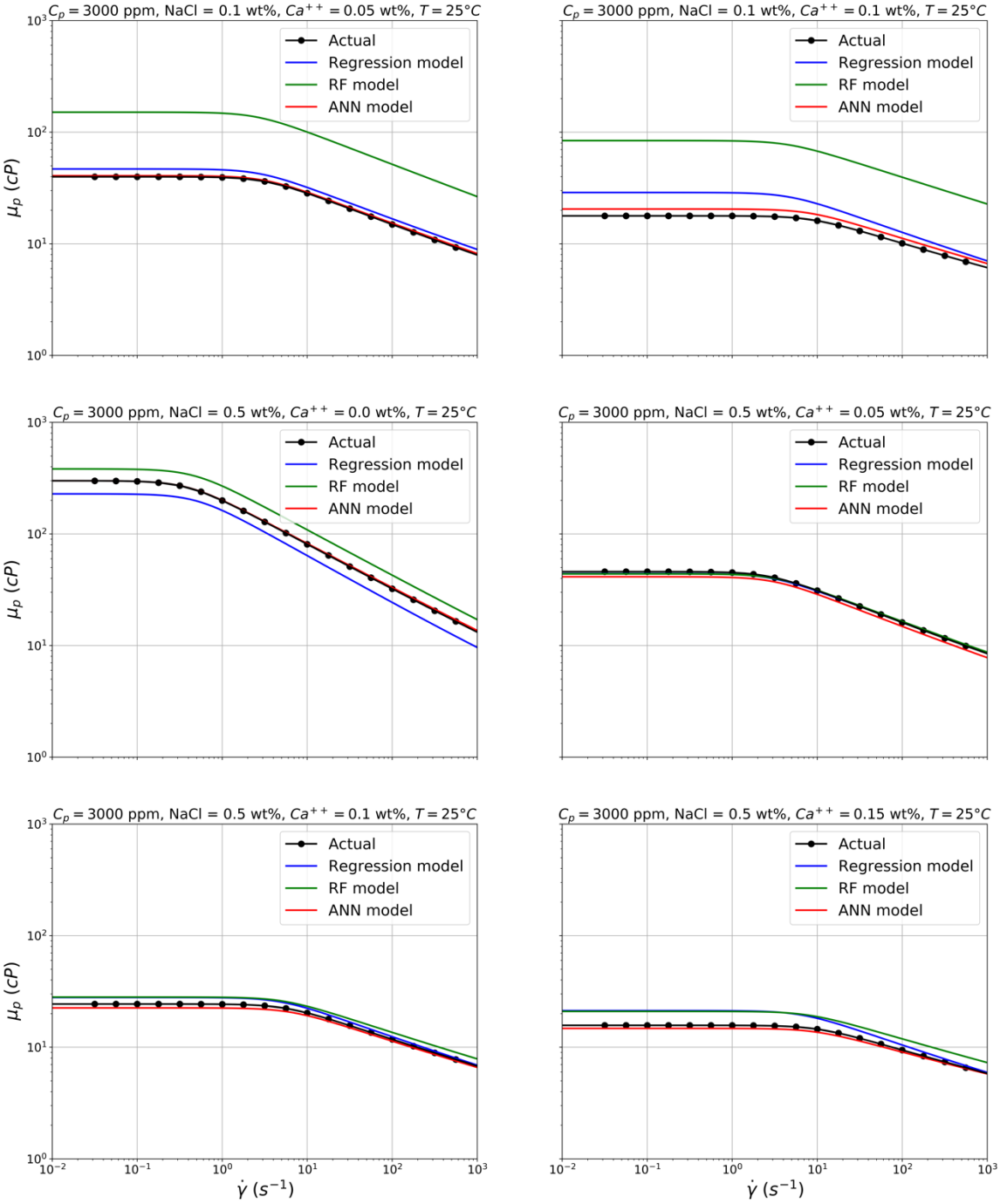
$C_p = 3000$ ppm, NaCl = 0.1 wt%, $Ca^{++} = 0.05$ wt%, $T = 25°C$
$C_p = 3000$ ppm, NaCl = 0.1 wt%, $Ca^{++} = 0.1$ wt%, $T = 25°C$
$C_p = 3000$ ppm, NaCl = 0.5 wt%, $Ca^{++} = 0.0$ wt%, $T = 25°C$
$C_p = 3000$ ppm, NaCl = 0.5 wt%, $Ca^{++} = 0.05$ wt%, $T = 25°C$
$C_p = 3000$ ppm, NaCl = 0.5 wt%, $Ca^{++} = 0.1$ wt%, $T = 25°C$
$C_p = 3000$ ppm, NaCl = 0.5 wt%, $Ca^{++} = 0.15$ wt%, $T = 25°C$
Actual
Regression model
RF model
ANN model
μ_p (cP)
$\dot{\gamma}$ (s^{-1})

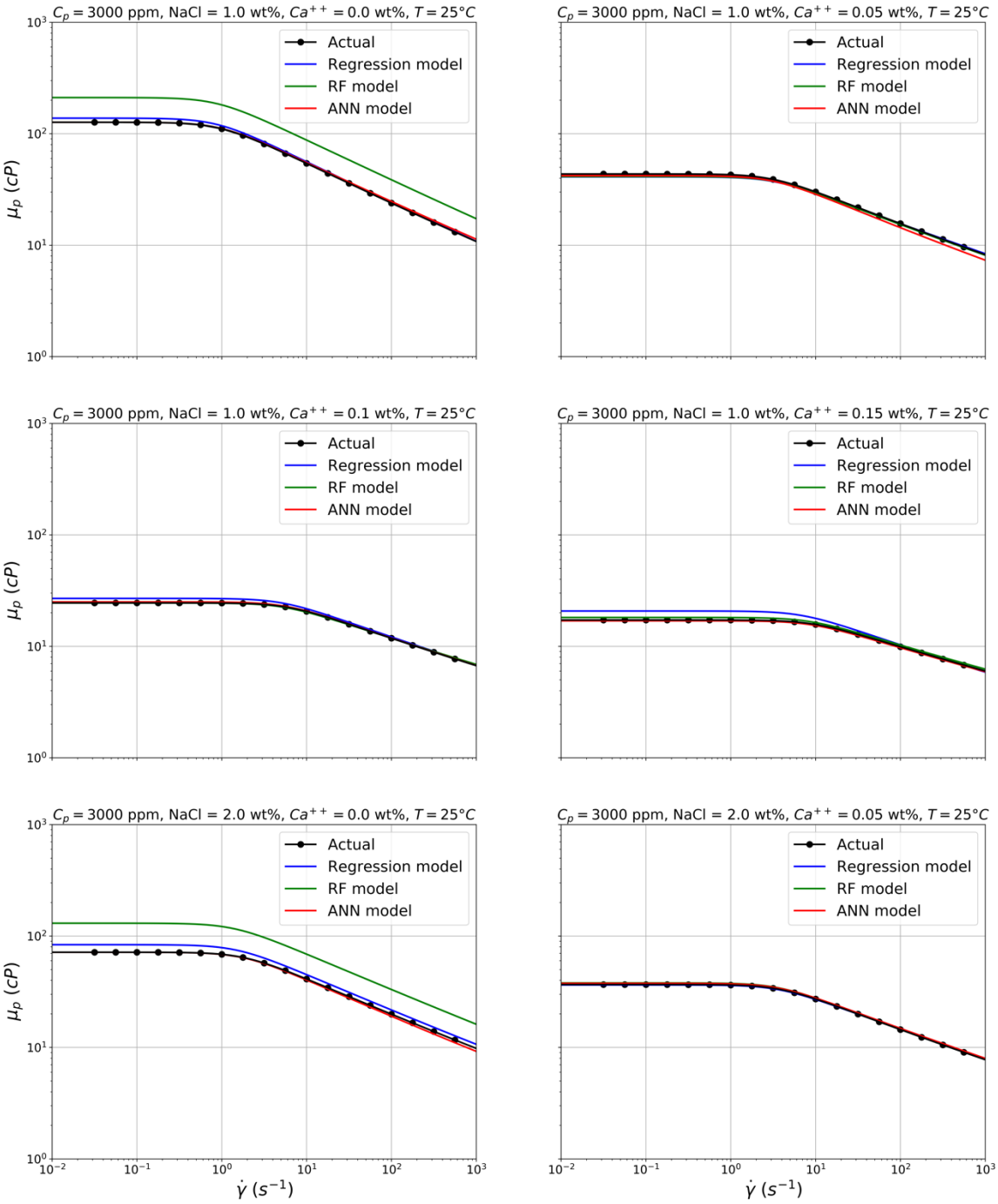
$C_p = 3000$ ppm, NaCl = 1.0 wt%, $Ca^{++} = 0.0$ wt%, $T = 25°C$
$C_p = 3000$ ppm, NaCl = 1.0 wt%, $Ca^{++} = 0.05$ wt%, $T = 25°C$
$C_p = 3000$ ppm, NaCl = 1.0 wt%, $Ca^{++} = 0.1$ wt%, $T = 25°C$
$C_p = 3000$ ppm, NaCl = 1.0 wt%, $Ca^{++} = 0.15$ wt%, $T = 25°C$
$C_p = 3000$ ppm, NaCl = 2.0 wt%, $Ca^{++} = 0.0$ wt%, $T = 25°C$
$C_p = 3000$ ppm, NaCl = 2.0 wt%, $Ca^{++} = 0.05$ wt%, $T = 25°C$
Actual
Regression model
RF model
ANN model
μ_p (cP)
$\dot{\gamma}$ (s^{-1})

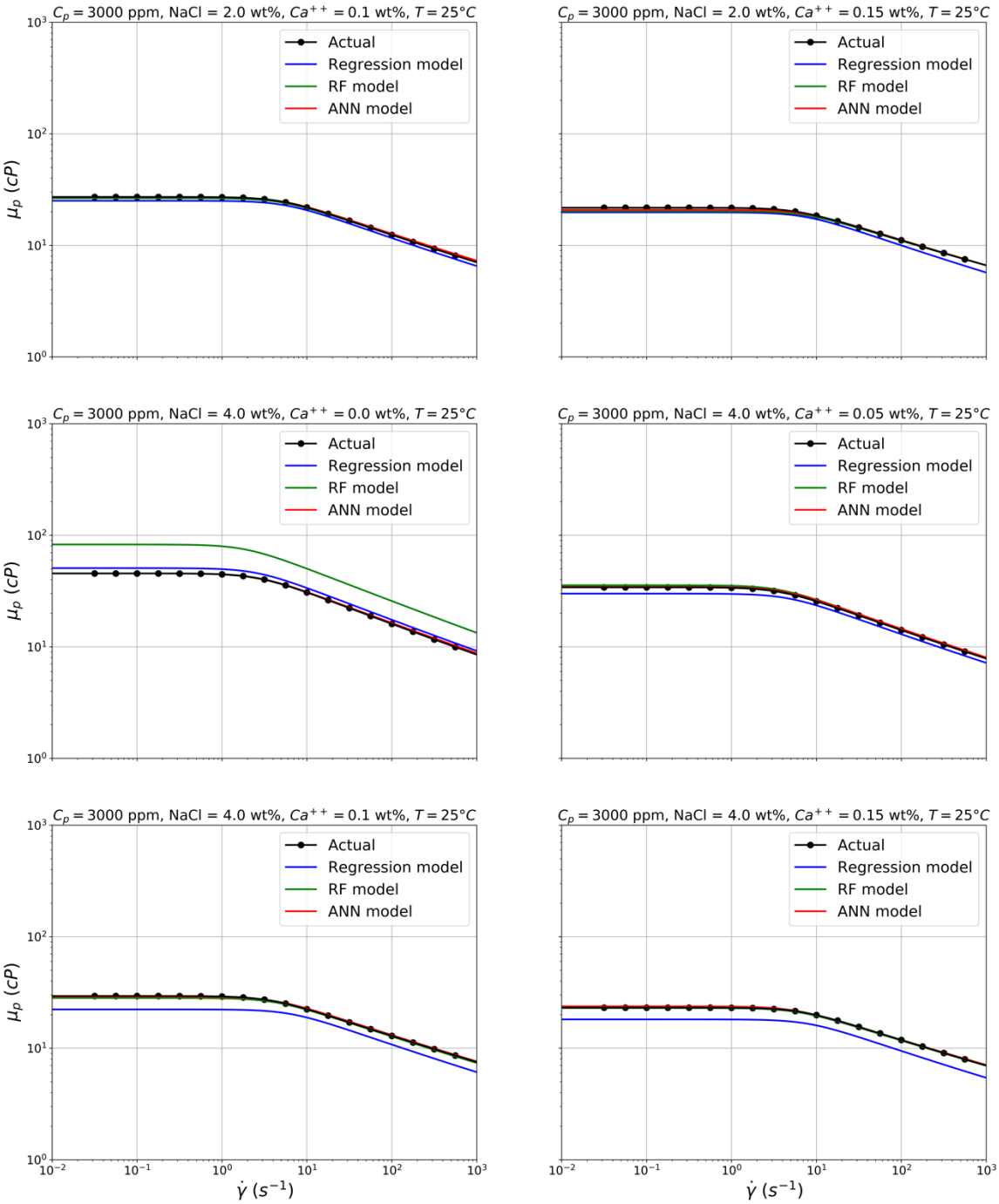

The following plots are at 2000 ppm polymer concentration, 1 wt% NaCl and different temperatures.

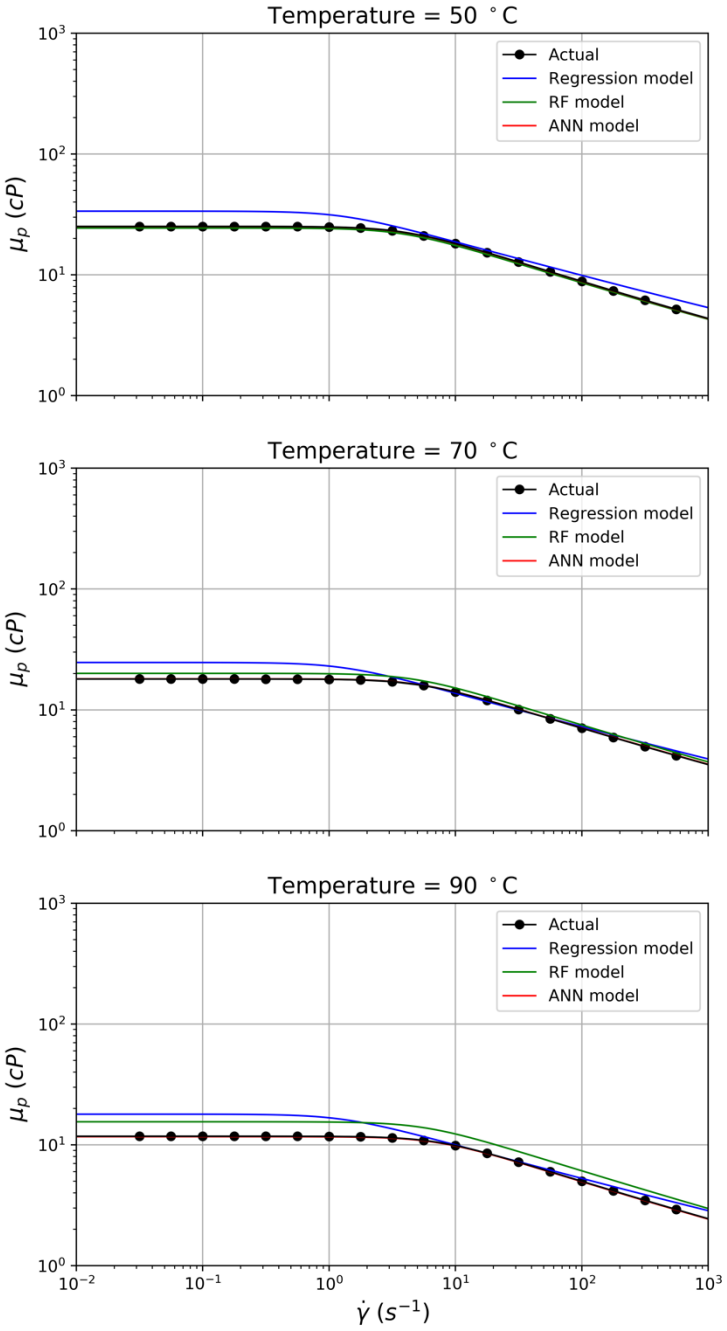
Temperature = 50 °C
Actual
Regression model
RF model
ANN model
μ_p (cP)
Temperature = 70 °C
Actual
Regression model
RF model
ANN model
μ_p (cP)
Temperature = 90 °C
Actual
Regression model
RF model
ANN model
μ_p (cP)
$\dot{\gamma}$ (s^{-1})

Appendix C. FP-3630S plots

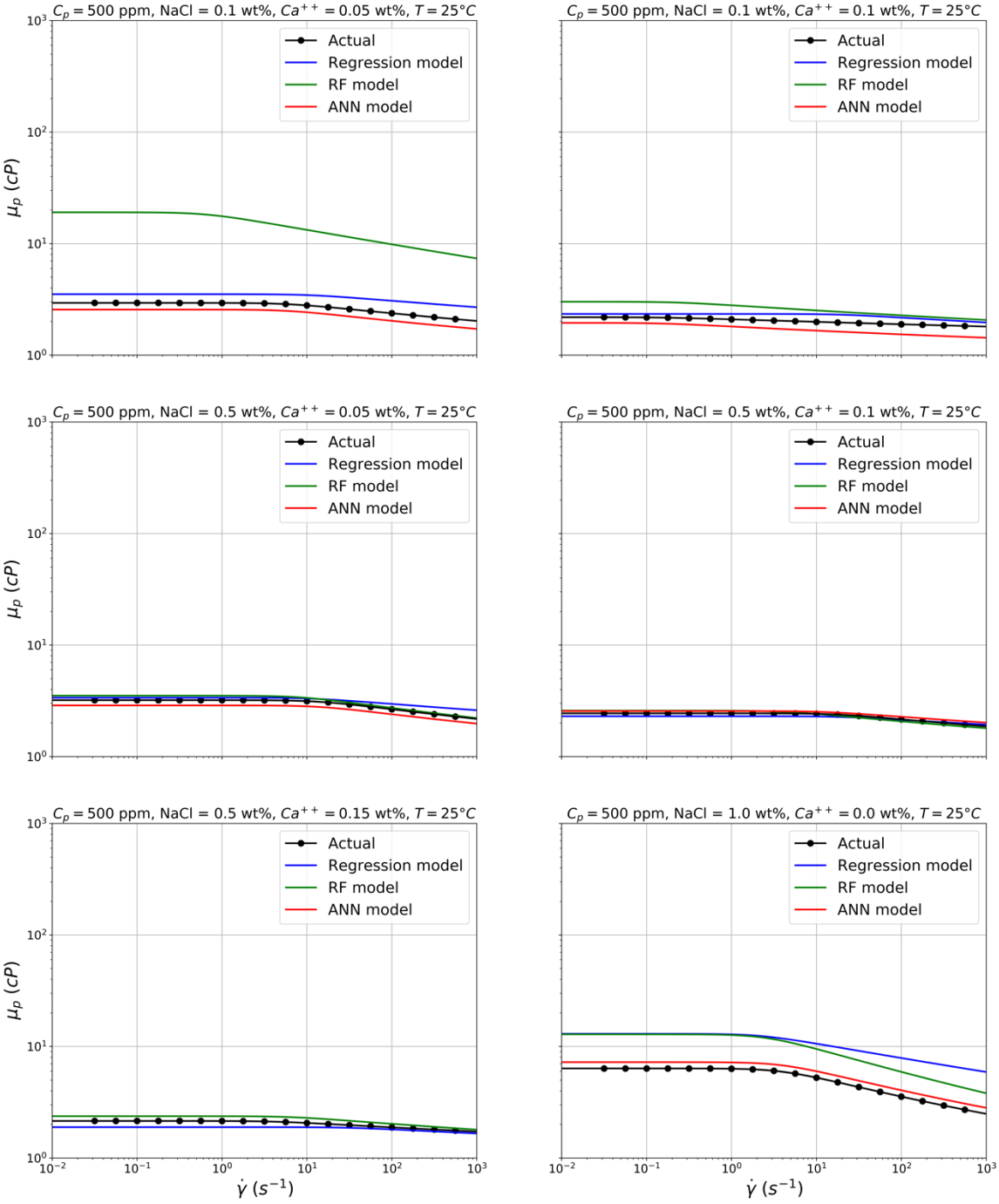

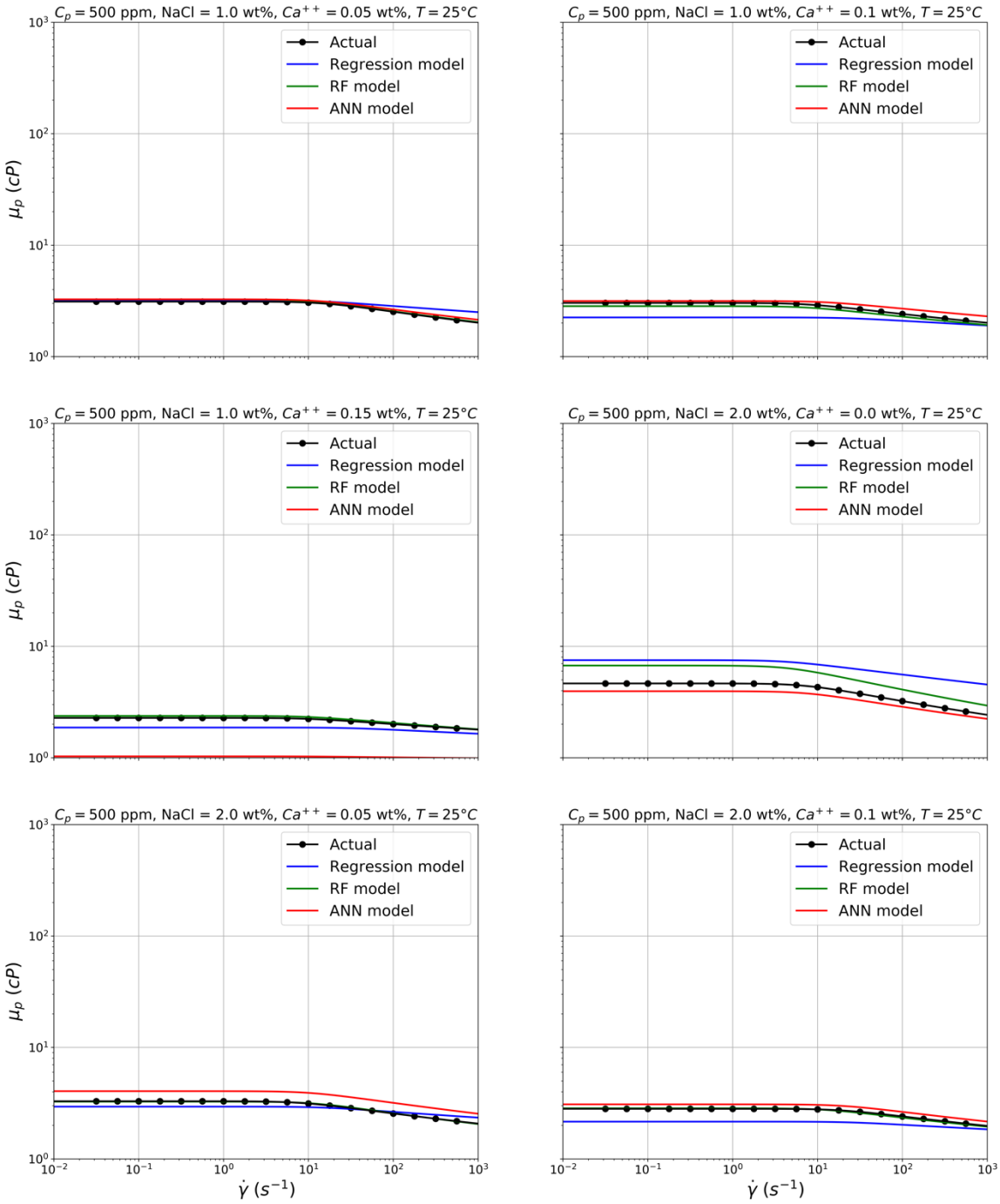
$C_p = 500$ ppm, NaCl = 1.0 wt%, $Ca^{++} = 0.05$ wt%, $T = 25°C$
$C_p = 500$ ppm, NaCl = 1.0 wt%, $Ca^{++} = 0.1$ wt%, $T = 25°C$
$C_p = 500$ ppm, NaCl = 1.0 wt%, $Ca^{++} = 0.15$ wt%, $T = 25°C$
$C_p = 500$ ppm, NaCl = 2.0 wt%, $Ca^{++} = 0.0$ wt%, $T = 25°C$
$C_p = 500$ ppm, NaCl = 2.0 wt%, $Ca^{++} = 0.05$ wt%, $T = 25°C$
$C_p = 500$ ppm, NaCl = 2.0 wt%, $Ca^{++} = 0.1$ wt%, $T = 25°C$
Actual
Regression model
RF model
ANN model
μ_p (cP)
$\dot{\gamma}$ (s^{-1})

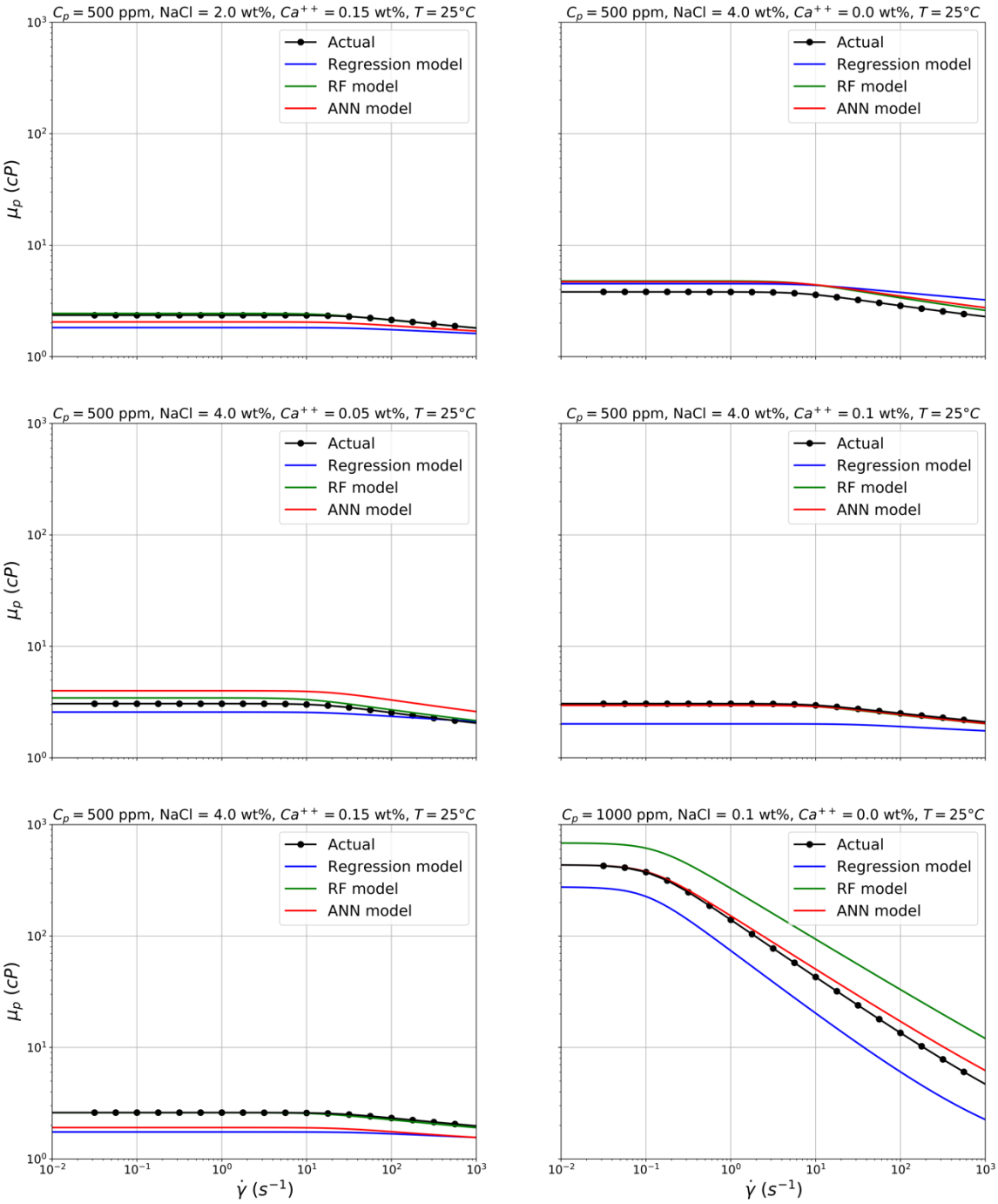
$C_p = 500$ ppm, NaCl = 2.0 wt%, $Ca^{++} = 0.15$ wt%, $T = 25°C$
$C_p = 500$ ppm, NaCl = 4.0 wt%, $Ca^{++} = 0.0$ wt%, $T = 25°C$
$C_p = 500$ ppm, NaCl = 4.0 wt%, $Ca^{++} = 0.05$ wt%, $T = 25°C$
$C_p = 500$ ppm, NaCl = 4.0 wt%, $Ca^{++} = 0.1$ wt%, $T = 25°C$
$C_p = 500$ ppm, NaCl = 4.0 wt%, $Ca^{++} = 0.15$ wt%, $T = 25°C$
$C_p = 1000$ ppm, NaCl = 0.1 wt%, $Ca^{++} = 0.0$ wt%, $T = 25°C$
Actual
Regression model
RF model
ANN model
μ_p (cP)
$\dot{\gamma}$ (s^{-1})

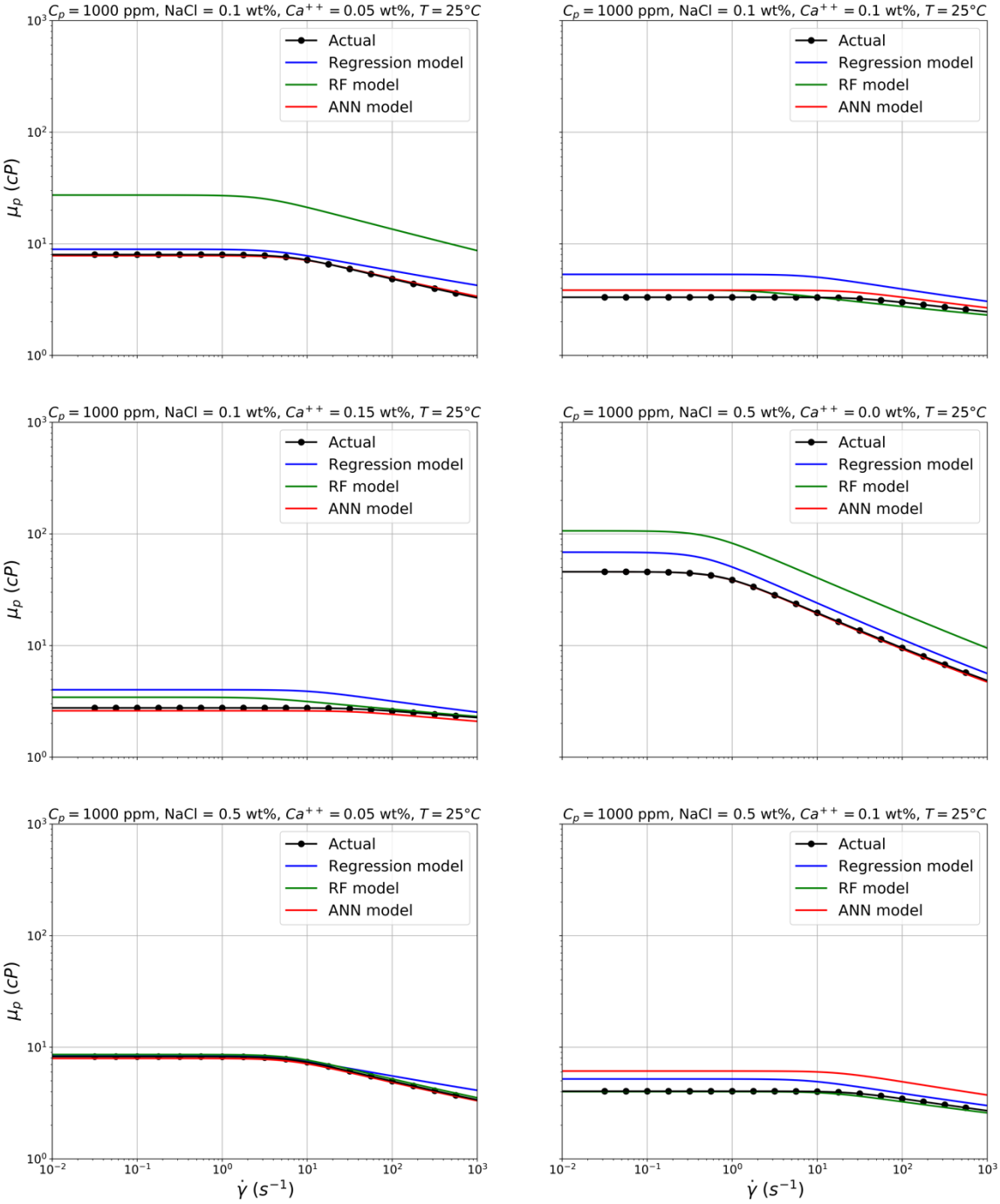
$C_p = 1000$ ppm, NaCl = 0.1 wt%, $Ca^{++} = 0.05$ wt%, $T = 25°C$
$C_p = 1000$ ppm, NaCl = 0.1 wt%, $Ca^{++} = 0.1$ wt%, $T = 25°C$
$C_p = 1000$ ppm, NaCl = 0.1 wt%, $Ca^{++} = 0.15$ wt%, $T = 25°C$
$C_p = 1000$ ppm, NaCl = 0.5 wt%, $Ca^{++} = 0.0$ wt%, $T = 25°C$
$C_p = 1000$ ppm, NaCl = 0.5 wt%, $Ca^{++} = 0.05$ wt%, $T = 25°C$
$C_p = 1000$ ppm, NaCl = 0.5 wt%, $Ca^{++} = 0.1$ wt%, $T = 25°C$
Actual
Regression model
RF model
ANN model
μ_p (cP)
$\dot{\gamma}$ (s^{-1})

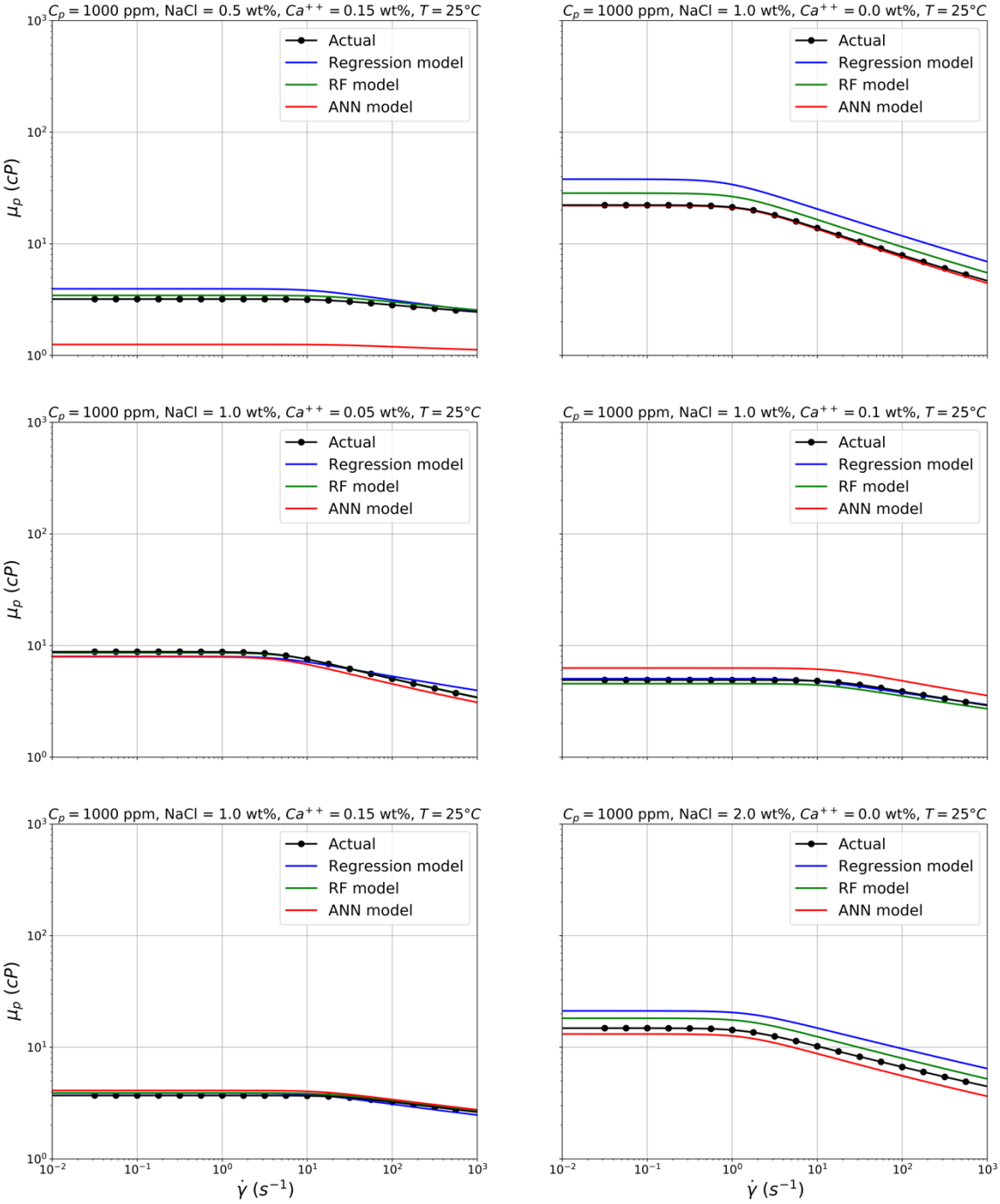
$C_p = 1000$ ppm, NaCl = 0.5 wt%, $Ca^{++} = 0.15$ wt%, $T = 25°C$
$C_p = 1000$ ppm, NaCl = 1.0 wt%, $Ca^{++} = 0.0$ wt%, $T = 25°C$
$C_p = 1000$ ppm, NaCl = 1.0 wt%, $Ca^{++} = 0.05$ wt%, $T = 25°C$
$C_p = 1000$ ppm, NaCl = 1.0 wt%, $Ca^{++} = 0.1$ wt%, $T = 25°C$
$C_p = 1000$ ppm, NaCl = 1.0 wt%, $Ca^{++} = 0.15$ wt%, $T = 25°C$
$C_p = 1000$ ppm, NaCl = 2.0 wt%, $Ca^{++} = 0.0$ wt%, $T = 25°C$
Actual
Regression model
RF model
ANN model
μ_p (cP)
$\dot{\gamma}$ (s^{-1})

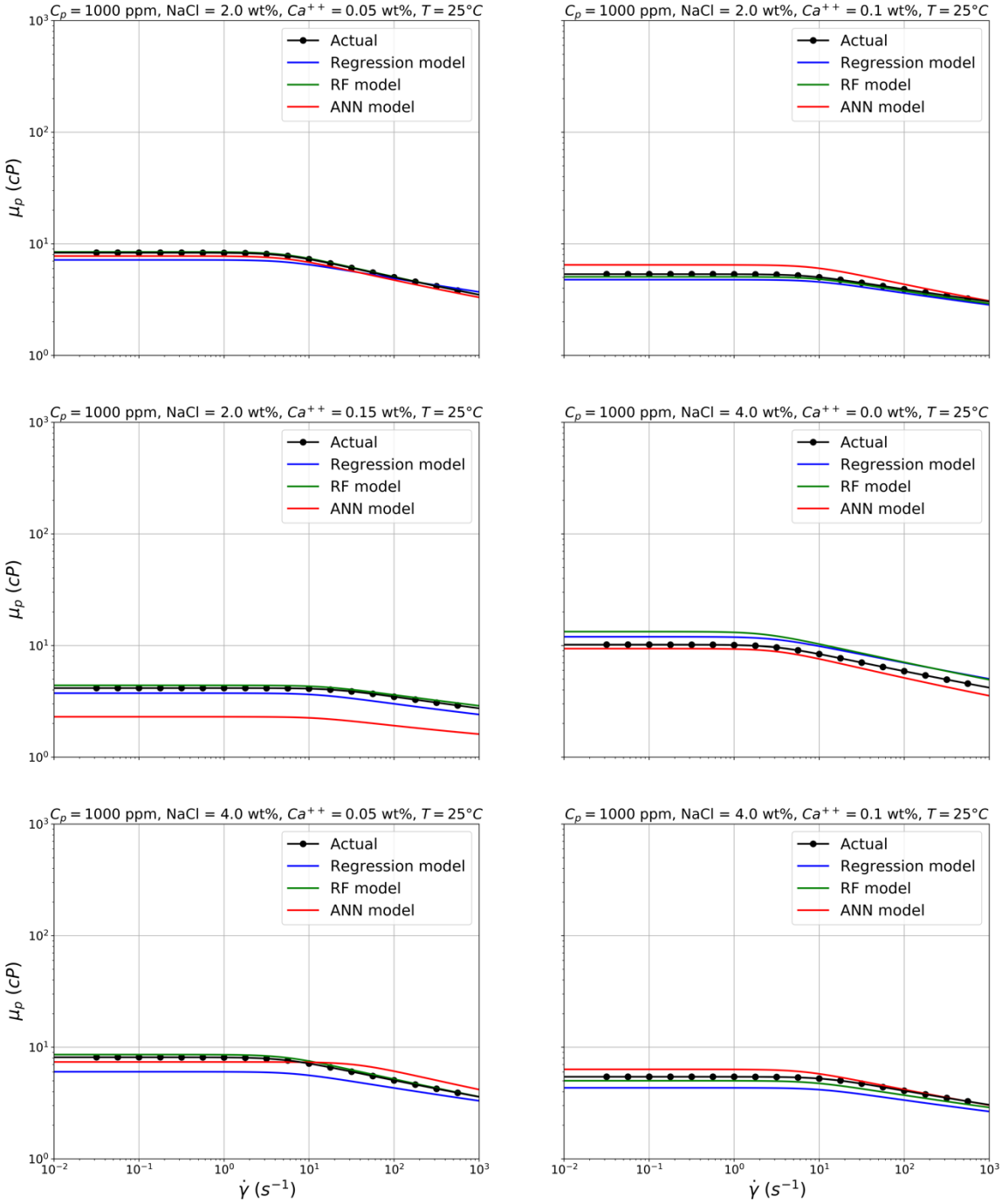
$C_p = 1000$ ppm, NaCl = 2.0 wt%, $Ca^{++} = 0.05$ wt%, $T = 25°C$
$C_p = 1000$ ppm, NaCl = 2.0 wt%, $Ca^{++} = 0.1$ wt%, $T = 25°C$
$C_p = 1000$ ppm, NaCl = 2.0 wt%, $Ca^{++} = 0.15$ wt%, $T = 25°C$
$C_p = 1000$ ppm, NaCl = 4.0 wt%, $Ca^{++} = 0.0$ wt%, $T = 25°C$
$C_p = 1000$ ppm, NaCl = 4.0 wt%, $Ca^{++} = 0.05$ wt%, $T = 25°C$
$C_p = 1000$ ppm, NaCl = 4.0 wt%, $Ca^{++} = 0.1$ wt%, $T = 25°C$
Actual
Regression model
RF model
ANN model
μ_p (cP)
$\dot{\gamma}$ (s^{-1})

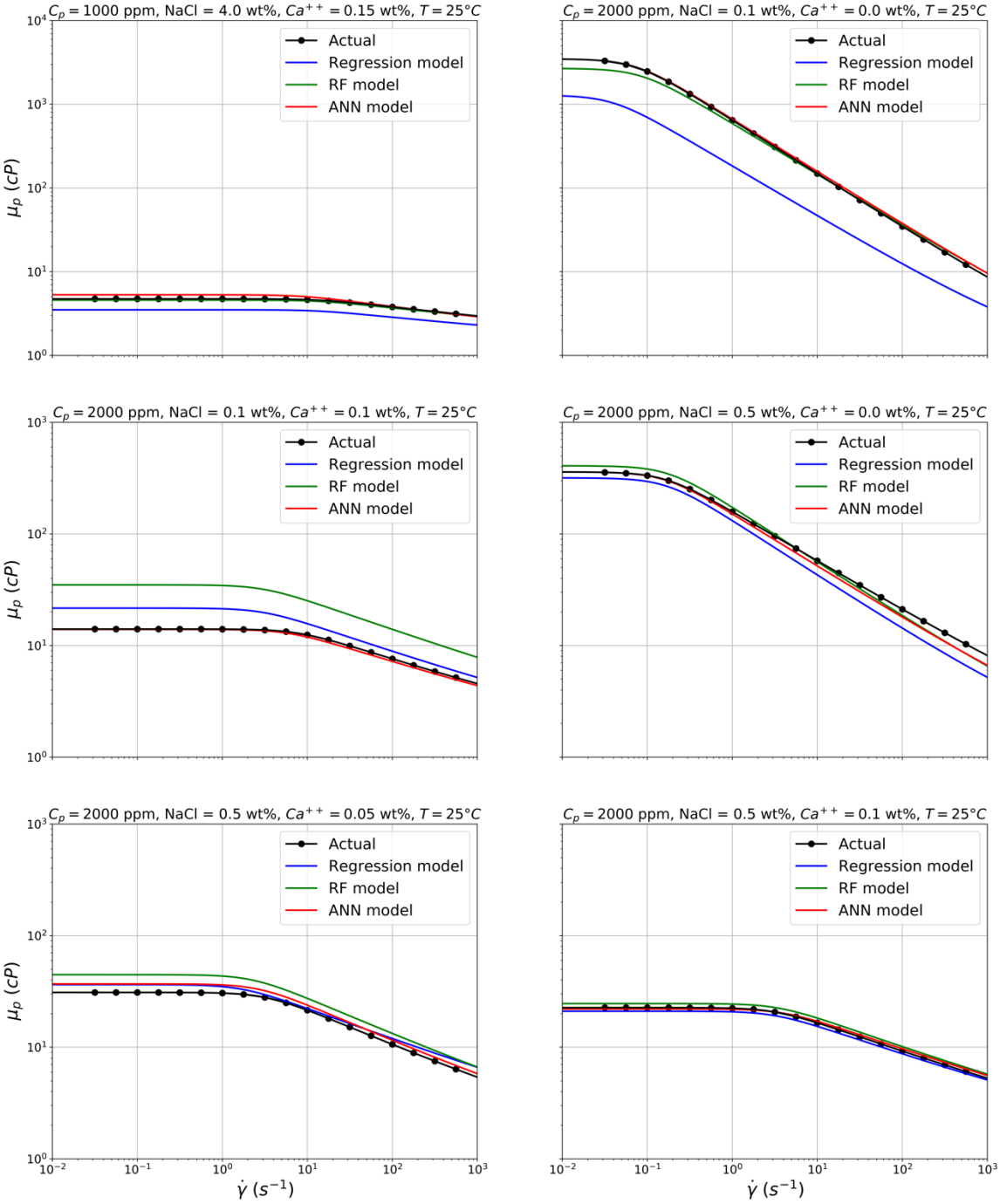
$C_p = 1000$ ppm, NaCl = 4.0 wt%, $Ca^{++} = 0.15$ wt%, $T = 25°C$
$C_p = 2000$ ppm, NaCl = 0.1 wt%, $Ca^{++} = 0.0$ wt%, $T = 25°C$
$C_p = 2000$ ppm, NaCl = 0.1 wt%, $Ca^{++} = 0.1$ wt%, $T = 25°C$
$C_p = 2000$ ppm, NaCl = 0.5 wt%, $Ca^{++} = 0.0$ wt%, $T = 25°C$
$C_p = 2000$ ppm, NaCl = 0.5 wt%, $Ca^{++} = 0.05$ wt%, $T = 25°C$
$C_p = 2000$ ppm, NaCl = 0.5 wt%, $Ca^{++} = 0.1$ wt%, $T = 25°C$
Actual
Regression model
RF model
ANN model
μ_p (cP)
$\dot{\gamma}$ (s^{-1})

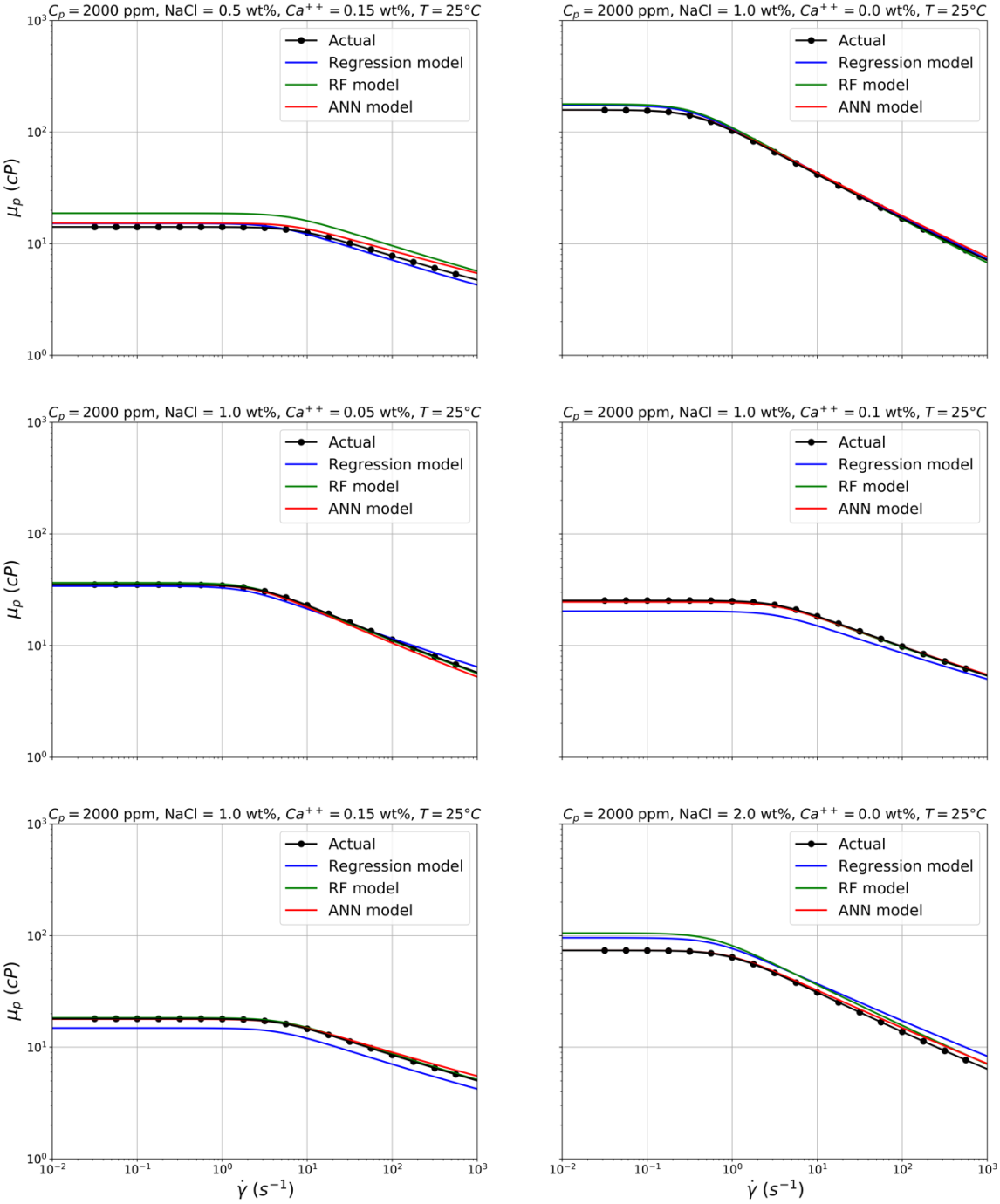
$C_p = 2000$ ppm, NaCl = 0.5 wt%, $Ca^{++} = 0.15$ wt%, $T = 25°C$
$C_p = 2000$ ppm, NaCl = 1.0 wt%, $Ca^{++} = 0.0$ wt%, $T = 25°C$
$C_p = 2000$ ppm, NaCl = 1.0 wt%, $Ca^{++} = 0.05$ wt%, $T = 25°C$
$C_p = 2000$ ppm, NaCl = 1.0 wt%, $Ca^{++} = 0.1$ wt%, $T = 25°C$
$C_p = 2000$ ppm, NaCl = 1.0 wt%, $Ca^{++} = 0.15$ wt%, $T = 25°C$
$C_p = 2000$ ppm, NaCl = 2.0 wt%, $Ca^{++} = 0.0$ wt%, $T = 25°C$
Actual
Regression model
RF model
ANN model
μ_p (cP)
$\dot{\gamma}$ (s^{-1})

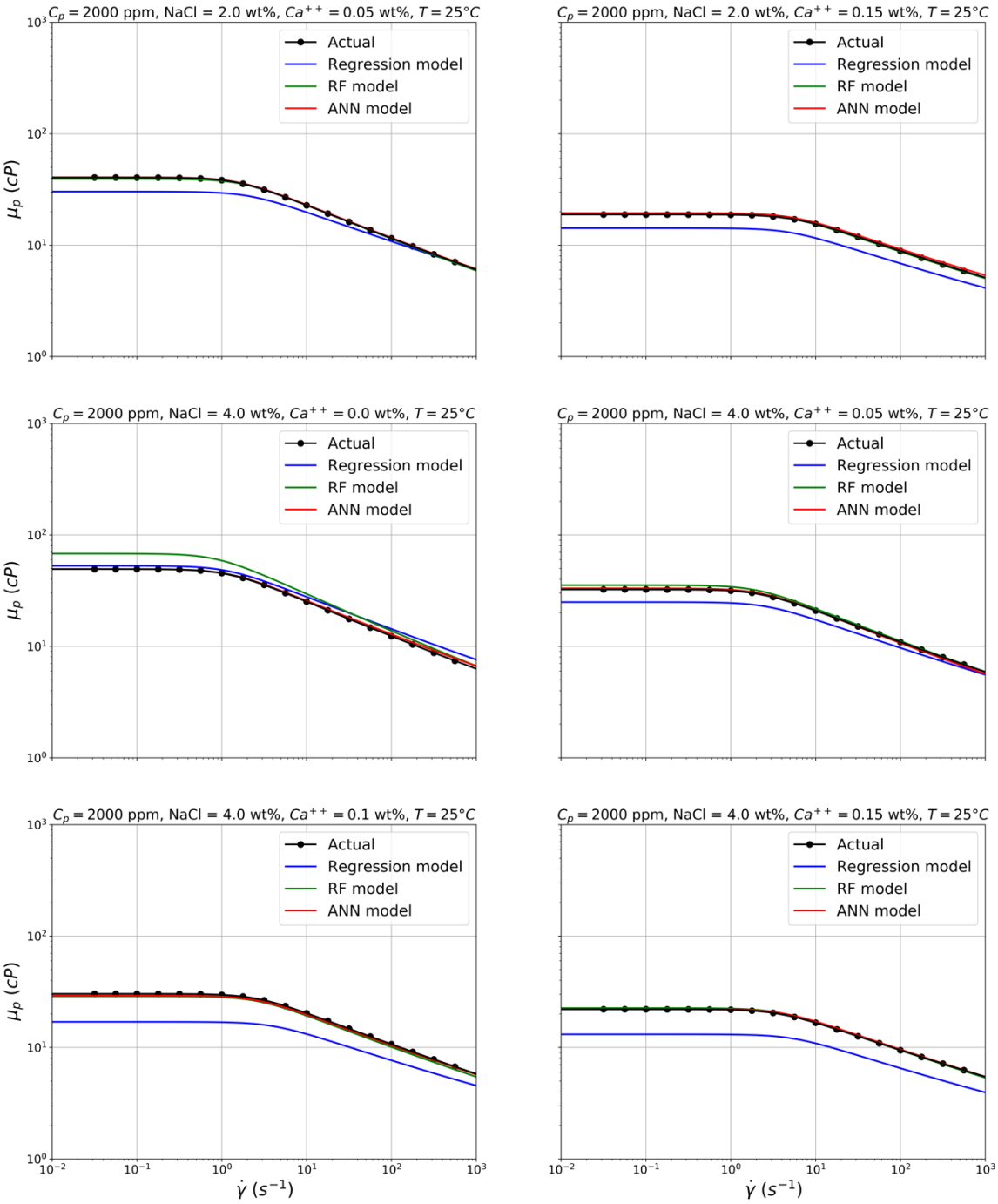
$C_p = 2000$ ppm, NaCl = 2.0 wt%, $Ca^{++} = 0.05$ wt%, $T = 25°C$
$C_p = 2000$ ppm, NaCl = 2.0 wt%, $Ca^{++} = 0.15$ wt%, $T = 25°C$
$C_p = 2000$ ppm, NaCl = 4.0 wt%, $Ca^{++} = 0.0$ wt%, $T = 25°C$
$C_p = 2000$ ppm, NaCl = 4.0 wt%, $Ca^{++} = 0.05$ wt%, $T = 25°C$
$C_p = 2000$ ppm, NaCl = 4.0 wt%, $Ca^{++} = 0.1$ wt%, $T = 25°C$
$C_p = 2000$ ppm, NaCl = 4.0 wt%, $Ca^{++} = 0.15$ wt%, $T = 25°C$
Actual
Regression model
RF model
ANN model
μ_p (cP)
$\dot{\gamma}$ (s^{-1})

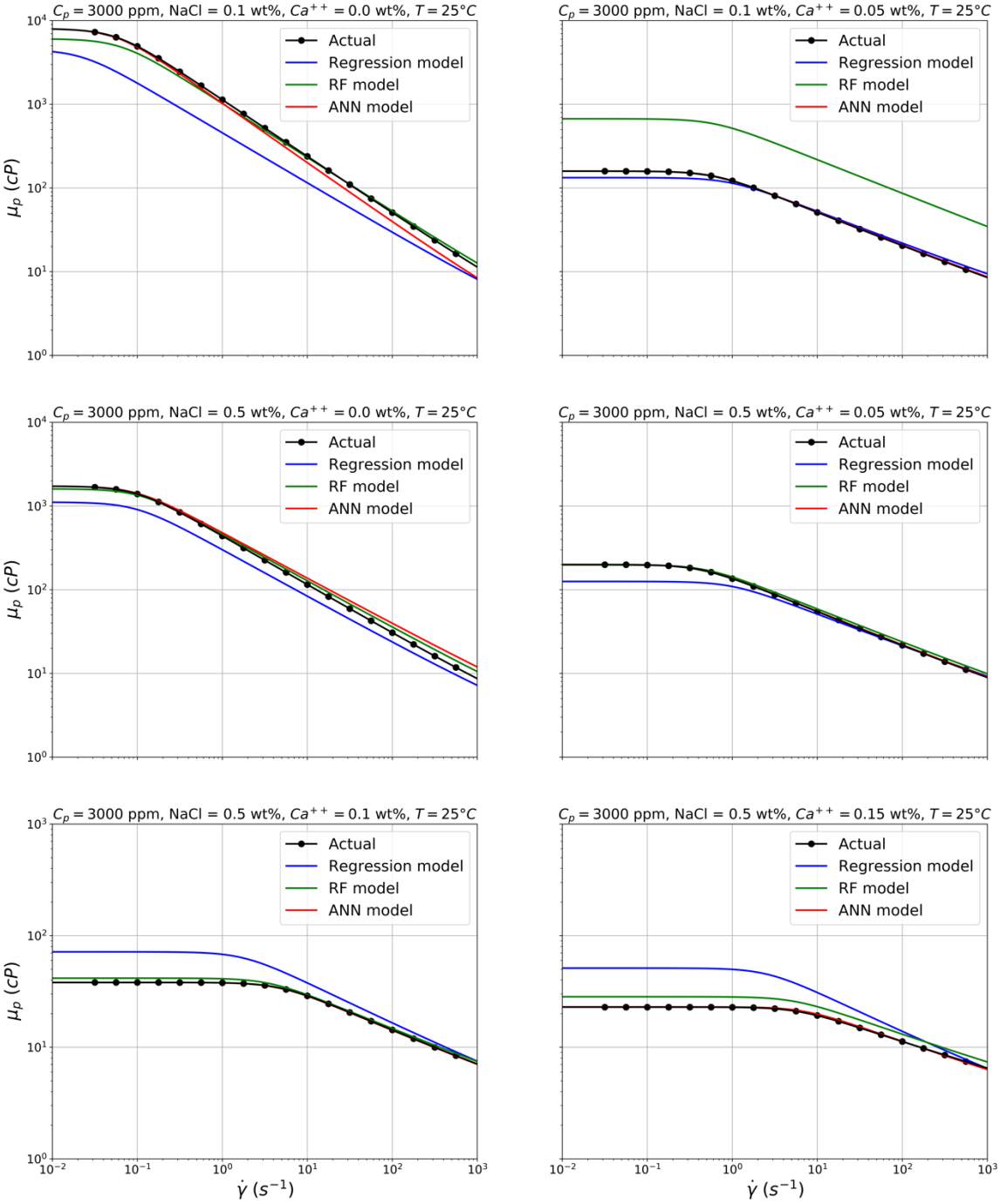
$C_p = 3000$ ppm, NaCl = 0.1 wt%, $Ca^{++} = 0.0$ wt%, $T = 25°C$
$C_p = 3000$ ppm, NaCl = 0.1 wt%, $Ca^{++} = 0.05$ wt%, $T = 25°C$
$C_p = 3000$ ppm, NaCl = 0.5 wt%, $Ca^{++} = 0.0$ wt%, $T = 25°C$
$C_p = 3000$ ppm, NaCl = 0.5 wt%, $Ca^{++} = 0.05$ wt%, $T = 25°C$
$C_p = 3000$ ppm, NaCl = 0.5 wt%, $Ca^{++} = 0.1$ wt%, $T = 25°C$
$C_p = 3000$ ppm, NaCl = 0.5 wt%, $Ca^{++} = 0.15$ wt%, $T = 25°C$
Actual
Regression model
RF model
ANN model
μ_p (cP)
$\dot{\gamma}$ (s^{-1})

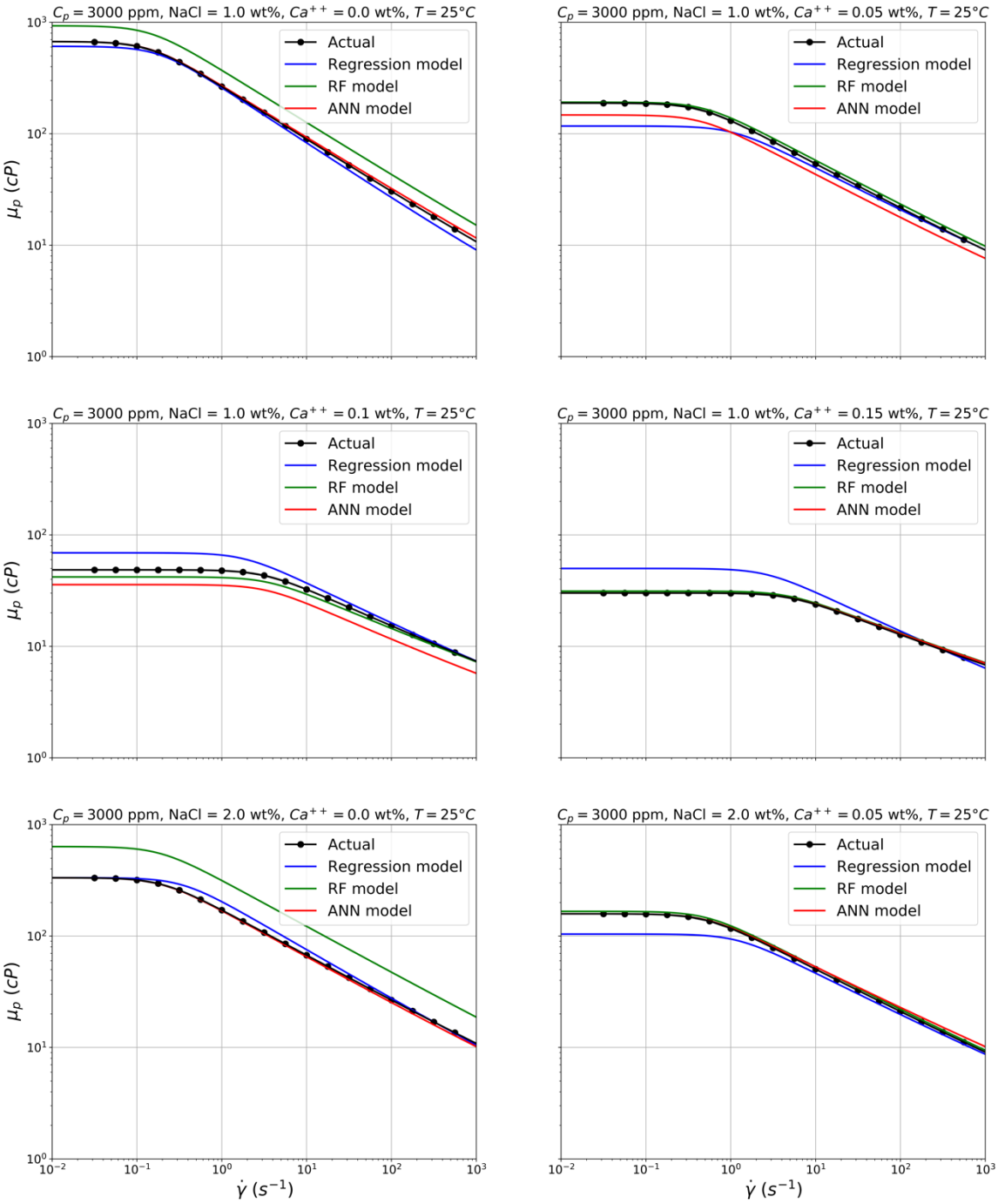
$C_p = 3000$ ppm, NaCl = 1.0 wt%, $Ca^{++} = 0.0$ wt%, $T = 25°C$
$C_p = 3000$ ppm, NaCl = 1.0 wt%, $Ca^{++} = 0.05$ wt%, $T = 25°C$
$C_p = 3000$ ppm, NaCl = 1.0 wt%, $Ca^{++} = 0.1$ wt%, $T = 25°C$
$C_p = 3000$ ppm, NaCl = 1.0 wt%, $Ca^{++} = 0.15$ wt%, $T = 25°C$
$C_p = 3000$ ppm, NaCl = 2.0 wt%, $Ca^{++} = 0.0$ wt%, $T = 25°C$
$C_p = 3000$ ppm, NaCl = 2.0 wt%, $Ca^{++} = 0.05$ wt%, $T = 25°C$
Actual
Regression model
RF model
ANN model
μ_p (cP)
$\dot{\gamma}$ (s^{-1})

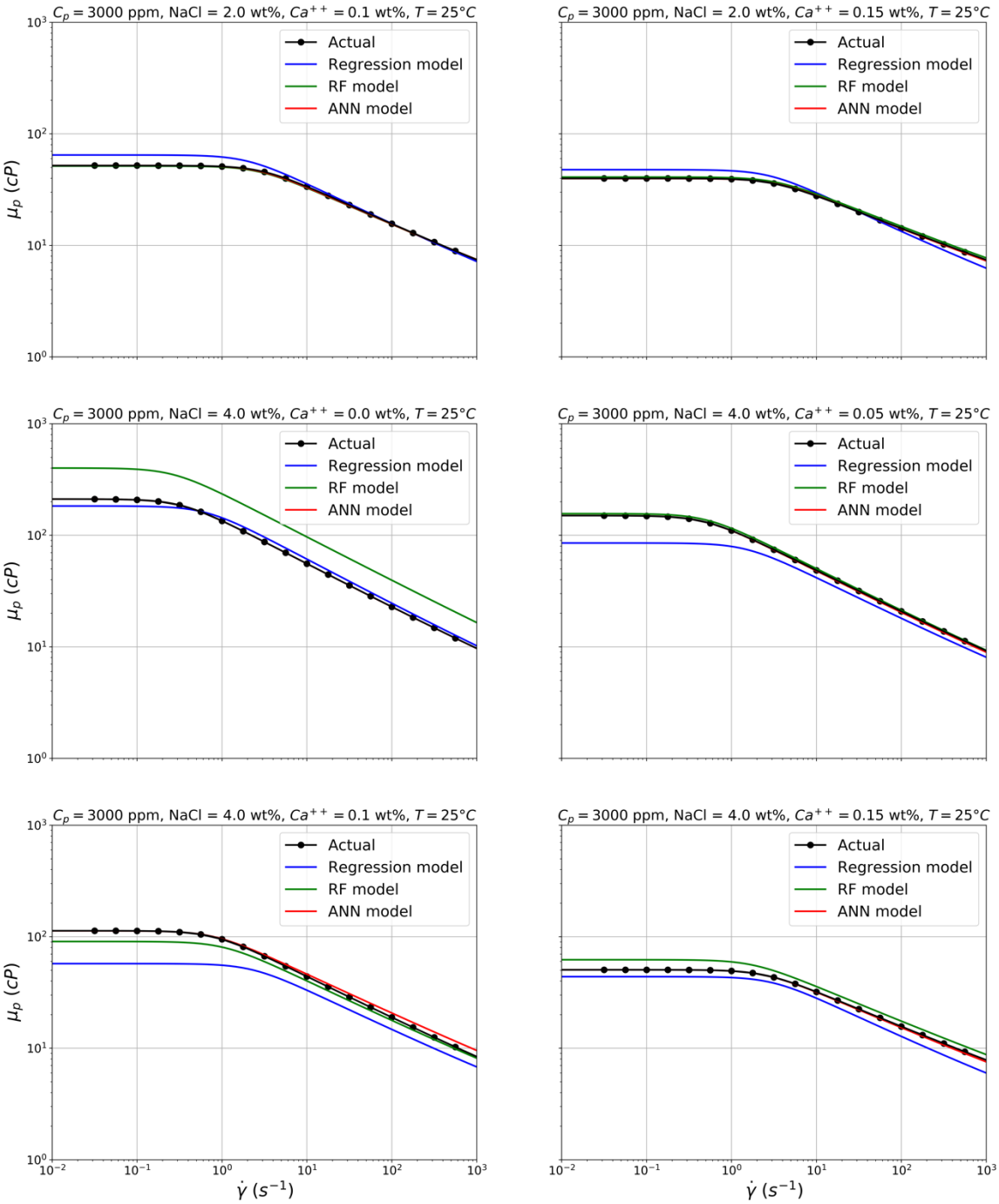

The following plots are at 2000 ppm polymer concentration, 1 wt% NaCl and different temperatures.

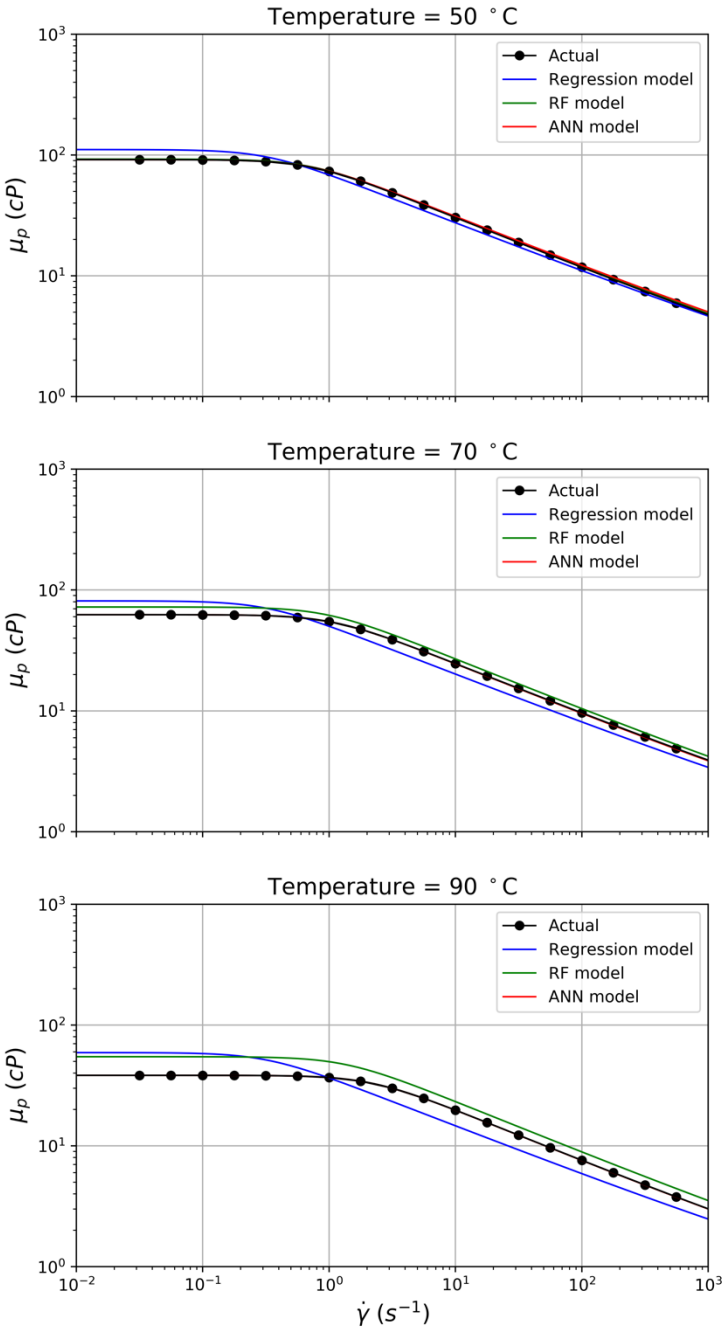
Temperature = 50 °C
Actual
Regression model
RF model
ANN model
μ_p (cP)
Temperature = 70 °C
Actual
Regression model
RF model
ANN model
μ_p (cP)
Temperature = 90 °C
Actual
Regression model
RF model
ANN model
μ_p (cP)
$\dot{\gamma}$ (s^{-1})

Appendix D. AN-125 plots

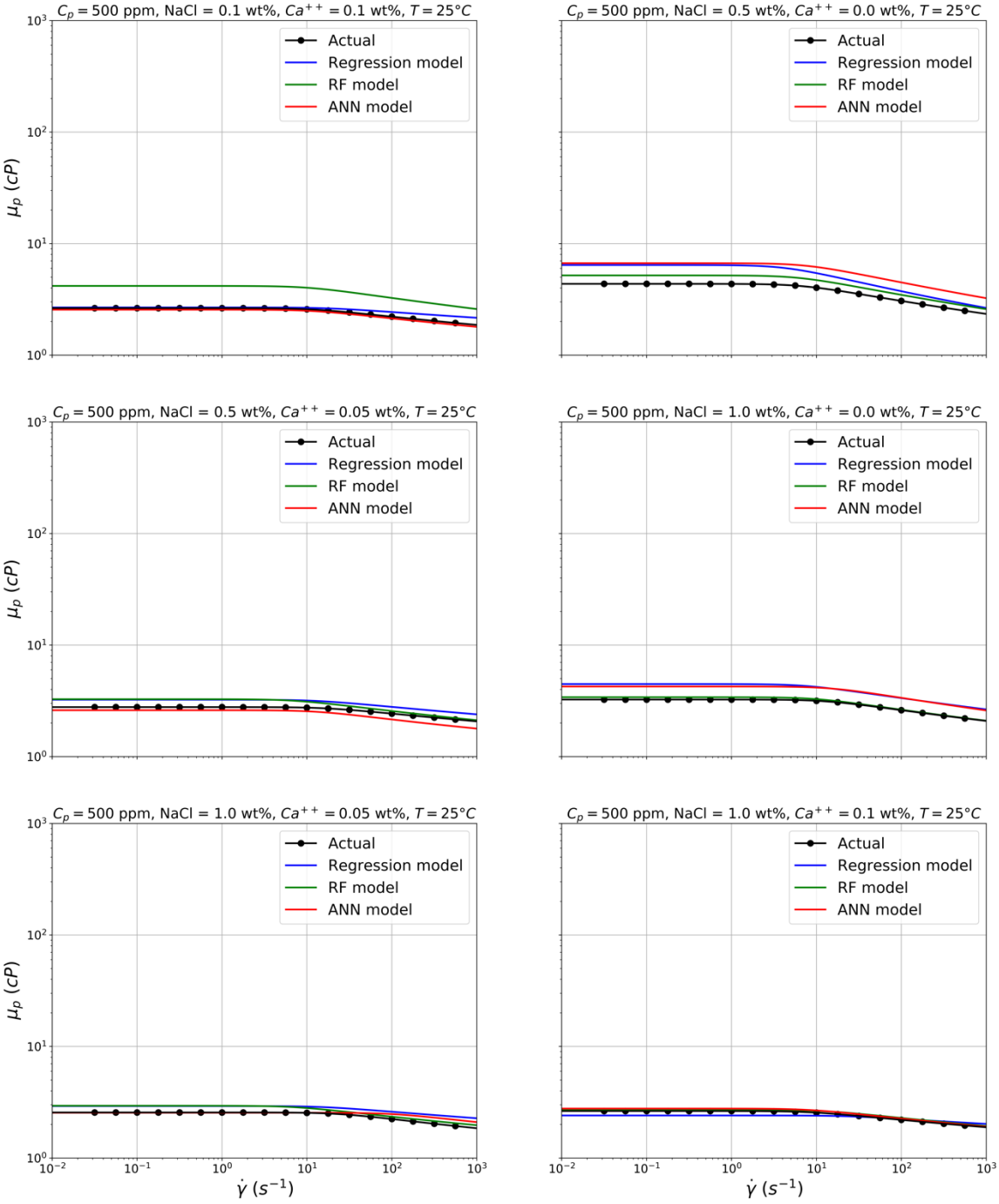

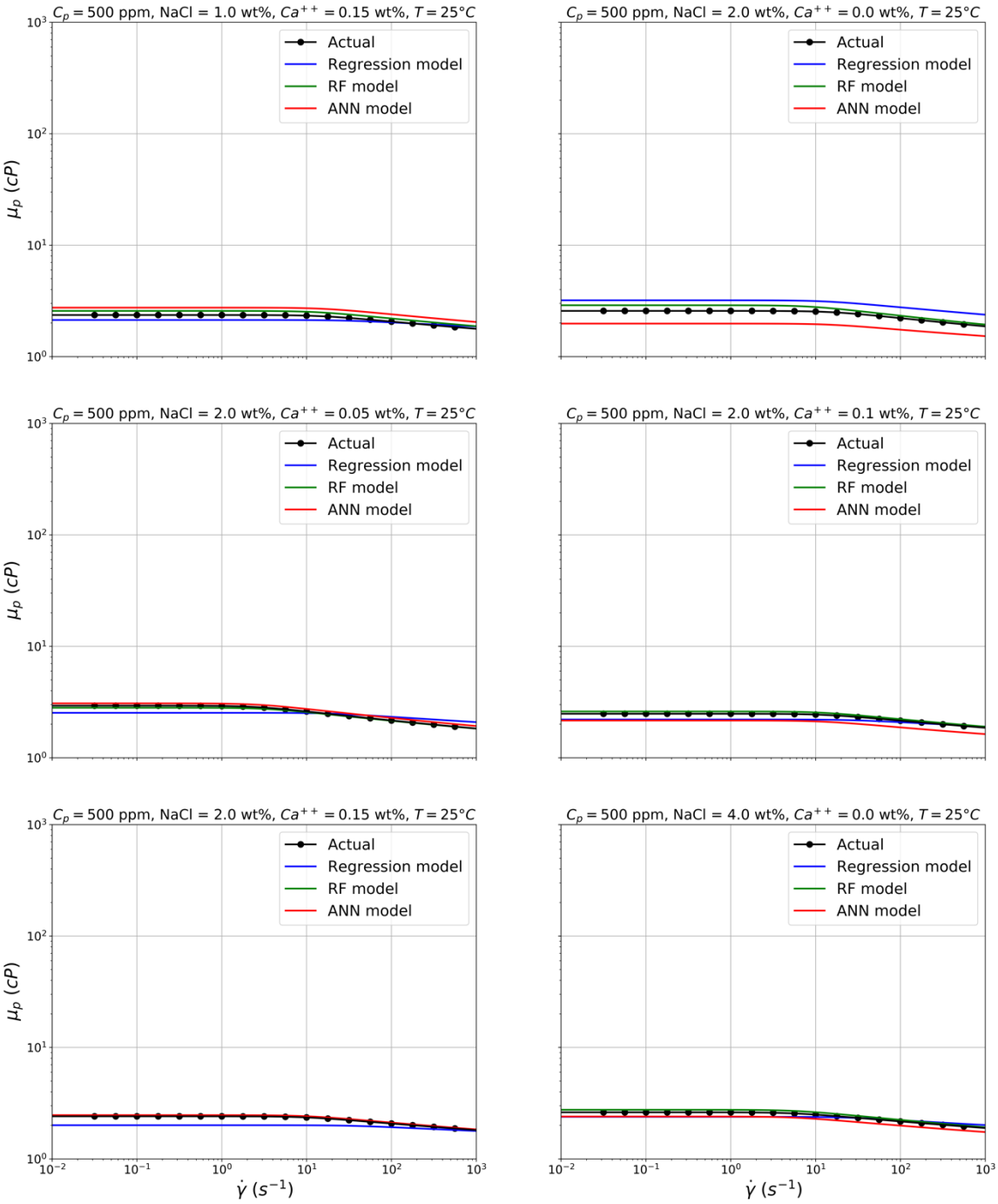
$C_p = 500$ ppm, NaCl = 1.0 wt%, $Ca^{++} = 0.15$ wt%, $T = 25°C$
$C_p = 500$ ppm, NaCl = 2.0 wt%, $Ca^{++} = 0.0$ wt%, $T = 25°C$
$C_p = 500$ ppm, NaCl = 2.0 wt%, $Ca^{++} = 0.05$ wt%, $T = 25°C$
$C_p = 500$ ppm, NaCl = 2.0 wt%, $Ca^{++} = 0.1$ wt%, $T = 25°C$
$C_p = 500$ ppm, NaCl = 2.0 wt%, $Ca^{++} = 0.15$ wt%, $T = 25°C$
$C_p = 500$ ppm, NaCl = 4.0 wt%, $Ca^{++} = 0.0$ wt%, $T = 25°C$
Actual
Regression model
RF model
ANN model
μ_p (cP)
$\dot{\gamma}$ (s^{-1})

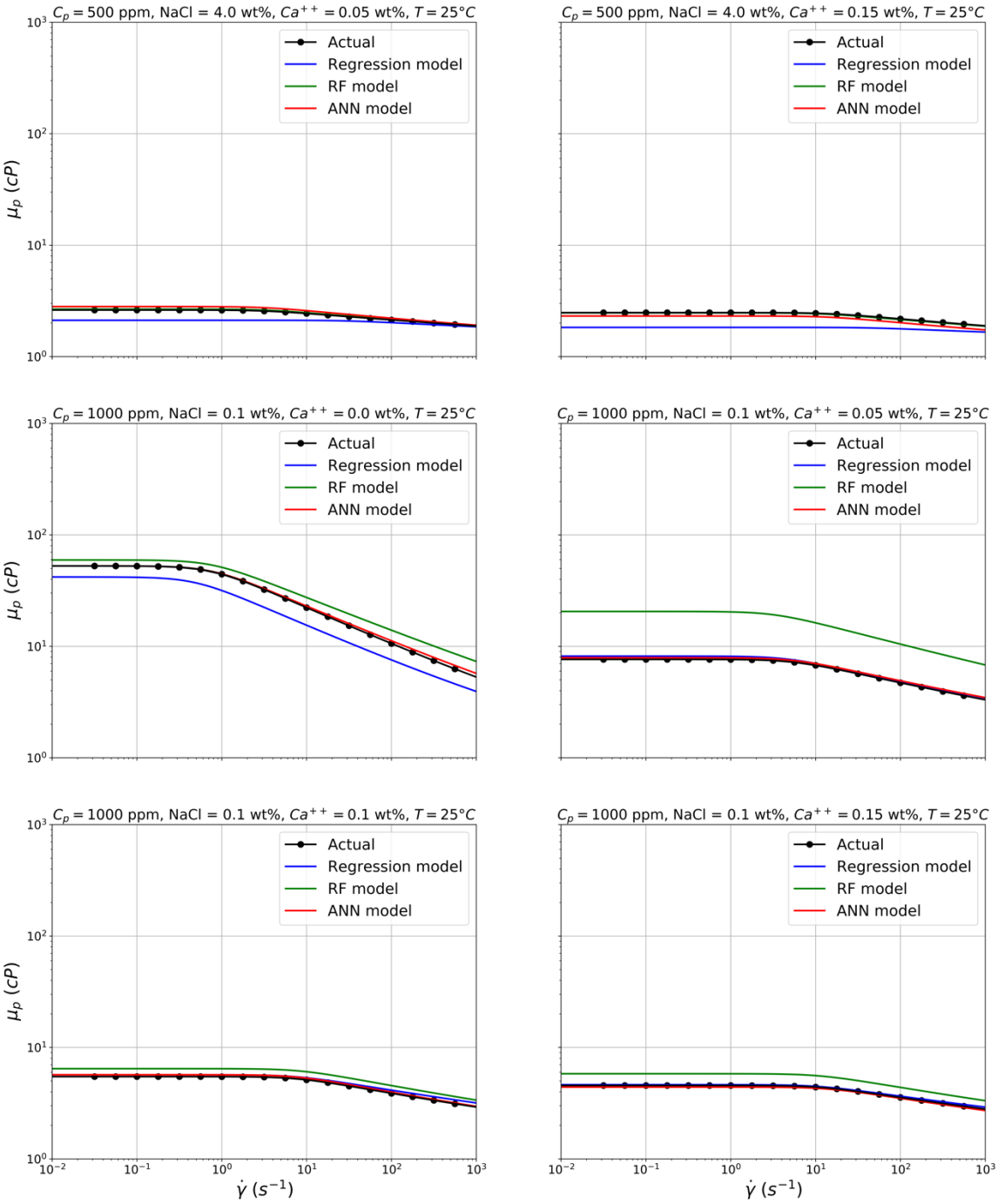
$C_p = 500$ ppm, NaCl = 4.0 wt%, $Ca^{++} = 0.05$ wt%, $T = 25°C$
$C_p = 500$ ppm, NaCl = 4.0 wt%, $Ca^{++} = 0.15$ wt%, $T = 25°C$
$C_p = 1000$ ppm, NaCl = 0.1 wt%, $Ca^{++} = 0.0$ wt%, $T = 25°C$
$C_p = 1000$ ppm, NaCl = 0.1 wt%, $Ca^{++} = 0.05$ wt%, $T = 25°C$
$C_p = 1000$ ppm, NaCl = 0.1 wt%, $Ca^{++} = 0.1$ wt%, $T = 25°C$
$C_p = 1000$ ppm, NaCl = 0.1 wt%, $Ca^{++} = 0.15$ wt%, $T = 25°C$
Actual
Regression model
RF model
ANN model
μ_p (cP)
$\dot{\gamma}$ (s^{-1})

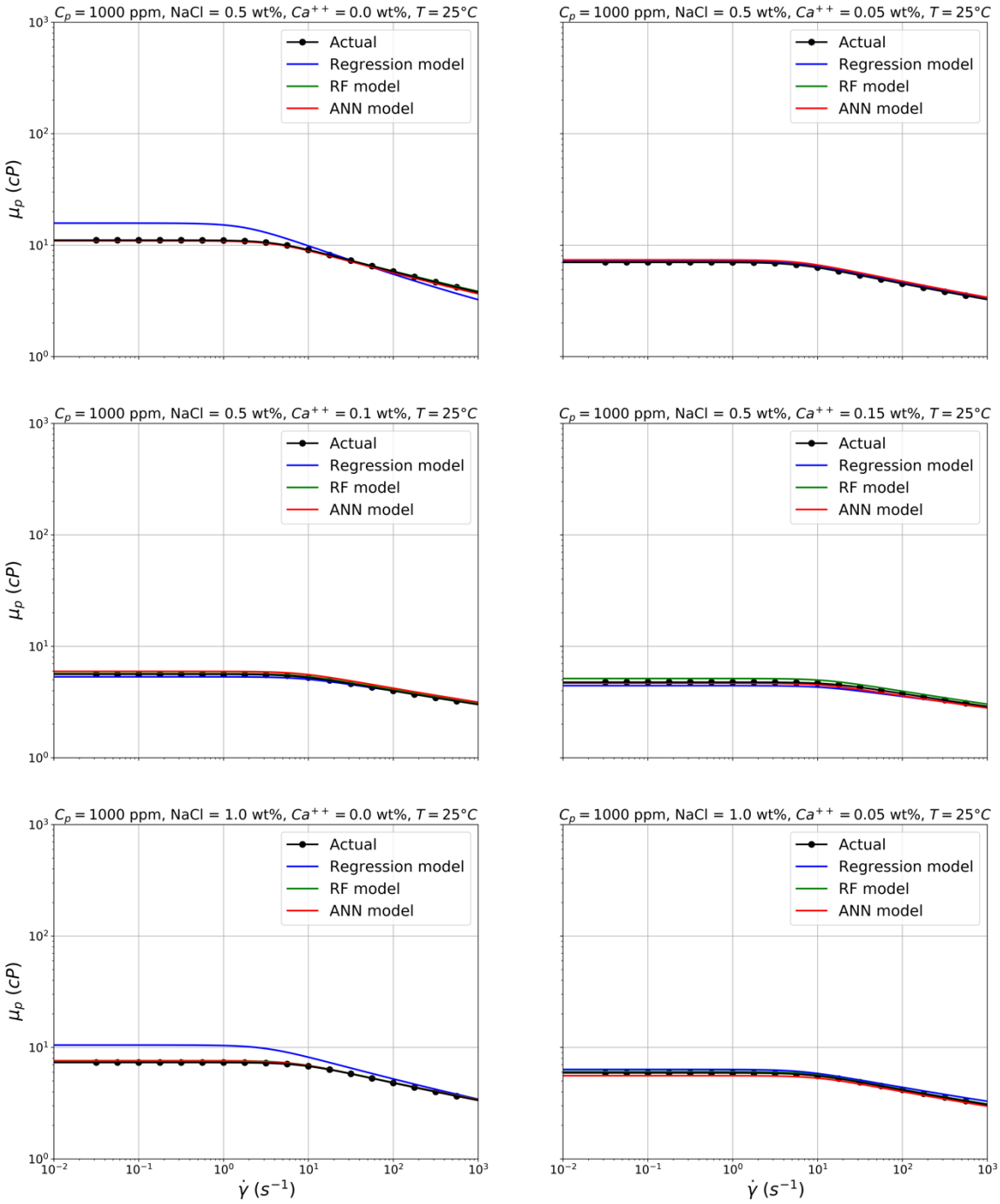
$C_p = 1000$ ppm, NaCl = 0.5 wt%, $Ca^{++} = 0.0$ wt%, $T = 25°C$
$C_p = 1000$ ppm, NaCl = 0.5 wt%, $Ca^{++} = 0.05$ wt%, $T = 25°C$
$C_p = 1000$ ppm, NaCl = 0.5 wt%, $Ca^{++} = 0.1$ wt%, $T = 25°C$
$C_p = 1000$ ppm, NaCl = 0.5 wt%, $Ca^{++} = 0.15$ wt%, $T = 25°C$
$C_p = 1000$ ppm, NaCl = 1.0 wt%, $Ca^{++} = 0.0$ wt%, $T = 25°C$
$C_p = 1000$ ppm, NaCl = 1.0 wt%, $Ca^{++} = 0.05$ wt%, $T = 25°C$
Actual
Regression model
RF model
ANN model
μ_p (cP)
$\dot{\gamma}$ (s^{-1})

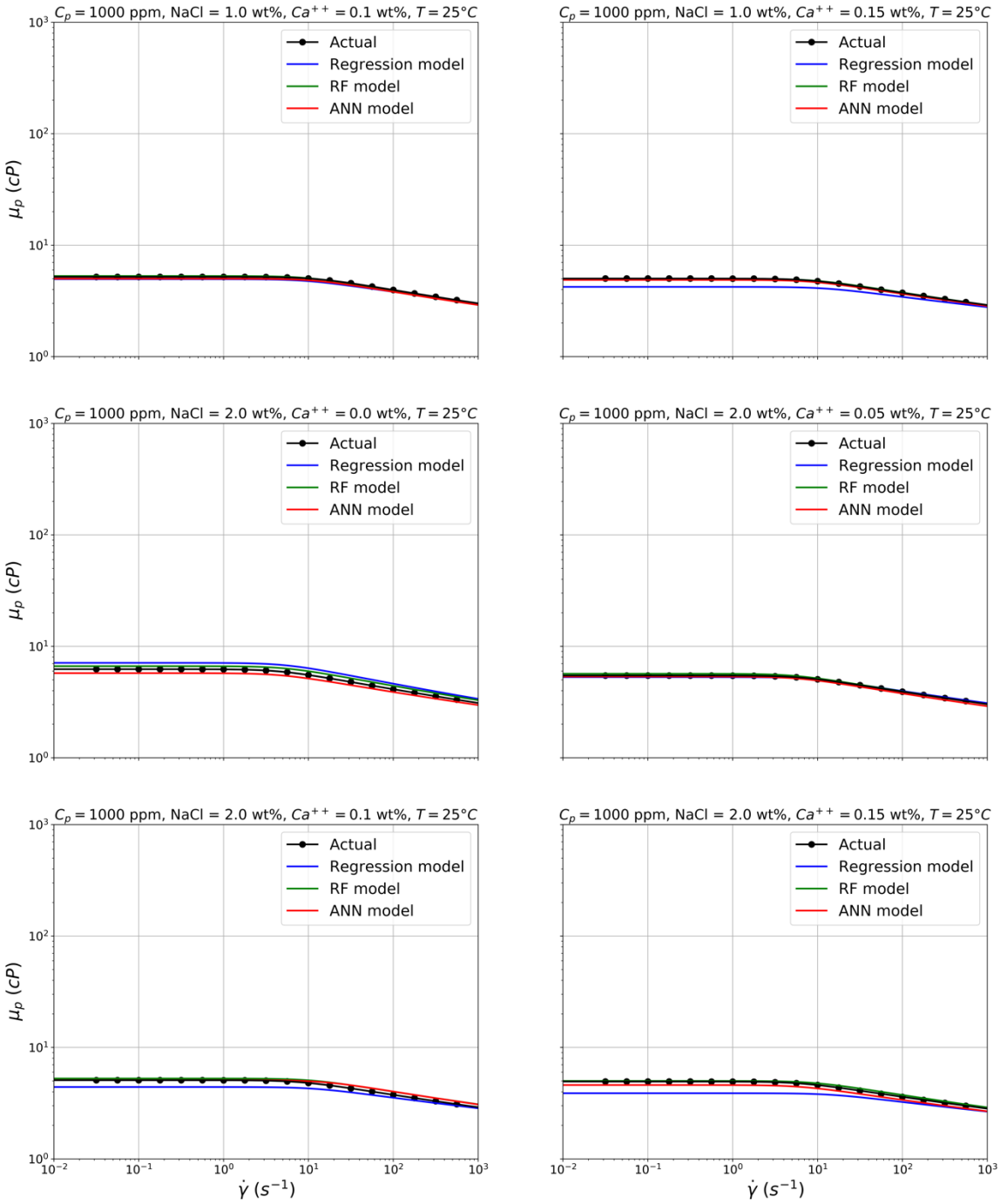
$C_p = 1000$ ppm, NaCl = 1.0 wt%, $Ca^{++} = 0.1$ wt%, $T = 25°C$
$C_p = 1000$ ppm, NaCl = 1.0 wt%, $Ca^{++} = 0.15$ wt%, $T = 25°C$
$C_p = 1000$ ppm, NaCl = 2.0 wt%, $Ca^{++} = 0.0$ wt%, $T = 25°C$
$C_p = 1000$ ppm, NaCl = 2.0 wt%, $Ca^{++} = 0.05$ wt%, $T = 25°C$
$C_p = 1000$ ppm, NaCl = 2.0 wt%, $Ca^{++} = 0.1$ wt%, $T = 25°C$
$C_p = 1000$ ppm, NaCl = 2.0 wt%, $Ca^{++} = 0.15$ wt%, $T = 25°C$
Actual
Regression model
RF model
ANN model
μ_p (cP)
$\dot{\gamma}$ (s^{-1})

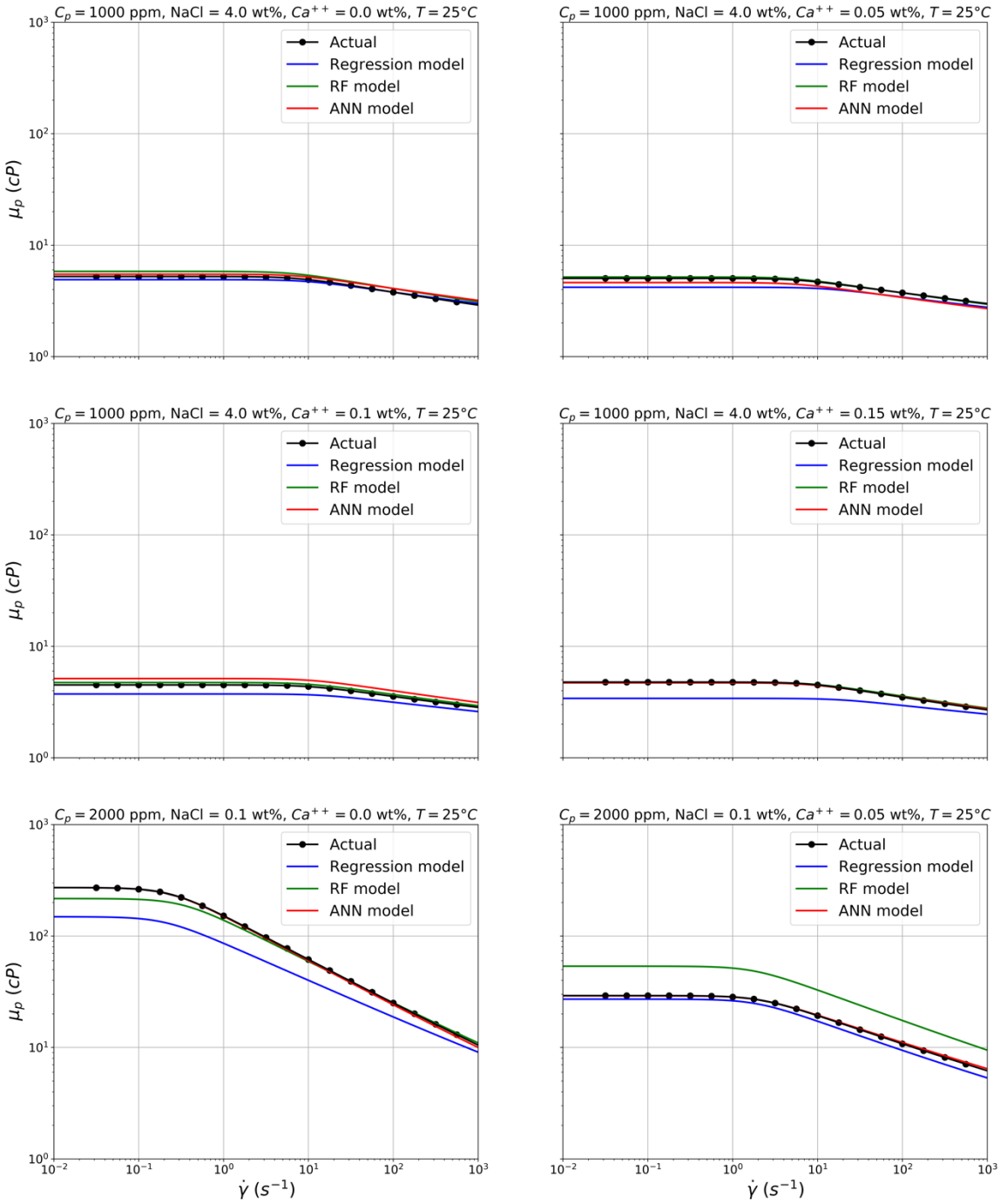
$C_p = 1000$ ppm, NaCl = 4.0 wt%, $Ca^{++} = 0.0$ wt%, $T = 25°C$
$C_p = 1000$ ppm, NaCl = 4.0 wt%, $Ca^{++} = 0.05$ wt%, $T = 25°C$
$C_p = 1000$ ppm, NaCl = 4.0 wt%, $Ca^{++} = 0.1$ wt%, $T = 25°C$
$C_p = 1000$ ppm, NaCl = 4.0 wt%, $Ca^{++} = 0.15$ wt%, $T = 25°C$
$C_p = 2000$ ppm, NaCl = 0.1 wt%, $Ca^{++} = 0.0$ wt%, $T = 25°C$
$C_p = 2000$ ppm, NaCl = 0.1 wt%, $Ca^{++} = 0.05$ wt%, $T = 25°C$
Actual
Regression model
RF model
ANN model
μ_p (cP)
$\dot{\gamma}$ (s^{-1})

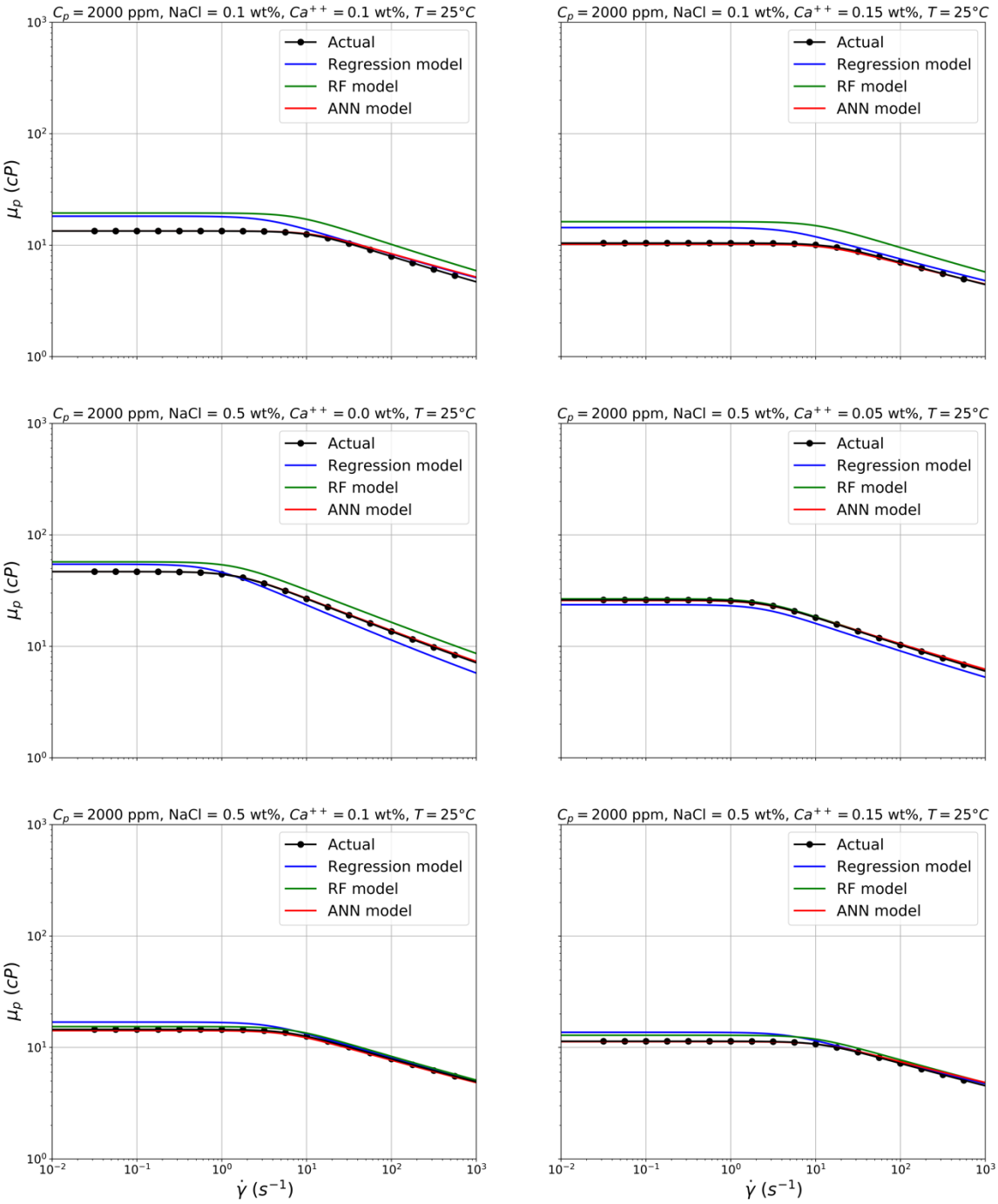
$C_p = 2000$ ppm, NaCl = 0.1 wt%, $Ca^{++} = 0.1$ wt%, $T = 25°C$
$C_p = 2000$ ppm, NaCl = 0.1 wt%, $Ca^{++} = 0.15$ wt%, $T = 25°C$
$C_p = 2000$ ppm, NaCl = 0.5 wt%, $Ca^{++} = 0.0$ wt%, $T = 25°C$
$C_p = 2000$ ppm, NaCl = 0.5 wt%, $Ca^{++} = 0.05$ wt%, $T = 25°C$
$C_p = 2000$ ppm, NaCl = 0.5 wt%, $Ca^{++} = 0.1$ wt%, $T = 25°C$
$C_p = 2000$ ppm, NaCl = 0.5 wt%, $Ca^{++} = 0.15$ wt%, $T = 25°C$
Actual
Regression model
RF model
ANN model
μ_p (cP)
$\dot{\gamma}$ (s^{-1})

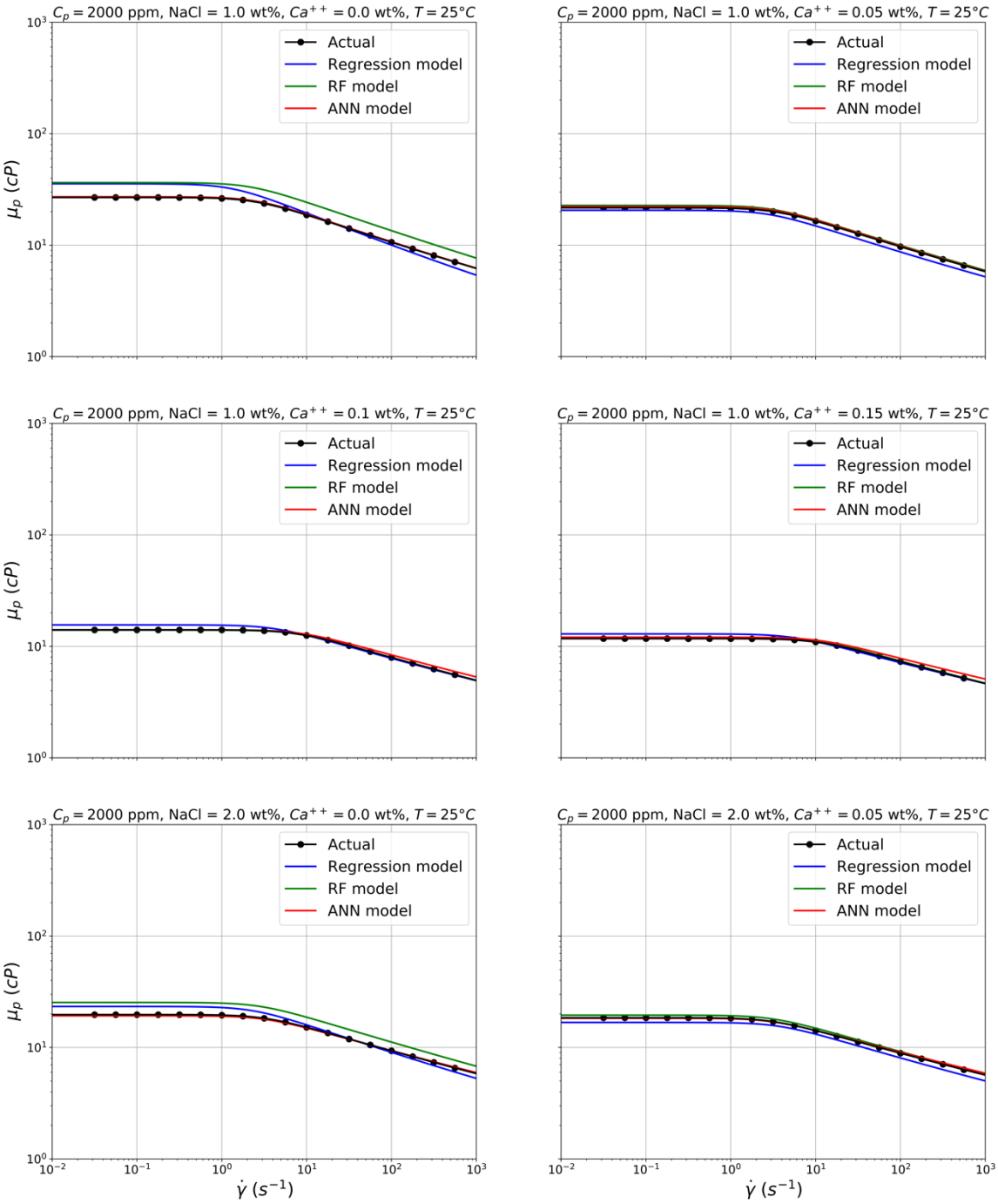
$C_p = 2000$ ppm, NaCl = 1.0 wt%, $Ca^{++} = 0.0$ wt%, $T = 25°C$
$C_p = 2000$ ppm, NaCl = 1.0 wt%, $Ca^{++} = 0.05$ wt%, $T = 25°C$
$C_p = 2000$ ppm, NaCl = 1.0 wt%, $Ca^{++} = 0.1$ wt%, $T = 25°C$
$C_p = 2000$ ppm, NaCl = 1.0 wt%, $Ca^{++} = 0.15$ wt%, $T = 25°C$
$C_p = 2000$ ppm, NaCl = 2.0 wt%, $Ca^{++} = 0.0$ wt%, $T = 25°C$
$C_p = 2000$ ppm, NaCl = 2.0 wt%, $Ca^{++} = 0.05$ wt%, $T = 25°C$
Actual
Regression model
RF model
ANN model
μ_p (cP)
$\dot{\gamma}$ (s^{-1})

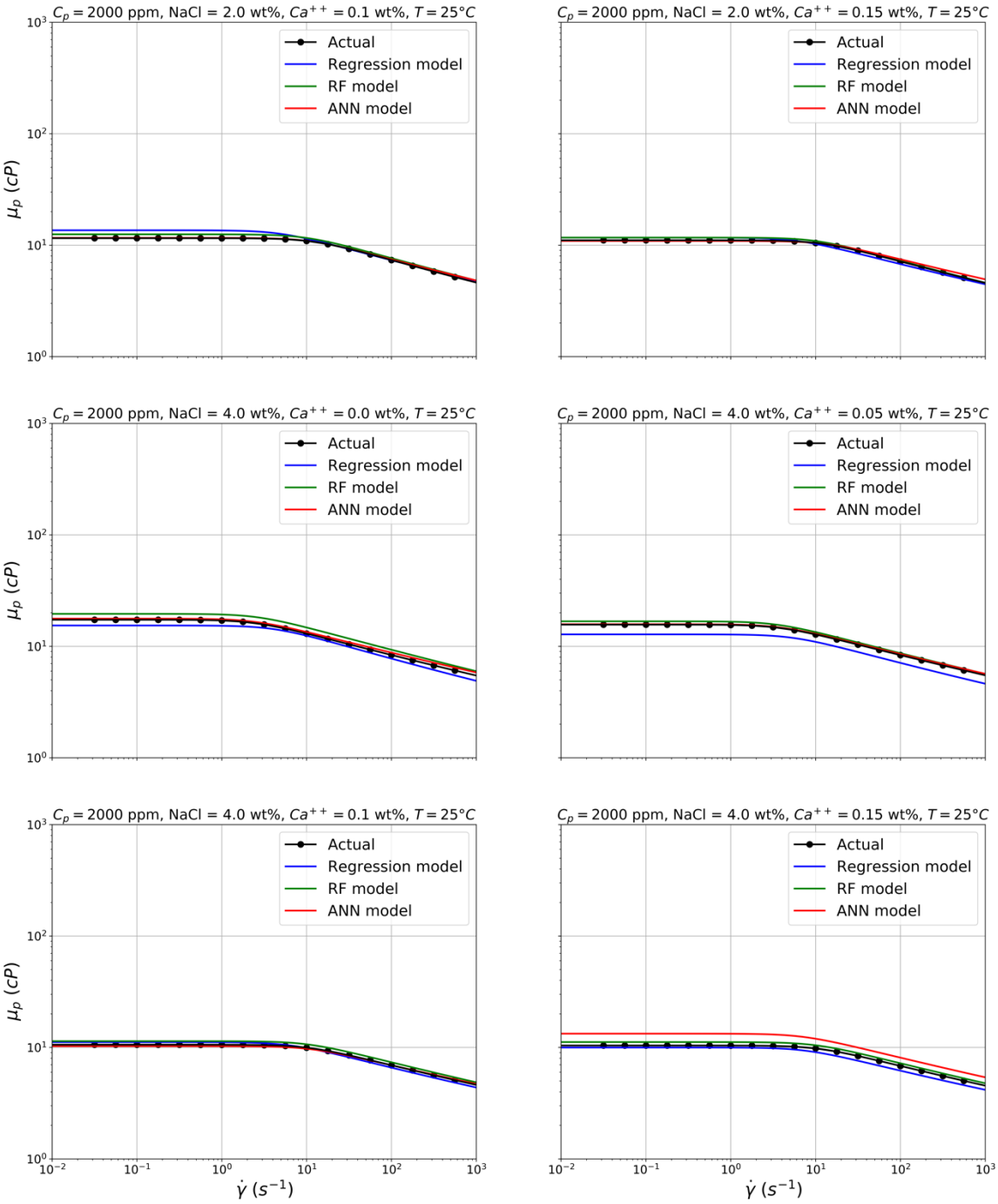
$C_p = 2000$ ppm, NaCl = 2.0 wt%, $Ca^{++} = 0.1$ wt%, $T = 25°C$
$C_p = 2000$ ppm, NaCl = 2.0 wt%, $Ca^{++} = 0.15$ wt%, $T = 25°C$
$C_p = 2000$ ppm, NaCl = 4.0 wt%, $Ca^{++} = 0.0$ wt%, $T = 25°C$
$C_p = 2000$ ppm, NaCl = 4.0 wt%, $Ca^{++} = 0.05$ wt%, $T = 25°C$
$C_p = 2000$ ppm, NaCl = 4.0 wt%, $Ca^{++} = 0.1$ wt%, $T = 25°C$
$C_p = 2000$ ppm, NaCl = 4.0 wt%, $Ca^{++} = 0.15$ wt%, $T = 25°C$
Actual
Regression model
RF model
ANN model
μ_p (cP)
$\dot{\gamma}$ (s^{-1})

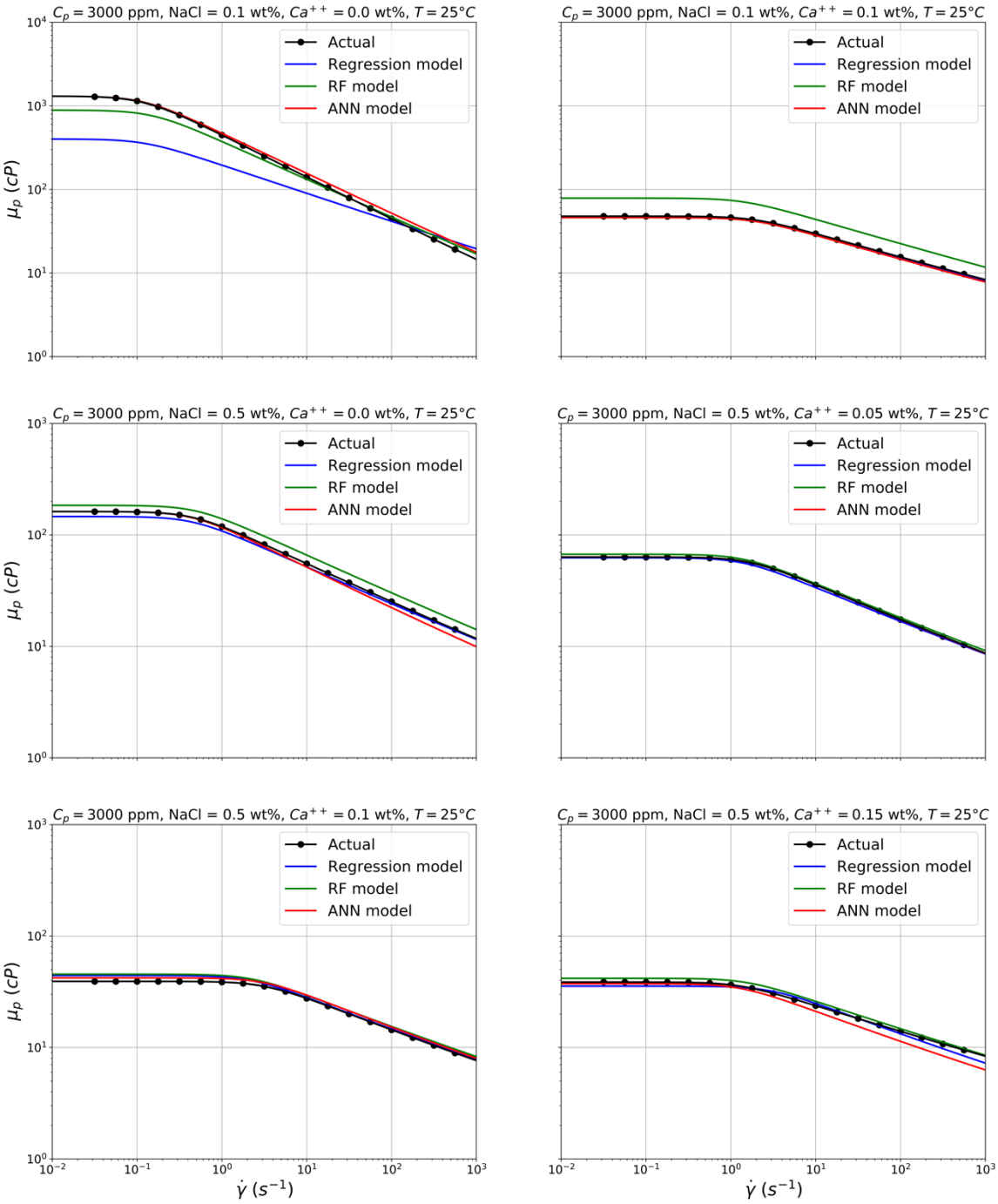
$C_p = 3000$ ppm, NaCl = 0.1 wt%, $Ca^{++} = 0.0$ wt%, $T = 25°C$
$C_p = 3000$ ppm, NaCl = 0.1 wt%, $Ca^{++} = 0.1$ wt%, $T = 25°C$
$C_p = 3000$ ppm, NaCl = 0.5 wt%, $Ca^{++} = 0.0$ wt%, $T = 25°C$
$C_p = 3000$ ppm, NaCl = 0.5 wt%, $Ca^{++} = 0.05$ wt%, $T = 25°C$
$C_p = 3000$ ppm, NaCl = 0.5 wt%, $Ca^{++} = 0.1$ wt%, $T = 25°C$
$C_p = 3000$ ppm, NaCl = 0.5 wt%, $Ca^{++} = 0.15$ wt%, $T = 25°C$
Actual
Regression model
RF model
ANN model
μ_p (cP)
$\dot{\gamma}$ (s^{-1})

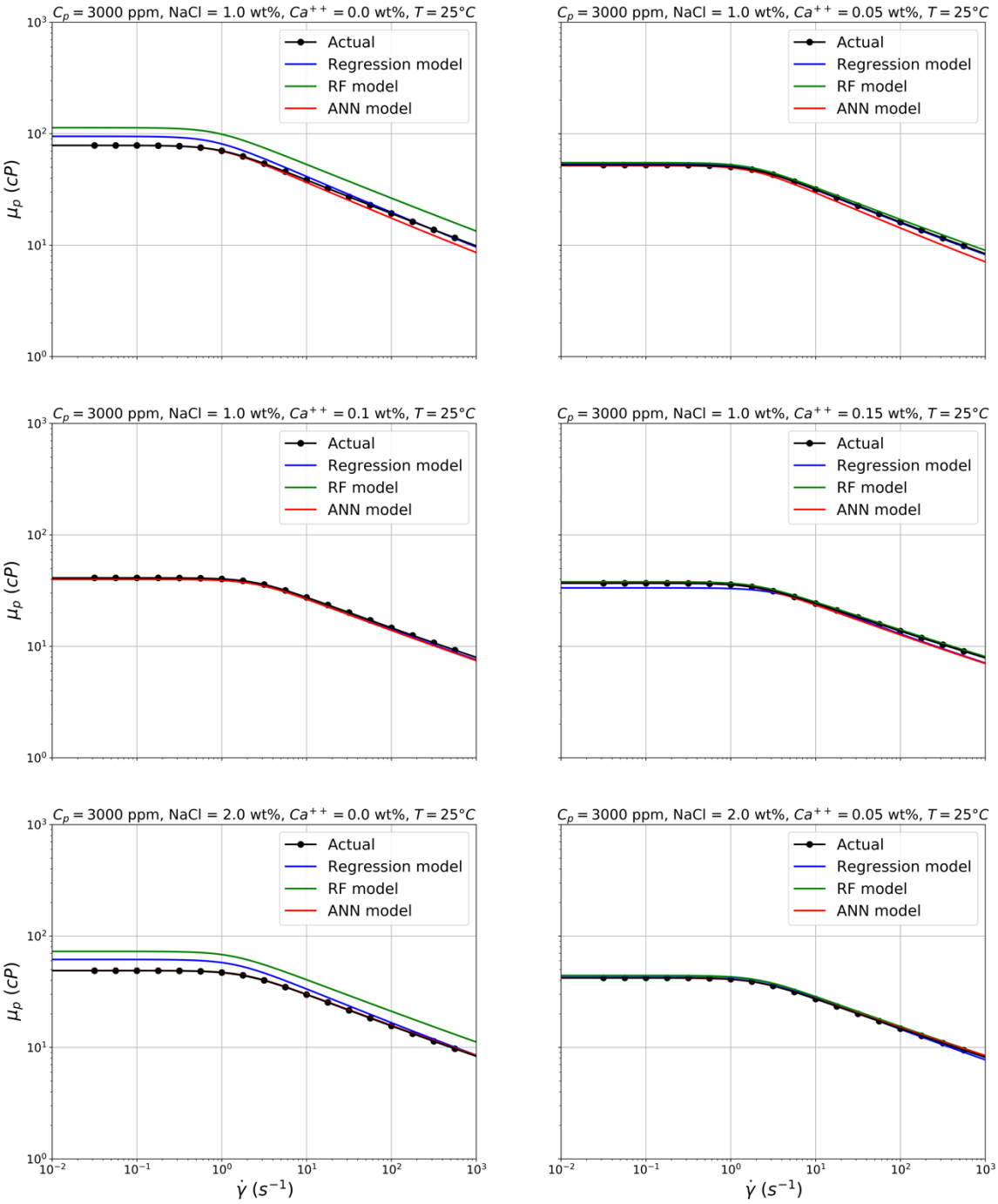
$C_p = 3000$ ppm, NaCl = 1.0 wt%, $Ca^{++} = 0.0$ wt%, $T = 25°C$
$C_p = 3000$ ppm, NaCl = 1.0 wt%, $Ca^{++} = 0.05$ wt%, $T = 25°C$
$C_p = 3000$ ppm, NaCl = 1.0 wt%, $Ca^{++} = 0.1$ wt%, $T = 25°C$
$C_p = 3000$ ppm, NaCl = 1.0 wt%, $Ca^{++} = 0.15$ wt%, $T = 25°C$
$C_p = 3000$ ppm, NaCl = 2.0 wt%, $Ca^{++} = 0.0$ wt%, $T = 25°C$
$C_p = 3000$ ppm, NaCl = 2.0 wt%, $Ca^{++} = 0.05$ wt%, $T = 25°C$
Actual
Regression model
RF model
ANN model
μ_p (cP)
$\dot{\gamma}$ (s^{-1})

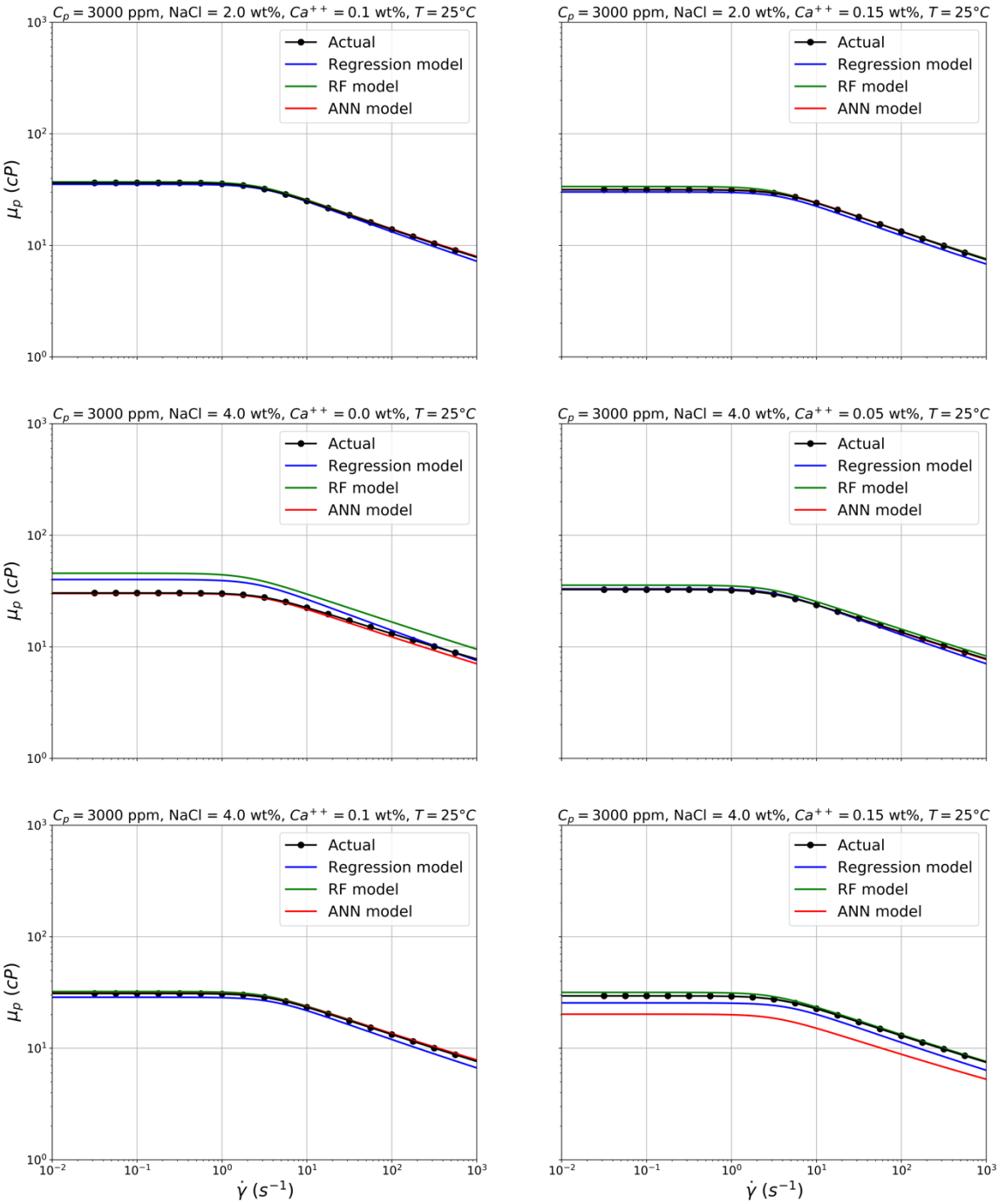

The following plots are at 2000 ppm polymer concentration, 1 wt% NaCl and different temperatures.

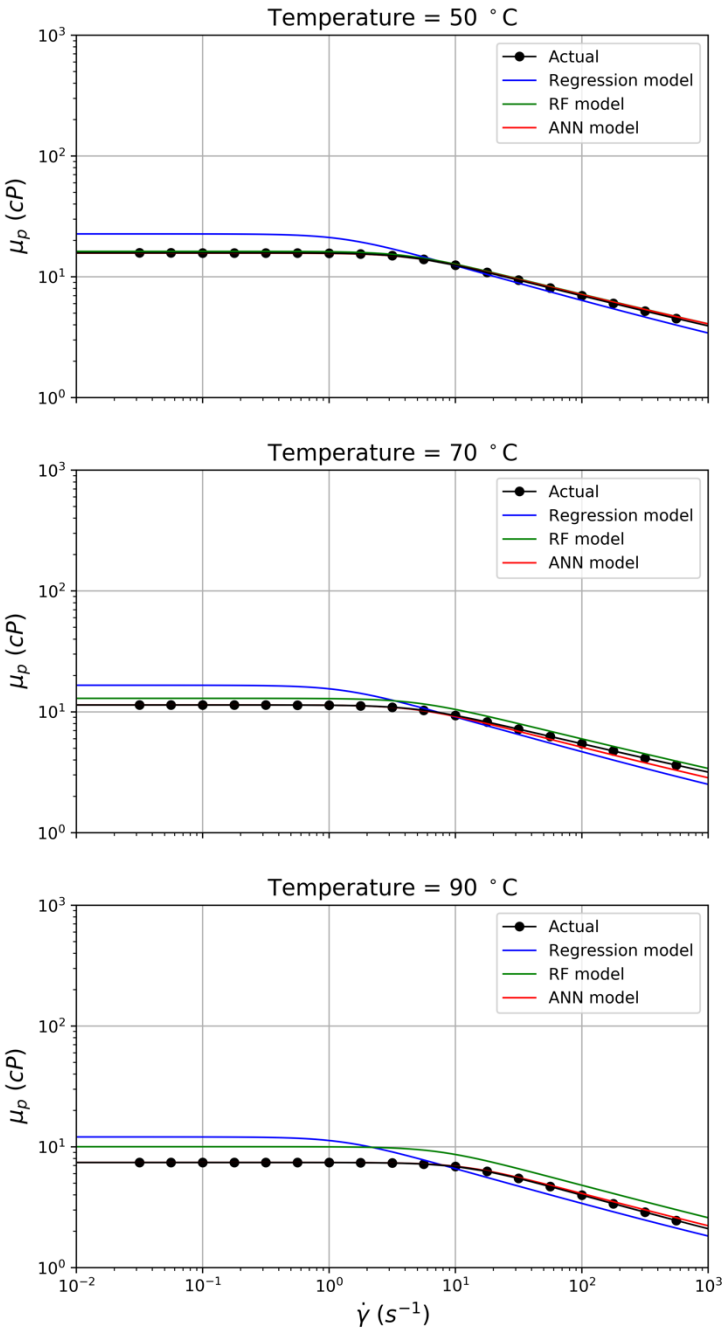
Temperature = 50 °C
Actual
Regression model
RF model
ANN model
μ_p (cP)
Temperature = 70 °C
Actual
Regression model
RF model
ANN model
μ_p (cP)
Temperature = 90 °C
Actual
Regression model
RF model
ANN model
μ_p (cP)
$\dot{\gamma}$ (s^{-1})

References

Abdel-khalik, S. I., Hassager, O., & Bird, R. B. (1974, December). Prediction of Melt Elasticity From Viscosity Data. *Polymer Engineering and Science, 14*(12), 859-867.

Al-Shalabi, E. W., Luo, H., Delshad, M., & Sepehrnoori, K. (2015). Single-Well Chemical Tracer Modeling of Low Salinity Water Injection in Carbonates. *SPE Western Regional Meeting.* Society of Petroleum Engineers.

Bird, R. B., Armstrong, R. C., & Hassager, O. (1987). *Dynamics of Polymeric Liquids* (Vols. 1: Fluid Mechanics, 2nd Edition). Wiley.

Bird, R. B., Hassager, O., & Abdel-khalik, S. I. (1974, November). Co-rotational Rheological Models and the Goddard Expansion. *AIChE Journal, 20*(6), 1401-1066.

Bird, R. B., Stewart, W. E., & Lightfoot, E. N. (1960). *Transport Phenomena.* Wiley.

Cannella, W. J., Huh, C., & Seright, R. S. (1988). Prediction of Xanthan Rheology in Porous Media. 353-368.

Carreau, P. J. (1972). Rheological Equations from Molecular Network Theories. *16*(1), 99-127.

Carreau, P. J., De Kee, D. C., & Chhabra, R. P. (1997). *Rheology of polymeric systems: principles and applications.* Hanser/Gardner Publications, Inc.

Castelletto, V., Hamley, I. W., Xue, W., Sommer, C., Pedersen, J. S., & Olmsted, P. D. (2004). Rheological and structural charactrization hydrophobically modified polyacrylamide solutions in the semidilute regime. *Macromolecules, 37*(4), 1492-1501.

Chang, H. L., Zhang, Z. Q., Wang, Q. M., Xu, Z. S., Guo, Z. D., Sun, H. Q., . . . Qiao, Q. (2006). Advances in Polymer Flooding and Alkaline/Surfactant/Polymer Processes as Developed and Applied in the People's Republic of China. *Journal of Petroleum Technology, 58*(02), 84-89.

Chauvetean, G. (1982). Rodlike polymer solution flow through fine pores: Influnce of pore size on rheological behavior. *J. Rheology, 26*(2), 111-142.

Chauveteau, G., & Zaitoun, A. (1981). Basic rheological behaviour of xanthan polysaccharide solutions in porous media: effects of pore size and polymer concentration. *First European Symposium on EOR.* Bournemouth, England.

Craig, F. (1971). *The Reservoir Engineering Aspects of Waterflooding.* Society of Petroleum Engineering.

Dake, L. P. (1978). *Fundamentals of reservoir engineering.* Elsevier Science.

Delshad, M., Asakawa, K., Pope, G. A., & Sepehrnoori, K. (2002). Simulations of Chemical and Microbial Enhanced Oil Recovery Methods. *SPE/DOE Improved Oil Recovery Symposium.* Tulsa, Oklahoma: Society of Petroleum Engineers.

Delshad, M., Kim, D. H., Magbagbeola, O. A., Huh, C., Pope, G., & Tarahhom, F. (2008). Mechanistic Interpretation and Utilization of Viscoelastic Behavior of Polymer Solutions for Improved Polymer-Flood Efficiency. *SPE/DOE Improved Oil Recovery* . Tulsa, Oklahoma: SPE.

Delshad, M., Pope, G. A., & Sepehrnoori, K. (1996). A compositional simulator for modeling surfactant enhanced aquifer remediation, 1 Formulation. *Journal of Contaminant Hydrology, 23*, 303-327.

Erincik, M. Z., Qi, P., Balhoff, M. T., & Pope, G. A. (2017). New Method to Reduce Residual Oil Saturation by Polymer Flooding. *SPE Annual Technical Conference and Exhibition.* San Antonio, TX: Society of Petroleum Engineers.

Flory, P. J. (1953). *Principles of Polymer Chemistry* . Cornell University Press.

Gao, C. H. (2014). Comprehensive Correlations to Calculate Viscosity of Partially Hydrolyzed Polyacrylamide. *SPE EOR Conference at Oil and Gas West Asia.* Muscat, Oman: SPE.

Green, D. W., & Willhite, G. P. (1998). *Enhanced Oil Recovery, Second Edition.* Richardson: Society of Petroleum Engineers.

Han, C. D. (2007). *Rheology and Processing of Polymeric Materials.* New York: Oxford University Press, Inc.

Hashmet, M. R., Onur, M., & Tan, I. M. (2014). Empirical Correlations for Viscosity of Polyacrylamide Solutions with the Effects of Concentration, Molecular Weight and Degree of Hydrolysis of Polymer. *Journal of Applied Sciences, 14*, 1000-1007.

James, G., Witten, D., Hastie, T., & Tibshirai, R. (2013). *An Introduction to Statistical Learning: With Applications in R.* Springer.

Jouenne, S., Heurteux, G., Hourcq, C., Joly, M., Questel, M., & Levache, B. (2019). Universal Viscosifying Behavior Of Acrylamide-based Polymers Used In EOR - Application For QA/QC, Viscosity Predictions And Field Characterization. *20th European Symposium on Improved Oil Recovery.* Pau, France: EAGE.

Kang, P.-S., Lim, J.-S., & Huh, C. (2013). A Novel Approach in Estimating Shear-Thinning Rheology of HPAM and AMPS Polymers for Enhanced Oil Recovery Using Artificial Neural Network. *Twenty-third International Society of Offshore and Polar Engineers.* Anchorage, Alaska, USA: ISOPE.

Kim, D. H., Lee, S., Ahn, C. H., Huh, C., & Pope, G. A. (2010). Development of a Viscoelastic Property Database for EOR Polymers. *2010 SPE Improved Oil Recovery Symposium* . Tulsa, OK: SPE.

Koh, H., Lee, V. B., & Pope, G. A. (2017). Experimental Investigation of the Effect of Polymers on Residual Oil Saturation. *SPE Journal, 23*(1), 1-17.

Lake, L. W. (1989). *Enhanced Oil Recovery.* Prentice Hall .

Lashgari, H., Pope, G., Balhoff, M., & Tagavifar, M. (2019). New and Improved Physical Property Models for Chemical Flooding Simulators. *SPE Reservoir Simulation Conference.* Galveston, Texas: Society of Petroleum Engineera.

Lee, S. (2009). *Development of a Comprehensive Rheological Property Database for EOR Polymers.* Master Thesis, University of Texas at Austin.

Lee, S., Kim, D., Huh, C., & Pope, G. A. (2009). Development of a Comprehensive Rheological Property Database for EOR Polymers. *2009 SPE Annual Technical Conference and Exhibition.* New Orleans: Society of Petroleum Engineers.

Levitt, D. B., & Pope, G. A. (2008). Selection and Screening of Polymers for Enhanced-Oil Recovery. *SPE/DOE Improved Oil Recovery Symposium.* Tulsa, Oklahoma: SPE.

Li, Z., & Delshad, M. (2014, June). Development of an Analytical Injectivity Model for Non-Newtonian Polymer Solutions. *SPE Journal, 19*(03), 381-389.

Lotfollahi, M., Koh, H., Li, Z., Delshad, M., & Pope, G. (2016). Mechanistic Simulation of Residual Oil Saturation in Viscoelastic Polymer Floods. *SPE EOR Conference at Oil and Gas West Asia.* Muscat, Oman: Society of Petroleum Engineers.

Lovell, P. A. (1996). Dilute Solution Viscometry . In *Comprehensive Polymer Science* (Vol. Volume 1). Elsevier Ltd.

Manrique, E. J., Muci, V. E., & Gurfinkel, M. E. (2007, December). EOR Field Experiences in Carbonate Reservoirs in the United States. *SPE Reservoir Evaluation & Engineering, 10*(6), 667-686.

Marsland, S. (2015). *Machine Learning An Algorithmic Perspective.* Taylor & Francis Group, LLC.

Martin, A. F. (1951). Toward a Referee Viscosity Method for Cellulose. *34*(363).

Masuda, Y., Tang, K., Miyazawa, M., & Tanaka, S. (1992, May). 1D Simulation of Polymer Flooding Including the Viscoelastic Effect of Polymer Solution. *SPE Reservoir Engineering*, 247-252.

Meter, D. M., & Bird, R. B. (1964, November). Tube flow of non-Newtonian polymer solutions: PART I. Laminar flow and rheological models. *AlChE Journal, 10*(6), 878-881.

Nasr-EI-Din, H. A., Hawkins, B. F., & Green, K. A. (1991). SPE 21028 Viscosity Behavior of Alkaline, Surfactant, Polyacrylamide Solutions Used for Enhanced Oil Recovery. *SPE International Symposium on Oilfield Chemistry.* Anaheim, California: SPE.

Olajire, A. A. (2014). Review of ASP EOR (alkaline surfactant polymer enhanced oil recovery) technology in the petroleum industry: Prospects and challenges. *Energy J., 77*, 963-982.

Russell, S. J., & Norvig, P. (2010). *Artificial Intelligance: A Modern Approach.* Prentice Hall.

Shah, P. P., & Parsania, P. H. (1984). Zero-shear viscosity of dilute to moderately concentrated solutions of poly[2-methoxy-4, 6-di-(p, p′-isopropylidene diphenyloxy)-s-triazine]. *Journal Journal of Macromolecular Science, Part B, 23*(4-6), 363-372.

Sheng, J. (2010). *Modern Chemical Enhanced Oil Recovery: Theory and Practice.* Gulf Professional Publishing.

Sorbie, K. S. (1991). *Polymer-Improved Oil Recovery.* Springer.

Stevenson, J. F. (1972). Elongational flow of polymer melts. *AIChE Journal, 18*(3), 540-547.

Tam, K. C., & Tiu, C. (1990). Role of ionic species and valency on the steady shear behavior of partially hydrolyzed polyacrylamide solutions. *Colloid Polym Sci.*(268), 911-920.

UTCHEM. (2018). *Volume II: Technical Documentation for UTCHEM 2018.1; A Three-Dimensional Chemical Flood Simulator.* Center for Petroleum and Geosystems Engineering, University of Texas at Austin.

Wang, H. Y., Cao, X. L., Zhang, J. C., & Zhang, A. M. (2009). Development and application of dilute surfactant-polymer flooding systemfor Shengli oilfield . *Journal of Petroluem Science and Engineering, 65*(1), 45-50.

Ward, J., & Martin, F. D. (1981). Prediction of Viscosity for Partially Hydrolyzed Polyacrylamide Solutions in the Presence of Calcium and Magnesium Ions. *SOCIETY OF PETROLEUM ENGINEERS JOURNAL, 21*, 623-631.

Xia, H., Wang, D., Wu, J., & Kong, F. (2004). Elasticity of HPAM Solutions Increases Displacement Efficiency under Mixed Wettability Conditions. *SPE Asia Pacific Oil and Gas Conference and Exhibition.* Society of Petroleum Engineers.

Young, R. J., & Lovell, P. A. (1991). *Introduction to Polymers.* Springer.

Zhao, F. L. (1991). *Chemistry in oil Production.* China: University of Petroleum.